NUMERICAL MODELLING OF WEST AFRICA REGIONAL SCALE AEROSOL DISPERSION

By

EMETERE Moses Eterigho Azuka
(Matric Number: 13PCE005329)

DECEMBER, 2016

NUMERICAL MODELLING OF WEST AFRICA REGIONAL SCALE AEROSOL DISPERSION

By

EMETERE, Moses Eterigho Azuka

(Matric Number: 13PCE005329)
B.Tech. Applied Physics (Ogbomoso)
M.Tech. Solid State Physics (Minna)

A THESIS SUBMITTED TO THE SCHOOL OF POSTGRADUATE STUDIES OF COVENANT UNIVERSITY, OTA, OGUN STATE, NIGERIA

IN PARTIAL FULFILMENT OF THE REQUIREMENTS FOR THE AWARD OF DOCTOR OF PHILOSOPHY (Ph.D) DEGREE IN PHYSICS, IN THE DEPARTMENT OF PHYSICS, COLLEGE OF SCIENCE AND TECHNOLOGY, COVENANT UNIVERSITY, OTA, OGUN STATE, NIGERIA

DECEMBER, 2016

ACCEPTANCE

This is to attest that this thesis is accepted in partial fulfilment of the requirements for the award of the degree of **Doctor of Philosophy** in **Physics in the Department of Physics, College of Science and Technology, Covenant University, Ota.**

Mr John A. Philip ……..

Secretary, School of Postgraduate Studies Signature & Date

Prof. Samuel T. Wara ……..

Dean, School of Postgraduate Studies Signature & Date

DECLARATION

I, **EMETERE Moses Eterigho Azuka**, (13PCE005329), declare that this research was carried out by me under the supervision of Prof. Marvel L. Akinyemi of the Department of Physics, Covenant University, Ota and Dr. Omololu Akin-Ojo of the Department of Physics, University of Ibadan, Ibadan. I attest that the thesis has not been presented either wholly or partly for the award of any degree elsewhere. All sources of data and scholarly information used in this thesis are duly acknowledged.

EMETERE Moses Eterigho Azuka ……..

Signature & Date

CERTIFICATION

We certify that the thesis titled "Numerical Modelling of West Africa Regional Scale Aerosol Dispersion" is an original work carried out by Mr. **EMETERE Moses Eterigho Azuka**, (13PCE005329), in the Department of Physics, College of Science and Technology, Covenant University, Ota, Ogun State, Nigeria, under the supervision of Prof. Marvel L. Akinyemi and Dr. Omololu Akin-Ojo. We have examined and found the work acceptable for the award of a degree of Doctor of Philosophy in Physics.

Prof. Marvel L. Akinyemi ……..

Supervisor Signature & Date

Dr. Omololu Akin-Ojo ……

Co-Supervisor Signature & Date

Dr. Mojisola R. Usikalu ….……

Head of Department Signature & Date

Prof. Charity U. Okujagu ....……

External Examiner Signature & Date

Prof. Samuel T. Wara …..……

Dean, School of Postgraduate Studies Signature & Date

DEDICATION

This work is dedicated to my beloved wife, Mrs. Jennifer Emetere, and mother, Mrs. Josephine Emetere.

ACKNOWLEDGEMENTS

I wish to express my profound gratitude to God the Father, God the Son (Christ Jesus) and God the Holy Ghost for the unfailing mercies, graces and inspirations. I salute the Chancellor of Covenant University, Dr. David O. Oyedepo, for his spiritual and intellectual commitment in ensuring that I see myself as a world class researcher. I sincerely acknowledge the financial supports of the management of Covenant University for sponsoring the publication of papers from this thesis. I personally wish to express my profound gratitude to the erstwhile Vice Chancellor, Covenant University, Prof. Charles K. Ayo, for his personal encouragement and fatherly push. I recognize the efforts of the Vice Chancellor, Covenant University, Prof. A. A. A. Atayero, for approving both publication and conference sponsorship during my programme. I appreciate the Head of Department, Physics, Dr. M.R. Usikalu, for her role during this programme.

I appreciate the efforts of my Lead Supervisor, Prof. Marvel L. Akinyemi, for the in-depth mentorship in the field. Thank you Ma for your patience and advice. I thankfully acknowledge my Co-Supervisor, Dr. Omololu Akin-Ojo, for his contribution to this work.

I appreciate the ceaseless support of my beloved wife, Mrs. Jennifer Emetere. I acknowledge the parental role of my beloved mother, Mrs. Josephine Emetere who has been holding the fort since the demise of my father-Mr. Christopher Emetere. I am indeed grateful for the moral support I received from my siblings and children.

I acknowledge the contribution of the faculty and staff of the Department of Physics, Covenant University Ota. I wish to thank all the reviewers and assessors of this thesis for their meaningful and timely contributions. God bless you all in Jesus name.

TABLE OF CONTENTS

CHAPTER FOUR: RESULTS AND DISCUSSION

LIST OF TABLES

LIST OF FIGURES

LIST OF FREQUENTLY USED SYMBOLS

Symbols	Interpretation	Unit
λ	Mean free path	m
d_a	Aerosol diameter	m
r_a	Aerosol radius	m
c	contaminant concentration	kg/m^3
ρ	Density	kg/m^3
t	Time	s
u_x, u_y, u_z	Wind speed in three directions	m/s
k_x, k_y, k_z	Turbulent diffusivity in three directions	m^2/s
C(x,y,z)	Mean concentration of diffusing pollutants	kg/m^3
Ky, Kx	Eddy diffusivities in the direction y- and z- axes	m^2/s
S	Source/sink term	kg/m^{3}s
$C_o x_o \delta(t,x)$	Initial solute concentration	kg/m^3
τ_a	Aerosol optical depth	Unitless
$\tau(\lambda)_{tot}$	Total optical depth	Unitless
$\tau(\lambda)_{Rayleigh}$	Optical depth of the Rayleigh scattering	Unitless
ψ_k (k = 1, …, N_a)	Concentrations of gaseous admixtures	kg/m^3
F^{gas} and F^{aer}	Emissions of gaseous admixtures and aerosols	Unitless
P^{nucl}	Operators of nucleation	Unitless
P^{cond}	Operators of condensation	Unitless
P^{coag}	Operators of coagulation	Unitless
P^{chem}	Operators of photochemical transformation	Unitless
dP	Pressure difference	mbar
dz	Height	m
dA	Surface area	m^2

g	Acceleration due to gravity	m/s^2
j	Atmospheric layer	Unitless
Q_e	Extinction efficiency	Unitless
D_L	Longitudinal dispersion coefficient	m^3/kgs
D_T	Transverse dispersion coefficient	m^3/kgs
$G_s(\lambda)$	Extra-terrestrial index	Unitless
AOD	Aerosol Optical Depth	Unitless
SWAMMA	Saharan West African Monsoon Multiscale Analysis	
AERONET	Aerosol Robotic Network	
NERC	Natural Environment Research Council	
AEOD	Aerosol Extinction Optical Depth	
NASA	National Aeronautics and Space Administration	

APPENDIX I: LIST OF TABLES

APPENDIX II: LIST OF FIGURES

Abstract

The danger of aerosols loading in the lower atmosphere of West Africa is a source of concern both at the short or long term. Currently, there are about 45% available data sets over West Africa; hence, it is difficult to ascertain the level of threat that life forms in this region would be exposed to in the nearest future. In this thesis, it was proposed that the current challenges bedevilling the functionality of measuring devices are more of systemic error than design error. The aim of the research is to develop a comprehensive model, that is, two main and supportive models for retrieving and forecasting atmospheric aerosols in West Africa. The governing equations that was developed in the expanded Stokes' regime were resolved using analytical and numerical techniques. The unified number was derived to address the aerosols transportation inadequacies which were verified on the aerosol size distribution over some locations in West Africa. Three types of data set were used for this study; thirteen years from Nigerian Meteorological Agency datasets for six locations in Nigeria, fourteen years MISR dataset for twenty eight locations across West Africa, ten years AERONET dataset for four locations across West Africa. The new dispersion model designed in this thesis was tested on the four indicators, that is, aerosol transport in the micro scale, aerosols transport in the macro scale, aerosol size distribution, and atmospheric field application. The dispersion showed accuracy in the four listed indicators. Moving aerosols layer over West Africa travels at a speed of 8 m/s to 15 m/s. The atmospheric and tuning constants across twenty eight locations in West Africa were documented for research and industrial use. The atmospheric and tuning constants over West Africa are within the range 0.3 to 1.2 and 0.4 to 0.7 respectively. The average aerosols retention over West Africa is 30% . The aerosols retention was as high as 79% over Ouagadougou-Burkina Faso in 2002. Also the aerosols retention was as low as 0.25% over Praia-Cape Verde in 2002. The highest aerosols rentention in Ilorin and Lagos is 14.9% and 12% respectively. The accuracy of the proposed models in West Africa was within 95% confidence bounds. The standard error (SE) was 0.006216 and R-square was 0.9468. It was concluded that the current state of aerosols loading requires urgent intervention to avoid excessive heat flux like the case of India. More so, the menace of climate change may be more visible in West Africa in the nearest future if necessary policies are not in place. Salient recommendations were made to curb the long term threats to life-form.

CHAPTER ONE

INTRODUCTION

1.1 Background of the Research

The unique distribution of aerosols over the West African region in the last decade is evident in its diverse effects on life forms (Oluwole, 2015), regional meteorology (Nicholson, 2013) and the ozone layer (Akinyemi, 2007). The satellite imagery of aerosols loading over West Africa from 2000-2015 show the implication of the impact of anthropogenic air pollution on human health, agricultural produce, thermal comfort and climate perturbations. Aerosols are suspension of small liquid or solid particles in air or gas. The sources of aerosols include vehicles exhaust (soot/black carbon, organics), industrial emissions (soot/black carbon, sulphate, organics, metals and nitrate), construction and agriculture emission (soot/black carbon, nitrate and soil), sea-spray (salt), biomass and fires (soot/black carbon, nitrate and organics) (Sun *et al.*, 2013). The general characteristic of any type of aerosol particles are its heterogeneous structure, that is, their different sizes, shapes and stoichiometry. There are two major types of aerosols; natural and man-made or anthropogenic aerosol. Aerosols sizes range from nanometers to tens of micrometers (Sun *et al.*, 2013; Zhao *et al*., 2015).

Also, aerosols can be atmospheric or non atmospheric aerosols (pollen, spores, bacteria, aerosol spray). The kind of aerosols considered in this research is the atmospheric aerosols particles (AAP). Atmospheric aerosols are particulate matter (solid, liquid or gas) suspended in air with diameters ranging between about 0.002 μm to 100 μm. There are two types of atmospheric aerosols, primary atmospheric aerosols and secondary atmospheric aerosols. Primary atmospheric aerosols (region A in Figure (1.1)) are particulates that emit directly into the atmosphere (for example, smoke, dust, sea-salt and volcanic ash) while secondary atmospheric aerosols (region B in Figure (1.1)) are particulates that are formed via gas-to-particles conversion processes in the atmosphere (for example, nitrates, and sulphates).

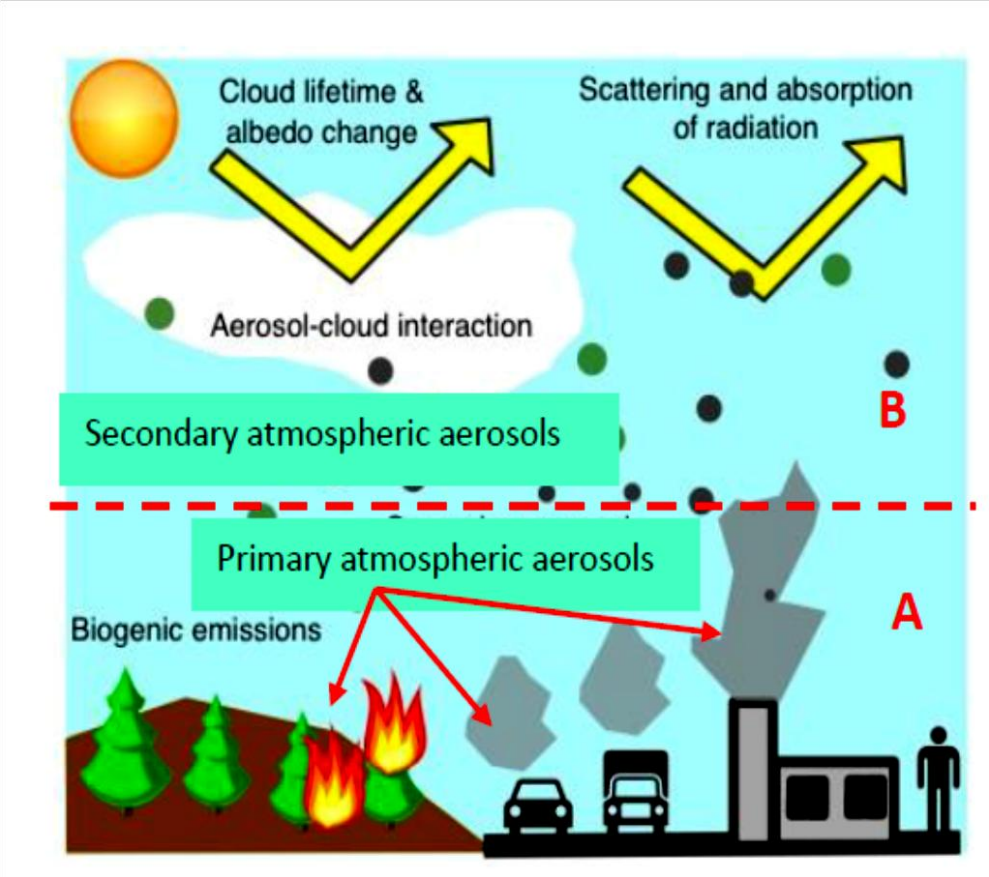

Figure 1.1: Primary and secondary atmospheric aerosols region (Shunsuke, 2004)

Atmospheric aerosol particles are either very absorbing or reflecting. They have limited lifetimes in the atmosphere (Sun *et al.,* 2013). Hence, satellite observations of aerosols are dynamic and cannot be described adequately via quantitative models. The particulate size of the atmospheric aerosol can be divided into its modal constituent's; coarse mode ($d > 2.5$ μm) and fine mode ($d < 2.5$ μm) which is divided into two: nuclei mode (about 0.005 μm $< d < 0.1$ μm) and accumulation mode (0.1μm $< d < 2.5$ μm). Here d is the diameter of the particulate. Aerosols in the accumulation mode have the following characteristics; dry diameters between 0.1 and 1 μm, high scattering efficiency, longest atmospheric lifetime, very active cloud condensation nuclei (CCN) formation (Shunsuke, 2004; Zhao *et al*., 2015).

Atmospheric aerosol particles have direct radiative forcing because of their ability to absorb or scatter solar and infrared radiation in the atmosphere. They reside in polluted regions (for example urban areas) and deplete direct solar radiation by an estimation of about 15%. Radiation forcing SI2000 climate model have been adopted by the NASA Goddard Institute for Space Studies to drive climate simulations for 1951–1998 (Hansen *et al*., 1997). The SI2000 climate model shows consistency with other climate models- with a sensitivity of 3/4 °C per W/m^2. The variability of aerosols in the atmosphere makes it difficult to quantify the aerosols' radiative forcing which is believed to have either positive or negative climatic influence depending on the aerosol size, life-time, complex refractive index, stoichiometry/composition and aerosol solubility. There have been efforts in the past to model the indirect and direct radiative forcing caused by atmospheric aerosols. Prominent amongst the model is the three dimensional model which was used to estimate aerosol radiative forcing in dust aerosol (Nabat *et al.,* 2015), sulphate aerosols (Jackson *et al.,* 2015), carbonaceous aerosols (Cao *et al.,* 2013), nitrate aerosols (Yang *et al.,* 2014) and sea salt aerosols (Spada *et al.,* 2015).

One of the advantages of aerosols is the initiation of fixation events for balancing carbon and nitrogen content in the atmosphere (Libault, 2014). Other benefits of aerosols includes the regulation of the cloud microphysics and lightning (Yuan *et al*., 2011). For example, aerosols act as cloud condensation nuclei (Zhao *et al.,* 2015); aerosols modify the atmospheric temperature structure (Brown, 2012); aerosols affect atmospheric electrification when the

charge separation and lightning increases with concentration of cloud condensation nuclei (CCN) up to the threshold of CCN> 2000 cm^{-3} (Mansel and Ziegler, 2013).

All species of atmospheric aerosols are released into the troposphere directly. Therefore, the effects of tropospheric aerosol particles on climate are very challenging to estimate. However, qualitative models are generally understood and accepted. Quantitative modelling remains a challenging task because of the limited information on aerosol properties (optical, chemical and physical). Meteorological parameters like temperature, relative humidity, emissivity, wind dynamics, air pressure, cloud formation, solar radiation and precipitation greatly influence the tropospheric aerosol distribution (Liu and Zhanqing, 2014). West Africa is a typical example of a region of large-scale circulation. This means that wind reversals in the lower levels of the atmosphere should be expected in West Africa. The climate of Africa is influenced by the West African Monsoon (WAM). WAM has been investigated over thirteen years by the African Monsoon Multidisciplinary Analyses (AMMA) programme which was launched in 2002 to understudy aerosols loading and precipitation trends over Africa. AMMA has various radiosonde stations in West Africa. Aside the AMMA programme, there are other programmes that are dedicated to the study of the WAM. However, over 59% data loss is observed on the data set harvested from ground and satellite stations. Many reasons have been adduced to this anomaly. For example, Polcher *et al.* (2011) observed that the main challenge of AMMA is the functionality of the instruments. The peculiarity of the challenge faced by AMMA is replicated in NASA-AERONET. It is about five years since some of the observation instruments have been replaced with a slight reduction of data loss to about 53%. How reliable is the remaining 47% of data acquired from ground and satellite measurements to weather forecast? Certainly, West Africa stands the risk of the Indian radiative forcing experience if more synergy and collaborative research is not encouraged. It is then wise to ask why instruments that worked perfectly in some regions of the world failed in West Africa.

In this thesis, it was proposed that the challenge is more systemic than design error. This challenge culminates into instruments not properly tuned to the corresponding atmospheric constants of the region. Atmospheric constants are used in ground and satellite weather stations to access the properties of aerosol or its distribution over a geographical region. Just

as aerosol models are used to determine the solar constant used for calibrating the sun photometer, the atmospheric constant could be obtained using the aerosols dispersion model. The atmospheric constant have been calculated and documented for industrial use in developed regions (Schotland *et al*., 1986; Welton *et al*., 2002). For example, if the Canadian general climate model (GCMII) is used, the tuning constants applied are 0.20 and 3.1 for Mace Head (Ireland), 0.26 for Dublin (Ireland), and 1.4 for Heimaey, Iceland. The use of automatic weather stations in developing regions without reconfiguring the constants encrypted in the CF-card leads to large data loss. Hence, there is the need to document reliable constants within the West African region.

There are many aerosol models which are categorized into three: the dispersion model, the photochemical model and the cloud model. In this thesis, the dispersion model was adopted because of the availability of ground and satellite data set obtained over the last fourteen years. Before adopting the dispersion model, it is best to know how the aerosols transport is described. Atmospheric aerosol behaves like particles in gaseous form, as such, it identifies with the Knudsen number (Sagert *et al*., 2015). Another parameter which defines the physical properties of the atmospheric aerosol is the Reynolds number (Norris *et al*., 2013) which is defined as the ratio of the inertial force to the frictional force of fluids (mainly in pipes). The Reynolds number, Re, determines the kind of flow during fluid transport. For example, a fluid flow is laminar when frictional forces dominate its transport ($Re < 1$). Also, a fluid flow is turbulent when inertial forces dominate its transport ($Re >> 1$). Stokes' law is also used to describe the physical properties of aerosols because it is valid for laminar flow around a solid sphere (Yuan *et al*., 2011).

Atmospheric aerosols are generally in the Stokes regime where Stokes' law is obeyed. The Stokes regime works on the condition that atmospheric aerosols are spherical. In reality, many aerosols are not spherical. For example, soot has irregular shapes and sizes. In this case, the dynamic shape factor is applied in Stokes law to account for the particle motion of the irregularly-shaped aerosol. The dynamic shape factor is defined as the ratio of the actual resisting force of a non-spherical particle to the resisting force of a spherical particle (at same condition of volume and density). Therefore in this thesis, it is proposed that the unified

number (which shall be derived in the third chapter) should be more relevant to describe aerosol transport especially in the lower atmosphere of West Africa.

1.2 Statement of the Problem

The extent of danger of aerosols loading over West Africa cannot be estimated because the theoretical validation of the aerosol dispersion model in the Stokes' regime has not been clarified by atmospheric scientists. There is need to quantify the myriads of challenges facing aerosols data set retrieval and provide a mathematical framework in the form of mathematical models for the development of future-computerized weather stations.

By definition, the Knudsen and Reynolds' numbers negate the principle of the Stokes' regime. Therefore, the inability of Knudsen and Reynolds' numbers to describe the peculiarity of aerosols transport remains a gap in the science of the atmosphere. This leads to a salient question of why scientists have not investigated the effects of moving fluids on a moving sphere. This basic error extends into the formulation of most aerosol models by generating erroneous atmospheric constants used for the computational coding of weather stations. Atmospheric constants vary on a regional basis.

1.3 Justification for the Research

This research would aid the understanding of the dynamics of aerosol and cloud interactions in West Africa. The research would also enable a more accurate weather forecast and data acquisition all year round in the region. It would aid the yearly estimation of pollution over West Africa and how best the region can mitigate its effect on health, agricultural produce, thermal comfort and climate perturbations.

1.4 Aim and Objectives of the Research

The aim of this research is to develop a theoretical model for retrieving and forecasting atmospheric aerosol which is expected to culminate into the development of future computerized weather station. The following objectives are presented to help in the actualization of the research aim:

i. Source for both satellite and ground data sets from various database networks;
ii. Analyse the data sets using theoretical (analytical) and mathematical (numerical) techniques which includes the development of models and solving the governing equations developed in the expanded Stoke's regime;
iii. Introduce a unified number to adequately capture the physics of the Stokes' regime;
iv. Sectionalize the challenges of the dispersion model in turbulent fluid conditions;
v. Carry-out a comparative study to validate the authenticity of the developed models with existing models by applying it to satellite and ground data sets to obtain the atmospheric constants over each location;
vi. Use meteorological measurement to retrieve aerosol optical depth in selected locations of West Africa;
vii. Explain the variation between the satellite and ground data sets; and use it to examine aerosols trends in regions of scanty data set;
viii. Explain the statistical analysis of ground and satellite observations to determine the aerosols retention in the atmosphere.

1.5 Limitation of the research

This research is theoretical. Satellite and ground data sets will be used to affirm the theories/models adopted. The variance between the satellite and ground observations is largely due to unavoidable atmospheric undulations which was explained in the thesis.

1.6. Scope of Study

The aerosol optical depth satellite observation covers twenty-eight locations across seventeen countries in West Africa. Two basic criteria used for selecting the locations within each country were human population and the grid system. Also, the aerosol optical depth ground observation covers four locations across West Africa. The meteorological ground measurements for six locations in Nigeria was analysed. The research examines the aerosols dispersion protocol in the lower atmosphere. The protocol includes aerosols dispersion, aerosols distribution, aerosols meteorological parameter and aerosols retention in the lower atmosphere.

The idea of the thesis is to seek ways of retrieving aerosols data set all year round in West Africa. The 2D and 3D dispersion model, as well as the unified number will be derived to aid further learning of the perculiar atmosphere over West Africa.

1.7. Structural Outlook of Thesis

The comprehensive model for forecasting aerosols loadings over West Africa is made up of four models, that is, two main and two supportive models. The supportive models are expected to compliment the main models if adopted in meteorological centers. To achieve the aim of this thesis, the literature background of the four models were discussed in chapter two. In chapter three, the location of study, as well as the conceptual formulation of different systems of equations were illustrated. The results of the four models were discussed in chapter four. In chapter five, salient recommendations and highlights of the main results were documented for onward execution by research centers, government of the West African countries and meteorological centers.

CHAPTER TWO

LITERATURE REVIEW

In this chapter, the general components of this thesis are discussed with emphasis limited to the scope of this thesis. In section 2.1, the details of the atmospheric aerosols were discussed with the aim of illustrating the basic physical and optical properties of aerosol. In section 2.2, the characteristics of aerosol in layers and sub-layers of the atmosphere were reviewed. The conditions for aerosol localization and its peculiar transport within the troposphere and stratosphere were examined. The types of dispersion models, their shortcomings and strengths were considered in section 2.3. In section 2.4, the science of the aerosol optical depth was explained. The statistical parameters used for the study were highlighted in section 2.5. Lastly, the meteorology of the West Africa region was reviewed in sections 2.6 and 2.7.

2.1 Properties of Aerosols

The components of aerosols are solely dependent on their sources which determine the physical properties and the constituents that determine the chemical properties (Moroni et al., 2015). The optical properties of aerosols are used to determine the type of microphysical transformation processes, that is, condensation, nucleation, and coagulation. The studies of the role of aerosols properties are complicated because its physical and chemical properties are highly variable in both time and space (Zhao *et al.,* 2015). Moreso, its optical properties are more challenging due to its complex refractive index which is dependent on its kind (sulphate, nitrate, sea salt and soot), size (nucleate mode, accumulation mode, fine mode, coarse mode), distribution of source, meteorological influences and life-time.

2.1.1 Physical Properties of Aerosols

The major properties of atmospheric aerosol have been substantiated in mathematical expressions in order to understand its predictability and applicability in meteorological

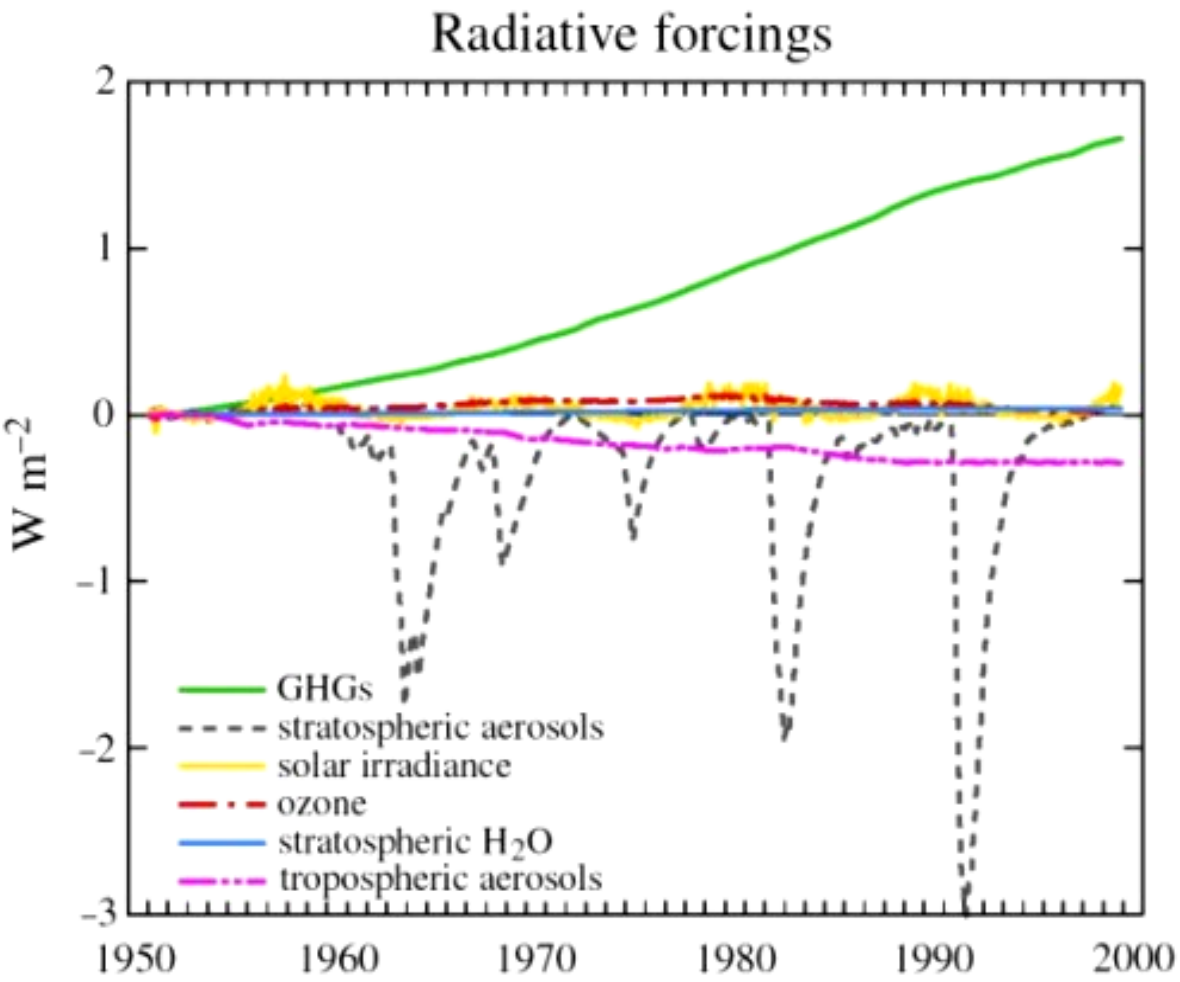

Figure 2.1: Radiative forcing due to changes of stratospheric and tropospheric aerosols, ozone, greenhouse gases and solar irradiance (Hansen et al., 1997)

terrains. For example, Hansen *et al*., (1997) simplified the radiative forcing of climate shown in Figure 2.1 below. The largest radiative forcing (Figure 2.1) are the positive forcing initiated by greenhouse gases (GHG) while the negative forcing are initiated by aerosols. Also, it can be seen in Figure 2.1 that both the positive and negative forcing have significant effect on the global temperature (Hansen et al., 1997). Aerosols indirect radiative forcing (especially in warm clouds) is traceable to two sources: aerosols cloud condensation nuclei and change in precipitation efficiency. Popular models used to estimate aerosols' indirect radiative forcing is the aerosol size-resolved model which has been used to show that the influential aerosols physical properties are important to estimate radiative forcing. For instance, the wind field activates the sea salt aerosols' size-segregated surface emission rates and its collective impact on the radiative forcing (Bjourn, 2015). Since the basic characteristic of atmospheric aerosols is its 'particles in gas' nature, it can be described using physical terms like radius of particulates, volume of particulates, conservation of mass, density of particulates and fluid flow rate.

The type of fluid flow is an important physical property which determines salient meteorological conditions like precipitation and earth's surface temperature. The fluid flow can be described by basic flow terminology like Knudsen number, Reynolds number, Prandtl number and Nusselt number. These terminologies are used in engineering and few of the terminologies (for example, Knudsen, Kn, and Reynolds', Re, number) have shown relevance in atmospheric physics. The Knudsen number is defined as the ratio of the mean free path of the gas molecules to the radius/diameter of the particle. It is mathematically expressed (Nicholson, 2013) as

$$Kn = \frac{\lambda}{r_a} = \frac{2\lambda}{d_a} \qquad (2.1)$$

where, r_a is the aerosol radius, d_a is the aerosol diameter and λ is the mean free path. The mean free path is defined as the average distance travelled by a molecule between successive collisions. The Reynolds number is defined as the ratio of the inertial force to the viscous force of fluid. A low Reynolds Number gives laminar flow while a high Reynolds Number gives turbulent flow. The Reynolds number in the atmospheric settings can be described in view of external airflow or internal fluid flow within the planetary boundary layer. The

mathematical expression for the Reynolds number (Norris et al., 2013) for fluid flow can be shown as

$$Re_f = \frac{\rho U_f d_a}{\mu} \quad (2.2)$$

where ρ is the density, μ is the viscosity of the fluid, d_a is the aerosols diameter and U_f is the mean velocity of that fluid. The convective activities within the lower atmosphere are responsible for the heat exchange between aerosols and the surrounding air. The Reynolds number for the convective exchange (Norris et al., 2013) could be written as

$$Re_a = \frac{\rho U_a d_a}{\mu} \quad (2.3)$$

where U_a is the mean velocity of that surrounding air.

The Stokes regime works on the condition that the atmospheric aerosols are spherical. In reality, many aerosols are not spherical. For example, soot has irregular shapes and sizes. In this case, the dynamic shape factor is applied to the Stokes' law to account for the particle motion of the irregularly-shaped aerosol. The dynamic shape factor, which is a qualitative parameter is defined as the ratio of the actual resisting force of a non-spherical particle to the resisting force of a spherical particle (at same condition of volume and density).

2.1.2 Optical Properties of Aerosols

Optical properties of aerosol particles have severe influence over the local radiative forcing and radiation balance of the earth. The interaction between aerosol and solar radiation can be described by its optical properties. The optical parameters used to describe the aerosol-solar radiation are the extinction and scattering coefficients, the aerosol depth and the single-scattering phase. These parameters are wavelength dependent. The aerosol optical properties are majorly described by the aerosol optical depth (at 500 nm wavelength) and the Angstrom exponent. The aerosol optical depth can be defined as the negative natural logarithm of the fraction of solar radiation that is not scattered or absorbed on a path by aerosol particles. Angstrom exponent describes the dependency of the aerosol optical thickness, or aerosol extinction coefficient on wavelength. There are several techniques adopted in recent times to

estimate optical properties. For example, aerosol radiative properties have been used to calculate its optical properties (Calvello *et al*., 2010) as shown in equation (2.4)

$$\tau(\lambda, j) = \sum_{i=1}^{a} Q_e(\lambda, r_i)\pi r_i^2 n(r_i, j) dz_j \quad (2.4)$$

where, $n(r_i, j)$ represents the aerosol number concentrations, dz_j is the height of the j-th atmospheric layer, Q_e is the extinction efficiency, a is the total number of aerosol sizes (in bins) and r_i is the particle's wet radius. The layers of aerosol mixture at certain wavelength (Calvello *et al*., 2010) can be calculated as

$$\sigma(\lambda, j) = \sum_{i=1}^{a} \tau(\lambda, r_i, j)\sigma(\lambda, r_i, j) / \sum_{i=1}^{a} \tau(\lambda, r_i, j) \quad (2.5)$$

$$g(\lambda, j) = \sum_{i=1}^{a} \tau(\lambda, r_i, j)\sigma(\lambda, r_i, j) g(\lambda, r_i, j) / \sum_{i=1}^{a} \tau(\lambda, r_i, j)\sigma(\lambda, r_i, j) \quad (2.6)$$

$\sigma(\lambda, j)$ is the aerosol mixture at layer 1 i.e. troposphere and $g(\lambda, j)$ is the aerosol mixture at layer 2 i.e. tropopause.

Equations (2.4 to 2.6) are aerosol radiative properties for the externally mixed aerosol components. The size distributions or lognormal distributions of aerosol (Li *et al.*, 2015) is given as

$$\frac{dN_i(r)}{dr} = \frac{N_i}{\sqrt{2\pi}\, r\, log\sigma_i\, ln10} \exp\left[\frac{1}{2}\left(\frac{logr - logr_{mod\,N,i}}{log\sigma_i}\right)^2\right] \quad (2.7)$$

where $r_{mod\,N,i}$ is the mode radius, σ_i measures the width of the distribution, and N_i is the total particle number density of the component *i* in particles per cubic centimeter. Since the mode radius of the volume distribution ($r_{mod\,V}$) is paramount, then the conversion is given as

$$r_{mod\,V} = r_{mod\,N} 10^{\left(3log^2(\sigma_i)\, ln10\right)} \quad (2.8)$$

The mass distribution are derived from

$$\frac{dm}{dlog(D)} = \frac{dM_i}{V_N . \log\left(D_{50,i+1}/D_{50,i}\right)} \quad (2.9)$$

where dM_i is the mass collected on the *i*-th stage (i=1–13), dm is the total mass collected over a specified period, V_N is the normalised sampled volume , and $D_{50,i}$ and $D_{50,i+1}$ are the cut-off equivalent aerodynamic diameters for the *i*-th stage and the *i*+1-th stage respectively (Calvello *et al*., 2010). The water-soluble part of aerosol particles originates from gas to particle conversion and consists of various kinds of sulphates, nitrates, organic and water-soluble substances. The soot represents the incombustible black carbon. Mineral aerosol or desert dust consists of a mixture of quartz and clay minerals. Antarctic aerosol or sulphate aerosol consists of a large amount of sulphate, that is, 75% H_2SO_4. It is considered only for calculating the aerosol optical depth. The aerosol hygroscopic growth factor is a parameter commonly used to quantify the increase in aerosol scattering relative to dry scattering at certain relative humidity (RH). It can be calculated (Liu and Zhanginq, 2014) as

$$\mathbb{f}_{RH} = \frac{\sigma_{sp}(RH)}{\sigma_{sp}(RH_{Ref})} \tag{2.10}$$

Here, $\sigma_{sp}(RH)$ is the aerosol scattering coefficients at a given RH, $\sigma_{sp}(RH_{Ref})$ is the aerosol scattering coefficients at a low reference RH. The aerosol hygroscopic growth factor may be monitored using the atmospheric thickness. The total atmospheric optical thickness is the sum of the optical thicknesses of the individual components and it is given by Zahra *et al*. (2010) as

$$\tau_T = \tau_{aer} + \tau_{ray} + \tau_{o_3} + \tau_{NO_2} + \tau_{H_2O} \tag{2.11}$$

Here, $\tau_{aer}$is the aerosol optical thickness, τ_{ray} is the Rayleigh scattering optical thickness of the gas molecules in the atmosphere, τ_{o_3} is the ozone optical thickness, τ_{NO_2} is the nitrogen dioxide optical thickness and τ_{H_2O} is the water vapor optical thickness. The Rayleigh scattering optical thickness of pressure P for light of wavelength λ is calculated using the approach by Hansen *et al*. (1997)

$$\tau_{ray} = 0.008569\lambda^{-4}(1 + 0.113\lambda^{-2} + 0.00013\lambda^{-4})P/P_o \tag{2.12}$$

where $P_o = 1013.25$ mbar is the standard surface pressure and λ is the wavelength in μm.

2.2 Characteristics of Atmospheric Aerosol Distribution

Aerosol particles with radii on the order of 0.1μm or less generally reside in the lower atmosphere. The aerosols kind determines the extent of the aerosols on climatic forcing. For example, sea salt aerosols are emitted into the atmosphere via bursting of bubbles which occurs at the surface of oceans. Therefore, over large oceanic areas, sea salt aerosols generate large chemical and physical interactions which are potent to influence climatic forcing. Dust-like mineral sea salt is a major product over many oceanic regions. Seinfeld and Pandis (1998) gave a schematic model of the distribution of an idealized ensemble of aerosol particles formed by a variety of processes (Figure 2.2). The sizes of the aerosol specie are essential for renowned impact on a global scale. Natural aerosols in the troposphere are probably four to five times larger than anthropogenic aerosols. However, local, regional and global variations in anthropogenic pollution may change this ratio significantly in certain areas (Seinfeld and Pandis, 1998).

Observations of urban aerosol dynamics in coastal regions depend on convective outflows which are limited because of the sporadic nature of convection and aerosol pathways for ventilating pollutants from the planetary boundary layer (PBL) to the free troposphere and beyond. Hence, the global circulation system greatly influences the localization of aerosols in the troposphere and stratosphere. One of the major challenges facing scientists concerning the nature of aerosols is the inability to adequately estimate aerosol distribution, aerosol-cloud interactions, and the physical and chemical properties of aerosols. Models are propounded to aid an in-depth understanding of aerosol distribution.

The vertical distribution of atmospheric aerosols is essential in estimating circulation of aerosols in the atmospheric layers; namely, troposphere, planetary boundary layer and the stratosphere (Figure 2.3). This kind of distribution defines the aerosols character, for instance, the transport of materials by winds from the continents and large seasonal differences in aerosol concentrations (Asmi *et al.*, 2015). The distribution of natural and anthropogenic sources of aerosol depend on certain atmospheric conditions like wind speed (Zhang *et al*., 2014), temperature, solar radiation and relative humidity (Liu *et al*., 2011).

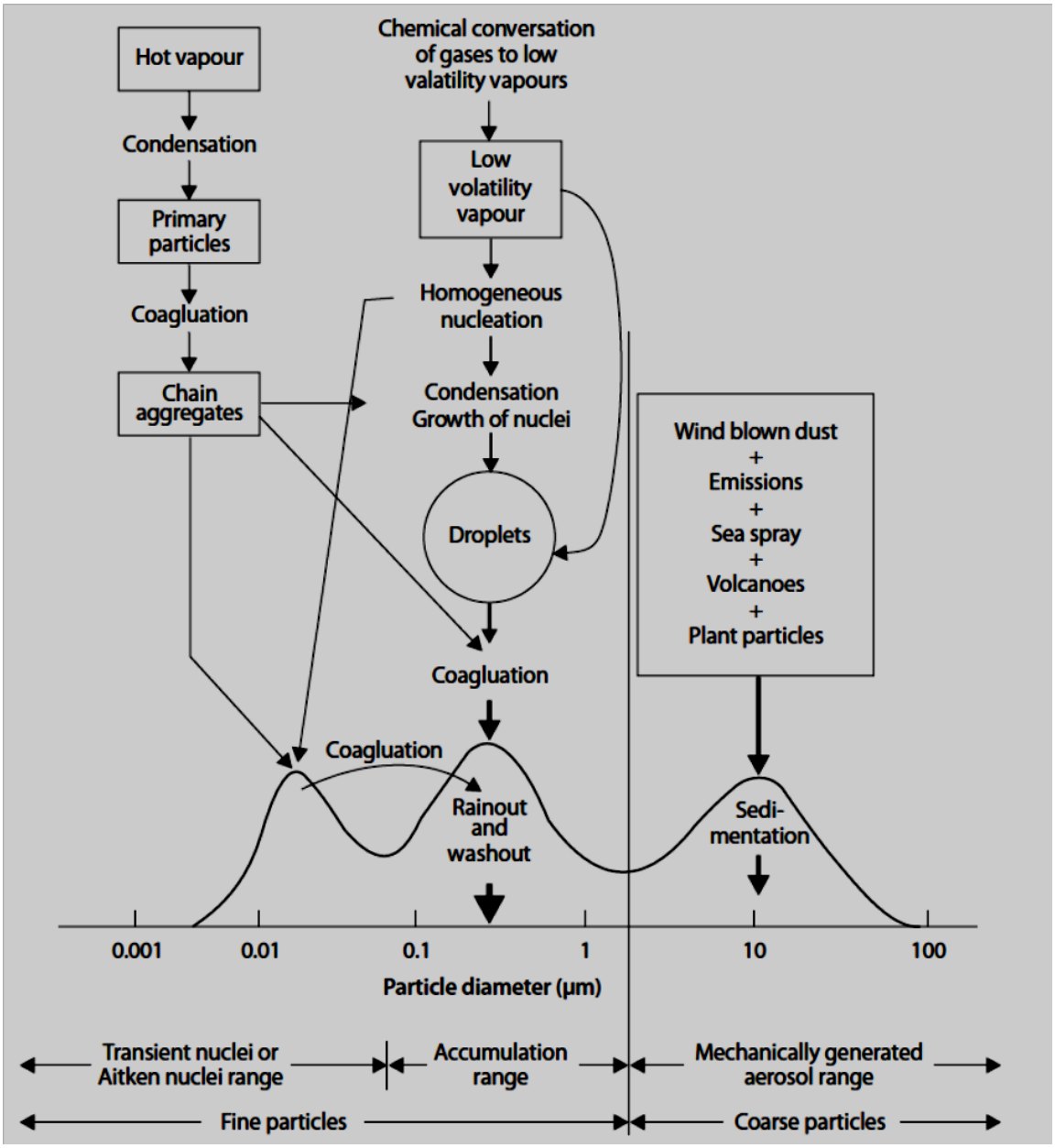

Figure 2.2: Schematic model of the distribution of an idealized ensemble of aerosol particles (Seinfeld and Pandis, 1998)

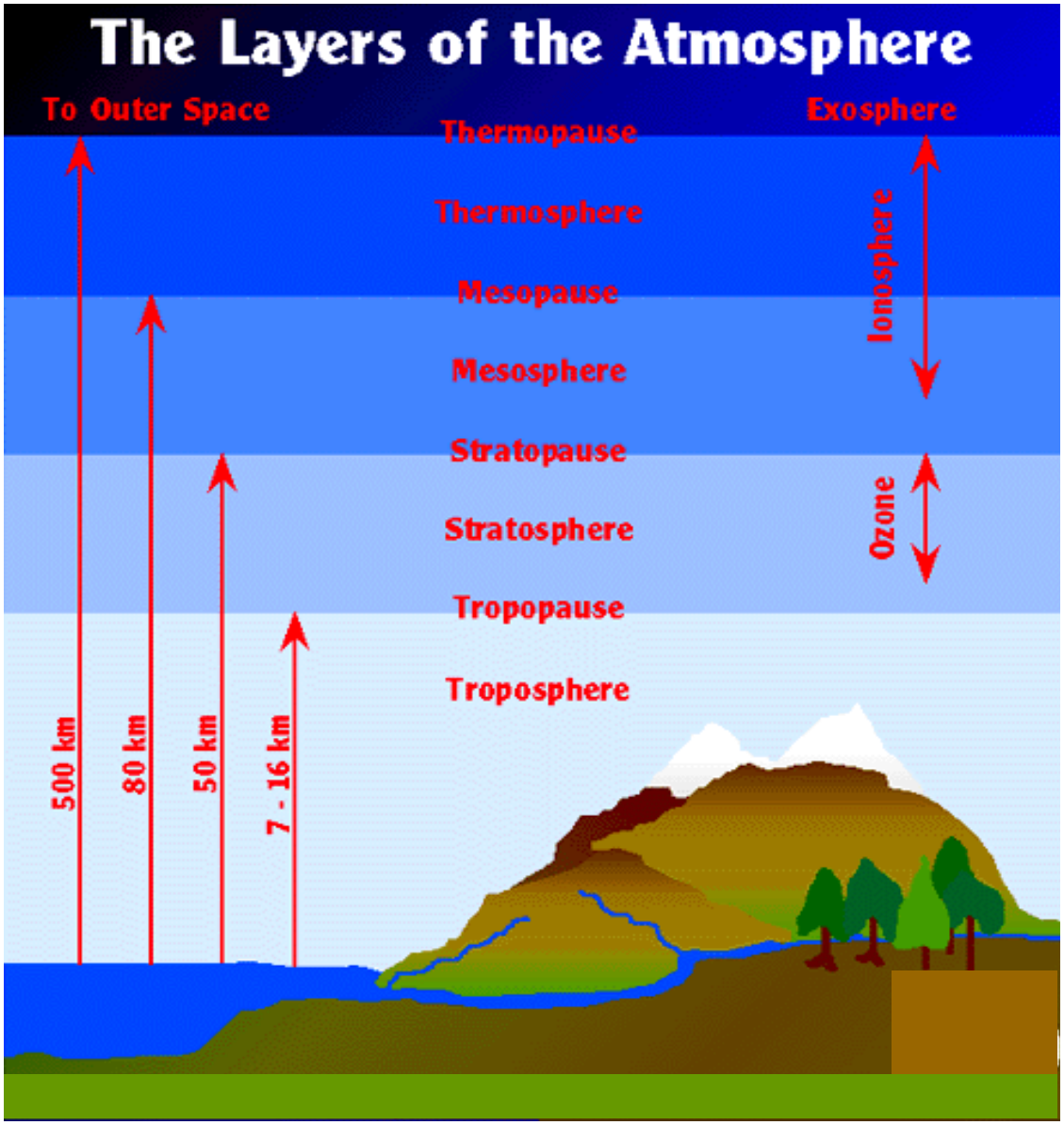

Figure 2.3: Atmospheric layers (NOAA, 2015)

2.2.1 Aerosol Distribution in the Troposphere

All species of aerosols are released into the troposphere directly. Therefore the effects of Tropospheric aerosol particles on climate are very challenging to estimate. However, the qualitative terms are generally understood and accepted. The quantitative terms remain a challenging task because of the limited information on aerosol properties (optical, chemical, physical). The meteorological parameters like temperature, relative humidity, emissivity, wind dynamics, air pressure, cloud formation, solar radiation and precipitation greatly influence the tropospheric aerosol distribution (Figure 2.4).

The direct radiative effects of absorbing aerosol can be mitigated or amplified- depending on the prevailing atmospheric condition. For example, when absorbing aerosols are located above bright clouds, it amplifies the warming effects. Also, the life cycle of aerosol specie depends on the residual atmospheric layer. For example, the life-time of atmospheric aerosol is much greater when it resides in the free troposphere than in the Tropical Tropopause Layer (TTL) because of the complex atmospheric processes at the later. The TTL is the region-above the troposphere that connects the convectively active levels of the tropical troposphere to the lower stratosphere and beyond (Asmi *et al.*, 2015; Akinyemi, 2007). The thermal tropopause is the warmest region of about 380K and located around 17 km from the earth's surface. This region initiates deep convection which initiates vertical mass transport into and across the tropopause region (Liu and Zhanqing, 2014). The investigation of the global vertical distribution of Tropospheric aerosols were made possible by the CALIPSO satellite via sectional gridding techniques. It is essential to understand the vertical distribution of aerosol in order to enable evaluation of global aerosol models.

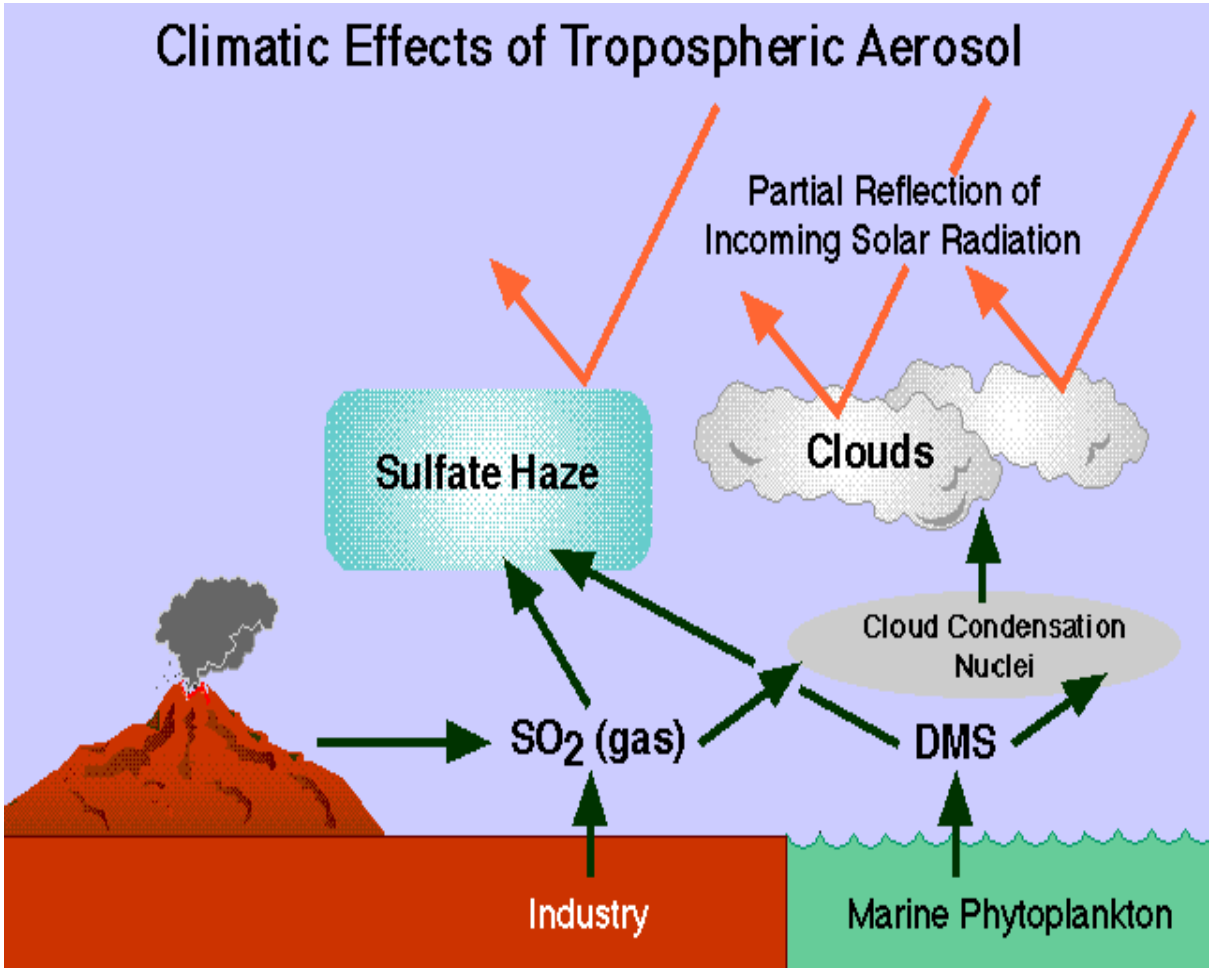

Figure 2.4: Sources, specie and reaction of tropospheric aerosol (NOAA, 2015)

2.3 Aerosol Advection-Dispersion Models

Most aerosol advection-dispersion models are on the regional scale. The component of a dispersion model includes regional climate, terrain and wind analyses. Therefore, extending a regional model to the complex global scale is a huge task-especially solving the large-scale intercontinental transport challenges. Hence, the regional scale advection-dispersion phase was reviewed in this section.

Recently, Zhang *et al*., (2014) investigated the global atmospheric aerosol transport model. This model was based on 3D advection-diffusion equations they generated via representing advection by wind and turbulent diffusion in a mathematical format. They extended the 2D advection-diffusion equation to 3D as shown

$$\frac{\partial c}{\partial t} + u_x \frac{\partial c}{\partial x} + u_y \frac{\partial c}{\partial y} + u_z \frac{\partial c}{\partial z} = k_x \frac{\partial^2 c}{\partial x^2} + k_y \frac{\partial^2 c}{\partial y^2} + k_z \frac{\partial^2 c}{\partial z^2} + \lambda c \qquad (2.13)$$

where c is contaminant concentration; t is time; u_x, u_y, u_z represent wind speed in the three directions x, y, z respectively; k_x, k_y, k_z represent turbulent diffusivity in three directions; λ is the climatic factor, which can be its emission source, chemical conversion, dry deposition and wet scavenging. The logarithmic distribution of the wind speed and the exponential function form of the turbulent diffusivity were incorporated into equation (2.13). The simulations were carried out at 83 points obtained from the NASA website. They adopted the Euler finite difference method for numerical simulation which has a horizontal resolution $4^o \times 5^o$ and a vertical direction - divided into 11 sub-layers.

The real and simulated values of atmospheric contaminant transport on global scale in 3D space for twelve months are shown in Figure 2.5. The accuracy of the technique is in doubt although the authors (Zhang *et al.,* 2014) acknowledged the narrowed application of the model to aerosols in a laboratory framework only.

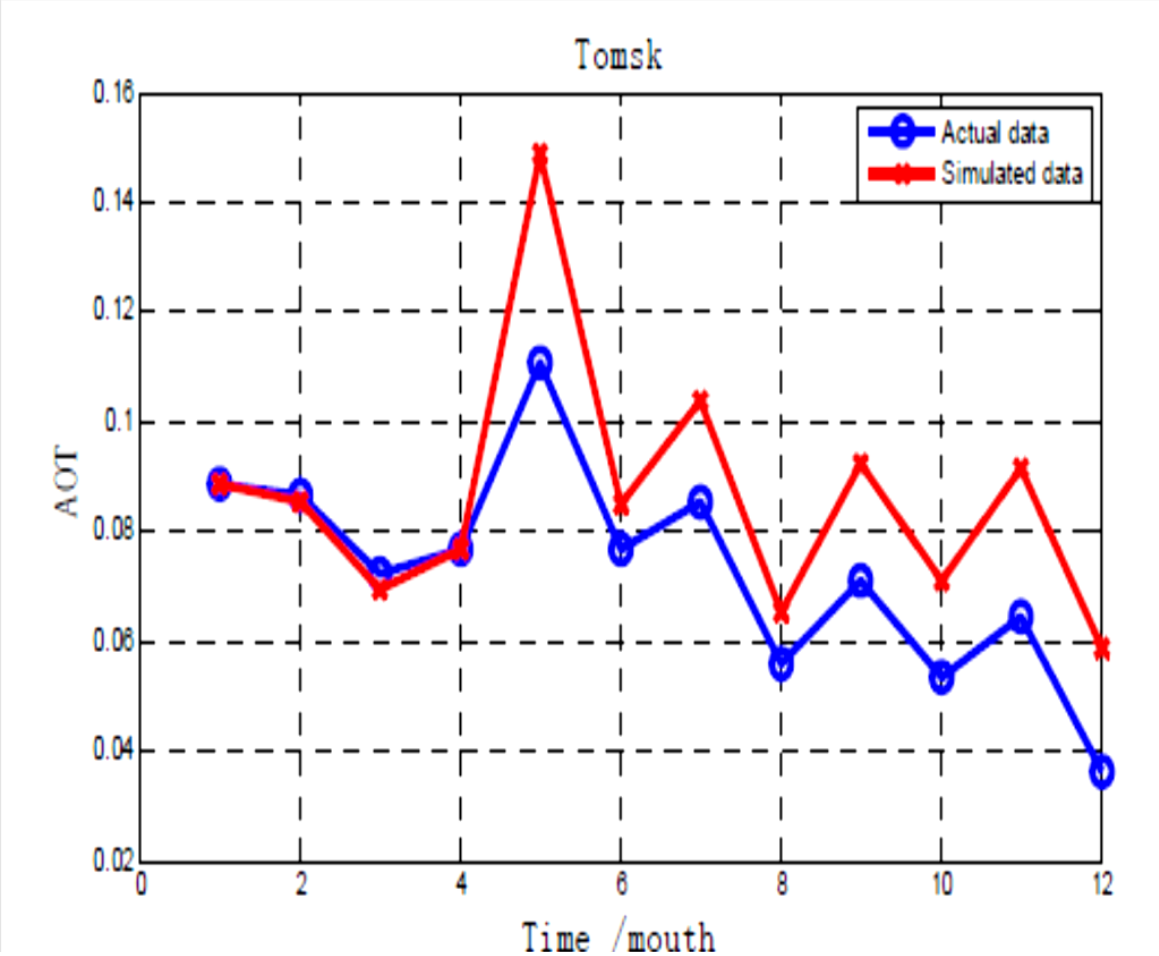

Figure 2.5: Real values and simulated values in one year in Tomsk (Zhang *et al.*, 2014)

First, the model, according to the authors ought to be an atmospheric contaminant transport on the global scale. The model ignored the regional climatic variables. Second, few of the assumptions made were too bogus for an in-depth study. For example, the initial condition ought not to be set to zero because the authors objective was to discuss a real system and not a virtual system. Therefore, the initial conditions for real pollutant concentration ought to be used instead. Third, in the second case studied, the authors also used the Kriging interpolation method to establish the initial condition of the concentration distribution of existing pollution. The Kriging interpolation method was adopted prematurely because the climatic consistency for the region was not considered first before applying the Kriging interpolation method. The numerical effect of the flaws in the model is affirmed in Figure 2.5. The simulated and real data set agreed till the month of April. Large variations between the simulated and real values extended from the month of May to December (Zhang *et al.*, 2014).

Holmes and Morawska (2006) reviewed dispersion models and its application to the dispersion of particles. They discussed the box model (BM) which operates on the principle of conservation of mass. The box model is applied when the survey or research site is treated as a box which obeys meteorological rules where pollutants emitted undergoes chemical and physical processes. Choo-in (2001) applied the box model to estimate the pollutants in a street tunnel in Thailand. The box model works perfectly when the air mass is well mixed and concentrations are uniform throughout. When the box is not defined, pollutants are formed within the box only; hence, the information on the local concentrations of the pollutants is considered as negligible. These inaccurate conditions make the box model unsuitable for describing the particle concentrations within a local environment. Like the shortcoming of the 3D model of Zhang *et al*. (2014), the box model does not consider the concentrations nor particle dynamics which are highly influenced by the local changes of the region's climate (for example, wind field and emissions).

The Gaussian model (GM) is the most popular model used in atmospheric dispersion modeling. Gaussian or plume models operate based on the Gaussian distribution of the 2D or 3D concentration of the plume under steady state conditions (Zhang et al., 2014). The Gaussian distribution of the plume is under certain influences like turbulent reflection from

the surface of the earth, dimension of transport, boundary layer (especially when the mixing height is low), stability classes or travel time from plume sources. As observed in other models mentioned earlier, the plume models have their shortcomings too; for instance, plume models use steady state approximations and assume that there is no interaction between plumes. Plume models do not consider the travel-duration between the plume source receptor. The accuracy of the plume model may be improved by including the chemical modeling to accurately predict the formation of particles by a post processing treatment of the results.

Ahmada (2011) worked on the dispersion of atmospheric pollutants using two dimensional advection diffusion equations. He started with the generalized advection-diffusion equation given below

$$\frac{\partial C}{\partial t} = \mu \frac{\partial^2 C}{\partial x^2} - u \frac{\partial C}{\partial x} \qquad (2.14)$$

and obtained the two-dimensional advection-diffusion equation given as

.

$$\frac{\partial C}{\partial t} - \mu \left(\frac{\partial^2 C}{\partial x^2} + \frac{\partial^2 C}{\partial y^2} \right) + u \frac{\partial C}{\partial x} + v \frac{\partial C}{\partial y} + \varpi C = \frac{f}{H} \qquad (2.15)$$

where C is the concentration of pollutants, H is the depth occupied by pollutants, u is the wind velocity or drift velocity, f is the power of the source, ϖ is the pollutant chemical activity coefficient of pollutants and μ is the horizontal diffusion coefficients. The boundary conditions used were the zero Dirichlet boundary condition, Neumann boundary condition and periodic boundary condition. The finite difference approach was adopted in order to obtain the numerical solutions of equation (2.15). The solutions for first order forward difference, first order backward difference, first order central difference, second order central difference, central differences for two dimensional functions of the Crank-Nicolson method were determined. The model propounded has three external parameters, namely the pollutant diffusion coefficient μ, the drift velocity of air u and the pollutant chemical activity coefficient ϖ. The shortcoming of this model is that it lacks a proper perspective towards real aerosol events. First, the model was more of a mathematical exercise because the regional or global climate condition was not factored into the model formulation. Also, the assumption

that the vertical movement of pollutant was insignificant is a gap to the model since in most aerosol advection dispersion or diffusion, the minimum three dimensional motions are observed.

Thongmoon *et al.* (2007) worked on the numerical solution of a 3D advection-dispersion model for pollutant transport-using the forward in time and centre in space (FTCS) finite difference method. The paper is an extension of the Choo-in (2001) box model but a different approach was applied to numerically model the transport of pollutants in a street tunnel as expressed in Figure 2.6. The model accounted for the length of the street, the height –roof or pavement of the street, and crosswind through the gaps in the side-walls of the tunnel.

The problem domain used to execute the multi-task model is given as

$$\Omega = \{(x, y, z); 0 \leq x \leq L, 0 \leq y \leq W, 0 \leq z \leq H\} \tag{2.16}$$

Applying the assumptions, that is, the wind flows horizontally, wind is uniformly constant within the tunnel, and that the dispersion is horizontally isotropic, the three-dimensional advection-diffusion is given as:

$$\frac{\partial C}{\partial t} + u\frac{\partial C}{\partial x} + v\frac{\partial C}{\partial y} = D_h\frac{\partial^2 C}{\partial x^2} + D_h\frac{\partial^2 C}{\partial y^2} + D_v\frac{\partial^2 C}{\partial z^2} \tag{2.17}$$

where u and v are constant wind speeds in the x and y-directions respectively. D_h and D_v are constant dispersion coefficients in the x and z-directions respectively. Three cases were considered by the authors. In the first case, the author examined a situation where there is no dispersive flux of the pollutant through the (solid) side-walls or through the base and roof. Here, the three-dimensional advection-diffusion was given as

$$\frac{\partial C}{\partial t} + u\frac{\partial C}{\partial x} = D_h\frac{\partial^2 C}{\partial x^2} + D_h\frac{\partial^2 C}{\partial y^2} + D_v\frac{\partial^2 C}{\partial z^2} \tag{2.18}$$

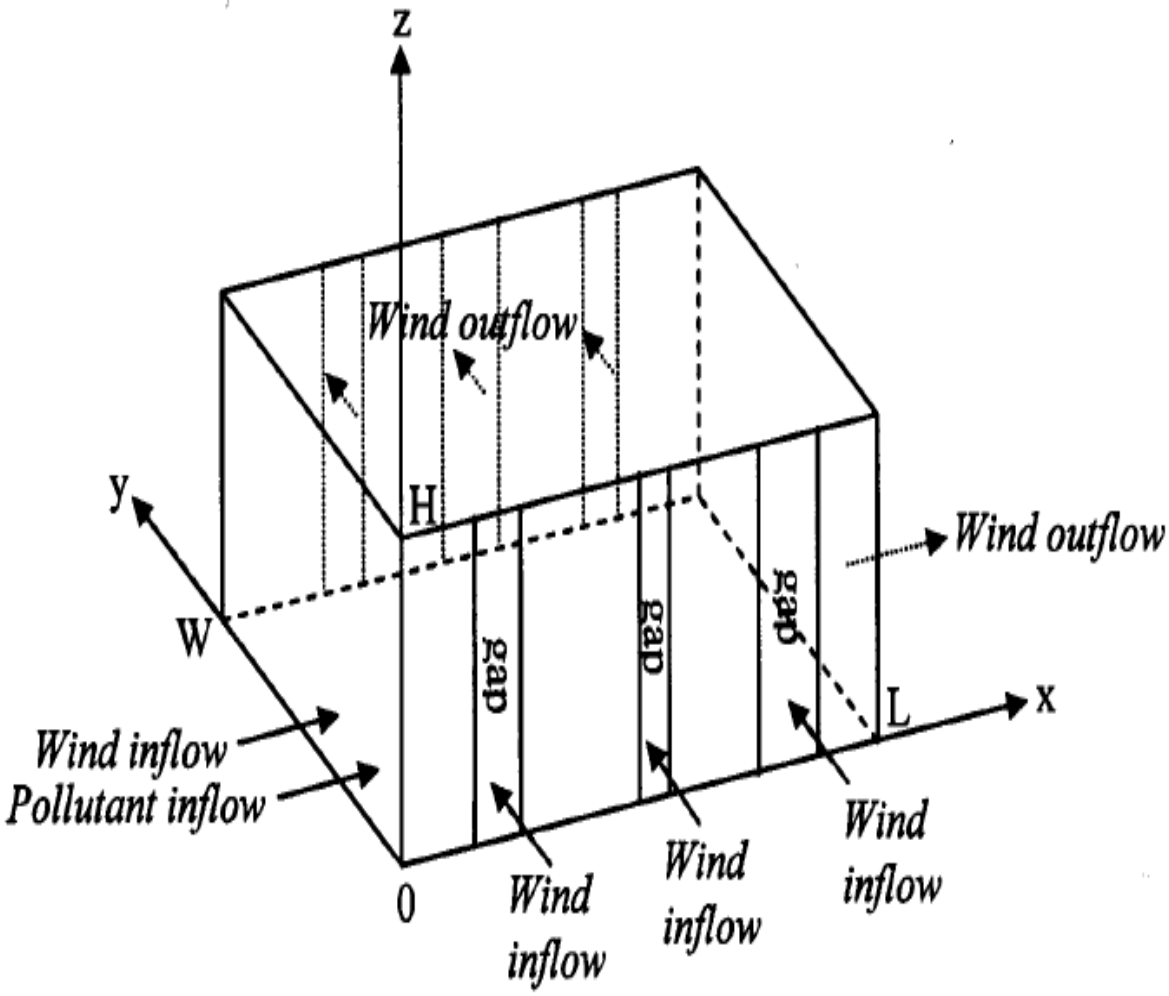

Figure 2.6: Pictorial model of street tunnel dispersion model. (Thongmoon *et al.*, 2007)

In the second case, the wind influences from the walls of the street are neglected. Equation 2.18 was applied to the second case but with different initial boundary conditions. The model lacked the realities of climatic influences although the authors adopted multiple initial and boundary conditions. Hence, its flaws follow the usual trend of the box model.

Benson *et al*. (2000) worked on the application of a fractional advection-dispersion equation. They used fractional derivatives to study the scaling behavior of plumes that undergo Levy motion. This scaling behavior is in time and space of the heavy tailed motion (Daitche and Tamas, 2014). However, the second-order dispersion arises for a thin tailed motion. Under this condition, very large motions are completely ruled out. Contrary to the thin tailed motion, the fractional advection-dispersion equation (FADE) considers a very large transition of particles which arise from high heterogeneity (Benson *et al.,* 2000). The FADE is effective (when the scaled α-stable density is known) to predict distances of particles in closed forms and their concentrations versus time. The FADE originates from simple experiments. that is, 1D tracer tests in a laboratory-scale sandbox as shown in equation (2.19). The 1D form of the FADE (Daitche and Tamas, 2014) can be written as

$$\frac{\partial C}{\partial t} = -v\frac{\partial C}{\partial x} + \mathfrak{D}p\frac{\partial^{\alpha} C}{\partial x^{\alpha}} + \mathfrak{D}(1-p)\frac{\partial^{\alpha} C}{\partial(-x)^{\alpha}} \qquad (2.19)$$

Here C is the concentration, t is time, v is the uniform mean velocity, x is distance in the direction of mean velocity, $\mathfrak{D}$ is the constant dispersion coefficient, $0 \leq p \leq 1$ describes the skewness of the transport process, and α is the order of fractional differentiation.

Burns (1996) had earlier postulated, through equation (2.19) that the α-stable transport within the sandbox lies within the heavy tailed breakthrough curves shown in Figure (2.8).

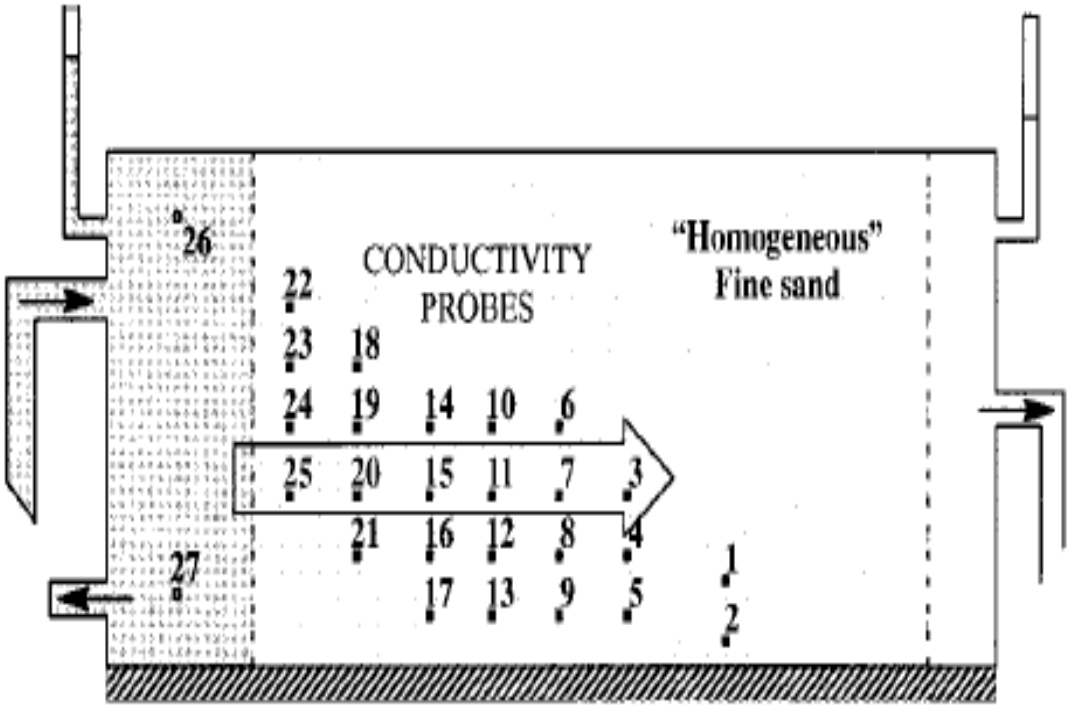

Figure 2.7: Schematic expression of the 1D experimental sandbox tracer tests (Burns, 1996)

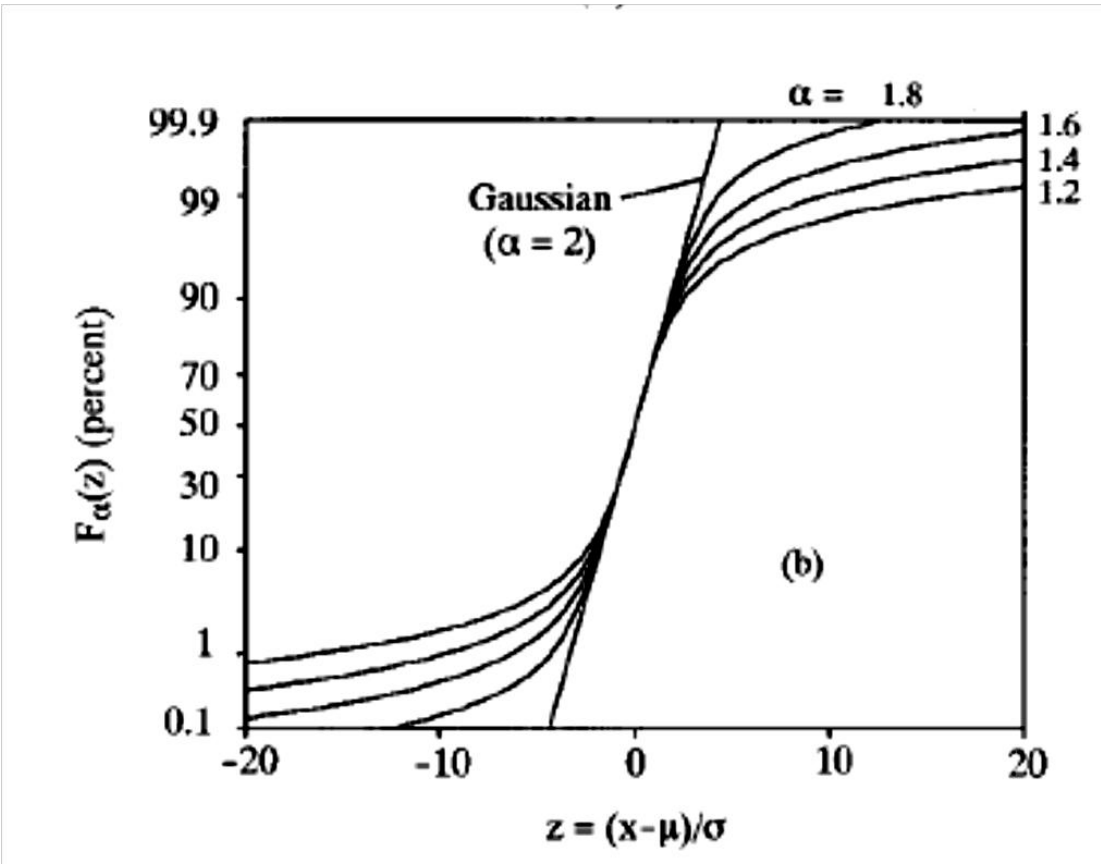

Figure 2.8: Solution of Equation (2.19) for α-stable distribution (Burns, 1996)

From Figure 2.8, when α = 2, the Gaussian plume appears as a straight line only if the concentration is normalized The slope of the straight line can be used to estimate the dispersivity of the transport medium. The sigmoid shape throughout the breakthrough curve (Figure 2.8) shows higher tail probabilities which correspond to the probe calibration ranges (Burns, 1996). Therefore, in order to model heavy-tailed plumes, such theory requires one or more transfer coefficients or distributions of coefficients. Garabedian *et al*. (1991) furthered the estimation of parameters by calculating the variance of the plume roughly along the direction of mean travel and suggested a second-order Fickian governing equation to be appropriate. Benson *et al*. (2000) solved the 1D equation shown below using the aquifer parameters

$$\frac{\partial C}{\partial t} + v\frac{\partial C}{\partial x} - \mathfrak{D}(\bar{x})\frac{\partial^2 C}{\partial x^2} = C_o x_o \delta(t,x) \qquad (2.20)$$

$$\frac{\partial C}{\partial g} + v\frac{\partial C}{\partial x} - \mathfrak{D}(\bar{x})\nabla^{\alpha} C = C_o x_o \delta(t,x) \qquad (2.21)$$

where $C_o x_o \delta(t,x)$denotes the initial solute concentration (C_0) spread over some injection distance x_0. $\delta(t,x)$ is the Delta function 'spike' which is defined as the area under all of the concentration versus distance curves. ∇^{α}denotes a symmetric fractional-order operator (p = 0), which is also known as the Riesz potential (Samko *et al*., 1993). The solutions of equations (2.20) and (2.21) can be seen in the simulation below. In the real axis, the predicted, measured and best fit Gaussian showed good level of accuracy (Figure 2.9a). This shows that in the laboratory, the FADE is perfect. Applying the same theory in a mimicked atmospheric field-substituting the real axis with the semi log axes, the levels of inconsistencies were high (Figure 2.9b). Hence, the shortcoming of the FADE is its inability to measure or predict observations of plumes in the field. So far, it has shown good success in observation of plumes in the laboratory. Secondly, FADE applies to porous earth transport rather than atmospheric porosity.

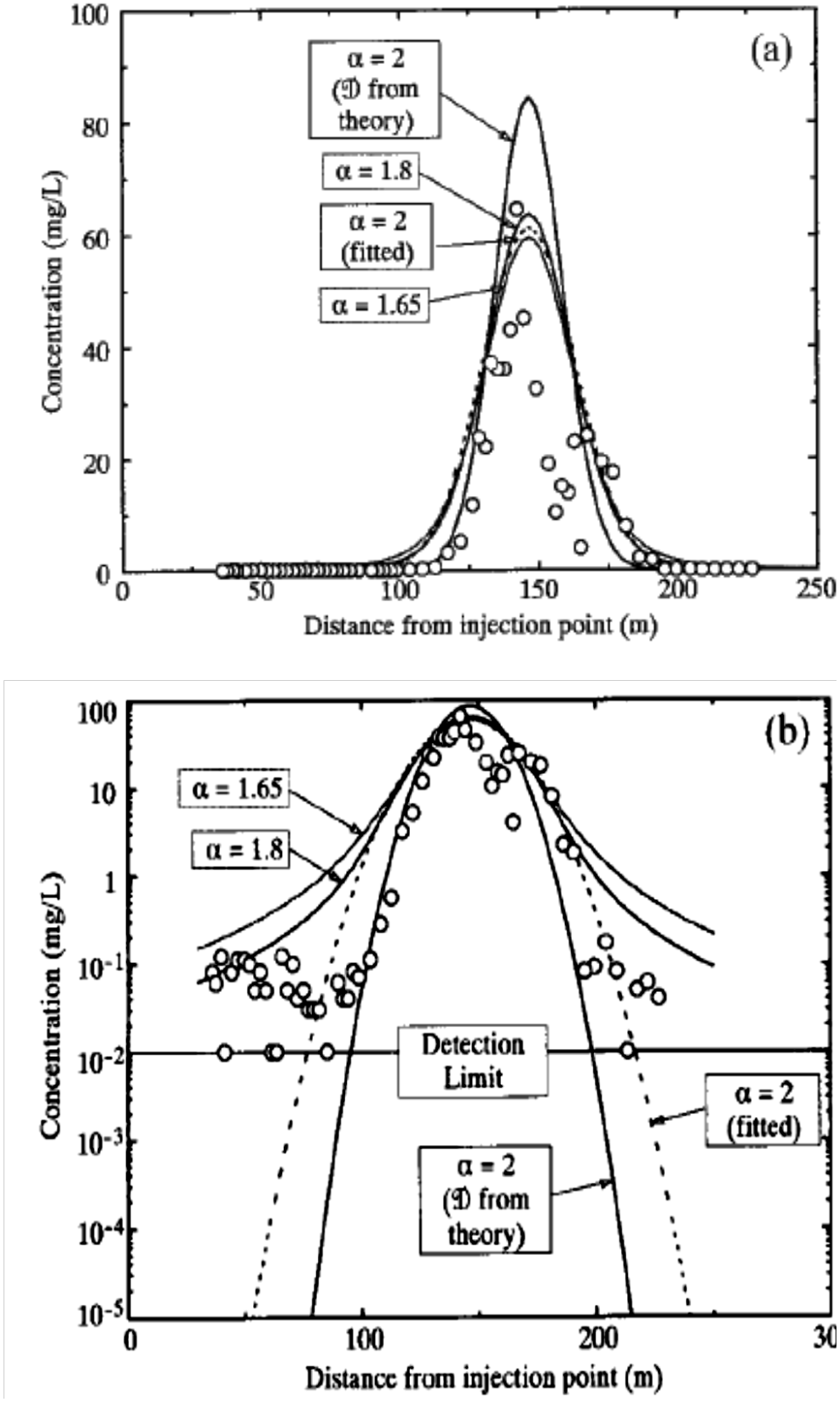

Figure 2.9 (a): Real axis along the plume core; (b): Semilog axis along the plume core. Solid line is the predictions, symbol is the actual measurement and dashed line indicates best fit Gaussian (Benson et al., 2000)

2.4 Aerosol Optical Depth

The AOD is a vital parameter that applies to determining air quality that affects environment and life-forms; monitoring volcanic and biomass pollution; forecasting and now-casting earth radiation budget and climate change; estimating variability of aerosols and its size distribution in the atmosphere. The greater the magnitude of the AOD at specified wavelengths, the lesser the chances of light at that wavelength to reach the Earth's surface. Aerosol optical depth is the measurement of transparency of the atmosphere. When AOD is less than 0.1 and 1.0, it indicates a crystal clear sky and very hazy conditions, respectively. AOD measures the amount of light lost due to the presence of aerosols or aerosols distributed on a vertical path through the atmosphere.

The sun photometer measures the AOD using the Beer-Lambert-Bouguer law where the voltage (V) is directly proportional to the spectral irradiance (I) measured by the sun photometer. The mathematical expression for the Beer-Lambert-Bouguer law (Faccani *et al*., 2009; He et al., 2012) is given

$$V(\lambda) = V_o(\lambda)d^2 \exp\left(-\tau(\lambda)_{tot} \times m\right) \tag{2.22}$$

where $\tau(\lambda)_{tot}$ is the total optical depth, and m is the optical air mass ,V_o is the extraterrestrial voltage, V is the digital voltage measured at wavelength λ, d is the ratio of the average to the actual Earth-Sun distance. The Beer-Lambert-Bouguer equation (He et al., 2012)could also be modified as

$$\tau_a = \frac{\left(In\left(\frac{V_o}{R^3}\right) - In\,(V - V_{dark}) - a_R\left(\frac{p}{p_o}\right)m\right)}{md} \tag{2.23}$$

where τ_a is the aerosol optical depth, V_o is the calibration constant for the sun photometer, R is the Earth-Sun distance, d is the day of the year, V and V_{dark} are the sunlight and dark voltages from the sun photometer respectively, a_R is the contribution of optical thickness of molecular (Rayleigh) scattering of light in the atmosphere, p is the station pressure, p_o is standard sea level atmospheric pressure, m is the relative air mass and written as $m = \frac{1}{\sin(\theta)}$, θ is the solar elevation angle.

The measurement of AOD is complex because aerosol is not solely responsible for the scattering or absorption of light. Other atmospheric constituents, for example, methane, ozone, nitrogen oxides, carbon (IV) oxide, water vapour scatter or absorb light, hence their joint AOD can be calculated as shown mathematically below (Liu et al., 2011) :

$$\tau(\lambda)_{aerosol} = \tau(\lambda)_{tot} - \tau(\lambda)_{water} - \tau(\lambda)_{Rayleigh} - \tau(\lambda)_{O_3} - \tau(\lambda)_{NO_2} - \tau(\lambda)_{CO_2} - \tau(\lambda)_{CH4} \quad (2.24)$$

where $\tau(\lambda)_{Rayleigh}$ is the optical depth of the Rayleigh scattering. Spectral aerosol optical depths at wavelength 440nm to 870nm are typically used to estimate the size distribution of aerosols. The size distributions of aerosols are better described by the Angstrom parameter (α) which can be calculated using two or more wavelengths. The most popular mathematical representation (Liu et al., 2011) of α is given as

$$\alpha = -\frac{d\ In\ \tau_a}{d\ In\ \lambda} \quad (2.25)$$

where τ_a is the aerosol optical depth, α is the Angstrom parameter and λ is the wavelength. When α is equal or greater than 2, a fine mode aerosol is dominant. When α is near zero, the coarse mode aerosol is dominant.

AOD can be measured using either ground (sun photometer) or remotely sensed techniques. AERONET is known for harnessing ground measurements. It gives quality data on all aerosol column properties. However, it has a major limitation of few sites in developing and remote regions. The principle of remotely sensed technique is based on the ability of satellite to capture particulates in the atmosphere through the reflection and absorption of visible and infrared light. Remote sensing technique is available on some sites. For example, Aura/OMI are used to obtain aerosol optical depth at ground pixel resolution of 0.25^o latitude/longitude grid and 1^o latitude/longitude grid resolution; Meteor-3, TOMS and NIMBUS 7 are used to obtain aerosol optical depth at ground pixel resolution of 1^o X 1.25^o latitude/longitude grid resolution. Other satellite sites for obtaining AOD are Moderate Resolution Imaging Spectroradiometer (MODIS), Advanced Very High Resolution Radiometer (AVHRR), MEdium Resolution Imaging Spectrometer (MERIS), Polarization and Directionality of the Earth's Reflectances (POLDER) over ocean and Multi-angle Imaging SpectroRadiometer (MISR), Advanced Along Track Scanning Radiometer (AATSR), Total Ozone Mapping

Spectrometer (TOMS), Ozone Monitoring Instrument (OMI), MODIS, Atmospheric Infrared Sounder (AIRS), TIROS Operational Vertical Sounder (TOVS) over land (NOAA, 2015).

The main importance of the AOD is to determine the aerosol size distribution. In this study, the aerosol size distribution was obtained using the Multi-angle Imaging SpectroRadiometer (MISR). The MISR was launched in 1999 to measure the intensity of solar radiation reflected by the planetary surface and atmosphere. It operates at various directions, that is, nine different angles (70.5^o, 60^o, 45.6^o, 26.1^o, 0^o, 26.1^o, 45.6^o, 60^o, 20.5^o) and gathers data in four different spectral bands (blue, green, red, and near-infrared) of the solar spectrum. The blue band is at wavelength 443nm, the green band is at wavelength 555nm, the red band wavelength 670nm and the infrared band is at wavelength 865nm. MISR acquire images at two different levels of spatial resolution; local and global mode. It gathers data at the local mode at 275 meter pixel size and 1.1 km at the global mode. Typically, the blue band is to analyse coastal and aerosol studies. The green band is to analyse Bathymetric mapping and estimating peak vegetation. The red band analyses the variable vegetation slopes and the infrared band analyses the biomass content and shorelines.

2.5 Statistical Tool for Data Analysis

The standard error (SE) of the mean was used next section to estimate the AOD population mean for each month of the year. SE technique used for this research captures the standard deviation of the monthly means over thirteen years. The standard error of the mean is expressed mathematically as (Brian, 1998)

$$SE = \frac{\sigma}{\sqrt{n}} \tag{2.26}$$

where $'SE'$ is the population standard deviation and $'n'$ is the population size.

Standard error measures the uncertainty in each AOD data set and the deviations of the monthly mean from the yearly mean. Standard deviation (σ) measures the amount of visible dispersion from the monthly mean. Like the SE, a low magnitude standard deviation signifies that the monthly mean is closer to the thirteen years mean also called expected value. Also, a high magnitude standard deviation signifies how far monthly mean is from the thirteen year mean. Standard deviation is given as (Brain, 1998)

$$\sigma = \sqrt{\frac{1}{N}\sum_{j=1}^{N}\left(y_j - \bar{y}\right)^2} \tag{2.27}$$

where y_j in the context of our research is the monthly-mean, $\bar{y}$ is the mean value of the thirteen years mean. The concept of variance is intrinsically connected with the effects of the difference between the monthly mean and the thirteen-year mean on the performance of the AOD. The coefficient of variation is the measure of a normalized dispersion of probability distribution within thirteen year mean for the AOD parameter used. In statistics, coefficient of variation is referred to as relative standard deviation and expressed in percentage. Coefficient of variation is not used for few meteorological parameters because of the inconsistency of its interval scale. For example, coefficient of variation is appropriate for the Kelvin scale and inappropriate for the Celsius scale, because the later's interval scale has both negative and positive values. Therefore, the coefficient of variation was adopted because the scale used has interval scale and it is appropriate for data set comparison between data sets of widely different yearly or monthly means. Coefficient of variation is represented mathematically as (Brian, 1998)

$$CV = \frac{\sigma}{\mu} \tag{2.28}$$

where σ is the standard deviation and μ is the monthly mean. Skewness, also known as skew(X) is a measure of the asymmetry of the probability distribution of the monthly mean about its thirteen-year mean. For a normal distribution, the skewness is equivalent to zero. The skewness value can be positive , negative, or undefined. When the skew is negative, it indicates that the mass of the distribution is concentrated on the right of the plotted graph, that is, left-skewed. When the skew is positive, the mass of the distribution is concentrated on the left of the plotted graph, that is, right-skewed. The Skew of a distribution can be written mathematically as (Brian, 1998; Brown 2016)

$$X = \frac{(\mu - \upsilon)}{E(|X - \upsilon|)} \tag{2.29}$$

where υ is the median, E is the expectation error.

Kurtosis (β) is any measure of the flattening or "peakedness" of the probability distribution of the monthly mean for each month of the year. Like skewness, kurtosis is a descriptor of the shape of a probability distribution which can be interpreted as $\beta > 3$ (Leptokurtic distribution- high probability for extreme values), $\beta < 3$ (Platykurtic distribution- probability

for extreme values is less than for a normal distribution) and β = 3 (Mesokurtic distribution - normal distribution). Kurtosis is mathematically written as (Brian, 1998; Brown 2016)

$$\beta = \frac{\mu^4}{\sigma^4} \qquad (2.30)$$

2.6. The West Africa Meteorology and the Aerosol impact

The West Africa region occupies a strategic location of the African continent. The region is located at the north of the equator and westward into the Atlantic Ocean. The region is unique because it encompasses major climatic zones. West Africa comprises of a dense rain forest along the coastal belt and extends to the sub-Sahelian savanna in the north. There are over 72 million hectares of forest in West Africa (Mari *et al*., 2011) which contributes to its ozone distribution. The life form activities within the region are somewhat unique via the aerosol loadings throughout each year. The aerosols loading across this region are uncontrolled for now due to industrial, agricultural, Sahara dust and domestic activity. This region experiences the monsoon signatures, such as, distinct seasonal shift in the prevailing winds, alternation between winter dry conditions and summer rainy conditions (Janicot *et al*., 2011).

The West Africa region is made up of eighteen countries namely Nigeria, Ghana, Benin, Burkina Faso, Cameroun, Cape Verde, Cote d'Ivoire, Equatorial Guinea, Gambia, Guinea, Guinea Bissau, Liberia, Mali, Mauritania, Niger, Senegal, Sierra Leone and Togo. According to the United State agency, the population of human in West Africa is over 300 million (Feedthenation, 2015). The predominant occupation is agriculture; hence, agricultural pollution from biomass burning is expected to be relatively high. Undoubtedly the aerosols loading over West Africa has influence on its climatic system. The explorative activities of funded projects (like AErosol RObotic NETwork (AERONET), AMMA, Dynamics-aerosol-chemistry-cloud interactions in West Africa (DACCIWA), West Africa Climate DRandD Project, Saharan West African Monsoon Multiscale Analysis (SWAMMA), West African Science Service Center on Climate Change and Adapted Land Use (WASCAL)) to unravel the climatic structure of West Africa and its relation to global climate has yielded much results with its peculiar challenges which is mainly finance.

DACCIWA is a project in the region funded by the European Union 7th Framework Program. The major objective is to investigate the emissions on the atmospheric composition over South and West Africa. The type of emissions-targeted include anthropogenic and natural. AERONET is a project funded by NASA's Goddard Space Flight Center and PHOtométrie pour le Traitement Opérationnel de Normalisation Satellitaire (PHOTONS). The project has over 18 ground-based sun photometers to measure aerosol optical thickness around West Africa. Currently, most of the sites are not fully functional.

The scientific challenges would be discussed in the later part of this section. AMMA is an international project which started in 2002 (Polcher *et al*., 2011) and its major objective is to unravel the West African monsoon (WAM) and its variability. The AMMA project spreads across many locations in West Africa. The AMMA utilize satellite data and diverse modelling studies. WASCAL is a large-scale project that focuses on designed programs to assist monitor and tackle climate change challenges in West Africa. SWAMMA is funded by Natural Environment Research Council (NERC) and its primary objective is to evaluate the role of Saharan monsoon, deep cumulonimbus convection and Saharan dust over Africa. Among the focus of this thesis is to determine the extent seasonal rainfall affects monsoon's boundary conditions- provided by the global climate system. West Africa Climate Project is intended to predict the frequency of droughts and flooding in West Africa; investigate the extent of involvement of the West Africa weather to understand the spread of common diseases like malaria, dengue and yellow fever.

2.6.1 The Features of the West African Climate System

The West African Monsoon (WAM) is characterized by strong precipitation and rich vegetation at the coastal regions of Nigeria, Ghana, Togo, Cape Verde, Cote d'Ivoire, Liberia, Sierra Leone, Guinea, Gambia and Senegal. Its precipitation variability is affected by many factors, for instance, global climate teleconnections and the yearly aerosols loading. The aerosols loading over West Africa can be monitored by aerosol optical depth measurements. Aerosol optical depth (AOD) is a vital parameter that applies to determining air quality that affects environment and life-forms; monitoring volcanic and biomass pollution; forecasting and now-casting earth radiation budget and climate change; estimating variability of aerosols

and its size distribution in the atmosphere. AOD can be measured using either ground (sun photometer) or remotely sensed technique. AERONET is typically known for harnessing ground measurements. It gives quality data on all aerosol column properties. However, it has a major limitation of few operational stations in developing and remote regions like West Africa.

The principle of remote sensing technique is based on the ability of satellite to capture particulates in the atmosphere through the reflection and absorption of visible and infrared light. Remote sensed data sets are available on some site. For example, Aura/OMI are used to obtain aerosol optical depth at ground pixel resolution of 0.25^{o} latitude/longitude grid and 1^{o} latitude/longitude grid resolution; Meteor-3, TOMS and NIMBUS 7 are used to obtain aerosol optical depth at ground pixel resolution of 1^{o} X 1.25^{o} latitude/longitude grid resolution. Other satellite sites for obtaining AOD are Moderate Resolution Imaging Spectroradiometer (MODIS), Advanced Very High Resolution Radiometer (AVHRR), MEdium Resolution Imaging Spectrometer (MERIS), Polarization and Directionality of the Earth's Reflectance (POLDER) over ocean and Multi-angle Imaging SpectroRadiometer (MISR), Advanced Along Track Scanning Radiometer (AATSR), Total Ozone Mapping Spectrometer (TOMS), Ozone Monitoring Instrument (OMI), MODIS, Atmospheric Infrared Sounder (AIRS), TIROS Operational Vertical Sounder (TOVS) over land.

Global climate teleconnections includes climatic oscillations and regional climate systems. The climatic oscillation includes El Nino-Southern Oscillation and North Atlantic Oscillation. The North Atlantic Oscillation originates eastward from the southwestern North Atlantic to Portugal and West Africa. The North Atlantic Oscillation is responsible for the abnormalities in temperature and precipitation patterns (NOAA, 2015). El Nino-Southern Oscillation (ENSO) is referred to as the most influential natural fluctuation of climate that occurs on interannual time-scales. ENSO originates in the tropical Pacific and extends globally to all climate systems. The Maden-Julian Oscillation (MJO) also influences temperature and precipitation patterns in Indian and West Africa monsoon. The regional climate systems include inter-tropical discontinuity, subtropical anticyclones, atmospheric winds, Jet stream, monsoons, sea surface temperature (SST) anomalies etc. Rainfall anomalies over the sub-

Saharan of West Africa are primarily triggered by sea surface temperature (SST) anomalies (Belen *et al*., 2015).

West Africa Region (WAR) experiences dry northeasterly winds coming from the Sahara Desert during the winter. This experience leads drastically to a reduction in rainfall. During summer season, West Africa region experiences low-level southwesterly winds and high rainfall rates (Segele *et al*., 2015). Popular models, such as, Global Circulation Models (GCMs) have failed to accurately simulate rainfall in the past and present over West Africa. This is because rainfall patterns in West Africa are complex in nature.

The general projections had been that the Sahelian coastline may experience a decrease in precipitation by around 15 to 20% by 2100 (IPCC, 2007). These coupled general circulation models (CGCMs) has different parameterizations to represent sub-grid scale processes such as clouds and boundary layer turbulence. They typically have different horizontal and vertical resolutions, hence, they enhance coupling between the atmosphere, ocean and land surface. Traditional CGCMs are unable to capture the monsoon because they cannot represent the complex, multi-scale interactions known to be associated with the monsoon. This explains the limitation of traditional models. Traditional model compulsorily parameterize the sub-grid scale processes. This makes the traditional model to capture the important feedbacks that occur between small scale convection.

The topography of West Africa monsoon is characterized by forest along the Guinea coast in the south of the region, shrub and grasslands in the Sahel in the mid-region, bare soil and desert in the north of the region. However, the largest aerosol emission sources in the West Africa monsoon are the mineral dust from the Sahara and Sahel through its northern region, and the biomass burning smokes from the southern region. The West Africa monsoon is also influenced by propagating mesoscale convective systems to the planetary scale circulation that drives the monsoon winds (Marsham *et al*., 2013). Haung and Dejun(2014) reported that aerosol-related events in West Africa can be traced back to African dust and smoke sources. For example, there is a reduction of precipitation when atmospheric aerosols is anomalously high. This is mostly experienced during boreal cold season, that is, from late autumn to

winter. Generally, the onset of the monsoon is typically in June, that is, during the wet season. In the lower troposphere (LT) of West Africa monsoon , the wind flow is characterized by the south-westerly while the upper troposphere (UT) is characterized by the Tropical Easterly Jet (Madhu 2014). Within the troposphere, the wind activity dictates the tropospheric ozone (Ziemke *et al*., 2015) which is initiated by biogenic emissions of volatile organic compounds (VOCs) from West Africa. The West African region is reported to be one of the sources of biogenic nitrogen oxides from lightning (Huang and Dejun, 2014). Marticorena *et al*., (2011) affirmed that biomass burning in West Africa is linked to agricultural practice and other anthropogenic activities which are located at latitudes south of 10^{o} N and the Southern Hemisphere outside of West Africa (between the equator and 10^{o} S).

The aerosols composition of the troposphere in West Africa monsoon was analysed using the flying programme of the African Monsoon Multidisciplinary Analysis (AMMA) project (Reeves *et al*., 2010). Reeves *et al*. (2010) gave details of the flying programme of AMMA. The measurements were carried out using Special Observational Periods 1 and 2 (SOP 1 and SOP 2) with the aircraft loaded with different sensors for chemical measurements. SOP 1 targeted month of June (the onset of the Monsoon development) using five research aircraft (three based in Niamey, Niger and two in Ouagadougou, Burkina Faso). SOP 2 targeted the months of July and August 2006 (when monsoon onset is maximum) using another five research aircraft (three based in Niamey, Niger and two in Ouagadougou, Burkina Faso). The research aircraft had their specific function. For example, ATR-42 focused on the lower troposphere, BAe-146 on the lower and mid-troposphere, Falcons on the upper troposphere and M55 on the upper troposphere/lower stratosphere. The research aircraft made comprehensive measurements of aerosols and trace gases, that is, their vertical and horizontal distribution from the planetary boundary layer to the lower stratosphere. The geographical location of the site ranges from 2^{o} N to 21^{o} N, and between 10^{o} W and 7^{o} E.

The major climatic zone of West Africa as shown in Figure (2.10) below- stretches across five latitudinal zones of 5° each namely zones 0 - 5°N, 5^{o} N - 10°N, 10^{o}N - 15°N, 15^{o} N - 20°N and 20^{o} N - 25°N. West Africa has tropical climate though the far northern portion of

West Africa is arid and stretches into the Sahara desert. The climatic zones of West Africa are shown in Figure (2.10) below.

Okonkwo (2014) discovered anomaly using observational analysis to investigate the relationships between the West Africa and the Mediterranean climate at interannual timescale. This discovery may be hinged on Tropical Easterly Jet (TEJ) which circulates across West Africa during the boreal summer season. TEJ is associated with the Mediterranean climate and emanates from the Asian monsoon. The four different climatic zones in West Africa are Sahelian zone, Sudano-Sahelian zone, Sudanian zone and Guinean zone. Sahelian zone is a region of perennial vegetation, the average annual precipitation ranges between 250 and 500 mm. The Sahel zone is dominated by the West Africa monsoon. As discussed earlier in section 2.6.1, large-scale circulation-transporting moisture from the Atlantic Ocean into the land is expected in Sahel zone. The Sahel zone is also characterized by wind reversal in the lower atmosphere. Sudano-Sahelian zone is a region where average annual precipitation ranges from 500 to 900 mm. Sudanian zone is a region of an average annual precipitation that ranges from 900 to 1100 mm. Guinean zone is a region of an average annual precipitation exceeding 1100 mm. Atmospheric circulation pattern in the four zones is controlled by some salient factors like African Easterly Jet (AEJ), Intertropical Convergence Zone (ITCZ), Intertropical Discontinuity (ITD), associated heat low (HL), Subtropical Jet (STJ), troughs and cyclonic centers associated with African Easterly Waves (AEW) and Tropical Easterly Jet (TEJ).

AEJ operates at mid troposphere (600-700mb) with maximum wind speed above 10m/s and travels to West Africa from the East Africa. The AEJ drives convection and rainfall patterns in the four climatic zones of West Africa (Ogungbenro and Tobi, 2014). ITCZ also contributes to the convective rainfall pattern through the south-north-south displacement. The Sahelian, Sudano-Sahelian and Sudanian climate zone are characterize by desert dust. Hence, the aerosol loading in such location is high. Desert dust is deposited mainly by wind erosion.

The finer dust particles diffuse to high altitudes and travels thousands of kilometers from its source (Das *et al*., 2013). This action explains the continual influence of aerosol loadings over

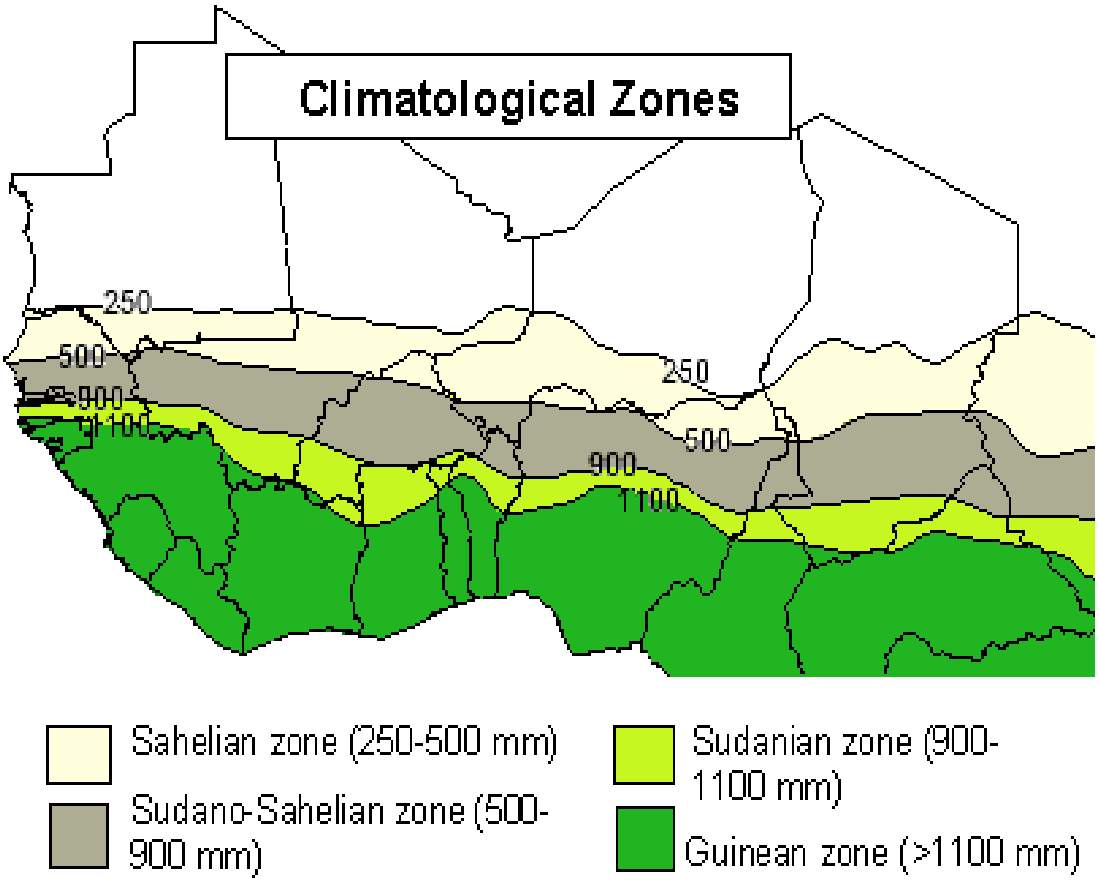

Figure 2.10: Climatic zones in West Africa-FAO. (Ogungbenro and Tobi, 2014)

the West African climate system. According to Huang and Dejun (2014) and Haywood *et al*.(2008), the aerosol emission pattern in West Africa is closely related to the seasonal north-to-south shift of the Inter-Tropical Convergence Zone (ITCZ). The AMMA project has studied the desert dust impact using ground-based lidars and airborne in-situ aerosol and gas measurements (Haywood *et al*., 2008). It was discovered that the desert dust transports through vertical distribution over West Africa during the dry monsoon. This pattern is influenced by the north-easterly Harmattan, AEJ and south-westerly trade winds.

2.6.2 Meteorological Exploration in West Africa and Its Challenges

In the previous section, the satellite exploration techniques were listed and discussed. The satellite sensors also (like the sun photometer) have their operational biases. These biases are documented in literatures (Faccani *et al*., 2009). This is one of the reasons ground station measurements are preferred to the satellite measurement. Another reason is that satellite measurement is limited beyond cloud-free pixels and has a reduced sensitivity in the lower atmosphere. The radiosonde (ground) stations are used to generate high digital vertical resolution of in situ wind, temperature, pressure, and humidity data. Financing radiosonde stations across the major parts of the West African monsoon is quite challenging. The introduction of funded projects (by AERONET and AMMA) to West Africa has enabled the present understanding of the West Africa monsoon . For example, the jet streak of the AEJ has been discovered to extend 10^{o}E using the AMMA experiment. Also, the funded projects have revealed that maximum aerosol optical depth occurs over West Africa (between 0 and 15 N) in December, January and February. Therefore, it is scientific to envisage more impactful meteorological influences in West Africa in the future. One of the present challenges of the funded projects in West Africa is the accuracy of the type of radiosonde. For example, the AMMA campaign in Africa used various radiosondes to execute their campaign. Each of the radiosondes are selected based on their biases in relative humidity measurements. The success of some of the radiosonde was limited due to specification of the manufacturer. Part of the challenges being multiple refractive indexes (MRI) of moving aerosol layer in the atmosphere (Figure 2.11).

The MRI is said to influence atmospheric measurements and most unsuccessful campaign were not directly on the instrument but on the inability of the manufacturer to compute the right parameter (atmospheric constants) into the compact flash card of the measuring instruments. For example, Vaisala RS80-A sondes has large dry biases and Vaisala RS92 has weakly moist biases. Bock *et al*. (2008) documented the biases of the radiosonde except for MODEM M2K2 sondes whose humidity biases are not known. The unknown biases of the MODEM M2K2 sondes and the loss of TEMP messages from reliable ground and satellite stations is a further affirmation to the need for documenting the atmospheric constant over each geographical area. Emphasis on the biases of the measuring instrument may be secondary at this moment. Nuret *et al*. (2008) admitted that the loss of TEMP messages from reliable stations is currently out of the scope of AMMA project. This means that explorative scientists working on West Africa have a task of calculating the right atmospheric constants that manufacturers of radiosondes must work with. In this chapter, it shall be proven that the atmospheric constant varies regionally because of the variance in aerosols loading. Another challenge of the present ground station across West Africa is the maintenance of the station.

Few AERONET station within West Africa has stopped operation while the existing station are not 100% functional, that is, based on the missing data available at http://aeronet.gsfc.nasa.gov/. Another challenge facing funded projects in West Africa is data gaps and retrieval problems (Faccani *et al*., 2009). For example, the convergence location of moisture in the Sahel climate zone is still unknown despite the availability of radiosonde stations across West Africa. This challenge has necessitated the use of European Center for Medium range Weather Forecasting (ECMWF) bias correction for AMMA measurements (Faccani *et al*., 2009). This development shows that the number of radiosonde stations over West Africa are grossly inadequate to understand the in-depth features of West Africa monsoon. Since the quality of forecast is based on data accuracy as well as developing accurate models, the nowcast or forecast of metrological station in West Africa is still questionable.

One of the advantages of satellite observation over ground observation is the enabled overview of the meteorological performance over any location. For example, the ozone

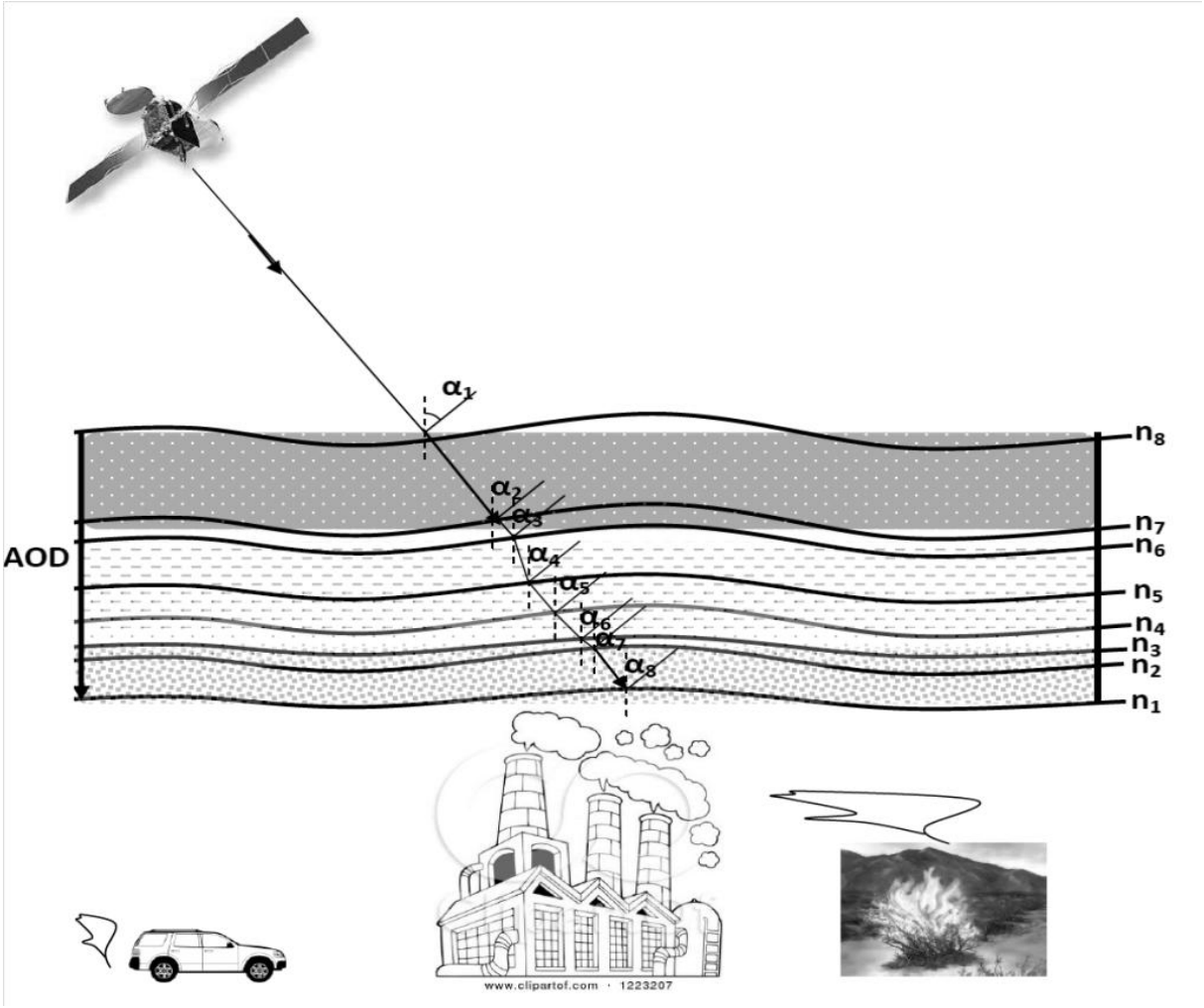

Figure 2.11: Illustration of the multiple refractive indexes

distribution over West Africa showed significant south–north gradient with lower and higher values over forested regions and the north of 12°N respectively (Adon *et al*., 2010); the emission of large amounts of biogenic volatile organic compounds (VOCs), NOx and O_3 are observed over the boundary layer in the Sahelian climate zones (Ferreira *et al*., 2010); the activities of the mesoscale convective systems (MCS) over the northern edge of the West African ITCZ in Sahel climate zone can be monitored (Nicholson, 2013). Though there had been successful satellite exploration in West Africa, the need for 'ground-truth' is eminent. For example, the aerosol-water cycle interactions over West Africa are currently investigated in the DACCIWA project.

Janicot *et al*. (2011) had explained the physics of the transporting marine and biogenic air masses and the dust-laden north-easterly dry winds. However, the success of the current DACCIWA project may shed more light into the complexity of the condensation nuclei (CCN) in West Africa. At this stage, satellite observations of tropical gravity waves (GW) over West Africa have not been properly explained by models. Interestingly, the AMMA project have launched ground observations and observed the relation between deep convection and gravity waves (Jewtoukoff *et al*., 2013). The aerosols loading over West Africa using the Total Ozone Mapping Spectrometer (TOMS) Aerosol Index (AI) and its corresponding effect over salient metrological parameters between 2002 and 2006 was observed to be quite significant. The satellite imagery obtained from the Modern Era Retrospective analysis for Research and Applications (MERRA) affirms the danger of the aerosols loading in West Africa. The climate peculiarity of West Africa- shown in Figures 2.12 and 2.13 affirm that deposited aerosols undergo a complex transport pattern.

Scientists have made several attempts to evaluate the mechanism of seasonal pollutant variation. For instance, the sun photometers were used to study column aerosol optical properties (He *et al*., 2012); Lidar systems were used to examine vertical profiles of atmospheric aerosols at high temporal and spatial resolution (Liu *et al*., 2011); EARLINET systems to determine the bottom and top layer heights of the aerosols in free troposphere (Sicard *et al*., 2015); and satellite imagery to investigate the optical, chemical and microphysical characterization of aerosol particles (Hussein *et al*., 2004). However, the

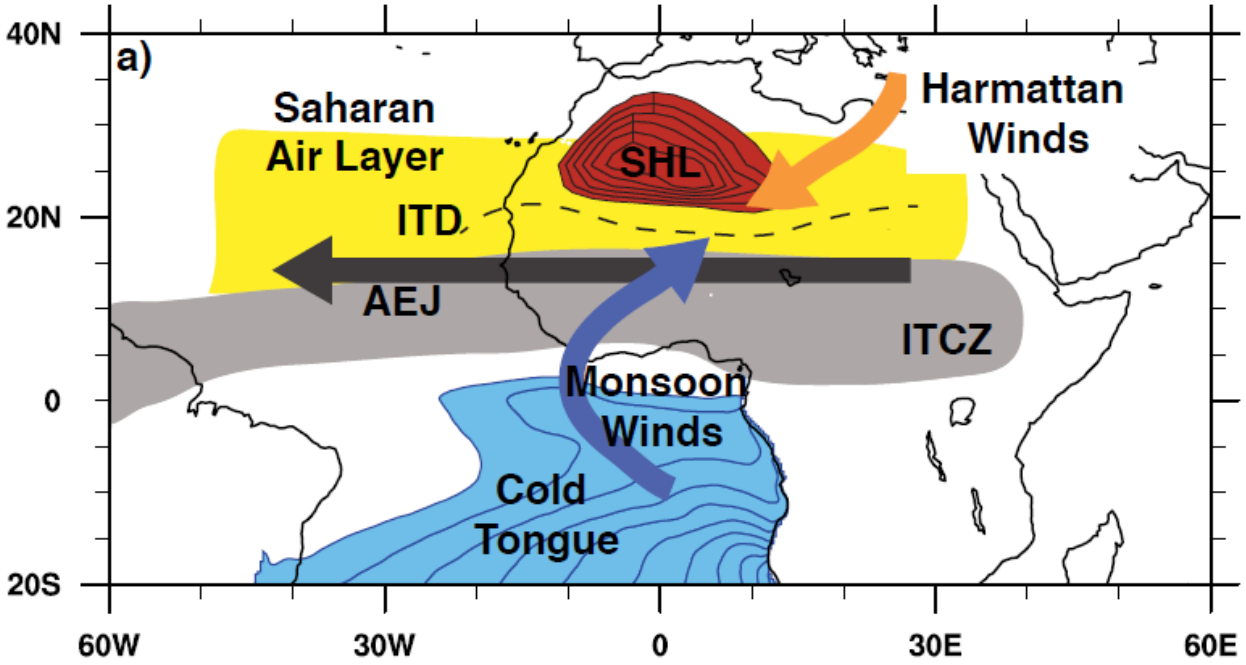

Figure 2.12: Saharan air layer, Intertropical discontinuity (ITD), African easterly jet (AEJ), Intertropical convergence zone (ITCZ), Harmattan winds, Monsoon winds, Atlantic cold tongue (Mari et al., 2011)

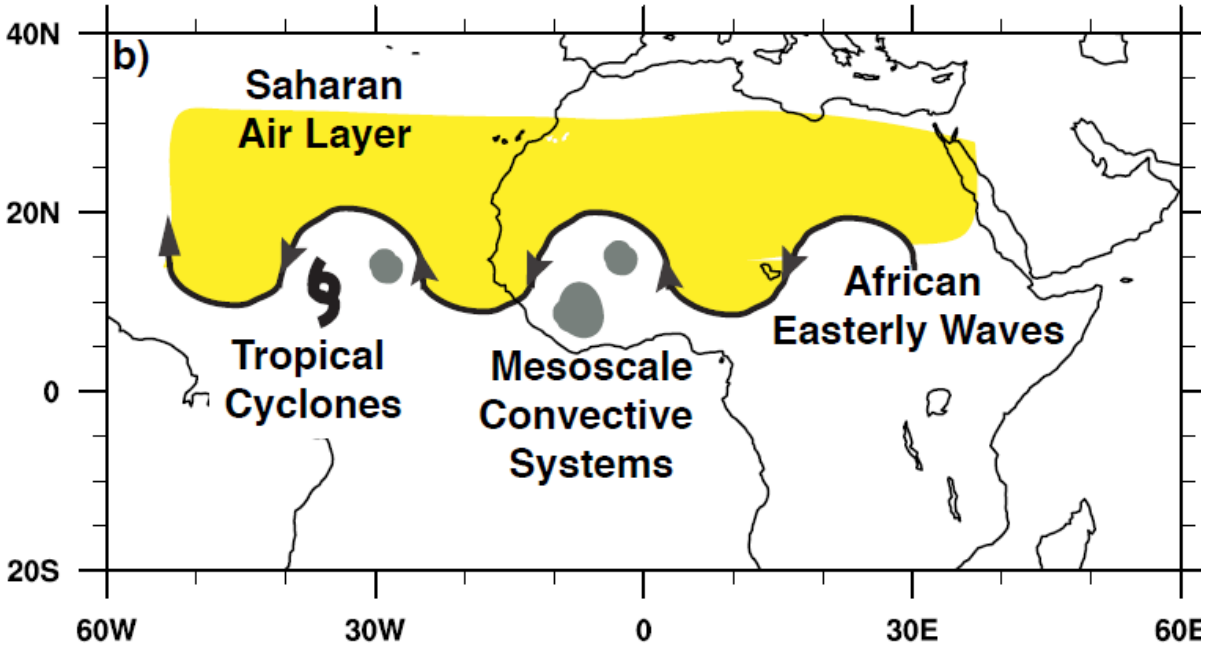

Figure 2.13: Mesoscale convective systems, African easterly waves, and Tropical cyclones (Mari et al., 2011)

behaviour of pollutants varies with respect to the contraction and expansion of both the frictionless and friction atmospheric layers. For example, frictionless or free tropospheric aerosols originate from long-range transport while tropospheric aerosols in the frictional layer (planetary boundary layer) originate from local sources and regionally transported aerosols.

The regional aerosols transport within the PBL is majorly influenced by marine air masses and the long-range transport of desert dust (Rajeev et al., 2000). Hence, the collective role of regional, localized and remote aerosol transport over an area makes it difficult to accurately determine the type of aerosol distribution or aerosols loading over an area per time. Wang et al. (2015) examined the relationship between AOD and some parameters like aerosol size distribution, refractive index and scattering albedo. Che et al. (2014) considered the AOD at some specific wavelength (500 nm and 675 nm) to determine the direct radiative forcing through its aerosol optical properties in rural, suburban and urban regions. The atmospheric radiative forcing exceeded $-200\ Wm^{-2}$, $-180\ Wm^{-2}$ and $-50\ Wm^{-2}$, at urban, suburban and rural respectively.

CHAPTER THREE

METHODOLOGY

3.1 Framework of Methodology

In section 3.2, the location of study and meteorology of West Africa was discussed to justify the volume of data collection and the mathematical assumptions adopted in succeeding sections. In section 3.3, the data collection approach was illustrated. The satellite data was obtained from Multi-angle Imaging SpectroRadiometer (MISR) and the Moderate Resolution Imaging Spectroradiometer (MODIS) database. The ground data set was obtained from the Aerosol Robotic Network (AERONET) radiosonde measurements and National Meteorological Centers. In section 3.4, theoretical and mathematical approach which include data analysis was explained. The mathematical approach includes the development of numerical model. First, a comparative study was carried out to validate the authenticity of the developed model with existing models. The developed model was used to generate the atmospheric constant as well as the aerosol size distribution over West Africa. The second model was developed to explain the variation between satellite data set of the MODIS and MISR. The third model was developed to examine aerosol trend in regions of scanty satellite data set.

3.2. Location of Region Studied

The location of study is West Africa (Figure 3.1). West Africa is comprised of Nigeria, Ghana, Togo, Cape Verde, Cote d'Ivoire, Liberia, Sierra Leone, Equatorial Guinea, Guinea Bissau, Gambia, Benin, Cameroun, Burkina Faso, Mauritania, Mali, Guinea and Senegal. The tropical climate is in dominance in the countries listed in the West African region.

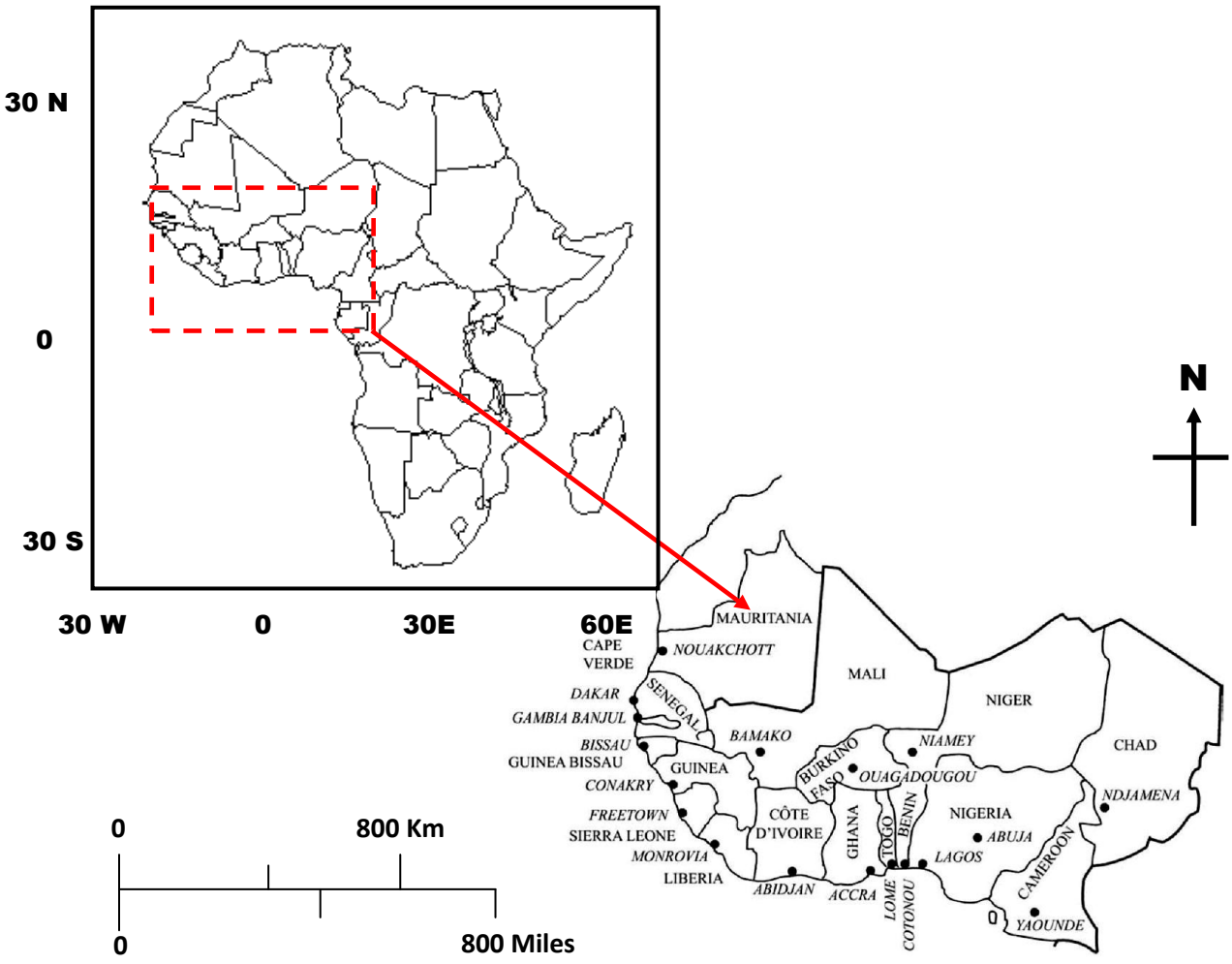

Figure 3.1: Map of West Africa

Nigeria is the most populous nation in the West Africa region with an area of about 923,768 km^2 within 4^oN - 14^oN latitude and 3^oE - 14^oE. It is surrounded by the Gulf of Guinea, Benin, Cameroon, Niger and Lake Chad in the south, west, east, north and northeast respectively. Major geographical features in Nigeria are River Niger and River Benue; Jos, Obudu and Mambilla Plateau; and Niger Delta, Ogun-Osun and Owena River basins. Nigeria has two seasons (that is, dry and wet season) and it is generally very humid and partially damp-seasonally.

Ghana is located between latitude 4° N and 12°N. The geographical features in Ghana includes plains, low hills, rivers, Lake Volta, ecoregions (coastline, sandy shore, scrub), plateau region (Kwahu Plateau and Ashanti uplands), mangroves. The climate system in Ghana is driven by tropical rain forest belt and heavily forested hills.

Togo is about 56,785 km^2 in its bounding area and located on latitude and longitude 8° N and 1°10′ E respectively. It is surrounded by Benin, Burkina Faso, Ghana and Bight of Benin in the east, north, west and south respectively. Benin consist of six geographical regions and two savanna plains regions. The geographical structures of Togo are tidal flats, sandy beaches, shallow lagoons and lakes.

Cape Verde is comprised of arid Atlantic islands that are located off the west coast of Africa in the mid-Atlantic Ocean. The geographical structure of Cape Verde are landscape, volcanoes, cliffs, islands, islets and high mountains. Cape Verde has an arid climate system. Soil erosions are frequent in Cape Verde due to high wind pattern and lack of natural vegetation.

Côte d'Ivoire is located in the sub-Saharan region on latitude 5°N to 10°N and longitude 4°W to 6°W. Côte d'Ivoire is surrounded by Liberia, Guinea, Mali, Burkina Faso and Ghana along the southwest, northwest, north-northwest, north-northeast and east respectively. Its land coverage bounds within an approximate area of 322,463 km^2. The geographical structure of Côte d'Ivoire includes plateau, tropical forest and coastal inland lagoons in the south. Its climate is warm and humid. Like most Sub-Saharan nation, it has three seasons; 'warm and dry' season around November to March, 'hot and dry' season around March to May, and 'hot and wet' season around June to October.

Liberia is located in the sub-Saharan region on latitude 6 °N and longitude 9 °W. Liberia is surrounded by North Atlantic Ocean, Côte d'Ivoire, Guinea and Sierra Leone in the southwest, northeast, northwest and west respectively. The geographical structure of Liberia includes hilly terrain, low mountains and rolling plains and plateau. It has two seasons; wet season around late April to mid-November, and dry season around December to March. Its climate is warm and humid.

Sierra Leone lies within the latitude of 6°N and 9°N, and longitude of 11° W and 13°W. Sierra Leone is surrounded by Guinea, Liberia and Atlantic Ocean in the northeast, southeast, and west respectively. Sierra Leone is bounded within an area of 71,740 km^2. Sierra Leone has four geographical regions: upland plateau, coastal Guinean mangroves, the wooded hill country, and the eastern mountains. It has two seasons; wet season around May to November, and dry season around December to May.

Equatorial Guinea can be found in the west central Africa and located on latitude 1°N to 3°N and longitude 8°E to 11°E. It is bounded within an approximate total area of 28,050km^2. The geographical structure of Equatorial Guinea includes Islands, volcanic formations and low hills. Its climate is warm with heavy rainfall, and high humidity. Equatorial Guinea has wet season around February to June and from September to December. Its dry season is from December to mid-February.

Guinea Bissau is located on latitude 11°N to 12°N and longitude 14°W to 15°W. It is bounded within an approximate total area of 36,125 km^2. Guinea Bissau geographical structure includes low coastal plain, Guinean mangroves and forest. Its climate is hot, dry, dusty harmattan haze in the dry season, and warm and humid in the wet season. Its wet season is from June to early October, and the dry season is from December to April.

The Gambia is located on latitude 13.2°N to 13.5°N and longitude 14°W to 16°W. It is bounded within an approximate total area of 11,295 km^2. It is the smallest country by land mass within the West African region. It is seldom referred to as an enclave of Senegal. Its climate is Hot and humid. It has two seasons; wet season around June to October, and dry season around November to May (Ourafrica, 2015).

Benin is located on latitude 6°N to 11°N and longitude 1°E to 2°E. It is bounded within an approximate total area of 112,622 km^2. Benin is surrounded by Togo, Burkina Faso, Niger, Nigeria and the Bight of Benin in the west, north, northeast, east and south respectively. Its climate is hot and humid. Its dry season (December to March) is influenced by dry Sahara winds.

Cameroon can be found in the west central Africa and located on latitude 2°N to 12°N and longitude 9°E to 15°E. It is bounded within an approximate total area of 475,440 km^2. Cameroon has five geographical zones whose climates and vegetation is noticeable or replicated accross geographical locations of Africa. This makes scientists describe Cameroon as "Africa in miniature". Its geographical structure includes mountains, Central African mangroves, desert, plateau, tropical rain forest, savanna grassland, rivers and ocean coastland (Ourafrica, 2015).

Burkina Faso is referred to as Sahel country and located on latitude 10°N to 14°N and longitude 0.7°W to 4°W. It is bounded within an approximate total area of 274,200 km^2. Its geographical structure includes forests in the south, desert in the north. Its climate is warm and humid. It has two seasons; wet season around May to September, and dry season around October to April.

Mauritania is located on latitude 16°N to 22°N and longitude 7°W to 17°W. It is bounded within an approximate total area of 1,030,700 km^2. Its geographical structure includes arid plains, cliff, plateau and oases. Its climate is hot with irregular rainfall.

Mali is located on latitude 16°N to 22°N and longitude 7°W to 17°W. It is bounded within an approximate total area of 1,240,192 km^2. Its geographical structure is mainly desert which is about 66% of its land mass. Mali has three natural zones; Sudanese zone, northern desert Saharan zone and central semi-desert Sahelian zone. Its climate is hot, sunny and dry.

Guinea is located on latitude 7°N to 12°N and longitude 8°W to 13°W. It is bounded within an approximate total area of 245,860 km^2. Guinea is surrounded by Guinea-Bissau to its northwest, Senegal to its north, Mali to its north northwest, Côte d'Ivoire to its west, Liberia to its southwest, and Sierra Leone to its south. Its geographical structure includes lowland, Guinean forest, highlands, southeastern rain-forest region.

Senegal is found in the coastal West African region and it is located on latitude 12°N to 16°N and longitude 13°W to 17°W. It is bounded within an approximate total area of 196 190 km^2. Senegal is surrounded by North Atlantic Ocean, Mauritania, Mali, and Guinea in the west, north, east and south respectively. Its climate is hot and dry. It has two seasons; wet season around June to October, and dry season around November to May (Ourafrica, 2015).

3.3 Data Collection

The data sets used for this study includes:

i. Fourteen years satellite data sets for twenty eight (28) locations across the West African region. Data can be obtained from https://gdata1.sci.gsfc.nasa.gov/daac-bin/G3/gui.cgi?instance_id=MISR_Daily_L3. Two basic criteria used for selecting the locations within each country were human population and the grid system;

ii. Ten years ground data sets were obtained for six locations across the West African region using the AERONET radiosonde measurement. Data can be obtained from http://aeronet.gsfc.nasa.gov/;

iii. Fourteen years ground data set were obtained from the Nigerian Meteorological Agency, Nigeria; and

iv. A set of 680,000 wind data from the Davis automatic weather station were analysed. The data logger was set to capture wind data every minute for the different wind directions - NE, SW, SE, NW, NNW, N, W, ESE, ENE, NNE, E, WSW, WNW, SSW and SSE. The location of study is Covenant University, Ota South-West Nigeria which is located on latitude 6.7^{o}N and longitude 3.23^{o}E. The data set studied were divided into night time (10pm to 11pm); afternoon time (2pm to 3pm) and morning time (4am to 5am).

The locations are illustrated in the Tables 3.1 – 3.3

Table 3.1: Satellite data set locations and the corresponding population (Tageo, 2015)

No	Countries	City	Population (2000)	Latitude (DD)	Longitude (DD)
1.	**Nigeria**	Lagos	8682200	6.450	3.470
2.		Kano	3412900	12.000	8.520
3.		Abuja	171800	9.07	7.48
4.		Ilorin	805800	8.500	4.530
5.		Enugu	625000	6.330	7.500
6.		Warri	530300	5.510	5.750
7.		Sokoto	525200	13.070	5.240
8.	**Ghana**	Accra	1719100	5.560	-0.200
9.		Bolgatanga	663100	6.690	-1.630
10.	**Benin**	Cotonou	818100	6.360	2.440
11.		Porto novo	234300	6.480	2.630
12.	**Burkina Faso**	Ouagadougou	996500	12.370	-1.530
13.	**Cameroun**	Yaounde	1187100	3.870	11.520
14.		Ngaoundere	352700	4.060	9.710
15.	**Cape Verde**	Praia	101000	14.930	-23.540
16.	**Cote D'ivoire**	Abidjan	3548400	5.330	-4.030
17.		Bondoukou	75300	8.030	-2.800
18.	**Equatorial Guinea**	Malabo	101600	3.740	8.790
19.	**Gambia**	Serekunda	225500	13.450	-16.680
20.	**Guinea**	Conakry	1851800	9.550	-13.670
21.	**Guinea Bissau**	Bissau	305700	11.870	-15.600
22.	**Liberia**	Monrovia	557500	6.310	-10.800
23.	**Mali**	Bamako	953600	12.650	-7.990
24.	**Mauritania**	Nouakchott	678700	18.090	-15.980
25.	**Niger**	Niamey	739600	13.520	2.120
26.	**Senegal**	Dakar	2613700	14.720	-17.480
27.	**Sierra Leone**	Freetown	1070200	8.490	-13.240
28.	**Togo**	Lome	695100	6.170	1.350

Table 3.2: National Meteorological Center, data set locations and the corresponding population (Tageo, 2015)

No	City	Population (2000)	Latitude (DD)	Longitude (DD)
	Nigeria			
1.	Lagos	8682200	6.450	3.470
2.	Abeokuta	556400	7.160	3.350
3.	Ibadan	3201500	7.380	3.930
4.	Ilorin	805800	8.500	4.530
5.	Ogbomosho	755400	8.080	4.180
6.	Oshogbo	437800	7.830	4.580
7.	Ondo	236600	7.090	4.840

Table 3.3: Ground data set locations and the corresponding population (Tageo, 2015)

No	City	Population (2000)	Latitude (DD)	Longitude (DD)
	Nigeria			
8.	Ilorin	805800	8.500	4.530
9.	Lagos	8682200	6.450	3.470
	Burkina Faso			
10.	Ouagadougou	996500	12.370	-1.530
	Cape Verde			
11.	Praia	101000	14.930	-23.540
	Niger			
12.	Banizoumbou	899327	13.788	1.42

3.4 Derivation of the Plume Dispersion Model

The plume dispersion models are mostly described in 2D. The implications of the 2D model have been discussed in Chapter Two. It was proposed that a good 3D model of plume dispersion analysis should account for salient parameters like the vertical dispersion method, the scattered dispersion and the horizontal dispersion. Each kind of dispersion are very significant both in the micro-scale and macro-scale analysis of atmospheric particulates dispersion within the lower atmosphere. Ground and satellite exploration in the West Africa region (as discussed in the previous section) have shown that the collective influence of dispersion sources within West Africa are complex to analyse due to various weather conditions. The full analyses of all the techniques are workable upon the following assumptions.

i. Inclusion of the mild diffusion at the downwind plain is significant to access the perturbations in the frictional layer of the atmosphere. Therefore to accommodate the excess weather perturbations, we assume that the measurement of the eddy diffusivity is between 2 -3 m^2/s, though in reality, it varies from place to place.
ii. The angles of deviation (α and β) depend on the wind convection and it does not exceed 180^o. This assumption is to control the theoretical experimentation within the frictional layer, that is, the planetary boundary layer of the lower atmosphere.
iii. The presence of air upthrust and air viscosity was made negligible because of the influence of the ground heat flux.
iv. The width of the plume depends on both the wind direction and coefficient of eddy diffusivity. This assumption enables the avoidance of bogus mathematical expressions for analyzing multi-source particulate dispersions.
v. The pollution particulates are uniformly distributed along the sampling site. This assumption necessitates the mathematical representation of satellite measurements
vi. The wind speed ranges 1 ms^{-1} and 0.72 ms^{-1} at 10 m above the ground (below the planetary boundary layer) during the dry and wet seasons respectively

The pictorial view of particulates dispersion (Figure 3.2) is necessary to appreciate the theoretical extension from a uni-source dispersion point to a multi-source dispersion point. The general effect seen through the ground or satellite measurement of the aerosol optical

depth is related to the multi-source. The model incorporates four equations; general dispersion equation, mild dispersion equation, turbulent dispersion equation and particulate deposition equation. The mild dispersion equation and turbulent dispersion equation applies to any dispersion source or pattern. The dispersion patterns depend on the dispersion source. For example, particulates from bush burning differs with respect to their geographical locations. As expressed in assumption (5) above, the particulate distribution from the various sources normalize under the control of wind direction and the eddy diffusivity in the sub-layer of the planetary boundary layer. Air particles at the mild dispersion region are the lightest by mass and energetic to interact with atmospheric current (Lovejoy *et al*., 2004). Hence, the analytical technique for developing the dispersion model can be illustrated using the diagram shown below.

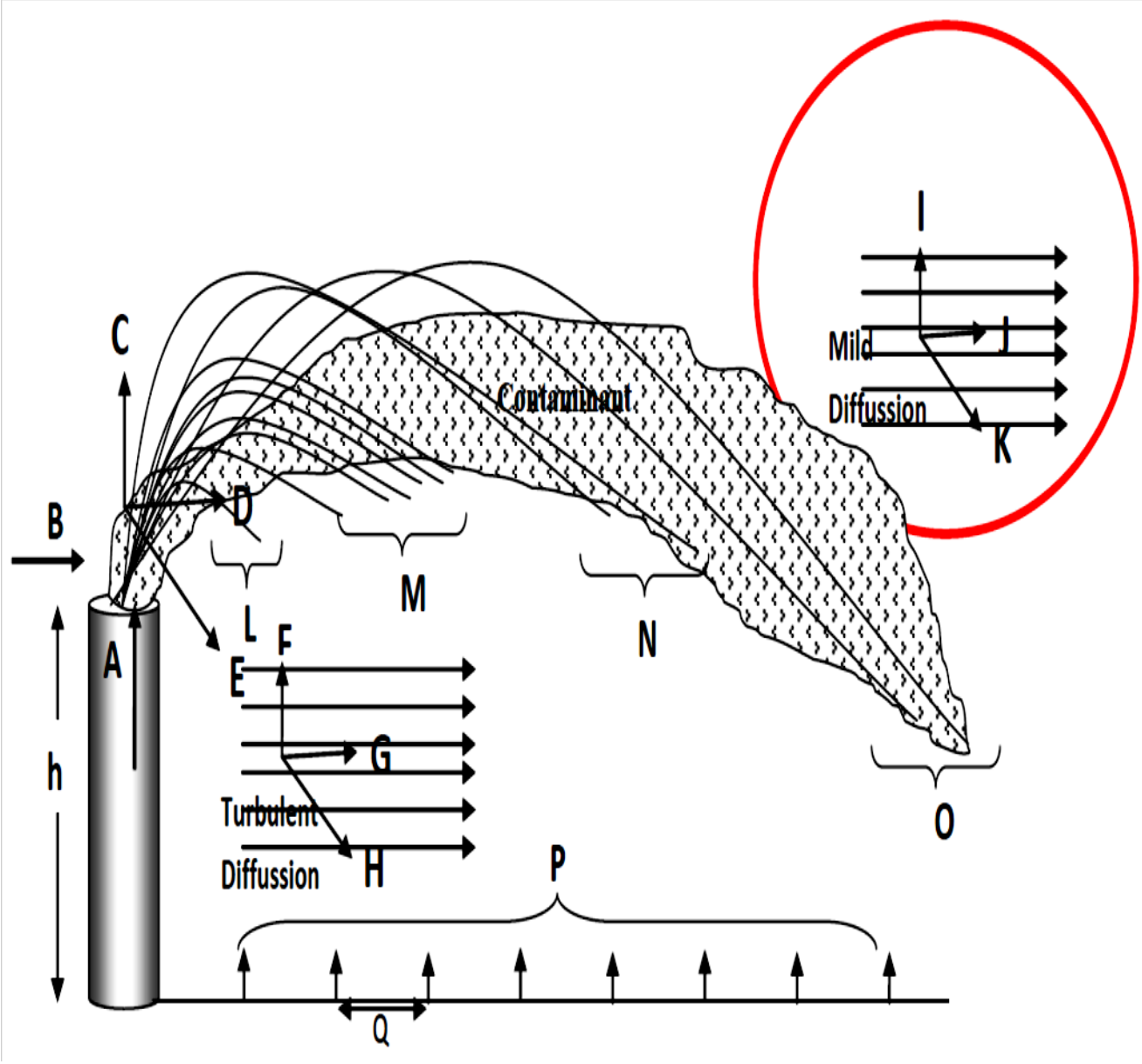

Figure 3.2: Pictorial analysis of the general dispersion model

The equations for each of the events in Figure 3.2 are shown below. The theoretical expressions for the different positions are as mathematically represented below:

Region **A**-**E** is the general particulate dispersion analysis as derived is shown in equations 3.1 – 3.5:

$$A = \frac{\partial C}{\partial t} \tag{3.1}$$

$$B = V\frac{\partial C}{\partial r} \tag{3.2}$$

$$C = V_z\frac{\partial C}{\partial z} \tag{3.3}$$

$$D = V_x\frac{\partial C}{\partial x} \tag{3.4}$$

$$E = V_y\frac{\partial C}{\partial y} \tag{3.5}$$

Where $V^2 = {V_x}^2 + {V_y}^2 + {V_z}^2$

Region **F**-**H** is the turbulent particulate dispersion analysis (equations 3.6 – 3.8)

$$F = \frac{\partial}{\partial z}\left(K_z\frac{\partial C}{\partial z}\right) \tag{3.6}$$

$$G = \frac{\partial}{\partial x}\left(K_x\frac{\partial C}{\partial x}\right) = 0 \tag{3.7}$$

$$H = \frac{\partial}{\partial y}\left(K_y\frac{\partial C}{\partial y}\right) \tag{3.8}$$

Region **I**-**K** is the mild particulate dispersion analysis (equations 3.9 – 3.11)

$$I = \frac{\partial}{\partial z}\left(K_{z2}\frac{\partial C}{\partial z}\right) \tag{3.9}$$

$$J = \frac{\partial}{\partial x}\left(K_{x2}\frac{\partial C}{\partial x}\right) = 0 \tag{3.10}$$

$$K = \frac{\partial}{\partial y}\left(K_{y2}\frac{\partial C}{\partial y}\right); \tag{3.11}$$

Region **L**-**O** is the particulate deposition analysis (equations 3.12 – 3.15)

$$L \approx \frac{2V_{1x}^3 V_y}{gV^2} \tag{3.12}$$

$$M \approx \frac{2V_{2x}^3 V_y}{gV^2} \quad (3.13)$$

$$N \approx \frac{2V_{3x}^3 V_y}{gV^2} \quad (3.14)$$

$$O \approx \frac{2V_{4x}^3 V_y}{gV^2} \quad (3.15)$$

V is the wind velocity (m/s), P is the air upthrust, C(x,y,z) is the mean concentration of diffusing pollutants of diffusing substance at a point (x,y,z) [kg/m^3], K_y, K_x is the eddy diffusivities in the direction of the y- and x- axes [m^2/s] and S is the source/sink term [kg/m^{3}s] The three set of governing equations 3.16 to 3.18 were obtained from equations 3.1 to 3.11:

$$\frac{\partial C}{\partial t} + V_x \frac{\partial C}{\partial x} - V_z \frac{\partial C}{\partial z} - V_y \frac{\partial C}{\partial y} = \frac{\partial}{\partial z}\left(K_z \frac{\partial C}{\partial z}\right) + \frac{\partial}{\partial y}\left(K_y \frac{\partial C}{\partial y}\right) + \frac{\partial}{\partial z}\left(K_{z2} \frac{\partial C}{\partial z}\right) + \frac{\partial}{\partial y}\left(K_{y2} \frac{\partial C}{\partial y}\right) - P + S \quad (3.16)$$

$$V_z \frac{\partial C}{\partial z} = \frac{\partial}{\partial z}\left(K_z \frac{\partial C}{\partial z}\right) + \frac{\partial}{\partial y}\left(K_y \frac{\partial C}{\partial y}\right) + \frac{\partial}{\partial x}\left(K_z \frac{\partial C}{\partial x}\right) \quad (3.17)$$

$$V_x \frac{\partial C}{\partial x} = \frac{\partial}{\partial y}\left(K_{y2} \frac{\partial C}{\partial y}\right) + \frac{\partial}{\partial z}\left(K_{z2} \frac{\partial C}{\partial z}\right) + \frac{\partial}{\partial x}\left(K_{z2} \frac{\partial C}{\partial x}\right) \quad (3.18)$$

Equation (3.18) is the mild dispersion equation which applies to all patterns of particulate dispersion source. The patterns of particulates dispersion in equation (3.18) can be further divided into several 2D equations.

First, the physics behind the individual gas molecule transport is mathematically expressed as

$$\left.\begin{aligned} V_x \frac{\partial C_1}{\partial x} &= \frac{\partial}{\partial y}\left(K_{y2} \frac{\partial C}{\partial y}\right) + \frac{\partial}{\partial z}\left(K_{z2} \frac{\partial C}{\partial z}\right) \\ V_x \frac{\partial C_2}{\partial x} &= \frac{\partial}{\partial z}\left(K_{z2} \frac{\partial C}{\partial z}\right) + \frac{\partial}{\partial x}\left(K_{z2} \frac{\partial C}{\partial x}\right) \end{aligned}\right\} \quad (3.19)$$

Equation (3.19) is the ascending particulate-mild dispersion equation, and

$$\left.\begin{aligned} V_x \frac{\partial C_1}{\partial x} &= \frac{\partial}{\partial y}\left(K_{y2} \frac{\partial C}{\partial y}\right) - \frac{\partial}{\partial z}\left(K_{z2} \frac{\partial C}{\partial z}\right) \\ V_x \frac{\partial C_2}{\partial x} &= -\frac{\partial}{\partial z}\left(K_{z2} \frac{\partial C}{\partial z}\right) + \frac{\partial}{\partial x}\left(K_{z2} \frac{\partial C}{\partial x}\right) \end{aligned}\right\} \quad (3.20)$$

Equation (3.20) is the descending particulate-mild dispersion equation.

3.5 The Complex Case: Application of the Dispersion Model to Obtain the Aerosol Size Distribution Model

The initial assessment of equation (3.16) was used to investigate the pollution from cement factory. The model showed excellent correspondence with experimental research on pollutant dispersion and depositions around the factory. Zhang *et al*. (2014) adopted equation (3.16) but represented $\lambda c = -P + S$. Where λ is the climatic factor and c is contaminant concentration. The climatic factor can be emission source, chemical conversion, dry deposition and wet scavenging. The logarithmic distribution of the wind speed and exponential function form of turbulent diffusivity was incorporated into the refined equation (3.18). However, the turbulent diffusivity with its corresponding wind speed cannot be related by mere assumption and subsequent use of the Kriging interpolation method. Therefore a comprehensive mathematical representation is required to appreciate the corporate influence of the wind direction in the plume stated in equations (3.17 and 3.18) which represents the turbulent and mild dispersion equation respectively. The mild dispersion equation describes the scenario in the free troposphere while the turbulent dispersion equation describes what happens below the planetary boundary layer. In the parametric study, both equations occur in 2D on the account of individual gas molecule transport. The ascending and descending particulate-mild dispersion is shown in equations (3.19 and 3.20). For a trivial case, equation (3.17) can be solved- using separation of variable C=X(x)Y(y) with the initial boundary conditions as X(0) =a; $X'(0) = 0$; Y(0) = a; $Y'(0) = 0$; Z(0) = b.

On the assumption that k_y and k_z are constants, then

$$V_z \frac{\partial C}{\partial z} = \left(K_z \frac{\partial^2 C}{\partial z^2}\right) + \left(K_y \frac{\partial^2 C}{\partial y^2}\right) + \left(K_z \frac{\partial^2 C}{\partial x^2}\right) \tag{3.21}$$

Using separation of variable technique, C(x,y,z)=X(x)Y(y)Z(z)

$$V_z XYZ' = k_z XYZ'' + k_y XY''Z + k_z X''YZ \tag{3.22}$$

Divide through by XYZ

$$V_z \frac{Z'}{Z} = k_z \frac{Z''}{Z} + k_y \frac{Y''}{Y} + k_z \frac{X''}{X} \tag{3.23}$$

Since equation (3.23) is a complex expression, it is assumed that the terms are individually equal to a constant.

$$V_z \frac{Z'}{Z} - k_z \frac{Z''}{Z} = \delta^2 \tag{3.24}$$

$$V_z \frac{Z'}{Z} - k_z \frac{Z''}{Z} - \delta^2 = 0 \quad (3.25)$$

$$k_y \frac{Y''}{Y} = \beta^2 \quad (3.26)$$

$$k_z \frac{X''}{X} = \gamma^2 \quad (3.27)$$

So that $\delta^2 = \gamma^2 + \beta^2$. Equations (3.24-3.27) can be restructured with respect to diffusivity

$$k_z Z'' - V_z Z' + \delta^2 Z = 0 \quad (3.28)$$

For V_z and k_z, the trial solution $Z = \exp(-pz)$ leads to

$$p = \frac{V_z \pm \sqrt{{V_z}^2 - 4k_z\delta^2}}{2k_z} \quad (3.28b)$$

For $V_z \gg 4k_z\alpha^2$, the solution becomes p = 0 and $p = \frac{V_z}{k_z}$

$$Y'' - \frac{\beta^2}{k_y} Y = 0 \quad (3.29)$$

$$X'' - \frac{\gamma^2}{k_z} X = 0 \quad (3.30)$$

Adopting the general solutions of $Z = Aexp(-pz) + C\exp(-pz)$, $X = A\sin(\frac{\gamma}{\sqrt{k_z}}x) + B\cos(\frac{\gamma}{\sqrt{k_z}}x)$ and $Y = C\sin\left(\frac{\beta^2}{\sqrt{k_y}}y\right) + D\cos(\frac{\beta^2}{\sqrt{k_y}}y)$ on the the initial boundary conditions that Y(π) = 0, X(π) = 0, Y(0) = 0, X(0) = 0. Then, the individual results is given as:

$$Z = b\exp\left(-\frac{V_z}{k_z}\, z\right) \quad (3.31)$$

$$Y = a\,Cos\left(\frac{\beta}{\sqrt{k_y}}\, y\right) \quad (3.32)$$

$$X = a\,Cos\left(\frac{\gamma}{\sqrt{k_z}}x\right) \quad (3.33)$$

In the sedimentation of aerosols by ultrasounds, D and B shows the relation of amplitude of speed of the weighed particle to amplitude of speed of a particle of gas (Antonnikova et al., 2013). Hence, D = B = a. Likewise, C = b. When the initial boundary condition is applied (Y(π)=0, X(π)=0), then $\frac{\beta}{\sqrt{k_y}} = \frac{n\pi}{2}$ or $\frac{\gamma}{\sqrt{k_z}} = \frac{n\pi}{2}$

Hence, the solution is given as

$$C(x,y,z) = a^2 b\cos\left(\frac{n\pi}{2}x\right)\cos\left(\frac{n\pi}{2}y\right)\exp(-\frac{V_z}{k_z}z) \quad (3.34)$$

Due to the typical problem of superposition in satellite or ground based measurement, the constructive inclusion of α and β to the angular displacement is adopted, hence, equation (3.34) can be transformed as

$$C(x,y,z) = a^2 \mathrm{bcos}(\frac{\mathrm{n}\pi}{2}x + \alpha)\cos(\frac{\mathrm{n}\pi}{2}y + \beta)\exp(-\frac{V_z}{k_z}\,z) \qquad (3.35)$$

a, b, n, α, and β are constants that would be determined using ground and satellite data set. From the above equation, a is known as the atmospheric/decay/growth constant, α and β is the phase difference, n is tuning constant, b is the multiplier constant. For easy representation, the three constants are referred to as meteorological constants.

In a detailed scenario, the ascending particulate-mild dispersion applies to atmospheric aerosols. Hence, other processes like nucleation should act on equation (3.16) to capture either the primary or secondary aerosol formation within an area. Aloyan *et al*., (2012) had described the change of concentrations of aerosol components for both advective transport (equation 3.22) and turbulent mixing (equation 3.23) as shown in equations (3.36 and 3.37) respectively

$$\frac{\partial C_i}{\partial t} + V_j \frac{\partial C_i}{\partial x_j} = F_i{}^{gas} - P_i{}^{nucl} - P_i{}^{cond} + P_i{}^{cHem} + \frac{\partial}{\partial x_j}\left(K_{jj}\frac{\partial C_i}{\partial x_j}\right) \qquad (3.36)$$

$$\frac{\partial \psi_k}{\partial t} + \left(V_j - \delta_{j3} w_g\right)\frac{\partial \psi_k}{\partial x_j} = F_k{}^{aer} + P_k{}^{nucl} + P_k{}^{cond} + P_k{}^{coag} + \frac{\partial}{\partial x_j}\left(K_{jj}\frac{\partial \psi_k}{\partial x_j}\right) \qquad (3.37)$$

where ($x_1 = x$, $x_2 = y$, $x_3 = z$), ($u_1 = u$, $u_2 = v$, $u_3 = w$); (j = 1, 2, 3); C_i (i = 1, …, N_g) and ψ_k (k = 1, …, N_a) are the concentrations of gaseous admixtures and aerosols, respectively; N_g and N_a are the numbers of the corresponding components; w_g is the gravitational settling; F^{gas} and F^{aer} are the emissions of gaseous admixtures and aerosols, respectively; P^{nucl}, P^{cond}, P^{coag} , P^{chem} are the operators of nucleation, condensation, coagulation, and photochemical transformation, respectively; k_{jj} is the turbulent diffusion coefficient along x, y, *z* coordinates, respectively. The physics of the turbulent advective transport of aerosols in the troposphere would be the combination of equations (3.36) and (3.37) when $F^{gas} = F^{aer}$ and $\psi_k = C_i$, $P^{chem} = P^{coag}$. Hence, the incorporation of equation (3.16) into the summation results of equations (3.36) and (3.37) is given as

$$\frac{\partial \psi_k}{\partial t} + \frac{\partial}{\partial y_j}\left(K_{jj}\frac{\partial \psi_k}{\partial y_j}\right) + \frac{\partial}{\partial z_j}\left(K_{jj}\frac{\partial \psi_k}{\partial z_j}\right) - \left(\frac{\partial}{\partial x_j}\left(K_{jj}\frac{\partial \psi_k}{\partial x_j}\right) + \frac{1}{2}\delta_{j3} w_g \frac{\partial \psi_k}{\partial x_j}\right) = {F_k}^{aer} + {P_k}^{coag} \quad (3.38)$$

Equation (3.38) was reduced to equation (3.39) on the assumption that $K_{jj}\frac{\partial \psi_k}{\partial y_j} \ll K_{jj}\frac{\partial \psi_k}{\partial z_j}$ and $K_{jj}\frac{\partial \psi_k}{\partial x_j} \ll K_{jj}\frac{\partial \psi_k}{\partial z_j}$, hence

$$\frac{\partial \psi_k}{\partial t} + \frac{\partial}{\partial z_j}\left(K_{jj}\frac{\partial \psi_k}{\partial z_j}\right) - \frac{1}{2}\delta_{j3} w_g \frac{\partial \psi_k}{\partial x_j} = {F_k}^{aer} + {P_k}^{coag} \quad (3.39)$$

The viability of ${P_k}^{coag}$ in the above equation is difficult because coagulation lowers the concentration of atmospheric particles and may be very tasking to obtain using numerical model (Lohmann *et al*., 2000). Therefore, it is assumed that the effect of particle collisions on the size distribution is negligible; hence, ${P_k}^{coag} = 0$. The numerical diffusion of the equation can be eliminated by introducing the condensational effects of aerosols emission ${F_k}^{aer}$. Hence,

$${F_k}^{aer} \approx \frac{\partial m_k}{\partial t} = D_k m - \frac{1}{3}\frac{\partial D m_k}{\partial \mu} \quad (3.40)$$

where m_k is the mass distribution, D is its mass transfer rate, and μ is the logarithm of particle diameter. If the particle diameter is assumed to be uniform, then $\frac{1}{3}\frac{\partial D m_k}{\partial \mu} \to 0$. Hence we propose that aerosol optical depth (τ) is written (Lohmann *et al*., 2000):

$$\tau = \frac{1}{D_k}{F_k}^{aer} \approx \frac{1}{D_k}\frac{\partial m_k}{\partial t} \quad (3.41)$$

Therefore, equation (3.39) transforms to

$$\frac{\partial \psi_k}{\partial t} + \frac{\partial}{\partial z_j}\left(K_{jj}\frac{\partial \psi_k}{\partial z_j}\right) - \frac{1}{2}\delta_{j3} w_g \frac{\partial \psi_k}{\partial x_j} = \tau D_k \quad (3.42)$$

Equation (3.40) describes both the optical and physical properties of the aerosols. Therefore, its application to solve live problems requires the adequate definition of the initial and boundary conditions. Initial and boundary conditions of pollutants are very important either in forecast or on the spot analysis. If the Initial and boundary conditions are based on large-scale simulation or climatological average values, the output of the forecast or analysis would be

error-prone (Wang *et al*., 2014). Therefore the initial and boundary conditions for vertical profile was adopted from Wang *et al*. (2014) and horizontal resolution from the NASA-Unified Weather Research and Forecasting.

In this section, the aerosol size distribution concept would be investigated in the light of equation (3.40). The mono-dispersion and poly-dispersion flows were considered by making N=2, $A = \frac{1}{2}\delta_{j3}w_g$, $K_{11} = K_a$, $K_{22} = K_b$, $\psi_1 = \psi_a$, $\psi_2 = \psi_b$, $D_1 = D_a$, and $D_2 = D_b$ (Aloyan *et al*. 2012) . This resulted into two mono-dispersion flow equations given below

$$\left(\frac{\partial K_a}{\partial z}\frac{\partial \psi_a}{\partial z} + K_a\frac{\partial^2 \psi_a}{\partial z^2} - A\frac{\partial \psi_a}{\partial x}\right) + \frac{\partial \psi_a}{\partial t} = \tau D_a \qquad (3.43)$$

$$\left(\frac{\partial K_b}{\partial z}\frac{\partial \psi_b}{\partial z} + K_b\frac{\partial^2 \psi_b}{\partial z^2} - A\frac{\partial \psi_b}{\partial x}\right) + \frac{\partial \psi_b}{\partial t} = \tau D_b \qquad (3.44)$$

The general term which describes the poly-dispersion flow is given as

$$\left(\frac{\partial}{\partial z}(K_a + K_b)\frac{\partial}{\partial z}(\psi_a + \psi_b) + K_a\frac{\partial^2 \psi_a}{\partial z^2} + K_b\frac{\partial^2 \psi_b}{\partial z^2} - A\frac{\partial}{\partial x}(\psi_a + \psi_b)\right) + \frac{\partial}{\partial t}(\psi_a + \psi_b) = (D_a + D_b) \qquad (3.45)$$

Since the dispersion sources are unpredictable on a larger scale, it is more convenient to assume a nearly uniform dispersion from all sources. This assumption was based on the Nigeria Meteorological Centers (NIMET) data set observations on uniform cloud cover index. The mixed state of both the mono-dispersion and poly-dispersion flows is therefore represented in a general term as

$$m\frac{\partial K}{\partial z}\frac{\partial \psi}{\partial z} + K\frac{\partial^2 \psi}{\partial z^2} - A\frac{\partial \psi}{\partial x} + \frac{\partial \psi}{\partial t} = \tau D \qquad (3.46)$$

where m is the number of dispersion sources. For simplification of the above equation, $\eta = \frac{\partial K}{\partial z}$ and $B = -A\frac{\partial \psi}{\partial x} + \frac{\partial \psi}{\partial t} - \tau D$, hence when equation (3.46) is wavelength dependent, it becomes

$$m\eta\frac{\partial \psi(\lambda,t)}{\partial z} + K\frac{\partial^2 \psi(\lambda,t)}{\partial z^2} + B = 0 \qquad (3.47)$$

Let the initial conditions be $\psi(0) = \alpha$, $\psi^{|}(0) = \beta$. The Laplace transform was applied to solve equation (3.47)

$$(\lambda, t) = (m\alpha\lambda - B)cosm\eta t + \beta sinm\eta t \quad (3.48)$$

If the term 'B' is minimum, B=0, then

$$A\frac{\partial\psi(\lambda,t)}{\partial x} + \frac{\partial\psi(\lambda,t)}{\partial t} - \tau D = 0 \quad (3.49)$$

Applying the Hermit polynomial

$$\psi(\lambda, t) = e^{2t\lambda - t^2} = e^{\lambda^2}.e^{(\lambda-t)^2} = \sum_{n=0}^{\infty} H_n(\lambda)\frac{t^n}{n}$$

Let $\lambda - t = u$, then $t = \lambda - u = 0$ and $-\frac{\partial}{\partial t} = \frac{\partial}{\partial u}$ is substituted into equation (3.49) to yield two governing equations

$$\frac{\partial\psi(\lambda)}{\partial x} = \tau(\lambda)D \quad (3.50)$$

$$\frac{\frac{1}{2}\delta_{j3}w_g}{D} - \frac{1}{D} = \tau(\lambda) \quad (3.51)$$

To solve for the turbulence or laminar flow, the initial and boundary conditions for the gravitational settling are

$$w_g = \begin{cases} Un < 0 & v = 0.3 \\ 0 \le Un \le 1 & v = 0.7 \\ 1 \le Un \le 2 & v = 1.36 \\ 2 \le Un \le 5 & v = 2.73 \\ 5 \le Un \le 10 & v = 7.57 \\ 10 \le Un \le 100 & v = 14.8 \\ Un > 100 & v = 30.3 \end{cases}$$

where v is the settling velocity (cm/s) and $\delta_{j3} = 1$. Hence, the formulation for the aerosol size distribution

$$ASD = \frac{\gamma}{D} \quad (3.52)$$

where γ is assumed to be unity with same unit as D.

3.6 Derivation of Unified Number

This subsection highlights the basic assumptions, concepts and definition of salient parameters needed for onward application.

Definition 1: Let the aerosol be the most active atmospheric content. Hence, the aerosol optical depth (AOD) for aerosols is adopted as

$$\tau(\lambda)_{aerosol} = \tau(\lambda)_{tot} - \tau(\lambda)_{water} - \tau(\lambda)_{Rayleigh} - \tau(\lambda)_{O_3} - \tau(\lambda)_{NO_2} - \tau(\lambda)_{CO_2} - \tau(\lambda)_{CH4} \tag{3.53}$$

where $\tau(\lambda)_{Rayleigh}$ is the optical depth of the Rayleigh scattering. $\tau(\lambda)_{water}$ is the optical depth of water, $\tau(\lambda)_{O_3}$ is the optical depth of ozone, $\tau(\lambda)_{NO_2}$ is the optical depth of nitrate oxides, $\tau(\lambda)_{CO_2}$ is the optical depth of carbon dioxide, $\tau(\lambda)_{CH4}$ is the optical depth for methane. Spectral aerosol optical depths at wavelength 440 nm to 870 nm are typically used to estimate the size distribution of aerosols.

Definition 2: Let the aerosols loading over an area be controlled by atmospheric forces. The rotation and the revolution of the earth have a resultant force effect on the moving aerosols (F_R). This kind of force is known as the Coriolis force. The pressure gradient force which controls the wind is given as F_w. The greater the F_w, the faster winds blow across the Stokes' regime. F_g is the gravitational force and F_u is the upthrust. The forces acting on the moving fluid (aerosol) in the moving sphere (Figure 3.3). Let the acceleration of the aerosol be 'a'.

$$a = \sqrt{a_x^2 + a_y^2} \tag{3.54}$$

During convective updraft the equation becomes

$$\left.\begin{aligned} F_R - F_w &= ma_x \\ F_u - F_g &= -ma_y \end{aligned}\right\} \tag{3.55}$$

Also, during deposition, the equation becomes

$$\left.\begin{aligned} F_W - F_R &= -ma_x \\ F_g - F_u &= ma_y \end{aligned}\right\} \tag{3.56}$$

$$a = \frac{1}{m}((F_W - F_R)^2 + (F_g - F_u)^2)^{\frac{1}{2}} \quad (3.57)$$

Theorem: The effect of the moving aerosol is the solution in equation (3.35). Let the effect of the moving aerosol on the multiple refractive index be illustrated in Figure 3.4.

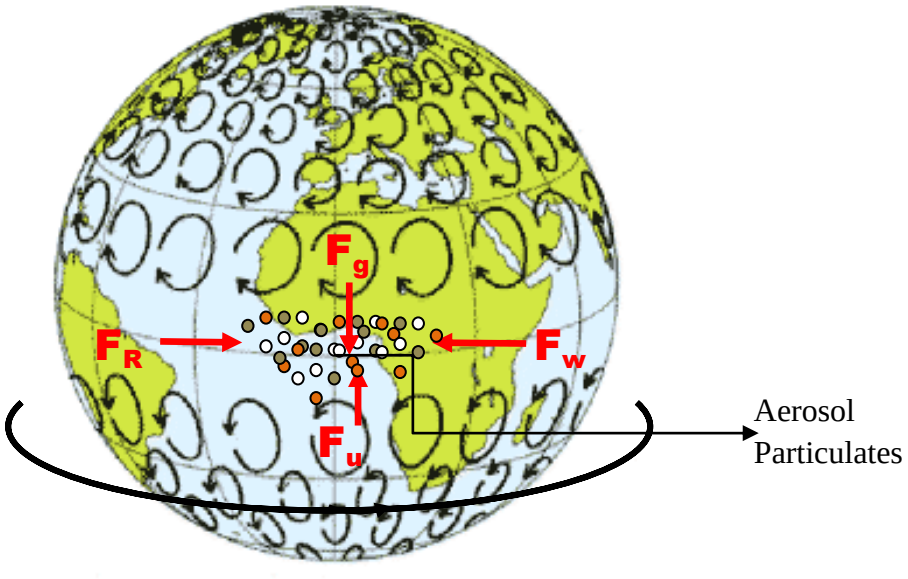

Figure 3.3: Forces acting on moving aerosols in atmosphere (Uno et al., 2012)

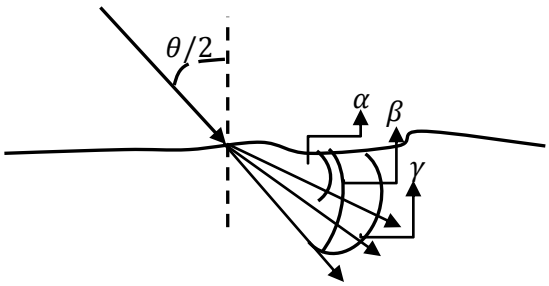

Figure 3.4: Moving effect of aerosols on refractive indexes

From the basic of refractive index

$$\left.\begin{aligned} sin\frac{\theta}{2} &= n_1 cos\alpha \\ sin\frac{\theta}{2} &= n_2 cos\beta \\ sin\frac{\theta}{2} &= n_3 cos\gamma \end{aligned}\right\} \quad (3.58)$$

$$\sin\theta = \left(sin\frac{\theta}{2} + sin\frac{\theta}{2}\right) cos\frac{\theta}{2} \quad (3.59)$$

$$\sin\theta = n_1 cos\alpha cos\frac{\theta}{2} + n_2 cos\beta cos\frac{\theta}{2} \quad (3.60)$$

The relative air mass could be written as $m = \frac{1}{\sin(\theta)}$

$$n = \frac{C}{\sin(\theta)} \quad (3.61)$$

Hence,

$$C = n^2 cos\alpha cos\frac{\theta_i}{2} + n^2 cos\beta cos\frac{\theta_1}{2} \ldots\ldots\ldots\ldots\ldots\ldots n^2 cos\gamma cos\frac{\theta_n}{2} \quad (3.62)$$

Proof: Show that the unified number is $Un = \frac{\rho C_p U_a}{h}\theta$

U_a is the mean velocity of that fluid, C_p is specific heat at constant-pressure, ρ is the density, h is the convective heat transfer coefficient and θ is the thermal ratio which defines the ratio of the average temperature of aerosol to the uniform temperature of the atmosphere.

From equation (3.57),

$$ma = ((F_W - F_R)^2 + (F_g - F_u)^2)^{\frac{1}{2}} \quad (3.63)$$

where

$$F_W = -\frac{1}{\rho}\frac{dP}{dx} \quad (3.64)$$

$$F_R = f_c u \quad (3.65)$$

$$F_g = \rho \times dz \times dA \times g \quad (3.66)$$

$$F_u = dP \times dA \quad (3.67)$$

where dP is the pressure difference, dz is the height, ρ is density, dA is the surface area, g is the acceleration due to gravity, u is wind speed, f_c is the Coriolis parameter.

$$m^2a^2 = \frac{1}{\rho^2}\left(\frac{dP}{dx}\right)^2 - 2f_cu\left(\frac{dP}{dx}\right) + {f_c}^2u^2 + \rho^2(dz)^2(dA)^2g^2 - 2\rho dz(dA)^2gdP + (dP)^2(dA)^2 \quad (3.68)$$

Since the volume of each particulate of the aerosols is been considered, then $(dA)^2 = 0$, then equation (3.68) is transformed to

$$m^2a^2 = \frac{1}{\rho^2}\left(\frac{dP}{dx}\right)^2 - 2f_cu\left(\frac{dP}{dx}\right) + {f_c}^2u^2 \quad (3.69)$$

$$m^2a^2 - {f_c}^2u^2 = \frac{1}{\rho^2}\left(\frac{dP}{dx}\right)^2 - 2f_cu\left(\frac{dP}{dx}\right) \quad (3.70)$$

$$m^2a^2 - {f_c}^2u^2 = \left(\frac{1}{\rho^2}\frac{dP}{dx} - 2f_cu\right)\frac{dP}{dx} \quad (3.71)$$

Hence, the solution can be given as

$$\frac{dP}{dx} = \frac{\rho^2\left(2f_cu \pm \sqrt{4{f_c}^2u^2 - \frac{4}{\rho^2}\left(m^2a^2 - {f_c}^2u^2\right)}\right)}{2} \quad (3.72)$$

$$\frac{dP}{dx} = \rho^2\left(f_cu \pm \sqrt{{f_c}^2u^2 - \frac{1}{\rho^2}\left(m^2a^2 - {f_c}^2u^2\right)}\right) \quad (3.73)$$

Let ${f_c}^2u^2 \gg m^2a^2$

$$\frac{dP}{dx} = \rho^2f_cu \pm \rho^2\sqrt{{f_c}^2u^2 + \frac{{f_c}^2u^2}{\rho^2}} \quad (3.74)$$

$$\frac{dP}{dx} = \rho^2f_cu \pm \rho^2f_cu\sqrt{1 + \frac{1}{\rho^2}} \quad (3.75)$$

If equation (3.75) is integrated with respect to x, then,

$$P = \rho^2f_cux \pm \rho^2f_cux\sqrt{1 + \frac{1}{\rho^2}} \quad (3.76)$$

Let $1 \gg \frac{1}{\rho^2}$

$$P = 2\rho^2f_cux \quad (3.77)$$

The principle of energy conservation $E = mC_p\Delta\theta$ and $P = mgh$ was applied to the equation (3.77)

$$\frac{EgA}{2f_c m} = \frac{\rho C_p U_a}{h}\Delta\theta \tag{3.78}$$

To account for the mass flow of aerosols across the atmosphere which is expected to change in temperature as the aerosols rises through altitude, equation (3.78) was divided with temperature T

$$\frac{EgA}{2f_c mT} = Un = \frac{\rho C_p U_a}{h}\theta \tag{3.79}$$

where $\theta = \frac{\Delta\theta}{T}$ is referred as the temperature ratios between the aerosol and its surroundings.

3.7 Mathematical Compilation of Dispersion Model

From equation (3.50),

$$\psi(\lambda) = \tau(\lambda)Dx \tag{3.80}$$

Hence, it can be compared with equation (3.34)

$$a^2 \mathrm{bcos}\left(\frac{\mathrm{n\pi}}{2}x\right)\cos\left(\frac{\mathrm{n\pi}}{2}y\right)\exp(-\frac{V_z}{k_z}z) = \psi(\lambda) = \tau(\lambda)Dx \tag{3.81}$$

Equation (3.81) gives three kinds of equations on the ground that D_x represents the first two terms of the left term.

$$\psi(\lambda) = a^2\tau(\lambda)\cos\left(\frac{\mathrm{n\pi}}{2}x\right)\cos\left(\frac{\mathrm{n\pi}}{2}y\right) \tag{3.82}$$

or

$$\psi(\lambda) = ab\tau(\lambda)\cos\left(\frac{\mathrm{n\pi}}{2}y\right)\exp(-\frac{V_z}{k_z}z) \tag{3.83}$$

or

$$\psi(\lambda) = ab\tau(\lambda)\cos\left(\frac{\mathrm{n\pi}}{2}x\right)\exp(-\frac{V_z}{k_z}z) \tag{3.84}$$

Equation (3.82) is most valid for the study because of the variability of V_z. More so, when aerosols are deposited into the atmosphere, V_z do not have a significant effect on its lifespan.

The term $\tau(\lambda)$ can be introduced into cosine on the platform of the 'abridged trigonometry hypothesis' to get

$$\psi(\lambda) = a^2 \cos\left(\frac{n\pi\tau(\lambda)}{2}x\right)\cos\left(\frac{n\pi\tau(\lambda)}{2}y\right) \tag{3.85}$$

Applying the principles of multiple refraction expressed in equation (3.62), equation 3.85 can also be written as

$$\psi(\lambda) = {a_1}^2 \cos\left(\frac{n_1\pi\tau(\lambda)}{2}x\right)\cos\left(\frac{n_1\pi\tau(\lambda)}{2}y\right) + \cdots \ldots {a_n}^2 \cos\left(\frac{n_n\pi\tau(\lambda)}{2}x\right)\cos\left(\frac{n_n\pi\tau(\lambda)}{2}y\right) \tag{3.86a}$$

3.8 Proof of the Abridged Trigonometry Hypothesis

Hypothesis 1: A term can be introduced into the cosine using the trigonometric principles

$$a\cos(n\theta) \approx \cos(an\theta) + \vartheta \tag{3.86b}$$

ϑ is the extensive term which emerge from the expansion of the main equation

Hypothesis 2: The power of the particular cosine depends on the term 'n'.

Proof: Observe the term indicated in red

$$\begin{aligned}
\cos(1\alpha) &= 1\cos\alpha \\
\cos(2\alpha) &= 2\cos^2\alpha + \vartheta \qquad (\vartheta = -1) \\
\cos(3\alpha) &= -3\cos\alpha + \vartheta \qquad (\vartheta = 4\cos^3\alpha) \\
\cos(4\alpha) &= -4\cos^2\alpha - 4\cos\alpha + \vartheta \qquad (\vartheta = 5\cos^4\alpha + 1) \\
\cos(5\alpha) &= 5\cos\alpha + \vartheta \qquad (\vartheta = 16\cos^5\alpha - 20\cos^3\alpha) \\
&\vdots \\
\cos(n\alpha) &= n\cos\alpha + \vartheta \qquad (\vartheta = \text{varying})
\end{aligned} \tag{3.86c}$$

3.9 Mathematical Resolution of Satellite Measurement Operations

Satellite measurement can be complex due to their specific functions in the orbit (Figure 2.11) and the functionality of their sensors. The physics of retrieving satellite imagery with respect to its orbiting time may foster data set variance between different satellite sensors. This fact is validated in the fourth chapter between data set retrieved from MODIS and MISR. The comparism between the ground data set from AERONET and satellite data set from MISR suggests that the large variance noticed in measuring aerosols optical depth needs to be resolved to provide a platform for data processing in regions where there are large missing data.

It was discussed in chapter 2 that the optical properties of aerosol particles have severe influence over the local radiative forcing and radiation balance of the earth. Aerosol radiative properties are used to calculate some of its optical properties as a function of wavelength (λ). This is essential because of the large travel distance in processing satellite images (Figure 2.11).

Hence, it is scientific to consider the aerosol optical depth in the light of wavelength as shown in equation (3.86d).

$$\tau(\lambda, j) = \sum_{i=1}^{a} Q_e\,(\lambda, r_i)\pi r_i^2 n(r_i, j) dz_j \tag{3.86d}$$

where, $n(r_i, j)$ represents the aerosol number concentrations, dz_j is the height of the atmospheric layer, j atmospheric layer, Q_e extinction efficiency, a represents the aerosol particles in all of 33 size bins and r_i is the particle's wet radius. The Zahra *et al*., (2010) technique proposed that the aerosol optical thickness can be obtained by subtracting the Rayleigh and ozone contributions from the total optical thickness. In this section, a new technique was introduced. The aerosol optical depth was estimated- using the spectral radiance. The technique was corroborated by the MISR observation. From past research, aerosol particles influence the global or spectral radiation budget (Zahra *et al*., 2010; Moroni *et al*., 2015). Therefore, we propose that the aerosol optical depth is directly related to the atmospheric emissivity. Hence, the Palluconi and Meeks (1985) concept was used to obtain equation (3.87) below:

$$LS_j = \left[\varepsilon_j L_j^{BB}(T) + \left(1 - \varepsilon_j\right) L_j^{sky}\right]\tau_j + L_j^{atm} \tag{3.87}$$

where LS_j is the spectral radiance observed by the sensor, L_j^{BB} is the spectral radiance from a blackbody at surface temperature *T*, L_j^{sky} is the spectral radiance incident upon the surface from the atmosphere, L_j^{atm} is the spectral radiance emitted by the atmosphere, ε_j is the surface emissivity at wavelength, τ_j is the spectral atmospheric transmission. The anomalies reported by numerous researchers on emissivity (Srivastava *et al*., 2010) was summarized by the assumption that $L_j^{sky} \approx L_j^{atm}$.

$$LS_j = \varepsilon_j \tau_j L_j^{BB}(T) + (1 + \tau_j - \varepsilon_j \tau_j) L_j^{atm} \quad (3.88)$$

It is expedient to investigate how much the satellite sensor can capture information in perturbed settings, for example, PBL. First, it is assumed that the total spectral radiance is not strictly dependent on the angular displacement of the sensor. Hence, the derivation of a sensor functioning formular is essential from the Planck's blackbody radiation model. Planck's blackbody radiation intensity distribution law is used to estimate the transient temperature by the thermal emission signals from the satellite sensors. Hatano *et al*. (2000) gave the mathematical expression of the emission signals collected originally by laboratory oscilloscope detectors. The principle can also be applied to the satellite sensors as shown in equation 3.89.

$$V_e(T) = \frac{R_\Omega A}{\pi} \int_{\lambda_1}^{\lambda_2} \int_{\phi_1}^{\phi_2} \int_{\theta_1}^{\theta_2} \epsilon_\lambda{}^1(\lambda, \theta, \phi, T) \tau(\lambda) G(\lambda) e_{\lambda b}(\lambda, T) cos\theta sin\theta d\theta d\phi d\lambda \quad (3.89)$$

where T is the temperature, θ and ϕ are the polar and azimuthal angles, λ is the wavelength, R_Ω is the impedance of the sensor, A is the area on the sample which is sensed by the sensor, $\epsilon_\lambda{}^1(\lambda, \theta, \phi, T)$ is the spectral directional emissivity, τ(λ) is the transmissivity of the sensor, G(λ) is the responsivity (A/W) of the sensor at different wavelengths, $e_{\lambda b}(\lambda, T)$ is the blackbody emissive power given as

$$e_{\lambda b} = \frac{2\pi C_1}{\lambda^5} \frac{1}{exp(C_2/\lambda T) - 1} \quad (3.90)$$

C_1=5.9555 X 10^7W$\mu m^4/m^2$, and C_2 =1.4388 X10^4 Kμm.

Equation (3.89) is further analysed using the separation variable technique which reduce the whole equation to

$$V_e(T) = \frac{R_\Omega A}{\pi} Y(\lambda, T).J(\theta).K(\phi) \tag{3.91}$$

where

$$\left.\begin{aligned} Y(\lambda,T) &= \int_{\lambda_1}^{\lambda_2} \epsilon_\lambda{}^1(\lambda,T)\tau(\lambda)G(\lambda)e_{\lambda b}(\lambda,T) \\ J(\theta) &= \int_{\theta_1}^{\theta_2} \epsilon_\lambda{}^1(\theta)cos\theta sin\theta d\theta \\ K(\phi) &= \int_{\phi_1}^{\phi_2} \epsilon_\lambda{}^1(\phi)d\phi \end{aligned}\right\} \tag{3.92}$$

Y(λ,T) represents the optical and thermal function. Further expansion of the Y(λ,T) confirms experimental results of thermal characterization of particulates within the planetary boundary layer. J(θ) represents the optical transport of the combined multilayered aerosols particulate. Therefore, spectral radiance from a blackbody at surface temperature T, is reduced to

$$LS_j = \frac{R_\Omega A}{\pi} \int_{\lambda_1}^{\lambda_2} \varepsilon_j \tau_j g_j L_j^{BB}(\lambda, T) \tag{3.93}$$

Combining equations (3.88) and (3.93) gives:

$$\left(\frac{R_\Omega A}{\pi} \int_{\lambda_1}^{\lambda_2} g_j L_j^{BB}(\lambda, T)\right) - L_j^{BB}(T) = \frac{(1+\tau_j-\varepsilon_j\tau_j)}{\varepsilon_j\tau_j} L_j^{atm} \tag{3.94}$$

Here R_Ω is the impedance of satellite sensor ($> 10M\Omega$), A is the area covered by the sensor (typically 100 x 100km scenes for ERS and 165 x 165kms for Radarsat Wide), g_j is the responsivity of the sensor at different wavelengths (preferable 0.62μm).

$$L_j^{BB}(T) = \frac{C_1}{\lambda_j^5 \pi [\exp\left(\frac{C_2}{\lambda_2 T}\right) - 1]} \tag{3.95}$$

where C_1= First radiation constant = 3.74151 X 10^{-16} (Wm^2), C_2= Second radiation constant = 0.0143879 (mK). The relationship between LS_j and L_j^{atm} was calculated by the Temperature Polynomial Expansion Scheme (TPES) for earth radiation (Uno *et al*., 2012). It is given as

$$L_j^{atm} = \left(\frac{2}{3}\right)^n LS_j \tag{3.96}$$

At low visibility conditions, the radiance scattered by the atmospheric aerosols comprise of a large portion of the total radiance. This kind of total radiance can be equated to the Angstrom parameter (Eck *et al*., 1999). The new transformation can be seen from Equations (3.97 to 3.98).

$$\alpha = -\frac{dIn\tau_a}{dIn\lambda} \tag{3.97}$$

Here α is the Angstrom parameter, τ_a is the aerosol optical depth, and λ is the wavelength.

$$\tau_a = -\lambda \exp\left(\frac{R_\Omega A}{\pi}\int_{\lambda_1}^{\lambda_2} g_j L_j^{BB}(\lambda, T)\right) \tag{3.98}$$

Hence, the concept of superposition of satellite sensors can be used to refine equation (3.86a)

$$\psi(\lambda) = {a_1}^2 \cos\left(\frac{\mathrm{n_1}\pi\tau(\lambda)}{2} + \alpha\right)\cos\left(\frac{\mathrm{n_1}\pi\tau(\lambda)}{2} + \beta\right) + \cdots \ldots {a_n}^2 \cos\left(\frac{\mathrm{n_n}\pi\tau(\lambda)}{2} + \alpha\right)\cos\left(\frac{\mathrm{n_n}\pi\tau(\lambda)}{2} + \beta\right) \tag{3.99}$$

3.10. General Comments on the Main Models

The essence of equation (3.42) is its active expression of the Stokes drag which is evident in the Stokes regime or creeping flow regime at small Reynolds numbers (Re < 0.5). At higher Reynolds numbers, the drag coefficient requires correction, that is, Knudsen number or Cunningham correction factor or both in some cases. The application of the Cunningham correction factor requires that a wide range of the Knudsen number $Kn = \frac{\lambda}{d_p} \leq 1000$ at low Reynolds number. The objective of this concept is to describe the uniqueness of the Stokes' velocity in understanding the dynamism of pollutants or particulates. The gravitational settling (w_g) in equation (3.42) requires the Stokes terminal velocity within the Stokes' regime. It is written as

$$v_g = \frac{D^2(\rho_p - \rho_{air})gC_c}{18\mu_{air}} \quad (3.100)$$

where, D is the diameter of particulates, ρ_p is its density, μ_{air} is the air dynamic viscosity, g is the gravity constant, C_c is the Cunningham coefficient and ρ_{air} is the air density. Where C_c is given as

$$C_c = 1 + \frac{2\lambda}{d_p}(1.257 + 0.4\exp(-0.55\frac{d_p}{\lambda})) \quad (3.101)$$

where λ denotes the molecular mean free path in the gas. Cunningham correction factor applies to the Stokes law settling velocity for minute particles at standard temperature and pressure. Cunningham correction factor is insignificant when being applied to the atmospheric dispersion problems because the settling velocities of the particles are extremely small compared to vertical motions. In order to achieve one of the objectives of this thesis i.e. introduction of the unified number, aerosol distribution size, the correction to the Stokes drag should incorporate adequate estimation of the aerosol size and the vertical motions.

To address this major problem, the Un which was derived in chapter 3 was adopted. The Unified number governs the convective phenomena between two interacting fluids (mono-dispersion and poly-dispersion flows) that are separated by a conducting medium. It was derived through the Poiseuille's criteria by the inclusion of two salient parameters, which are the known atmospheric forces and the temperature profiles. The basic operation of this model concentrates on the vertical motion along the z-axis and how to relate the unified number to the concept of determining the aerosol size distribution. By definition, the Reynolds and Un are defined by two common parameters which are air density and wind speed.

The importance of numerical models in interpreting atmospheric measurement cannot be overemphasized because it is a tool which simplify as well as elaborate the anomalies of direct measurements. The mathematical or numerical model may be used to examine either the micro-scale or macro-scale of a region. One major requirement of a good air quality model is its ability to operate within the macro scale and micro scale of a regional model. This quality strengthens the results and judgments of forecasting pollution events within regional models. Very few mathematical or numerical models satisfy this basic requirement. This has led to the call for several improvements in the secondary requirements such as

particle formation, mixing, lifetime and decay rate for developing numerical or mathematical models (Doraiswamy et al., 2010). Taking a cue from literature (Vladutescu et al., 2013), the optical parameters that explains the aerosols are sensitive to the size distribution over an area and the chemical composition which is dependent on the relative humidity over the area.

A micro scale in this research is defined as the space within a near homogenous sub layer of the troposphere. In this case, we consider the residual layer of the troposphere. Therefore, at the residual layer of the PBL, the aerosol content dynamics mimics the aerosol density distribution solution given by McKibbin (2008). Hence,

$$a = \frac{Q}{4\pi\sqrt{D_L D_T t_1^2}} \tag{3.102}$$

where, Q is the mass of the particle released above the ground from the Ewekoro cement factory – Nigeria, D_L is the longitudinal dispersion coefficient, D_T is the transverse dispersion coefficient, t is the time taken for the aerosol to reside at each layer, V_x is the wind velocity (m/s). In the mild diffusion region, $D_L = D_T$ because the particles becomes lighter and more energetic (Lovejoy et al., 2004; Gouw et al., 2006) and reaches its quasistationary level at about 1000s (Yemakov et al., 2003). Hence, equation (3.102) may be written as $a = \frac{Q}{4000\pi D_T}$, then

$$\delta = \frac{Q}{4000\pi D_T} \exp\left(\frac{n^2}{V_x}\right) \tag{3.103}$$

From the refined equation (3.103), the wind velocity is a major function of the aerosol content dynamics (δ).

The formation of theoretical or mathematical models used to explain the physics of the aerosols transport have severally suffered set-back which ranges from the initial or boundary conditions, bogus formulations for turbulent or mild fluid flow, misconceptions about the Stokes' regime and assumptions of the wind analysis. The comprehensive incorporation of all known and unknown factors which creates wide variation between satellite or in-situ measurements and mathematical models can be achieved by adopting a seasonal duration. Each season lasts for a period of three months, December to February (DJF), March to May

(MAM), June to August (JJA) and September to November (SON). Hence, the simulation of equations (3.48), (3.50) and (3.51) were considered to examine the effects of the dispersion model to aerosol size distribution. The mass transfer rate was obtained in equation (3.51) and then applied in equation (3.52). The mass transfer rate in the atmosphere influences the growth and evaporation of the particulates.

3.11. Aerosol Optical Depth Retrieval from Meteorological Measurement

Earlier in the previous chapter, it was explained that one of the ways PBL eliminates aerosol is through rainfall. This technique of retrieving AOD from meteorological measurement was adopted from the Kumierczyk-Michulec (1993) aerosol optical depth equations

$$\tau_a(\lambda) = a\left[\frac{E_{tot}(\lambda)}{G_s(\lambda)\beta^{-1}\cos(\theta)T_r(\lambda)} - \frac{(1-T_r{}^b(\lambda))}{cT_r(\lambda)}\right] \quad (3.104)$$

where b = 0.95, c = 2, $E_{tot}(\lambda)$ is the total irradiance, λ is the wavelength, $T_r(\lambda)$ is the transmittance functions for Rayleigh scattering, β is the correction factor for the Earth-Sun distance. $G_s(\lambda)$ is the extra-terrestrial index which can be determined by

$$G_s(\lambda) = \left(\frac{GH}{J}\right) \quad (3.105)$$

G is the cloud cover index, H is the relative humidity index, J is the rainfall index. The constants highlighted in equation (3.105) can be contested based on regional weather peculiarities and global climate change.

Through the aid of the meterological data sets that was obtained for selected locations in Nigeria (Abeokuta, Ondo, Oshogbo, Ibadan, Lagos and Ilorin), the following equations were derived. The cloud cover for each location is highlighted in equation (3.106), the relative humidity for each location is highlighted in equation (3.107) and the rainfall for each location is highlighted in equation (3.108). The arrangement of the location in each formular are Abeokuta, Ondo, Oshogbo, Ibadan, Lagos and Ilorin respectively.

$$\frac{G}{(h-h_0)} = \begin{Bmatrix} x_5 \\ \frac{2}{70}x_1 + \frac{3}{70}x_2 + \frac{5}{70}x_3 + \frac{20}{70}x_4 + \frac{40}{70}x_5 \\ \frac{45}{70}x_5 + \frac{23}{70}x_6 + \frac{2}{70}x_7 \\ \frac{39}{70}x_5 + \frac{31}{70}x_6 \\ \frac{14}{70}x_3 + \frac{34}{70}x_4 + \frac{22}{70}x_5 \\ \frac{3}{70}x_3 + \frac{2}{70}x_4 + \frac{44}{70}x_5 + \frac{21}{70}x_6 \end{Bmatrix} \tag{3.106}$$

$$\frac{H}{(h-h_0)} = \begin{Bmatrix} \frac{8}{70}y_4 + \frac{14}{70}y_5 + \frac{22}{70}y_6 + \frac{26}{70}y_7 \\ \frac{6}{70}y_4 + \frac{14}{70}y_5 + \frac{20}{70}y_6 + \frac{30}{70}y_7 \\ \frac{12}{70}y_4 + \frac{10}{70}y_5 + \frac{21}{70}y_6 + \frac{27}{70}y_7 \\ \frac{9}{70}y_4 + \frac{13}{70}y_5 + \frac{27}{70}y_6 + \frac{21}{70}y_7 \\ \frac{31}{70}y_5 + \frac{23}{70}y_6 + \frac{16}{70}y_7 \\ \frac{4}{70}y_1 + \frac{6}{70}y_2 + \frac{6}{70}y_3 + \frac{7}{70}y_4 + \frac{13}{70}y_5 + \frac{13}{70}y_6 + \frac{21}{70}y_7 \end{Bmatrix} \tag{3.107}$$

$$\frac{J}{(h-h_0)} = \begin{Bmatrix} \frac{21}{70}z_1 + \frac{7}{70}z_2 + \frac{13}{70}z_3 + \frac{17}{70}z_4 + \frac{12}{70}z_5 \\ \frac{13}{70}z_1 + \frac{9}{70}z_2 + \frac{13}{70}z_3 + \frac{9}{70}z_4 + \frac{20}{70}z_5 + \frac{6}{70}z_6 \\ \frac{15}{70}z_1 + \frac{10}{70}z_2 + \frac{8}{70}z_3 + \frac{28}{70}z_4 + \frac{9}{70}z_5 \\ \frac{15}{70}z_1 + \frac{10}{70}z_2 + \frac{9}{70}z_3 + \frac{29}{70}z_4 + \frac{7}{70}z_5 \\ \frac{10}{70}z_1 + \frac{14}{70}z_2 + \frac{19}{70}z_3 + \frac{16}{70}z_4 + \frac{5}{70}z_5 + \frac{4}{70}z_6 + \frac{3}{70}z_7 \\ \frac{22}{70}z_1 + \frac{6}{70}z_2 + \frac{11}{70}z_3 + \frac{29}{70}z_4 + \frac{2}{70}z_5 \end{Bmatrix} \tag{3.108}$$

The general formula from their individual relationship with the AOD is given as:

$$\tau(\lambda) = (\frac{GH}{J} + U) \times constant \tag{3.109}$$

where, τ is the aerosol optical thickness, G is the cloud cover, H is the relative humidity, J is the rainfall, U is the unknown parameter and $h - h_0$ height difference from ground. The constants in equation (3.109) are the fraction of the event obtained via measuring the length of the colour in the imagery. Two methods were adopted to incorporate equations (3.106 – 3.108) into equation (3.105); sectional or polynomial and general approach. The general

approach entails summing the various parameters as a single unit. This method is error prone though its accuracy depends on the geographical area considered. The sectionalized method is more specific in the mathematical point of view. However, the area under consideration in Nigeria may be relatively small to use the sectionalized approach. Hence, the general appraoch is better in this respect.

Hence, the general approach can be written as:

$$\left.\begin{aligned}\frac{G}{(h-h_0)} &= \frac{2}{70}x_1 + \frac{3}{70}x_2 + \frac{22}{70}x_3 + \frac{56}{70}x_4 + \frac{220}{70}x_5 + \frac{52}{70}x_6 + \frac{2}{70}x_7 \\ \frac{H}{(h-h_0)} &= \frac{4}{70}y_1 + \frac{6}{70}y_2 + \frac{6}{70}y_3 + \frac{42}{70}y_4 + \frac{64}{70}y_5 + \frac{103}{70}y_6 + \frac{155}{70}y_7 \\ \frac{J}{(h-h_0)} &= \frac{96}{70}z_1 + \frac{61}{70}z_2 + \frac{73}{70}z_3 + \frac{117}{70}z_4 + \frac{55}{70}z_5 + \frac{10}{70}z_6 + \frac{5}{70}z_7\end{aligned}\right\} \qquad (3.110)$$

CHAPTER FOUR

RESULTS AND DISCUSSION

4.1 Mathematical Outlook of Observations

In this chapter, there are seven sections. Section 4.2 corroborated the unified number in analyzing aerosols in the Stokes regime. Section 4.3 sectionalized the challenges of the dispersion model in turbulent fluid into micro and macro scale. Section 4.4 analysed the data sets using the developed model in the expanded Stoke's regime to determine the aerosol size distribution. Section 4.5 elaborated on the developed model in the expanded Stoke's regime to mathematically validate the concept of satellite superposition and the likely error of adopting the satellite data set. In section 4.6, the comprehensive documentation of the atmospheric constants in selected locations of West Africa was achieved. In section 4.7, the improvised technique for discovering the aerosols loading using meteorological dataset was illustrated. This technique was designed to retrieve past aerosol optical depth over West Africa. In section 4.8, the statistical analysis of ground and satellite observations were explained to determine the aerosols retention in the atmosphere.

4.2 Dynamics of Particulates: Validation of the Unified Number

The features of air density and wind speed with respect to time are shown in Figures 4.1 and 4.2. The wind speed events within December to February were analysed to ascertain its variability as shown in Table 4.1. From the comprehensive data set obtained from the Davis weather station, it took a maximum time of thirteen minutes for specific wind pattern of the same direction and speed to regain its original state within the different specified time studied, for instance; NE to SS and back to NE at the speed of 4m/s. Since atmospheric ventilation, stagnation and recirculation are air flow conditions that either aid or hinder quick dispersion (Kumar et al, 2011), the fluid dynamics of the 13 minutes events were examined

Table 4.1: Data of the wind direction for December-January-February

Wind Direction	Max. Wind Speed (m/s)	Volume of Data	Max. Wind Speed (m/s)	Volume of Data	Max. Wind Speed (m/s)	Volume of Data
	December		**January**		**February**	
SE	2.2	14	6.3	156	5.4	128
S	4	29131	6.3	121	6.7	250
NW	4.9	75	6.7	2554	6.3	2421
NNW	6.7	20	4.5	919	3.1	531
NE	3.6	21	4.5	1168	4.0	1389
N	4	1536	4	1536	-	-
ESE	4.5	85	5.8	494	3.6	374
ENE	4	60	5.8	148	4.5	3398
NNE	4.5	42	4.5	721	3.6	601
E	4.5	530	4.5	294	4.5	1681
WSW	4	244	7.2	3293	7.2	6391
WNW	2.7	92	7.2	2284	6.7	2867
W	3.6	367	7.6	4908	7.6	5900
SW	3.1	222	5.8	700	5.8	1694
SSW	2.7	63	4.5	153	8.5	234
SSE	2.1	44	6.7	70	6.3	129
Static	-	1235	-	987	-	1121

using the Knudsen, Reynolds and Un. From literature (Nicholson, 2013), the peculiarity of the West Africa monsoon informed the choice of February for full investigation of the above mentioned events. In Figure 4.2, the maximum wind speed within the defined duration was observed to have a high tendency of instability in the afternoon. The lowest speed (within the defined duration) was noticed in the morning with a high tendency of stability (Figure 4.3).

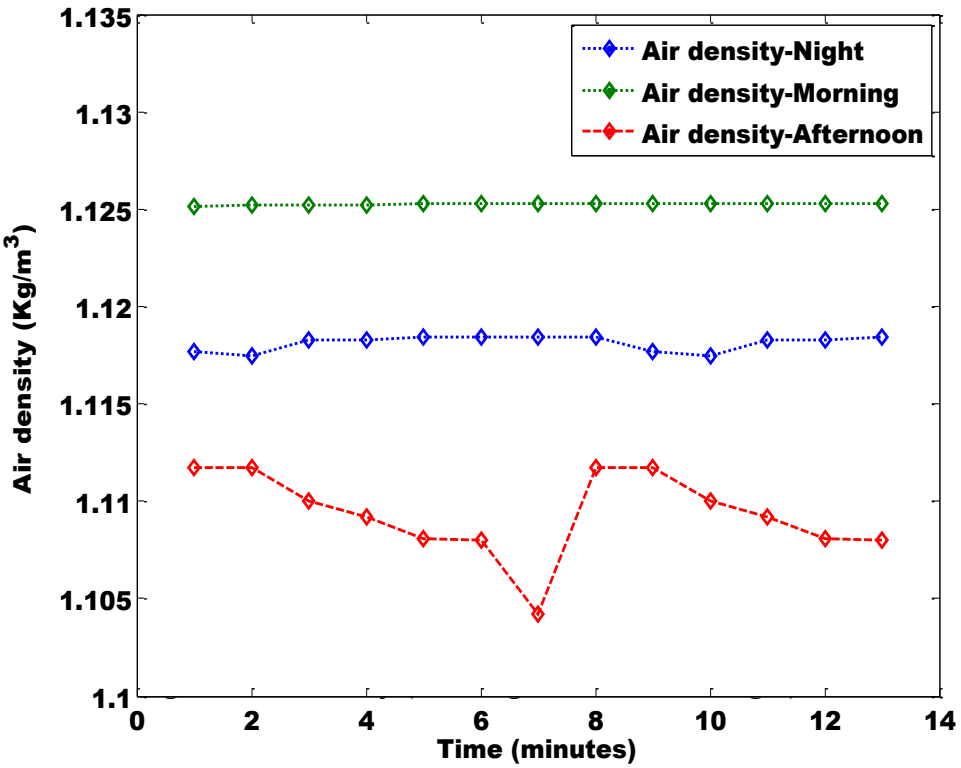

Figure 4.1: Air density (morning, afternoon and night) Ota

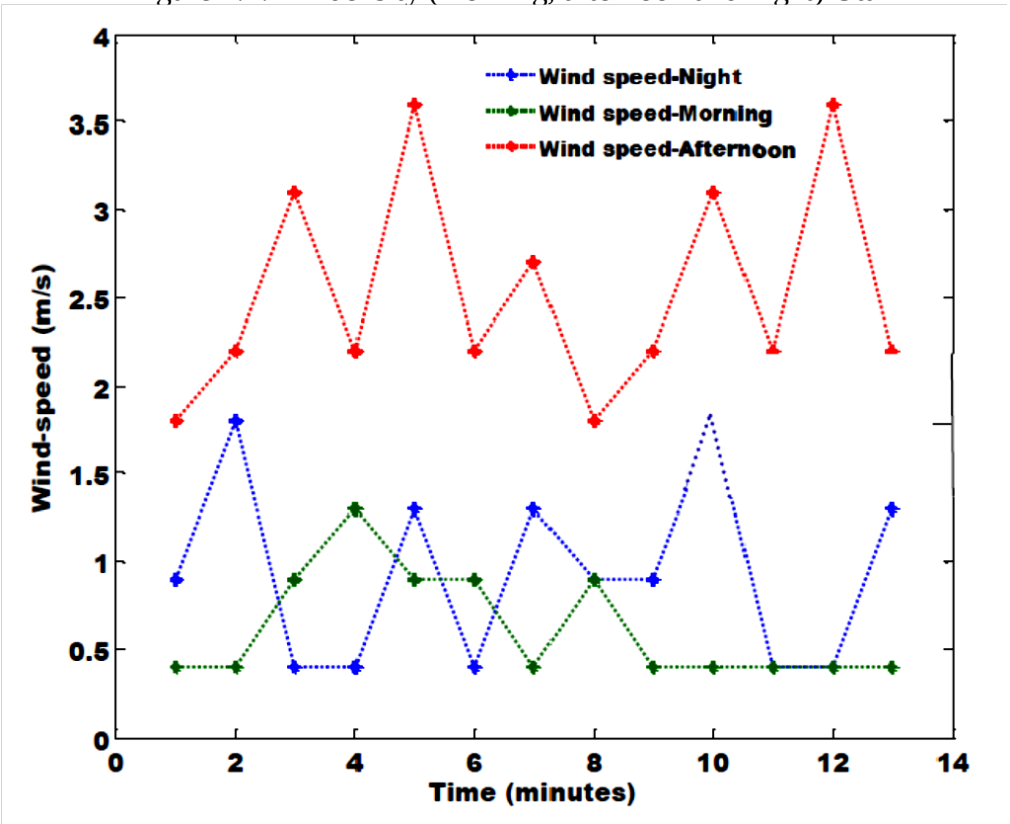

Figure 4.2: Wind speed (morning, afternoon and night) Ota

The validity of the unified number on atmospheric field was tested using the range of the ratio $(\frac{C_p}{h})$ with values 0.1, 0.3, 0.5 and 0.9 on the afternoon data as shown in Figure 4.3. The direct relationship of $\frac{C_p}{h}$ on the test results affirmed that its influence on the general result is moderate and can be relied upon for analysis. The general analysis for the morning afternoon and night data (Figure 4.4) shows that the Un results agree with the trending of the primary data of the wind speed (Figure 4.2). Also, the results of the Reynolds number at D = 0.001 nm is shown in Figure 4.5. This result further affirms the validation of Un for atmospheric fields.

The analysis of the Knudsen number (Kn) showed a wide variation with respect to time as applied to the atmospheric field. Figure 4.6 showed the Kn for night. The agreement of the highest peaks for night in Figure 4.2 and Figure 4.5 was noticed-showing that the Kn may be relevant to explain the night flows in the location of study. The Kn feature deviates gradually from morning (Figure 4.7) to afternoon (Figure 4.8). This shows that the Kn becomes more inaccurate to capture the dynamics of the lower atmosphere when the turbulence in the lower atmosphere increases. The analysis of the turbulence effect on the aerosol size distribution is expressed in the solution of equation (3.42).

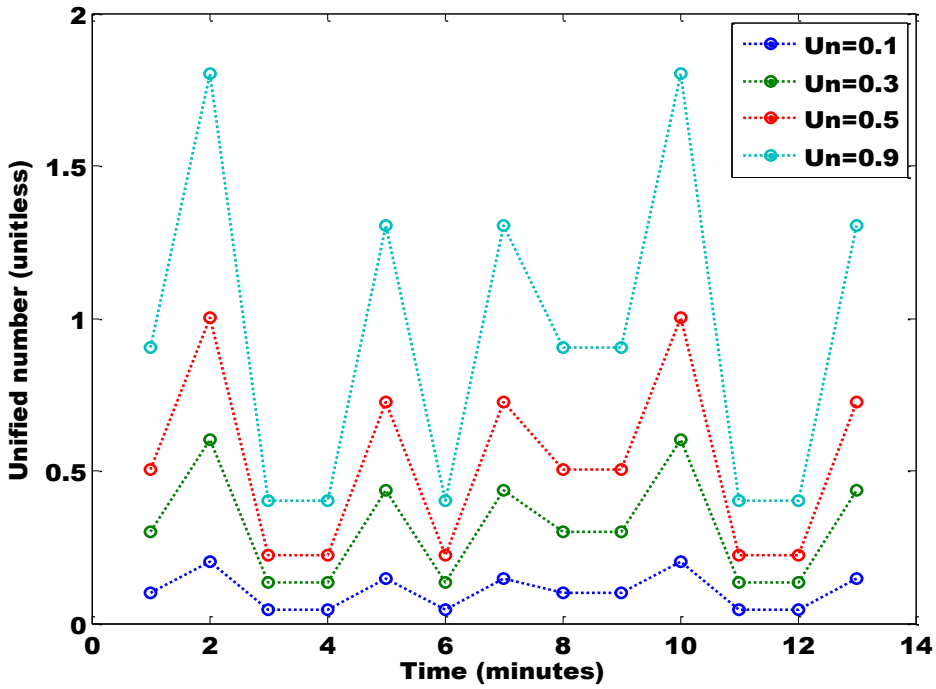

Figure 4.3: The effect of $\frac{C_p}{h}$ on the unified number for Ota.

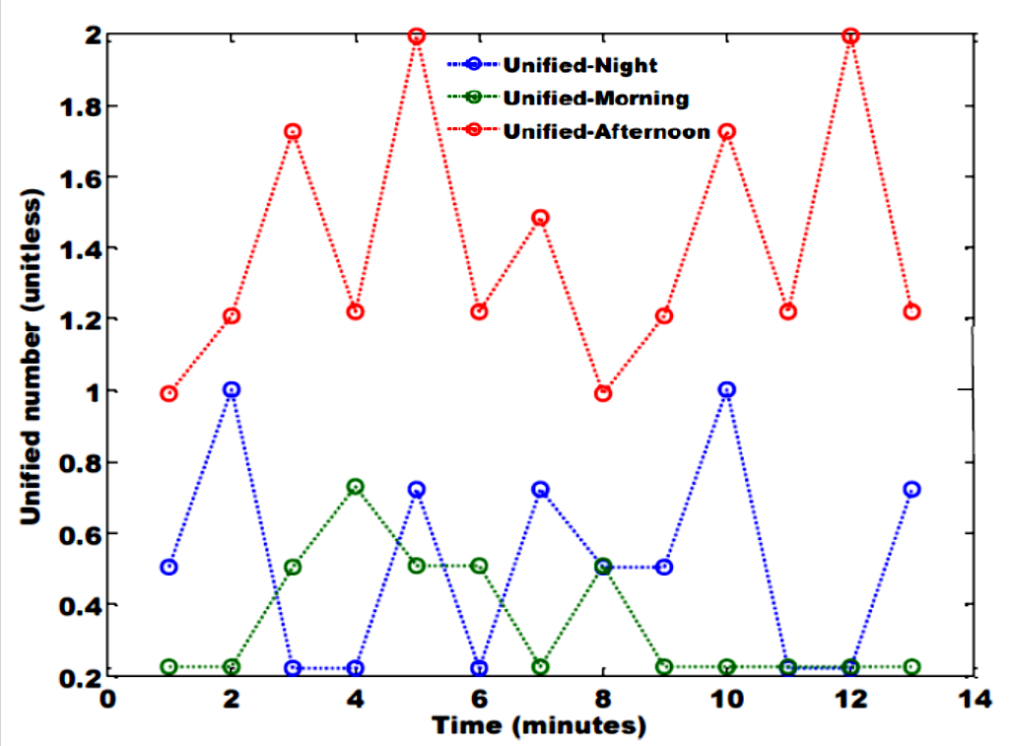

Figure 4.4: Unified number for morning, afternoon and night (Ota).

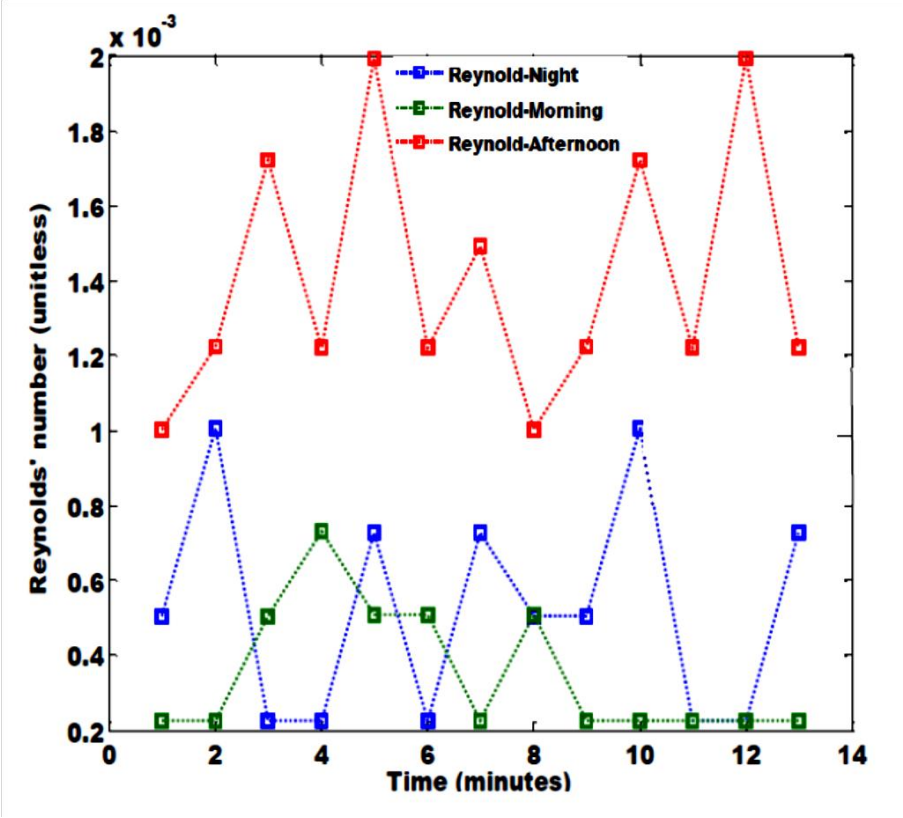

Figure 4.5: Reynolds number for morning, afternoon and night (Ota)

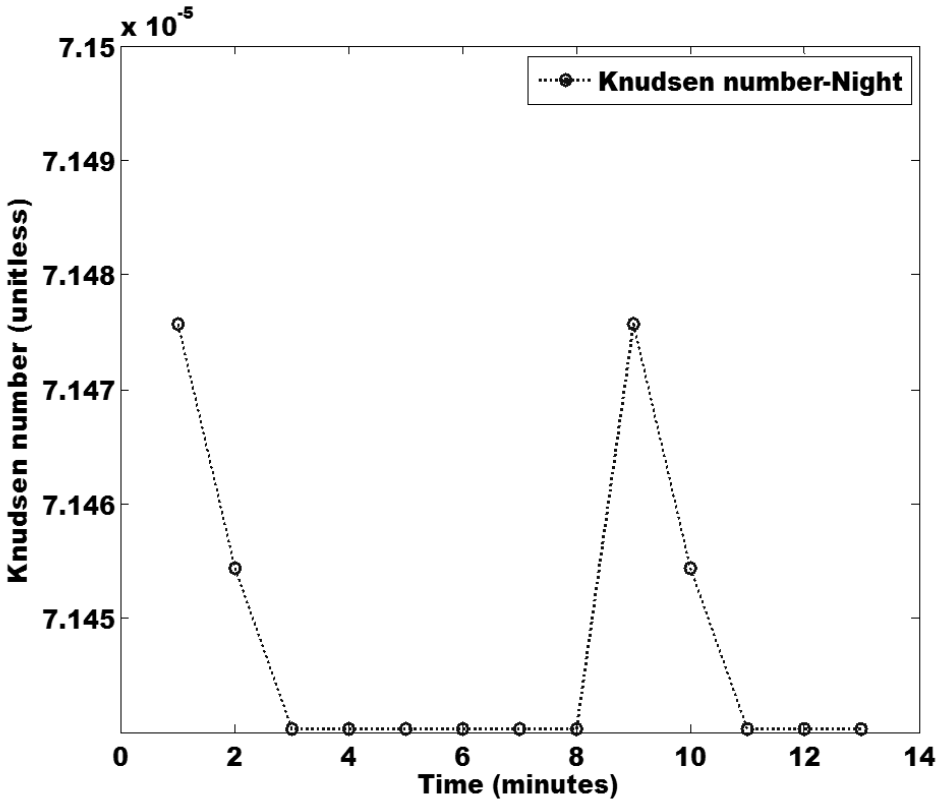

Figure 4.6: Knudsen number for night (Ota)

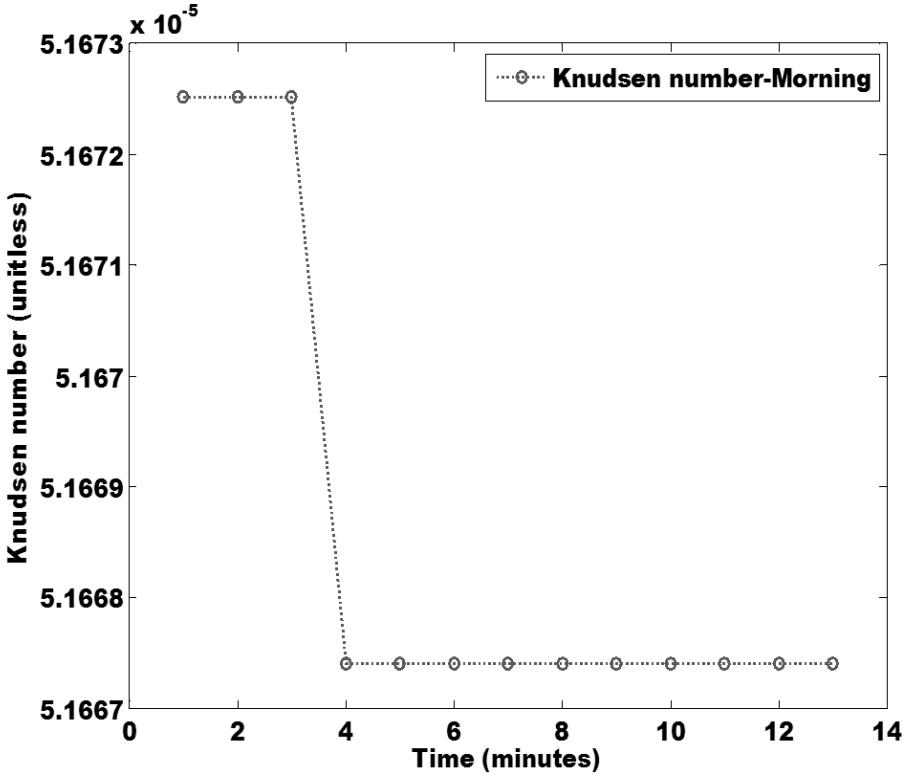

Figure 4.7: Knudsen number for morning (Ota).

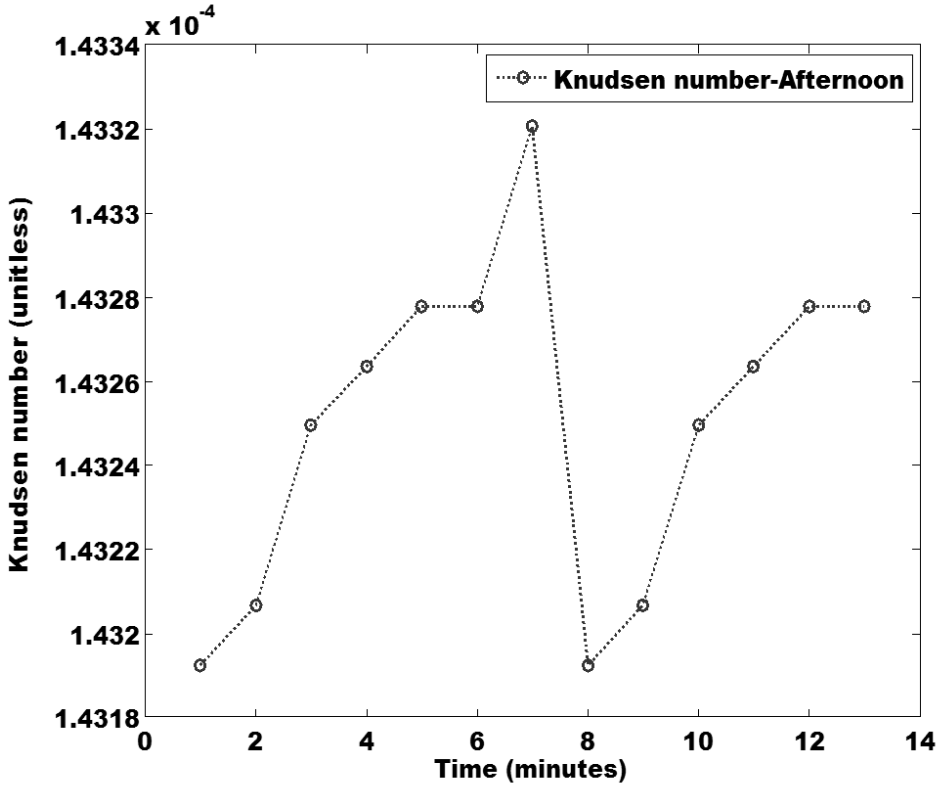

Figure 4.8: Knudsen number for afternoon (Ota)

4.3 Dynamics of Particulates: The Micro and Macro-Scale Analysis

This section describes the features of aerosol transport in micro and macro scale events using the numerical model. In this section, the objectives are to validate an initially developed model (equation 3.99) both on the micro-scale and macro-scale; to estimate the 2D diffusion dynamics of aerosols in practical terms.

The results in Figures 4.9 to 4.13 shows that the microscale of aerosol dispersion at 15 m/s has significant impact on the larger scale which was calculated as 8 m/s. This is a further proof (considering the wind analysis in the previous section) that air pollution is largely dependent on the metrological conditions within a specified location. The meteorological conditions dictates the kind of emission, particulates mixing rates, particulate deposition or decay rates and the type of dispersion of air pollution (Uno *et al.*, 2006). The adequate involvements of the meteorological influence are basic requirement for the formulation of an accurate numerical model. For example, one of the main successes of the PSU/NCAR mesoscale model (MM5) is the nowcast of dusts carried by strong northerly wind in the planetary boundary layer (PBL). Sun et al. (2013) showed the difficulties of simulating the evolution of weather systems with respect to its wind fields that controls aerosol transport in the PBL.

However, the approach that have been adopted was able to estimate the mass concentration of pollutants to be between 3×10^{14} to 3×10^{15} Kg/m^3 (Figure 4.15). Therefore, in contrast to Sun et al. (2013) which based its estimation on wind properties, precipitation, mixing of fonts; the adequate account of the aerosol activity in the troposphere can also be explained with respect to tuning constant and unified number which is peculiar to the viscosity of the atmosphere.

The summation of the above listed indicators in form of a comprehensive numerical model is quite scientific. Some numerical models have used the semi-Lagrangian scheme to address the momentum, energy and mass conservation (Sun *et al.,* 2013). In the characterization of the aerosol transport, Gazala et al. (2006) gave an assumption that the Total Ozone Mapping Spectrometer (TOMS) aerosol index (AI) is proportional to the dust burden and optical depth. This assumption was duplicated by Wen-Yih *et al.* (2013) who developed a 4D Purdue Regional Climate Model (PRCM) which characterized the evolution of the interaction between weather and dusts. However, in the results that would be further discussed in

succeeding sections, it should be shown that the errors on the adequate estimation of aerosol content might have been solved finally.

4.3.1 Verification of Dispersion Model on a Micro Scale Event

The verification of the dispersion model on a micro scale event was achieved using wind parameters that were obtained from the Davis Weather Station (as a case study) which is located at Covenant University at the altitude of 35 m and about 5 km radius to Ewekoro cement factory (the source of the pollutant), which is located at latitude 6.93^{o}N and longitude 3.21^{o}E, using Google map straight-line. It is within the tropical rainforest belt of Ogun state, southwest-Nigeria. The topography of Ewekoro is classified as a southern upland (Gbadebo and Amos, 2010). It has an area of 594 km^{2}. First, the theoretical expectation of δ (Figure 4.9 - 4.11) was determined by assuming that the chunk of the mass of the particle released above the ground from the cement factory is about 4-10 kg within 1000 s. The wind speed range was determined from the Davis Pro II weather station. Three cases were considered, which are: when the mass (Q) ejected do not decay (Figure 4.9); when the mass (Q) ejected have a logarithmic decay (Figure 4.10) and when the mass (Q) ejected have an exponential decay (Figure 4.11).

Figure 4.9 shows that when particulates do not decay in the micro scale, four levels of change are expected as the wind increases at 10 m/s, 20 m/s, 26 m/s and 30 m/s. Since the aerosols particulate dispersion in the micro scale is given as 15 m/s, It means that aerosol dynamic content is about magnitude 6. This is dangerous for the lifeform in such area. Like Figure 4.9, when the mass (Q) ejected have a logarithmic decay, four levels of change are expected as the wind increases at 10 m/s, 20 m/s, 26 m/s and 30 m/s. However, in Figure 4.10, the maximum aerosol dynamic content is magnitude 1.8. The maximum aerosol dynamic content of exponential decayed mass was 0.9. This shows that pollution in micro-scale may be less harmful is its ejected mass decays exponentially.

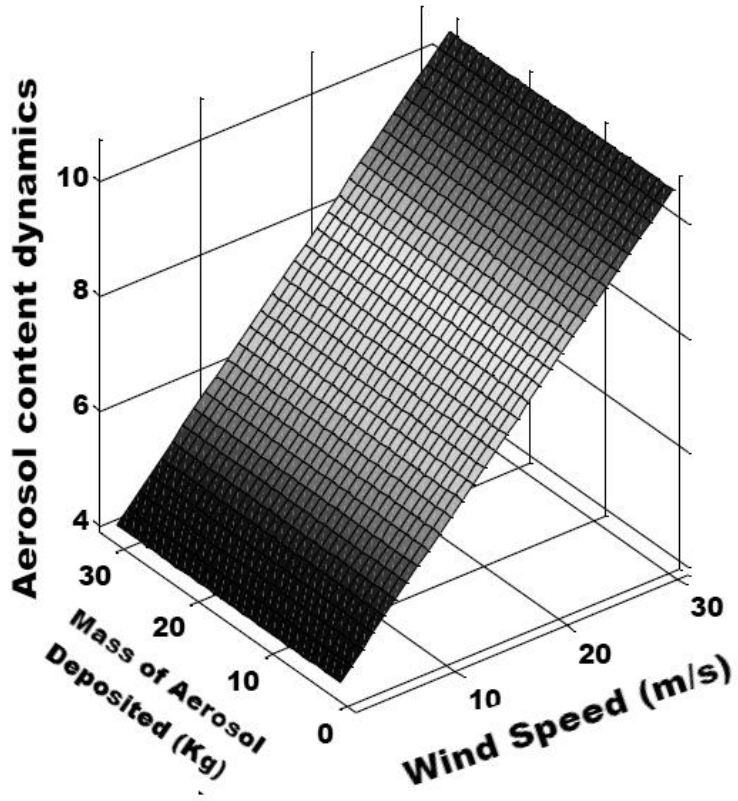

Figure 4.9: Non-decay of the ejected mass (Q)

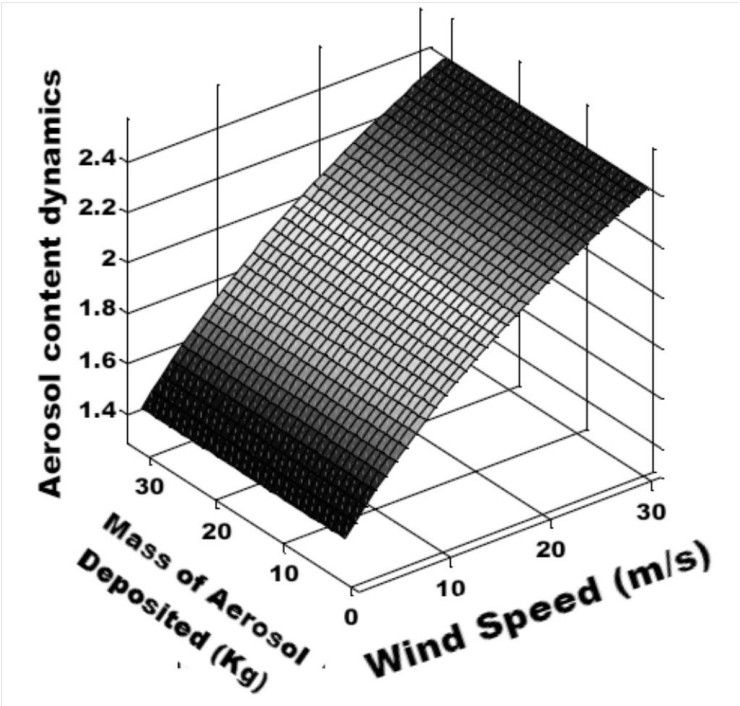

Figure 4.10: Logarithmic decay of ejected mass (Q)

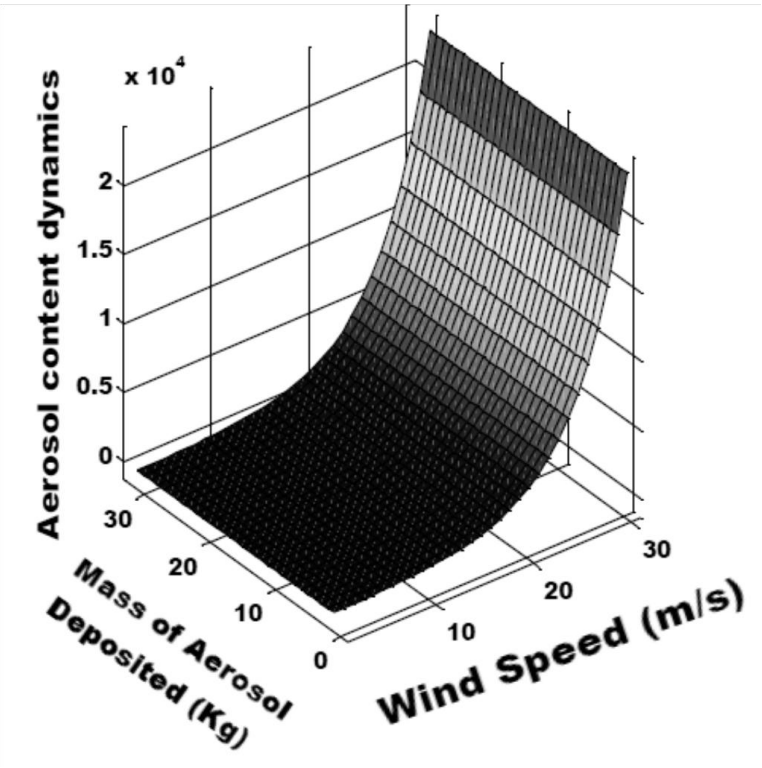

Figure 4.11: Exponential decay of ejected mass (Q)

When the mass ejected do not decay or vanish, the planetary boundary layer (PBL) experiences massive aerosols loading which increases linearly as shown in Figure (4.9). This means that life forms will be exposed to radiative heating effects which are as a result of either massive absorption or scattering of radiation from the sun by the aerosols. When the mass ejected are decaying exponentially or logarithmically, the aerosols loading in the planetary boundary layer are reduced by rainfall or wind. However, the tendency of the aerosols loading to concentrate at specified sub-layer of the PBL such as surface layer may be enhanced by human activities. This possibility is represented in the term P and S in equation (3.16). The aerosol content dynamics increases in magnitude in either of the cases mentioned earlier. This shows that the wind speed is the trigger for aerosol advection or deposition.

4.3.2 Verification of Dispersion Model on a Macro Scale Event

The pollutant dispersion from its source possesses same characteristics as shown in Figures 4.12 and 4.13, that is, large volume of diffusing pollutants concentrate at about 100 m above its dispersion source. The maximum range of the diffusing particulates at a maximum speed of 5 m/s is about 100 m. The volume of pollutant at this point is very low (Figure 4.12). At macro-scale dispersion (Figure 4.13), the same characteristics shown in the micro scale is experienced. The difference between the micro and macro-scale is that the maximum speed of the macro-scale is less than 4.4 m/s while that of micro scale reaches as high as 8.5 m/s.

This low speed enables the pollutants to acquire maximum range of about 15 km. The type of aerosols in Figures 4.14a-d is made-up of dust, smoke and soot. This could be justified considering the fact that this period coincides with the harmattan dry season period along the West African coast. It could be observed by their transport in the y-direction (Figures 4.14b and 4.14d) that the aerosols travel at about 8.5 m/s towards the ocean. The implication of this result is that atmospheric aerosols build-up with time to herald turbulence within the lower atmosphere. If the aerosols have longer lifetime, its distribution has the tendency of shifting from one location to the other as observed in Figures 4.14b to 4.14d. In Figure 4.14b, most of the accumulated aerosols remain at the coastal portions of Nigeria, Ghana, Cote d'Ivoire and parts of Liberia. The aerosol concentration in Figure 4.14d shifts off coast to Cape Verde,

thereby increasing its aerosols loading as confirmed later in the ground data set in section 4.8. The Total Ozone Mapping Spectrometer (TOMS) aerosol index (AI) observation for January of 2000-2003 of West Africa (shown in Figure 4.14) affirm the shifting tendency of built-up aerosols that is travelling at low speed through long distances. This aerosol absorbs ultraviolet (UV) rays as they traverse from the coast of Ghana, Nigeria and Liberia towards Cape Verde. UV absorbing aerosol is dependent on the altitude, hence, the higher the aerosol altitude, the greater the fraction of affected molecular radiation. In view of the above-discussion, the UV absorbing aerosols might be affected by the northeast monsoon, chemical transformations and removal processes with time.

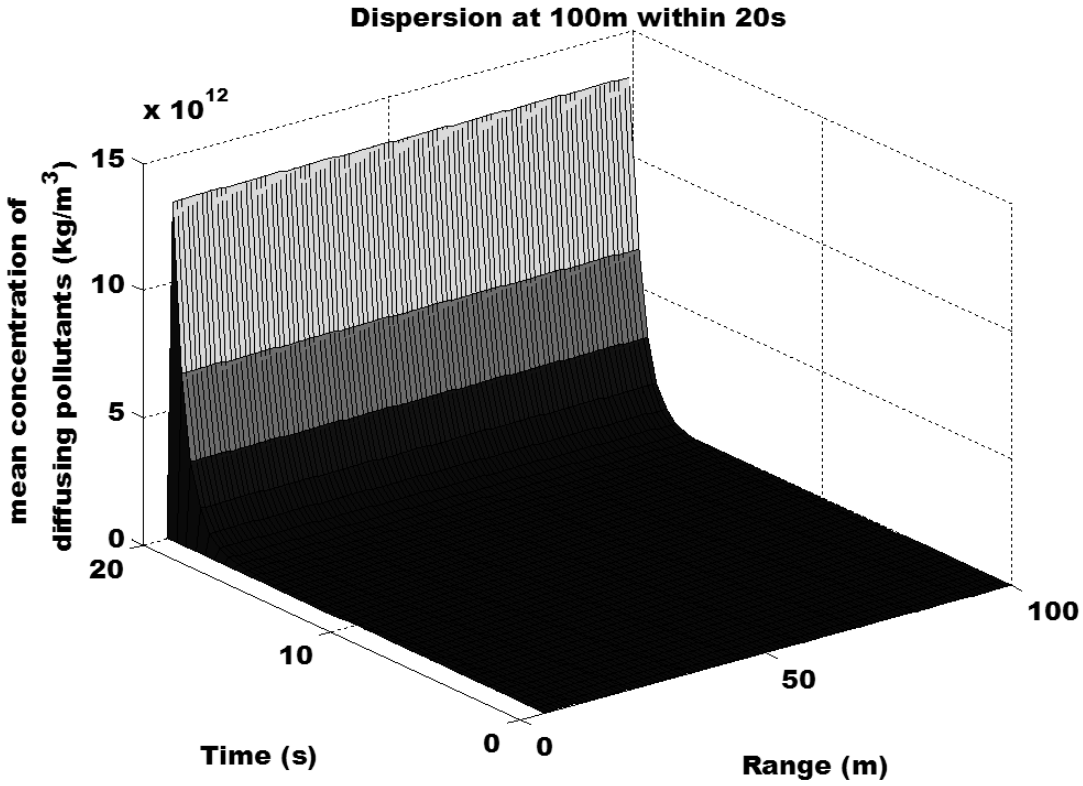

Figure 4.12: Micro scale analysis of diffusing pollutants (Ewekoro).

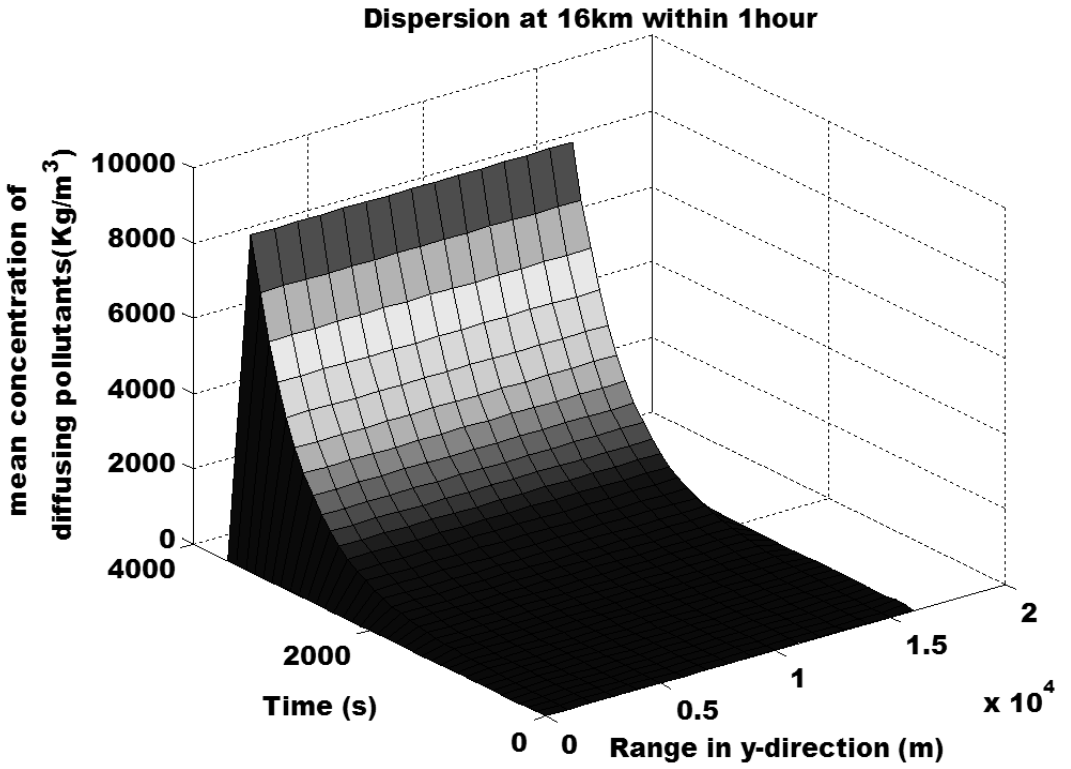

Figure 4.13: Macro scale analysis of diffusing pollutants (West Africa)

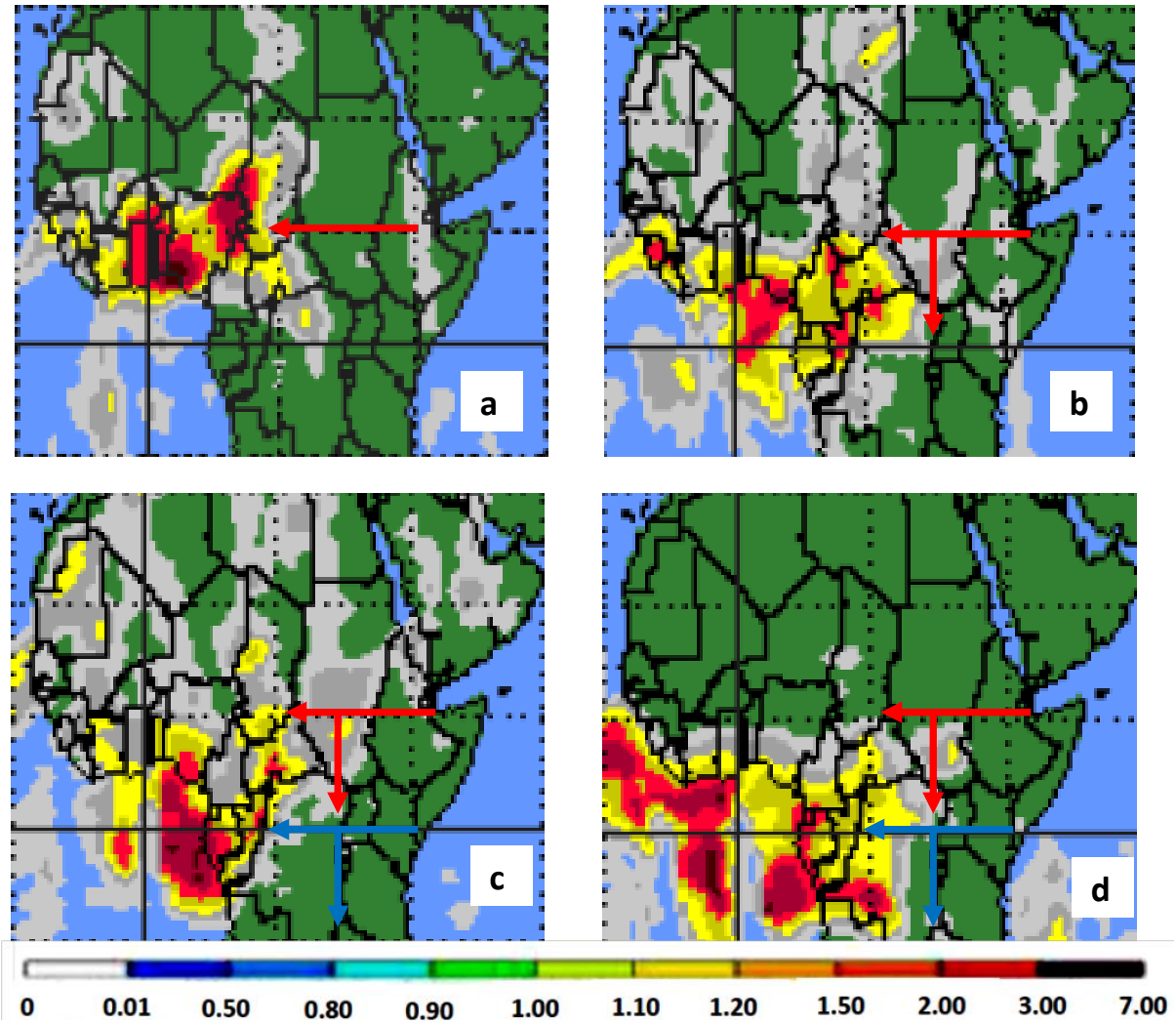

Figure 4.14: Moving aerosol shifting towards the coastal plain (a) January 2000 (b) January 2001 (c) January 2002 (d) January 2003. Arrow shows the direction of shift (NASA, 2015)

The shift from the red arrow in the year 2000 southward and its continuous glaring shifts (the blue arrow) in 2001, 2002 and 2003 affirmed the macro scale functionality of the model. The shift may be due to the Global Climate Teleconnections (GCT), however the science at which this aerosols shift is unique based on the region under consideration. GCT includes climatic oscillations and regional climate systems. The climatic oscillation includes El Nino-Southern Oscillation and North Atlantic Oscillation. The North Atlantic Oscillation originates eastward from the southwestern North Atlantic to Portugal and West Africa. Hence, a scientific gap exists on the aerosols transport along the gradual annual shift caused by GCT. Further analysis on the y-axis transport as viewed by the satellite observation (Figure 4.14) has aided the understanding of the physics of aerosols transport with respect to the changing angular satellite imagery capture. For example, the MISR operates at various directions, that is, nine different angles (70.5^o, 60^o, 45.6^o, 26.1^o, 0^o, 26.1^o, 45.6^o, 60^o, 20.5^o) and gathers data in four different spectral bands (blue, green, red, and near-infrared) of the solar spectrum.

The two evidences, theoretical and satellite observations shown in Figures 4.13 and 4.14, give the idea of complex nature of aerosols which could only be expressed using numerical simulations. The micro scale analysis of the range in y-direction reveals that aerosols size distribution over the PBL sub-layers may be turbulent at certain range. As explained in Figure 4.13, the possibility of obtaining unique aerosol size distribution especially when they begin to coagulate by inelastic collision has been established. For example, Figures 4.14a and 4.14c show the intermittent aerosol size distribution towards Liberia, Sierra Leone, and Guinea in 2000 and 2002 respectively. The magnitude of the aerosols loading keep changing as observed in Figures 4.15 and 4.16. The wind pattern and the convective activities near the coastal ties may be partly responsible for the aerosols loading extension. The lifetimes of the aerosols dispersed in the y-direction in 2002 may be lower than the previous year (Figure 4.14c). The macro scale analysis of the aerosol size distribution (Figure 4.17) showed that the aerosols loading is more dependent on space than time in the y-direction. This is also affirmed in Figures (4.14a-d). Here, the first proposition was enacted that there is the possibility that collisions of aerosol particles reduce their number concentration. However, it does not affect the conservation of the total particulate mass. This idea can be affirmed by the numerical simulations in Figures 4.15 and 4.16.

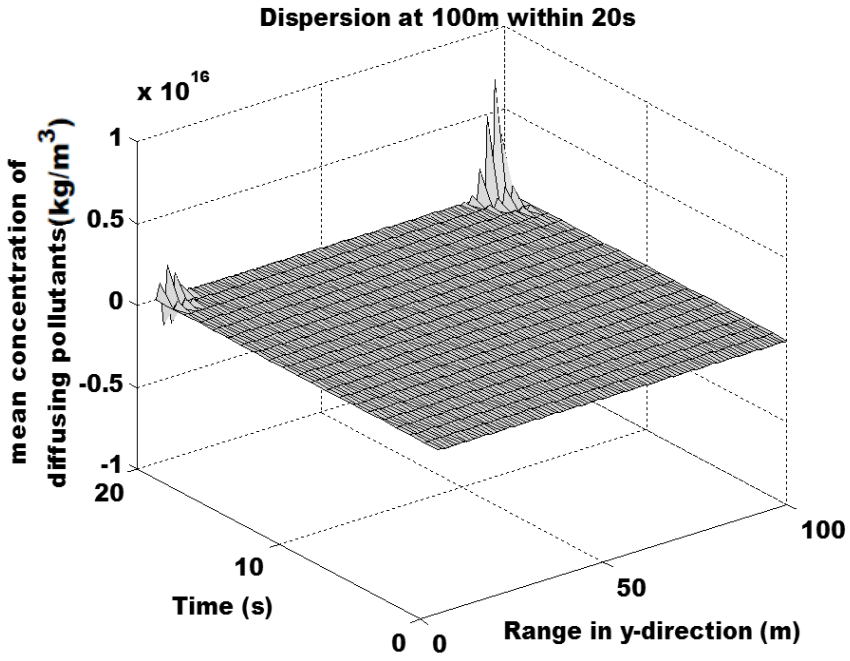

Figure 4.15: 3D macro scale analysis of diffusing pollutants in the y-axis

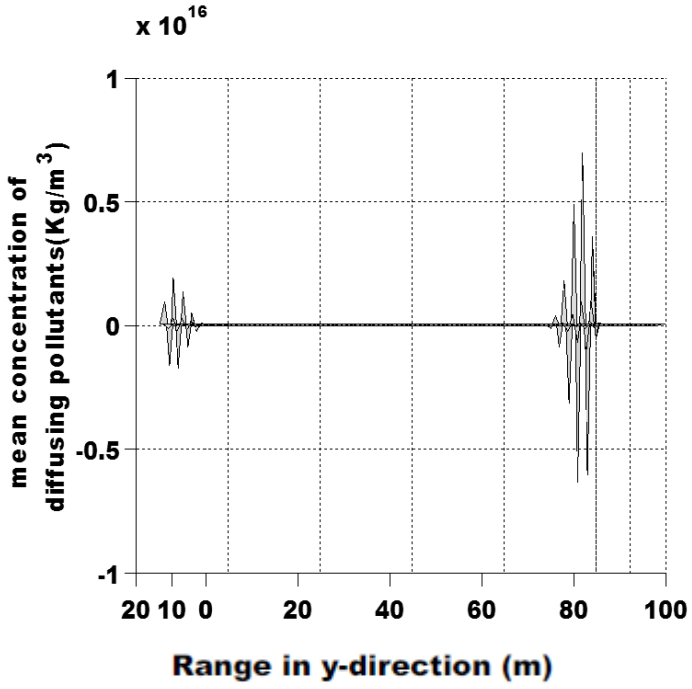

Figure 4.16: 2D macro scale analysis of diffusing pollutants in the y-axis

The numerical prediction (Figure 4.18) shows that the aerosols loading could travel 15 km - 17 km within an hour under the set condition.

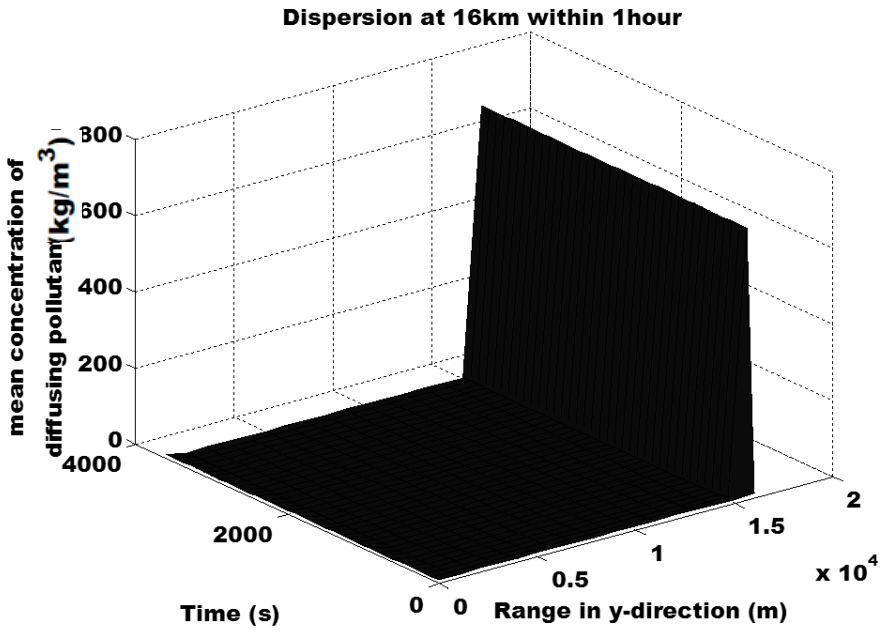

Figure 4.17: 3D macro scale analysis of diffusing pollutants in the y-axis

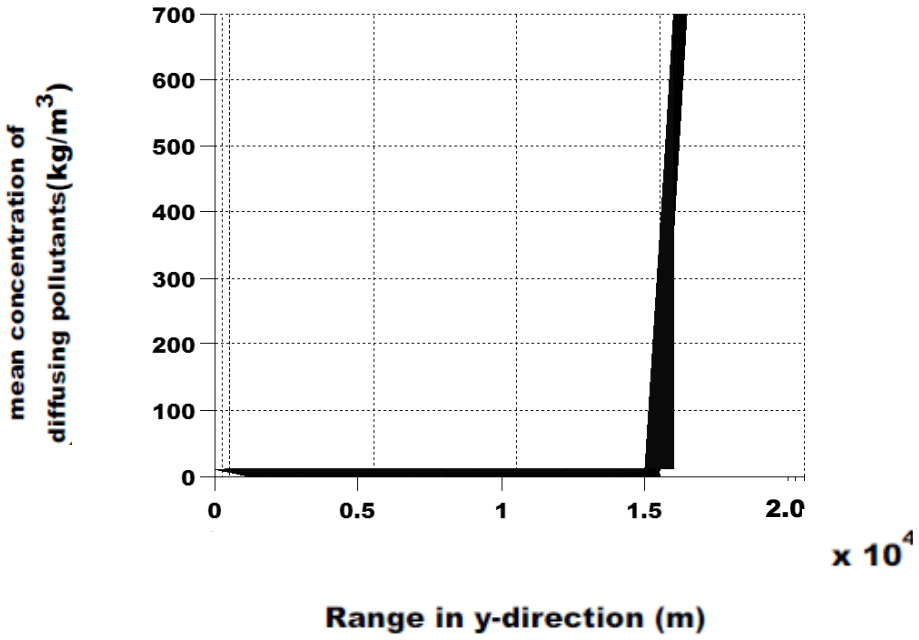

Figure 4.18: 2D macro scale analysis of diffusing pollutants in the y-axis

4.4 Dynamics of Particulates: The Aerosol Size Distribution Experimentation

The rate of mass transfer for Lagos (Figure 4.19) was highest in August to December. The values of the rate of mass transfer for August, September, October, November and December over this station is given as 3.9, 3.85, 3.78, 4.21 and 4.2 respectively. The highest rate of mass transfer in November and December can be explained by the fact that anthropogenic pollution is a common activity between October to February (the dry season) which engender from wild, wood, dung, domestic, industrial, automobile and agricultural fires. However, the significant increase of wildfire aerosol in Africa is traceable to about 70 % of the total area burned worldwide annually (Giglio et al., 2010). The summation of biomass burning and other aerosol plume sources affect the climate system of the area. Hence, that was the main reason for calculating the aerosol retention concept in section 4.9.

Another insight from the rate of mass transfer concept (Figure 4.19) is the vertical and horizontal transport patterns of the plume which lead to several physical and chemical protocols in the atmosphere. The continuous aerosols loading in the atmosphere could lead to a complex comprehension of regional circulation and seasonal pollutant variation.

The AERONET data set of 2012 for Lagos was considered in the study because mass transfer rate was observed to be highest within 2000 to 2013 data set. It was observed that waavelength 865 nm had the highest value of the rate of mass transfer. This figure was supported by the statistical analysis conducted by Wang et al. (2014) which revealed that the highest average values of parameters could be attained at wavelength 440-1020 nm.

It was observed that the mass transfer rate increases almost linearly in the last quarter of the year 2012 (Figure 4.19). The infrared band varies from the blue, red and green bands. However, the point of similarity lies within the drop of the mass transfer rate in June and a gradual rise till August for all bands. From literatures, rainfall or precipitation atmospheric cleansing reduces the atmospheric aerosols content (Gwen and Cederwall, 2004). This effect leads to a reduction in aerosols scattering and improved atmospheric visibility. Despite the highest rainfall and hydrological disaster (Nnaemeka *et al.,* 2015) recorded in 2012, a negligible effect on the mass transfer rate was noticed (Figure 4.19) as a result of the wind pattern peculiar to Lagos (Sanusi and Abisoye, 2011).

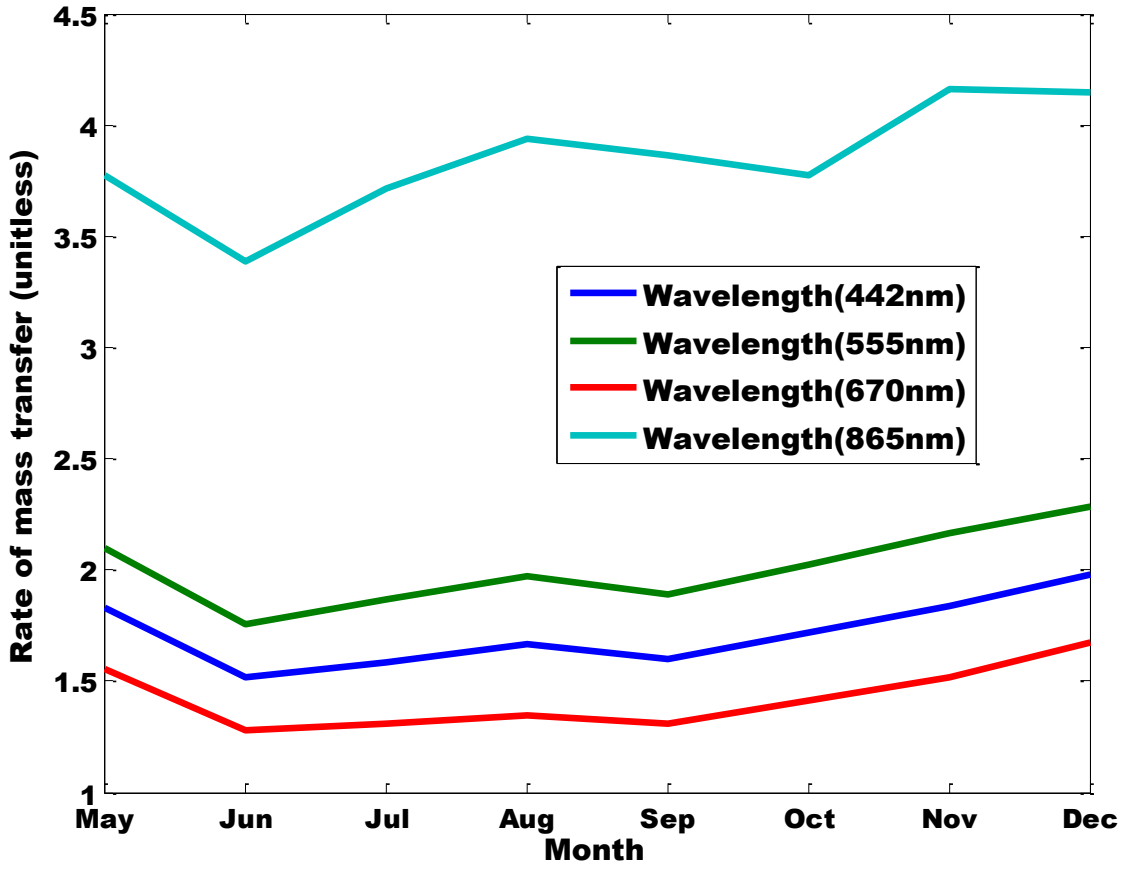

Figure 4.19: Available mass transfer rate data retrieved from AERONET for the year 2012, Lagos

The comparative analysis of the known and proposed models for aerosol size distribution shown in Figures 4.20 and 4.21 validates equation (3.52). The trending of both models was perfect though its magnitude varied. This model-trend agrees that the errors due to the effects of moving fluids on a moving sphere as deduced by earlier researchers had been eliminated using the aerosol dispersion model. The novelty of this research is the parameterization of bands of either a satellite or ground sensor to individually determine the aerosol size distribution over a specific area per time. Since, the kinetic mass transfer rate has direct influence over gaseous and condensed phases of aerosols, the aerosol size distribution is expected to display the increase or decrease in volatility and bulk diffusivity. The Eck's model (Eck et al., 1999) shown in equation (4.1) shows an aerosol size range of 0.1 to 3.6 μm between May and December while the proposed model showed an aerosol size range of 0.1 to 0.8 μm in the same period.

$$\alpha = -\frac{\ln\left(\frac{\tau(\lambda_1)}{\tau(\lambda_2)}\right)}{\ln\left(\frac{\lambda_1}{\lambda_2}\right)} \qquad (4.1)$$

where α is aerosol size distribution, τ is the aerosol optical depth and λ is the wavelength.

These results further confirmed the gap observed in the Eck's model, that is, the model expands the fundamental errors of the retrieval protocols. Hence, the proposed model shows the actual aerosol size distribution over Lagos with the major peaks recorded in June and September of 2012. The twelve months aerosol size distribution in 2013 shows four peaks at February, April, July and September (Figures 4.22 and 4.23). The significant peak shift of the mid- year (between June and September) aerosol size distribution of 2012 and 2013 (June to July) is noteworthy.

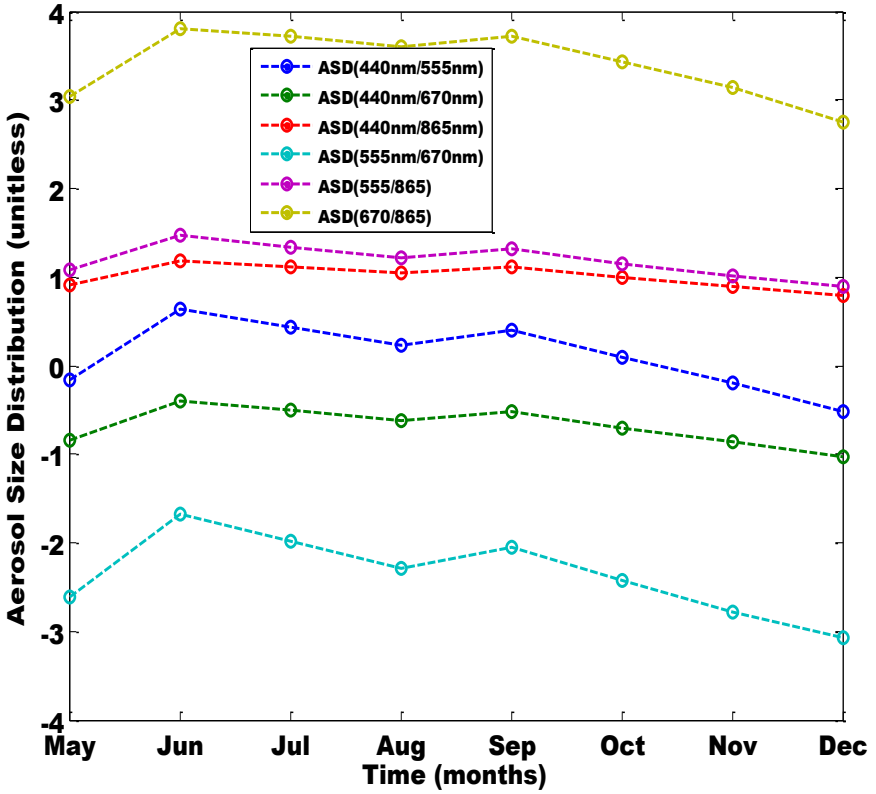

Fig. 4.20: Aerosol size distribution via Equation (4.1) for 2012, Lagos

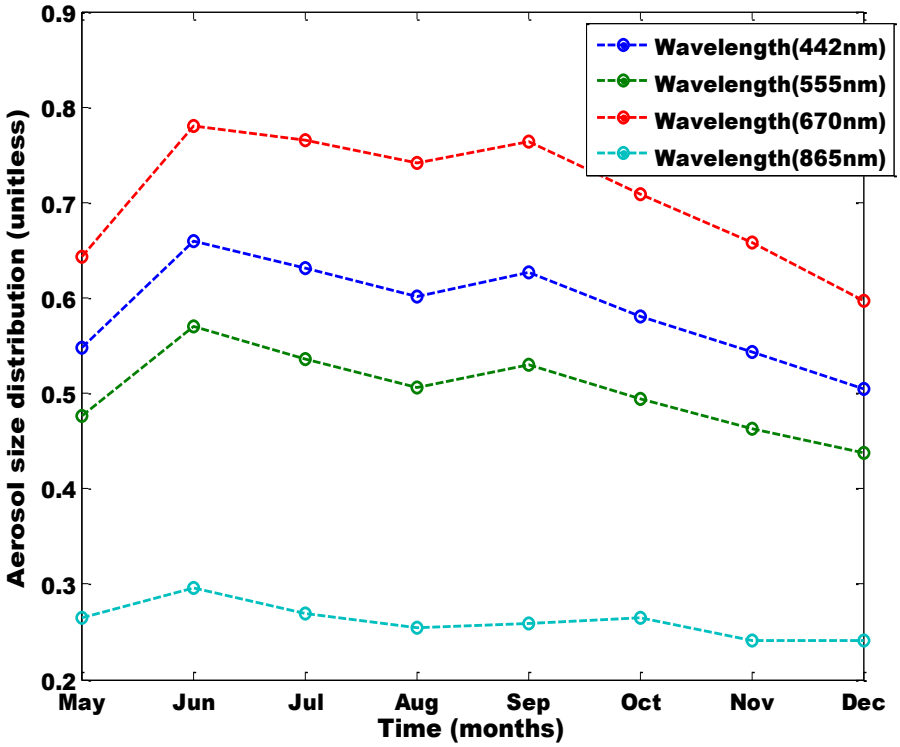

Figure 4.21: Aerosol size distribution via the dispersion model for 2012, Lagos

A complete one year data was considered for 2013 (Figures 4.22 and 4.23). Both models gave the same trends for each band. However, the unified number for this result increased, that is, Un = 1.36. This shows that the turbulence flow determines the aerosol size distribution (ASD) pattern or magnitude. May to October had the highest ASD build-up.

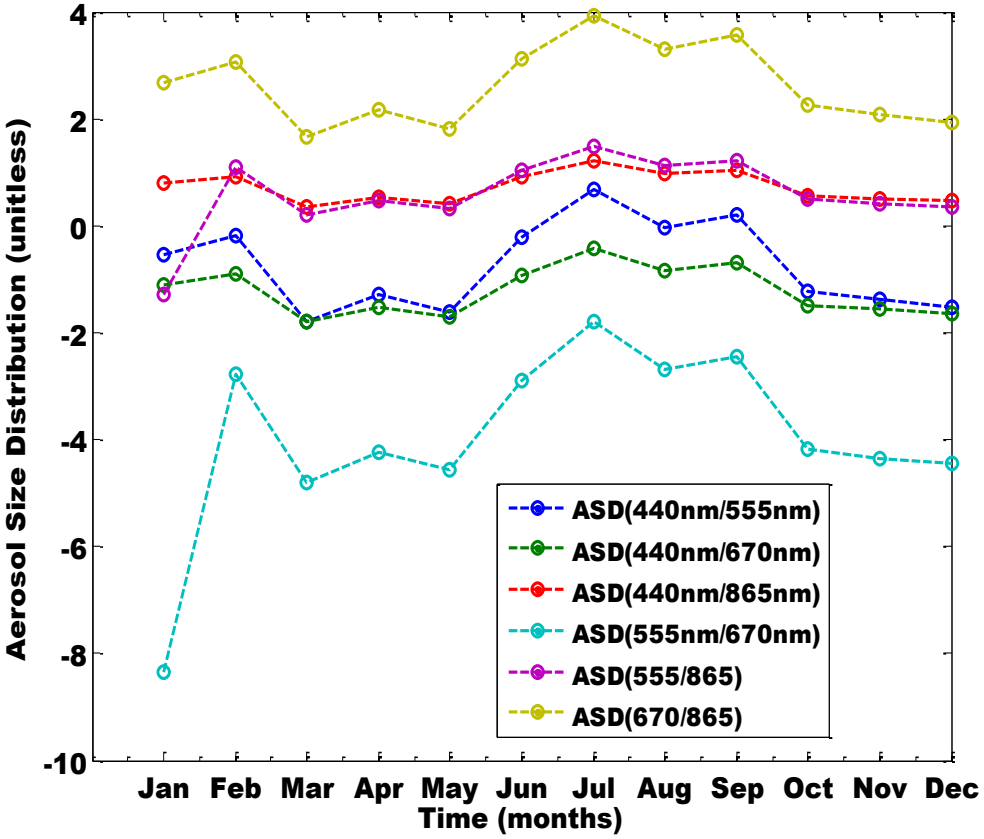

Figure 4.22: Aerosol size distribution via Equation (4.1) for 2013, Lagos

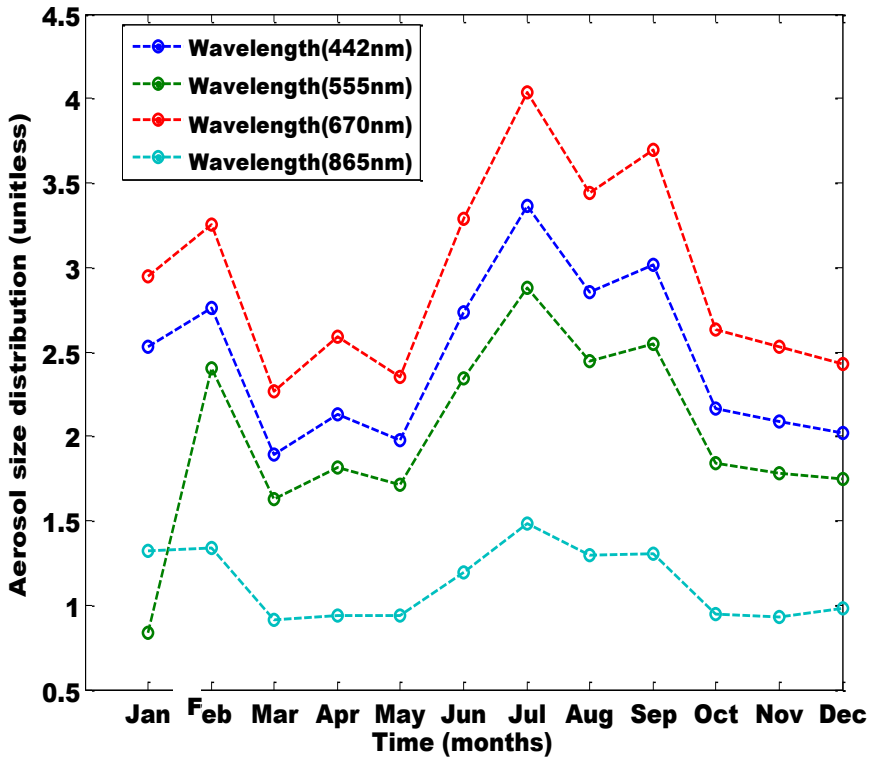

Figures 4.23: Aerosol size distribution of the proposed model for 2013, Lagos

Figures 4.20 to 4.23 show that the retrieval model developed was able to illustrate vital information of the independent spectral aerosol optical depth. Hence, the analysis of the aerosol optical depth can be achieved using single wavelength of a specified satellite band. The adoption of the dispersion plume model in equations (3.17 - 3.20) to determine the aerosol size properties of the coastal urban region is unique (as illustrated in Figure 4.24). However, there lies the possibility of multiple refractive index which varies with respect to the number of dispersion sources, volume of pollutant dispersed, the decay or aging constant and mixing of the tropospheric column (Figure 4.24). Hence, equation (3.34) maybe used to assess the refractive indexes which have been proposed as the atmospheric constant over a particular region or area.

The above results show that the unified number captured both the westerly and easterly air masses which determine the aerosol loading or transport over regions as earlier demonstrated by Figures 4.2 to 4.4. The shape, size and magnitude of aerosol defined in Figure 4.3 affirmed the existence of at least four modes of aerosol particles; coarse mode, nucleation mode, aitken mode and accumulation mode. For example, when Un = 0.1, it is likely that the aerosol mode would be in the accumulation mode, Un $\leq$ 0.3, the aitken mode is likely present, Un $\leq$ 0.5, the nucleation mode is likely present, Un $\geq$ 0.9, the coarse mode is likely present. It shows that in the afternoon, more of the coarse mode and little of nucleation were observed in Figures 4.4. This may be as a result of an increased in day time anthropogenic activities.

However, the transport of the aerosol and the determination of the number size distribution may be complex due to vertical mixing, nucleation, coagulation, plume dilution and condensational growth (Wu et al., 2002). This difficulty was solved by equation (3.48) which is a refinement of equation (3.34). The vital aerosol property, that is, plume dilution ($\eta = \frac{\partial K}{\partial z}$) was included to monitor aerosol number size distribution at whatever layer 'm' when performing a more systematic experimentation. In the night, the minute analysis showed the presence of three modes; nucleation, aitken and accumulation mode. As demonstrated earlier in Figure 4.4, it was observed that the nucleation mode and accumulation mode was more pronounced at the peaks and trough. The morning showed the presence of three modes with majority at the accumulation mode.

The seasonal analysis showed the features of the mass transfer rate, which is a vital property that defines transportation and distribution of aerosol particles. The highest mass transfer during the raining season was noticed in August (Figures 4.19). The month of August fosters mass transfer rate using vertical mixing and plume dilution. The presence of the easterly wind can be seen from September to December. This event is thus important in determining the aerosol size distribution over a geographical location. Figure 4.23 showed that the aerosol size distribution is lower from October to January. Hussein et al. (2004) explained that this occurrence was due to lower total number concentration. This may be due to massive coagulation and nucleation which occurred from May to July. The magnitude of the coagulation and nucleation during May to July determine the extensive effect to succeeding months. For example, in Helsinki, the effect extended to February (Hussein et al., 2004) while the effect in Lagos (Figure 4.23) extended to January. January to March (JFM) and August to October (ASO) showed same pattern. However, the difference between both seasons is the modal structure which may be due to the presence of long term aerosols. If this assumption is true, this means that about 15% of the long term aerosol extends to the ASO. These features were obtained using the parametric retrieval technique explained in Figure 4.24.

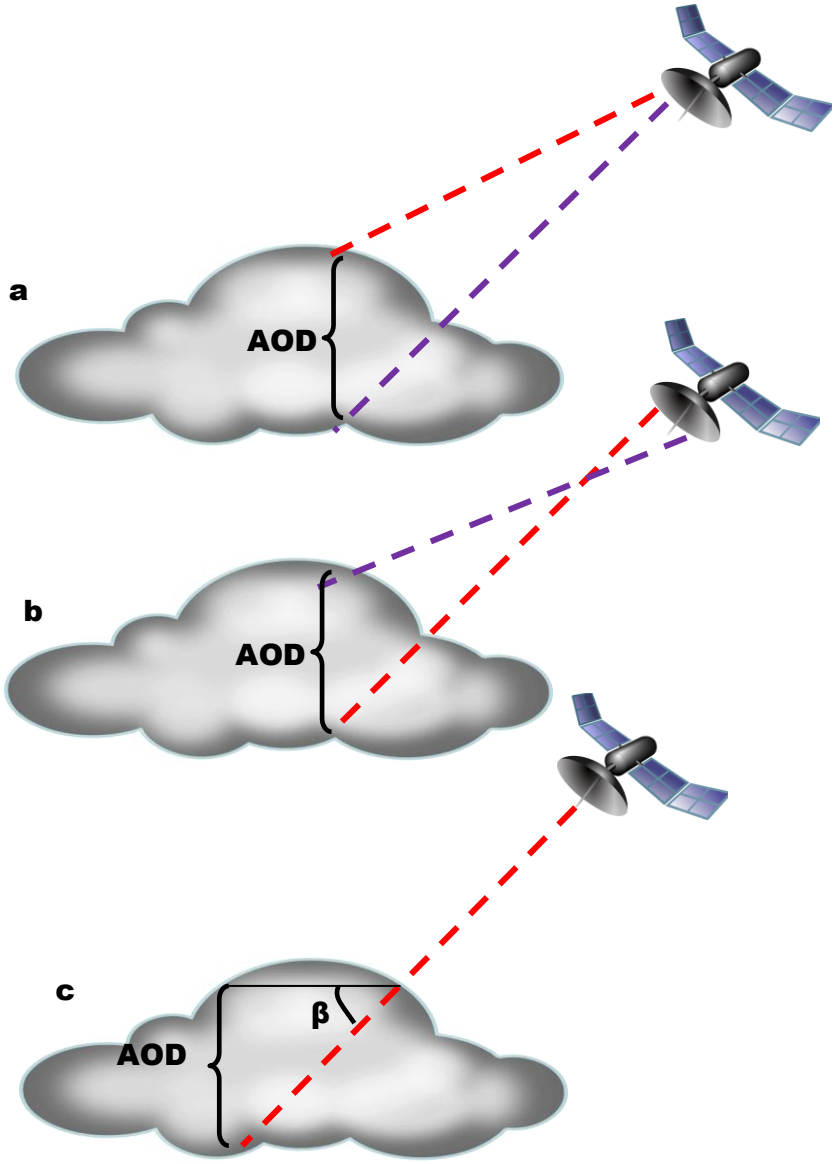

Figure 4.24: Illustration of the existing satellite retrieval pattern with the proposed model

4.5 Mathematical Resolution of Satellite Superposition

Four bands of the Multi-angle Imaging Spectro Radiometer (MISR), that is, infrared, red, green and blue were considered in this section. The green band is unique because it is almost the mean of all minimum and maximum AOD of other bands. The corresponding spectra band on the MODIS was compared with the green spectra band on the MISR as shown in Table 4.2. Two remote scenes were adopted; the emergency radio service (ERS) scenes 100 x 100 km for spectral radiance and the Radarsat scenes 165 x 165 km for spectral radiance. It was observed from calculation that the green band of MISR intersect with four bands on the MODIS. Fortunately these intersected bands are located within the Land/Cloud/Aerosol boundaries and Land/Cloud/Aerosol properties. L_j^{BB} and L_{j2}^{BB} represents the MODIS and MISR respectively in Table 4.2. The L_{j2}^{BB} in the green band corresponds to the spectral radiance of the MODIS' first, second and sixth band. These results may suggest that the MISR results have little anomalies, that is, spectral resolutions. This can be affirmed in Figures (4.25a to 4.25j) below.

Unlike the optical properties of aerosols and clouds (OPAC) and cirrus clouds models which operates at 61 wavelengths (between 0.25 and 40 μm) and 67 wavelengths (between 0.28 and 40 μm) respectively, the MISR is easier to work with because it has only 4 wavelengths. In this section, the focus was the wavelengths 500 nm, 550 nm, 388 nm and 555 nm on the MISR to buttress the band superposition theory explained in Table 4.2 and Figure (4.25a to 4.25j). The pictorial analysis for 2007 shown in Figures (4.25a and 4.25b) reveals a better NASA-Giovanni satellite sensitivity for AOD at a wavelength 550 nm than for aerosol extinction optical depth (AEOD) at a wavelength 550 nm. Also, the pictorial analysis shown in Figures (4.25d and 4.25e) reveals a better NASA-Giovanni satellite sensitivity for AEOD at a wavelength 388 nm than for AOD at a wavelength 388 nm. The AOD at a wavelength 500 nm (Figure 4.25c) is less sensitive. In 2013, the satellite imagery (Figures 4.25f to 4.25j) follows the same feature shown in 2007. The trend is same within 2007 to 2013.

Table 4.2: Corresponding MODIS Bands in the MISR Green Band

Band width (nm)	L_j^{BB} (W/m^2) 10^{-9}	L_{j2}^{BB} (W/m^2) 10^{-9}	τ_a (μm)	τ_{a2} (μm)	Central Wavelength (nm)
545-550	7.9192	21.560	0.5475	0.5475	547.50
545-555	11.564	31.483	0.5500	0.5500	550.00
545-560	16.828	45.813	0.5525	0.5525	552.50
545-565	24.402	66.436	0.5550	0.5550	555.00

The extended effect of sensor adaptation is clearer when the AERONET-aerosol optical depth ground data was compared with the satellite data set over Ilorin, Nigeria (Figure 4.26) for the year 2001. The disparity in both measurements may be trivially explained as the interference of clear and cloudy sky. More technically, the superposition theory which have been proven numerically may be responsible for the major and minor defaults of satellite measurements. It was observed that no superposition occurred for two days, that is, 10th January and 20th April in 2001 because on the raw satellite and ground data sets, the values were almost the same. These dates were obtained from the intersection between the ground and satellite data set. The individual term on the right side of equation (3.62) is synonymous to the solution of a 3D dispersion model. This means that part of the satellite sensor adaptation may be affected by the relative motion between the moving aerosol layers in the atmosphere and the moving earth. This could also be one of the reasons the green band of MISR intersect with four bands on the MODIS (Table 4.2).

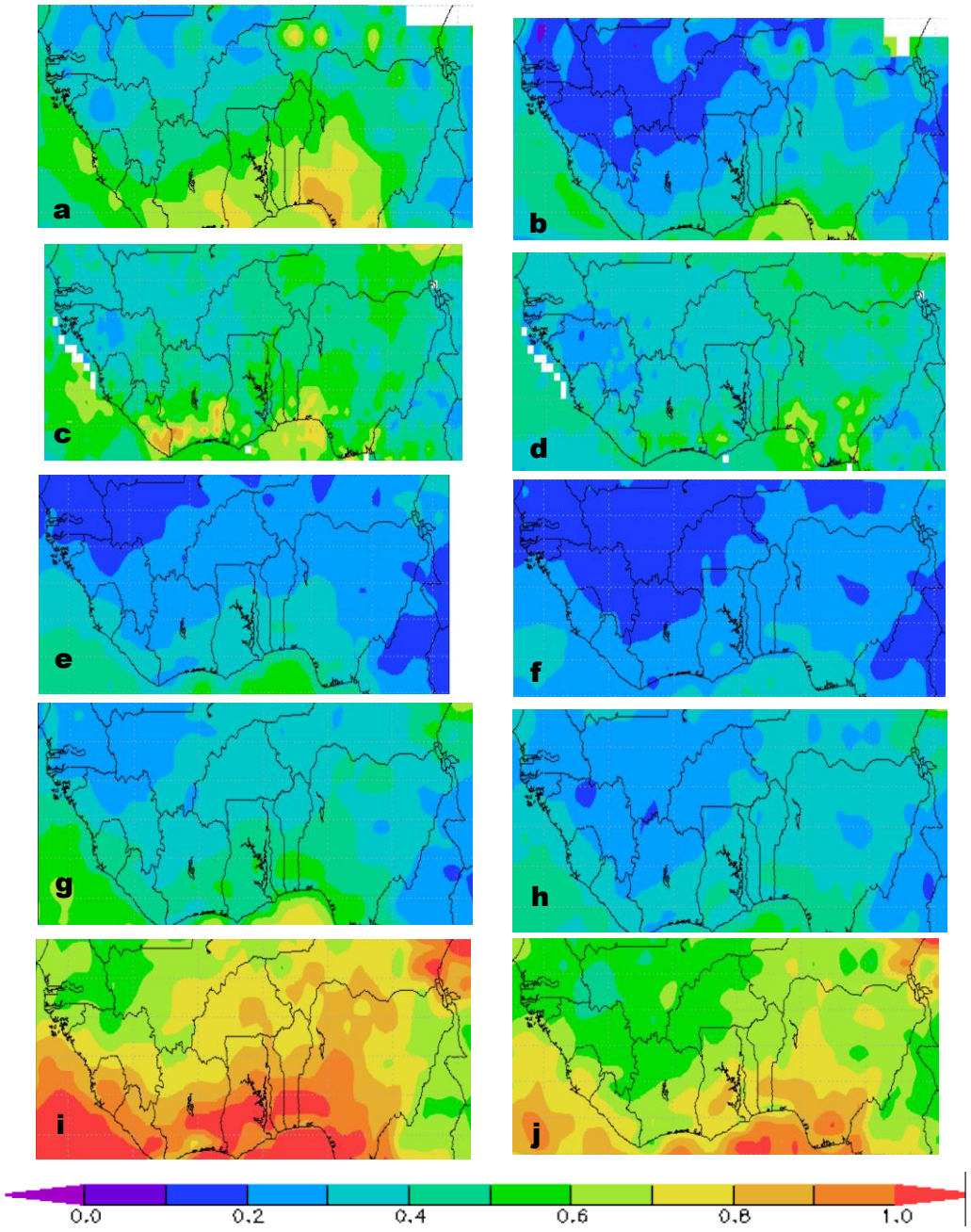

Figure 4.25 (a): AOD at λ=550nm, 2007; (b): AOD at λ=555nm, 2007;
(c): AEOD at λ=500nm, 2007; (d): AOD at λ=388nm, 2007;
(e): AEOD at λ=388nm, 2007; (f): AOD at λ=550nm, 2013;
(g): AOD at λ=555nm, 2013; (h): AEOD at λ=500nm, 2013;
(i): AEOD at λ=388nm, 2013; (j): AOD at 388nm, 2013

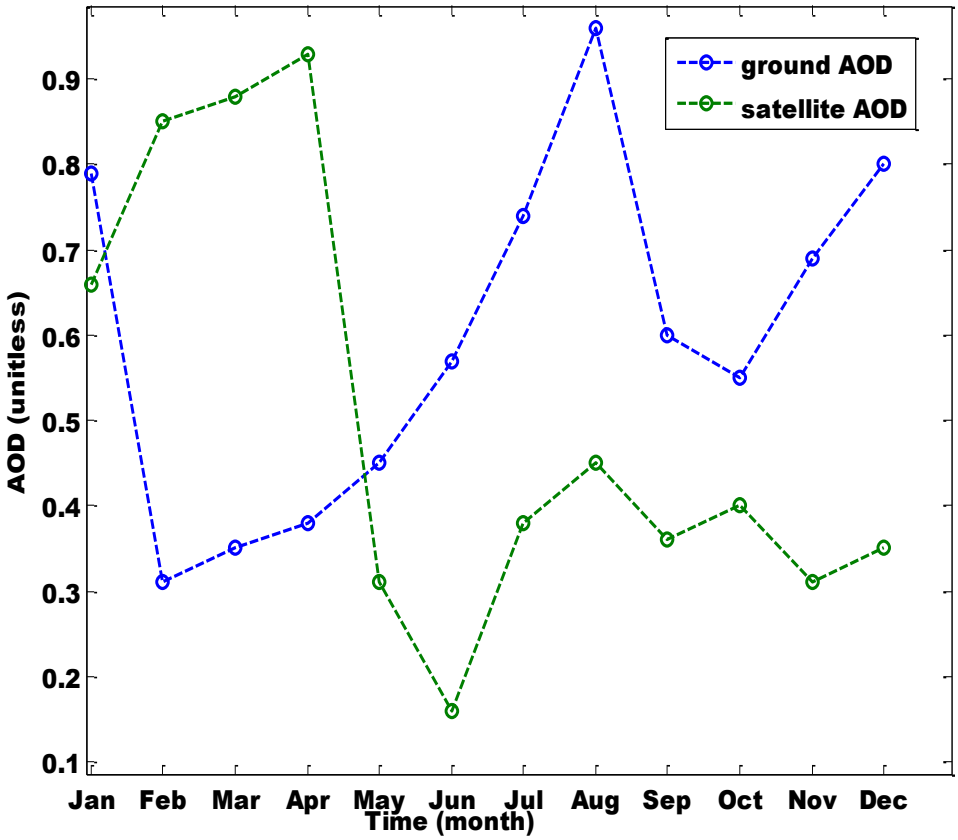

Figure 4.26: Ground and Satellite measurement for Ilorin, Nigeria (2001)

Figure 4.6 shows the ground data set for Ilorin which is presently the only AERONET station in Nigeria. Hence, it was used to verify the result in section 4.5. The comparism of the ground and satellite data set over Ilorin shows that there is variance in the algorithm of MISR (satellite) and AERONET (ground) data. The AOD data between the two instruments had a negative correllation value of -0.23.

4.6 Documentation of Atmospheric Constants: Overview of Selected Locations in West Africa

In this section, the technique for obtaining the atmospheric constants and tunning constants were discussed in-depth. A yearly MISR and proposed model performance was carried-out from 2000 to 2013 for the following locations: Abuja, Lagos, Sokoto, Ilorin, Kano and Mubi. The other locations were discussed in a generalized term. For this analysis, the AOD at 440 nm were considered at random since all the wavelengths, that is, 440 nm, 555 nm, 670 nm and 865 nm follow the same trend or pattern as shown in Figure 4.27. Sokoto was used to test the 4 wavelengths of the MISR because it is among the few locations that had above 93% data sets annually.

Figure 4.27 shows that all wavelength converge at January and December. Maximum AOD is obtained at 440 nm wavelength which is closest to the infra-red wavelength. Visible light spread between 400 nm to 800 nm. It shows that the wavelegth of the AOD tends more to the infra-red than to the ultra-violet end of the electromagnetic spectrum.

The general performance of the AOD within 2000 to 2013 for Abuja is shown in Figure 4.28. The trend of the AOD distribution in Abuja is shown in Figures 4.29a to 4.29d. The accurate curve fitting of the proposed model was used to derive the atmospheric constant as shown in Appendix III: Table 4.3. The data for March was far beyond the proposed model-showing the dynamism of the aerosols loading in March, 2008. However, the data set for March tallies with other years. The dynamism of March and April keeps dropping per year. This uncertain AOD drop in March and April through 2000 to 2013 may be due to a reduced recirculation zone. The loadings for December increased in the last five years while January is unpredictably varying. The variation in January may be due to the influx of Sahara dust

aerosol by the northeast winds. Scanty data was observed in June, July and September. No data was seen for August. Retrieving data using satellite sensor between June and September is difficult because of moisture contents (Adebiyi et al., 2015).

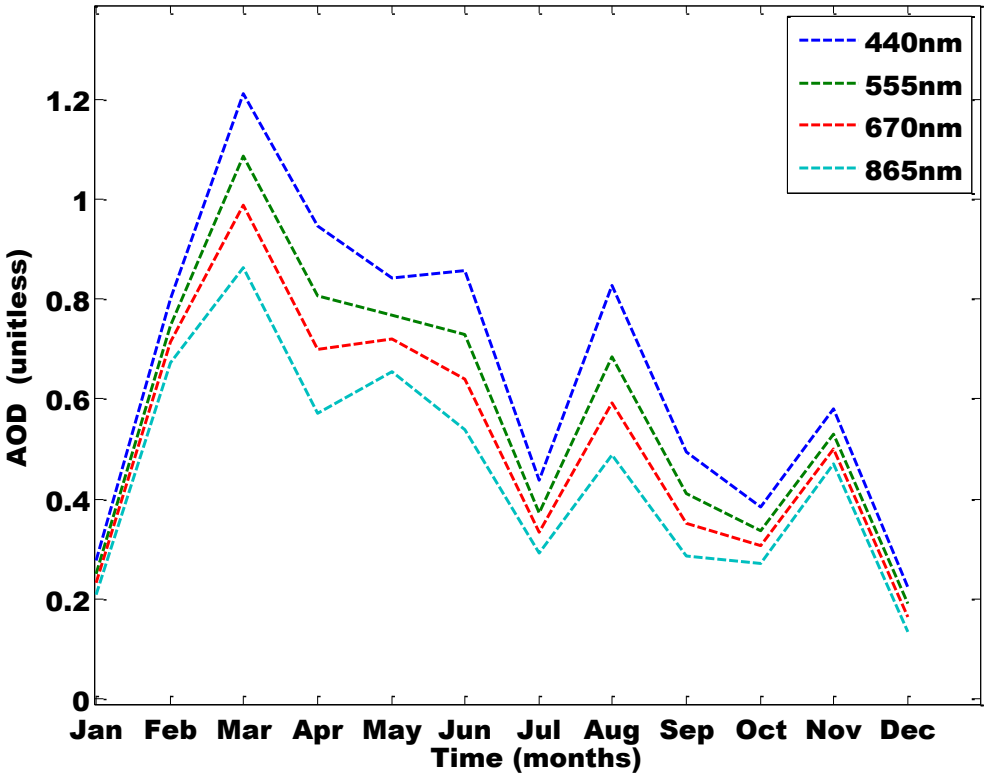

Figure 4.27: Simulation of AOD for different MISR wavelengths over Sokoto for the year 2001

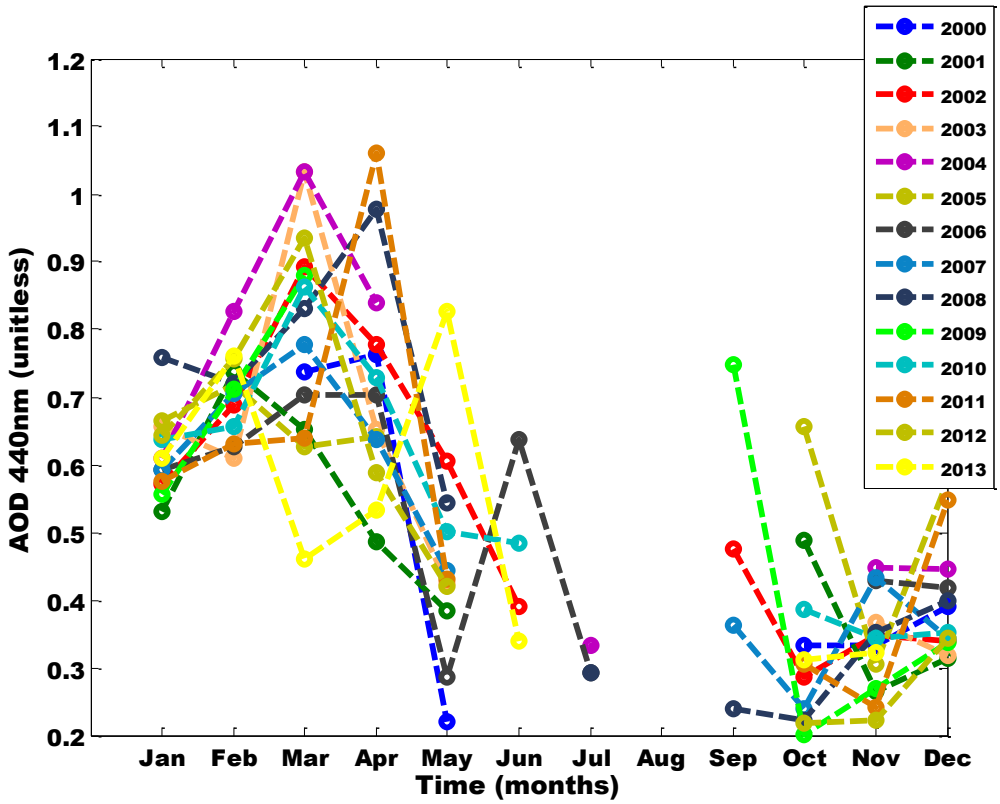

Figure 4.28: AOD pattern for Abuja (2000 – 2013)

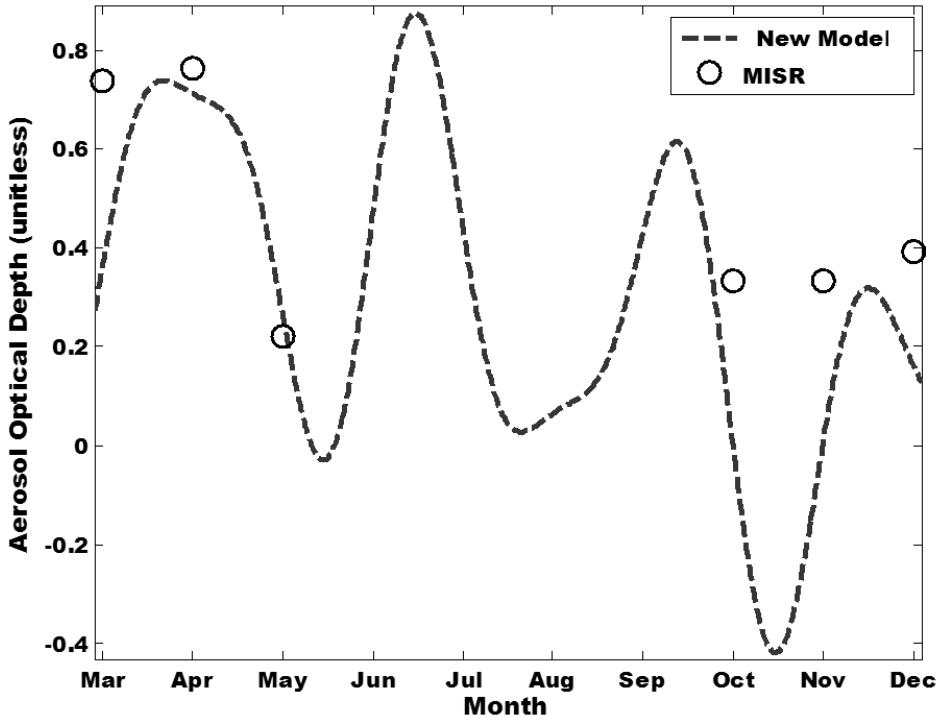

Figure 4.29a: AOD for new model and MISR (Abuja) for the year 2000

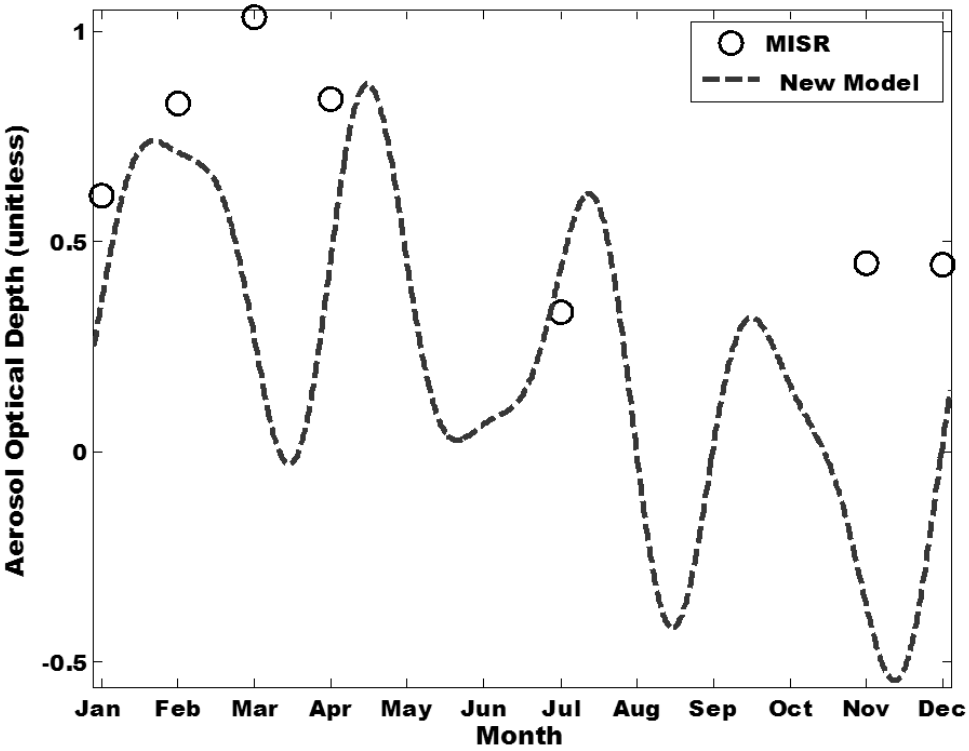

Figure 4.29b: AOD for new model and MISR (Abuja) for the year 2004

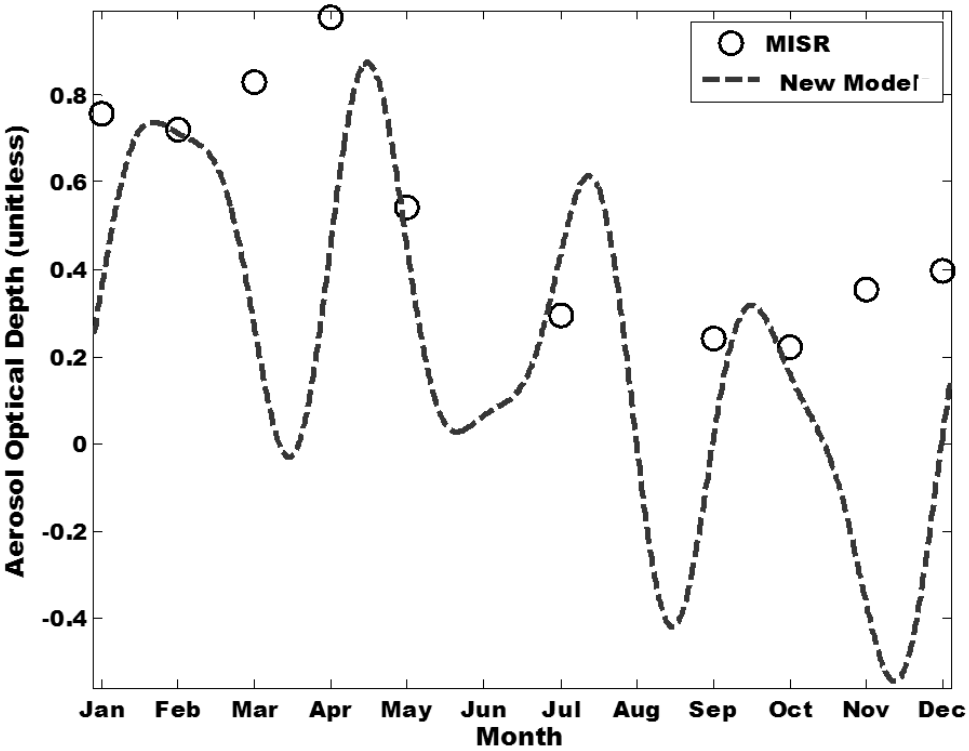

Figure 4.29c: AOD for new model and MISR (Abuja) for the year 2008

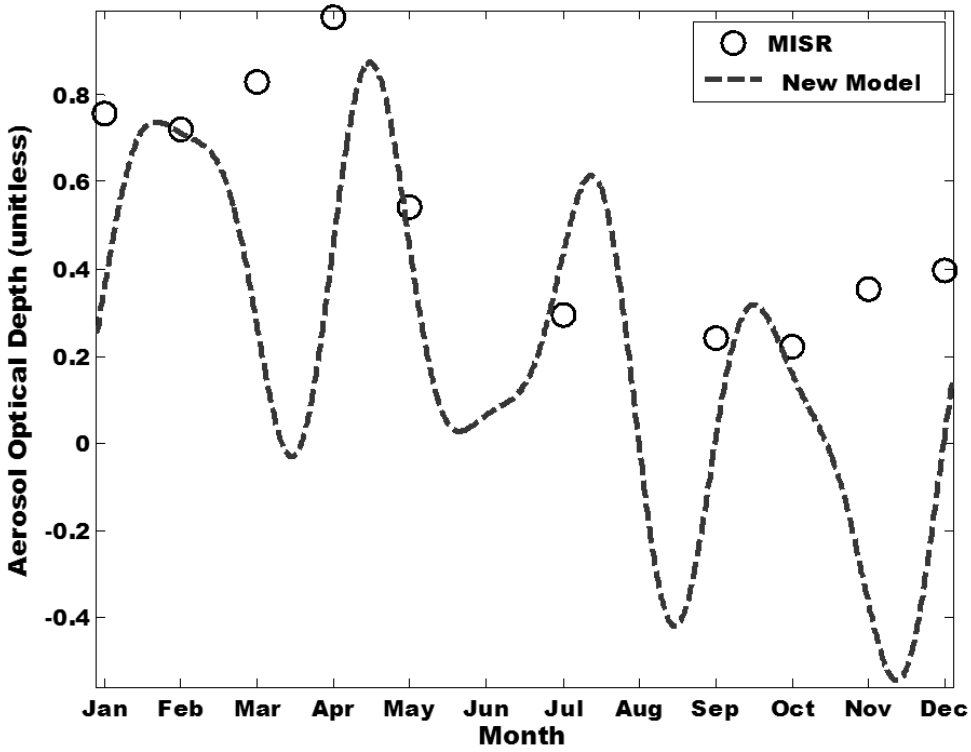

Figure 4.29d: AOD for new model and MISR (Abuja) for the year 2012

The AOD variation in Lagos (Figure 4.30) is unstable partly due to massive moisture updraft due to its location. However, AOD data retrieval in Lagos (Figure 4.31a - d) is relatively stable compared to Abuja. This may be due to stratospheric aerosols which emanates from the oceanic recirculation (Hasebe and Noguchi, 2015). May, 2000 was clearly out of the proposed model. This signifies an extra atmospheric activity in May, 2000. The reason may not be easily adduced because data before the event is not available on the NASA –MISR portal. Interestingly, the month of May from 2001-2013 was in conformity with the proposed model. June and August, 2005 was not in conformity with the proposed model. The anthropogenic activities increased and the recirculation activity enhanced the combination of both the tropospheric and stratospheric aerosols (Hasebe and Noguchi, 2015). In general, the AOD trend for fourteen years follow a positive parabolic curve with minimum at the presumed raining season. An important factor is that aerosols in Lagos are more of carbonated and dust aerosols which can be reduced by rainfall.

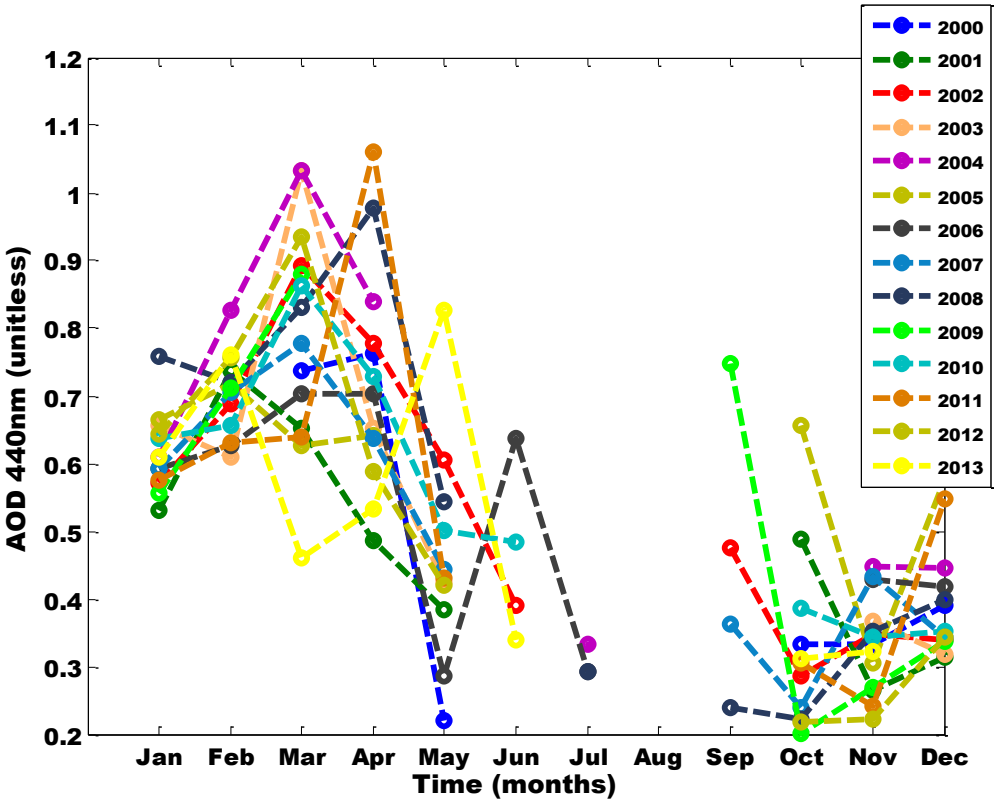

Figure 4.30: AOD pattern for Lagos (2000 – 2013)

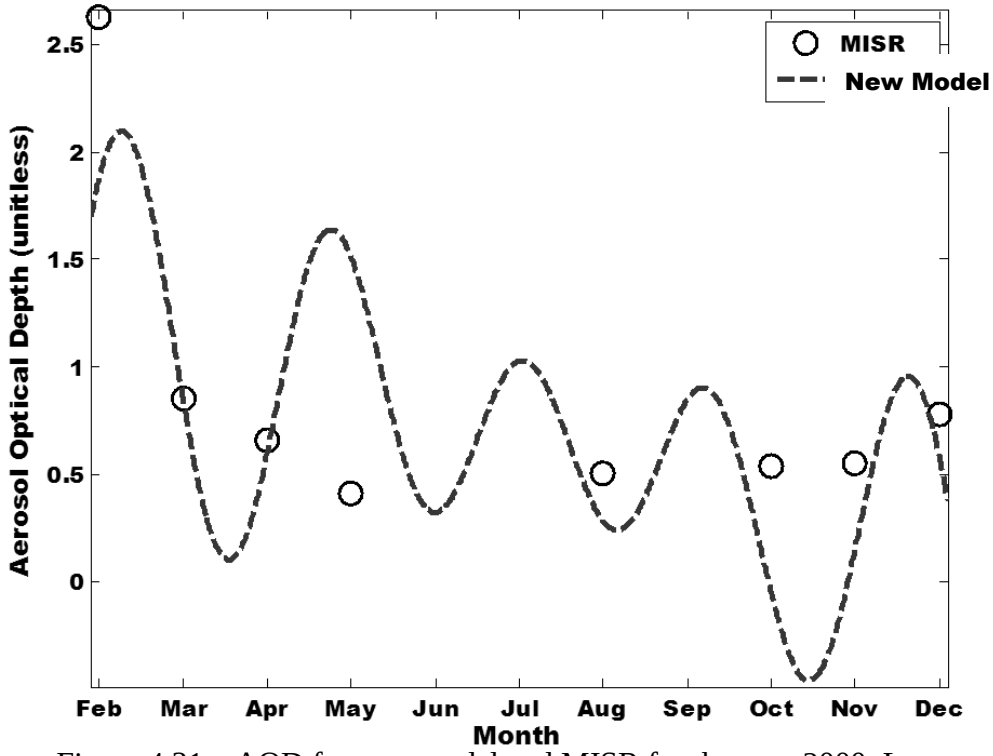

Figure 4.31a: AOD for new model and MISR for the year 2000, Lagos

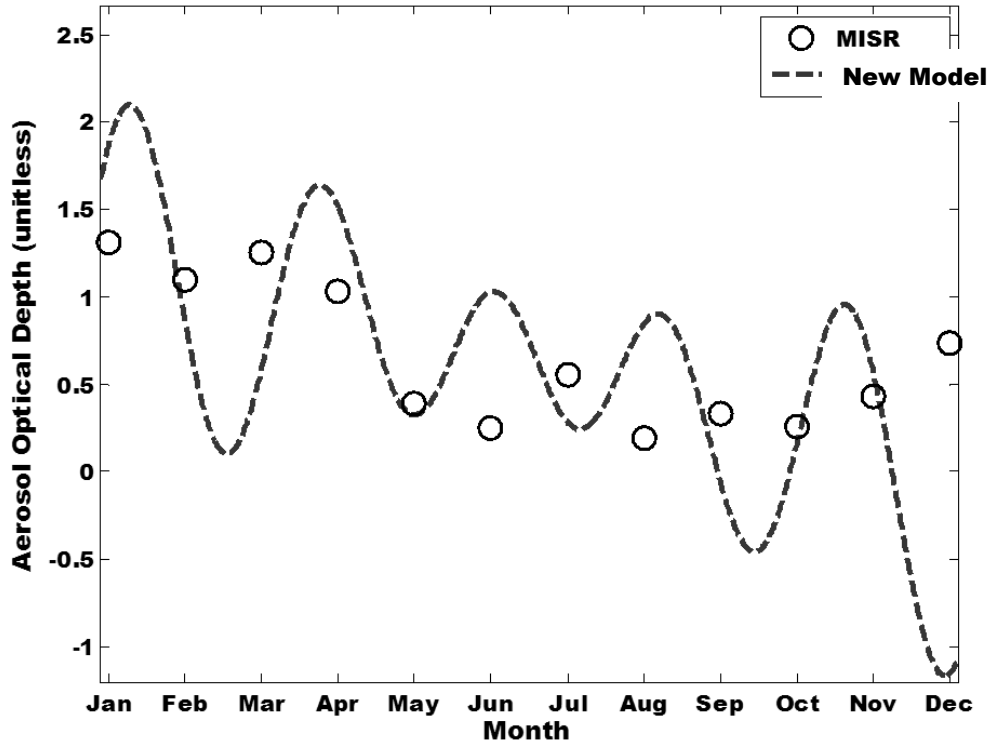

Figure 4.31b: AOD for new model and MISR for the year 2002, Lagos

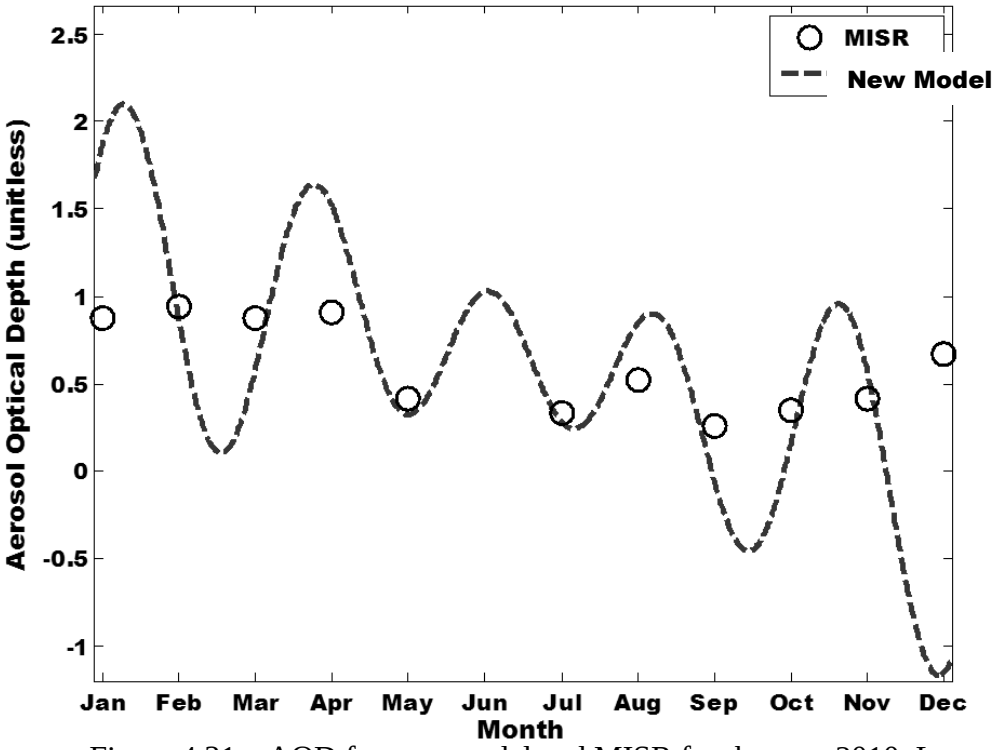

Figure 4.31c: AOD for new model and MISR for the year 2010, Lagos

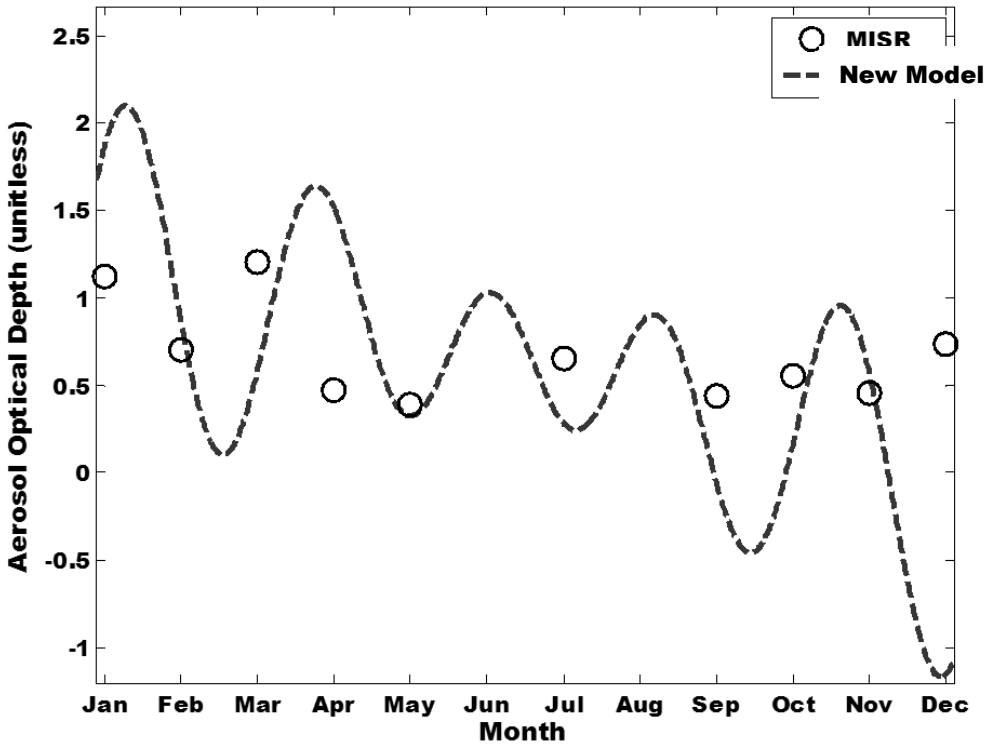

Figure 4.31d: AOD for new model and MISR for the year 2012, Lagos

Sokoto AOD pattern (Figure 4.32) is a gamma distribution with maximum impact in April. The aerosols content in Sokoto gradually reduced from April to December showing that almost same kind of aerosol physical properties exist in Sokoto and Lagos. Unlike Lagos, Sokoto records a low anthropogenic activity as shown from the data in October to December. From literature (Nnaemeka et al., 2015), it can be deduced that the low anthropogenic activity is due to population at both cities. Secondly, Lagos is a highly industrialized region, so it is expected that the anthropogenic activity should be higher than most cities in West Africa. The individual performance of the AOD trend for Sokoto using the proposed model shows that September to December consistently do not fit into the model (Figure 4.33a to 4.33d). The recirculation activity over Sokoto should be high during this period. A more detailed ground-truth exercise is suggested to be carried out in Sokoto.

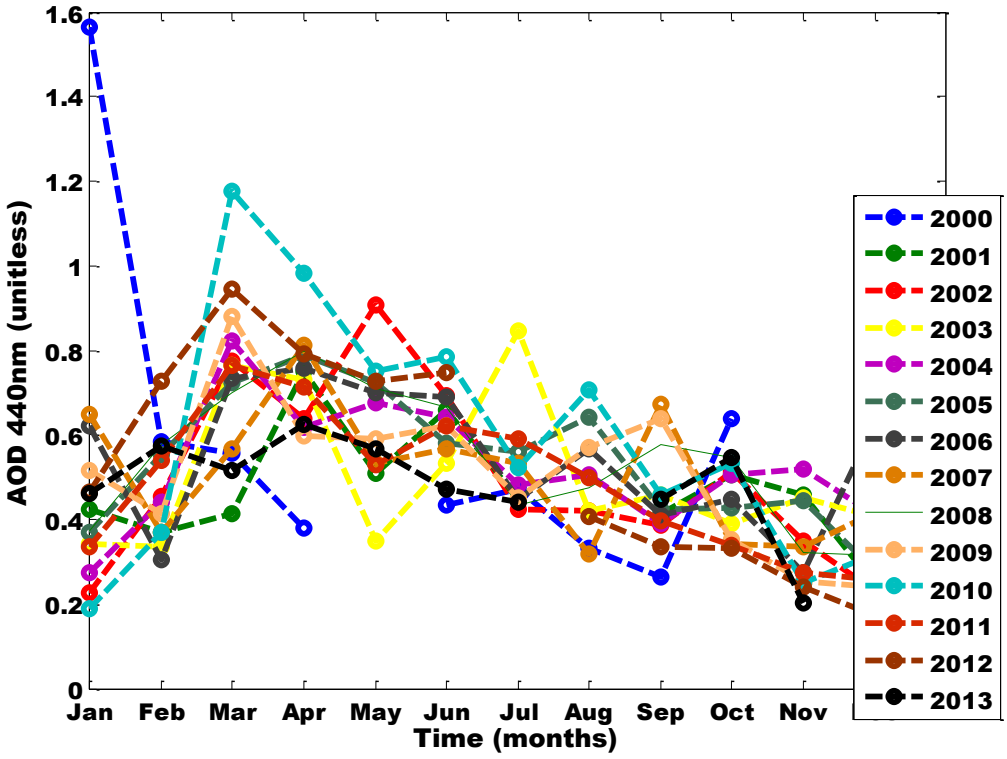

Figure 4.32: AOD pattern for Sokoto (2000 – 2013)

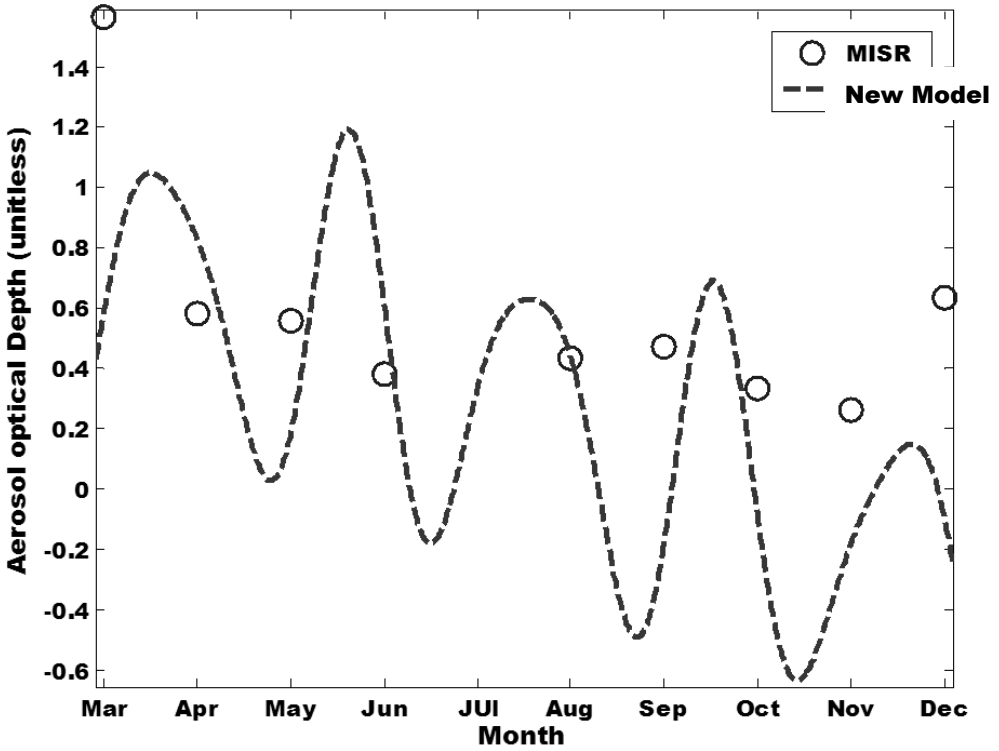

Figure 4.33a: AOD for new model and MISR for the year 2000, Sokoto

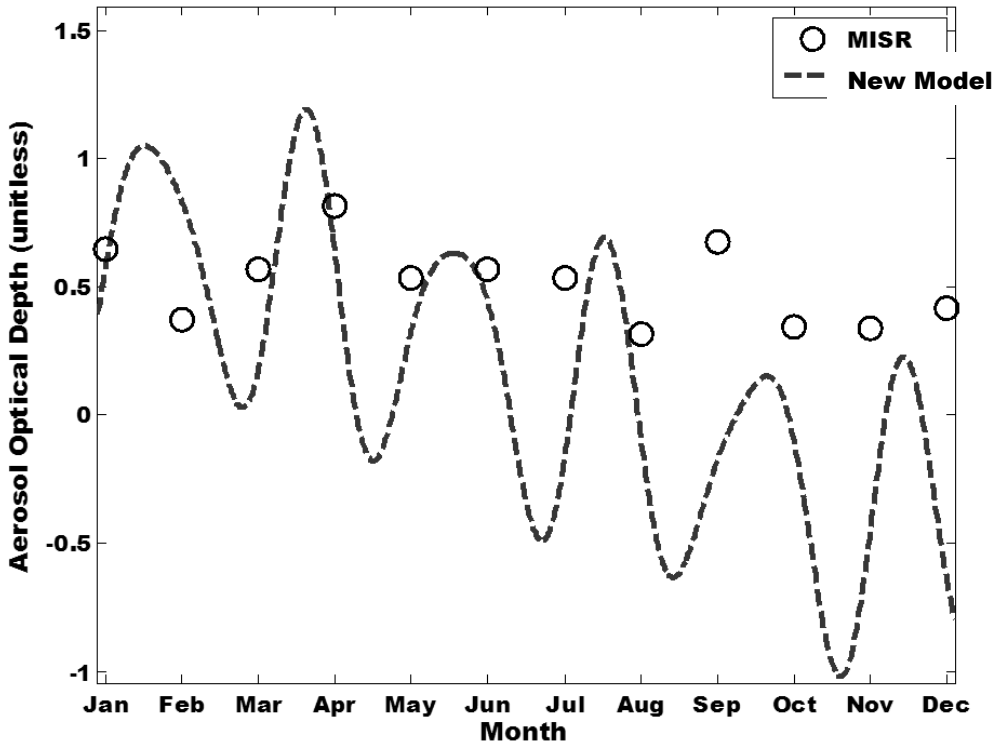

Figure 4.33b: AOD for new model and MISR for the year 2007, Sokoto

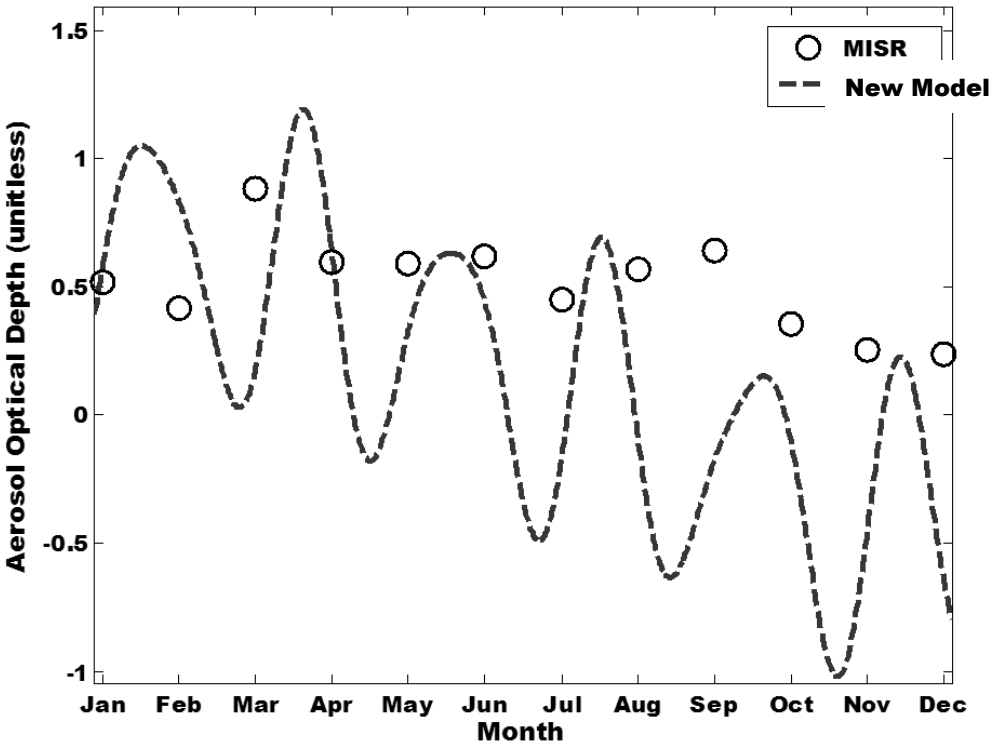

Figure 4.33c: AOD for new model and MISR for the year 2009, Sokoto

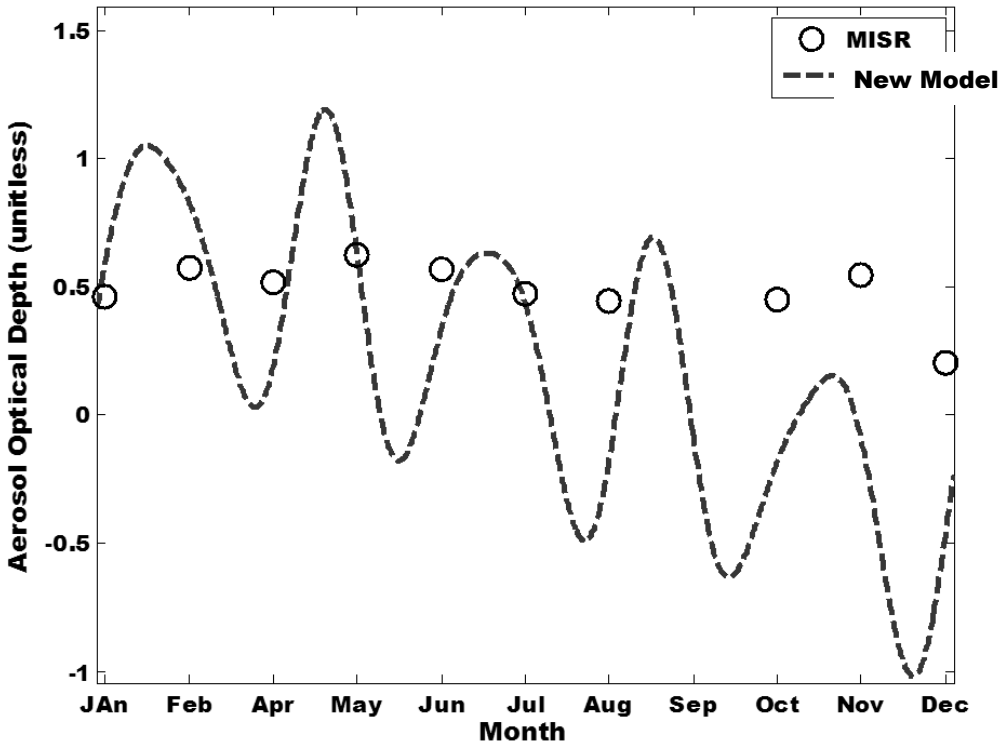

Figure 4.33d: AOD for new model and MISR for the year 2013, Sokoto

Ilorin has scanty AOD data for June to September (Figure 4.34). This may be due to presence of moisture or fog (Falaiye et al., 2015). Unlike Lagos, its AOD is majorly influenced by tropospheric aerosols. These kinds of aerosols are majorly dust particulates. The AOD pattern drops consistently from the highest value in February to September (Figure 4.35). This means the aerosols loading in Ilorin are majorly reduced by rainfall. The data set for December consistently differ from the proposed model. Unlike Sokoto, Ilorin has an AERONET ground station. From the AERONET ground measurement shown in Figure 4.26, it can be induced that the aerosols build-up as a result of the northeast winds from October to December. The cumulative aerosols loading from anthropogenic activities and dust influx in December surpass the expected outcome as predicted by the proposed model. From literature, Falaiye et al. (2015) adduced that bush burning activities is usually high around December.

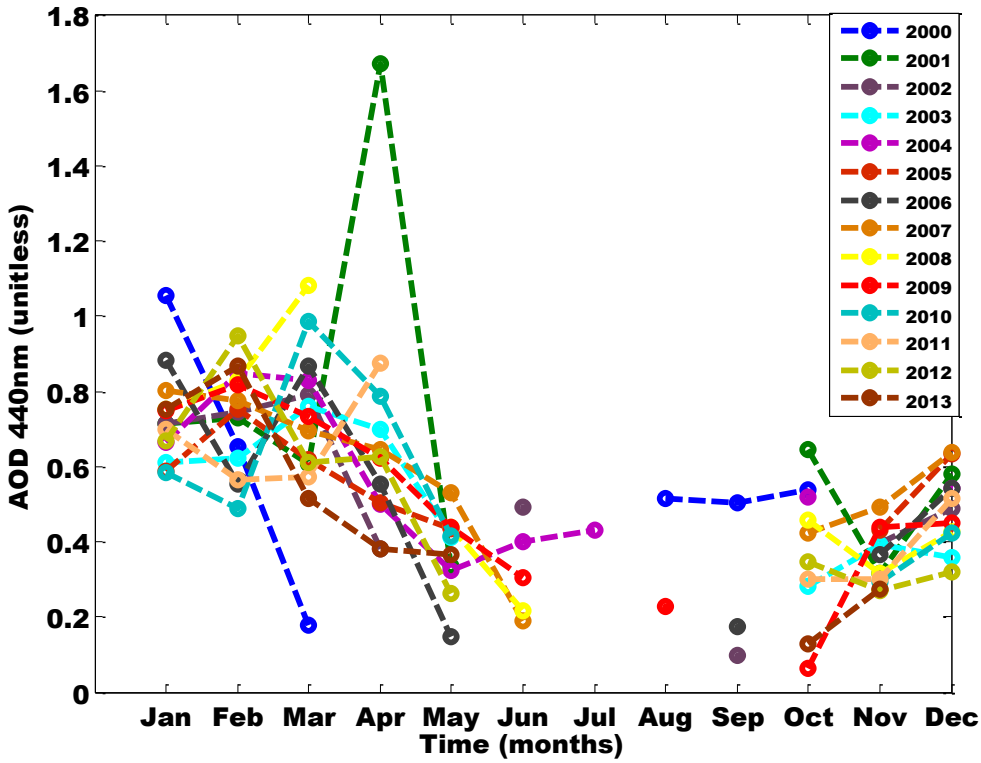

Figure 4.34: AOD pattern for Ilorin (2000 – 2013) Ilorin

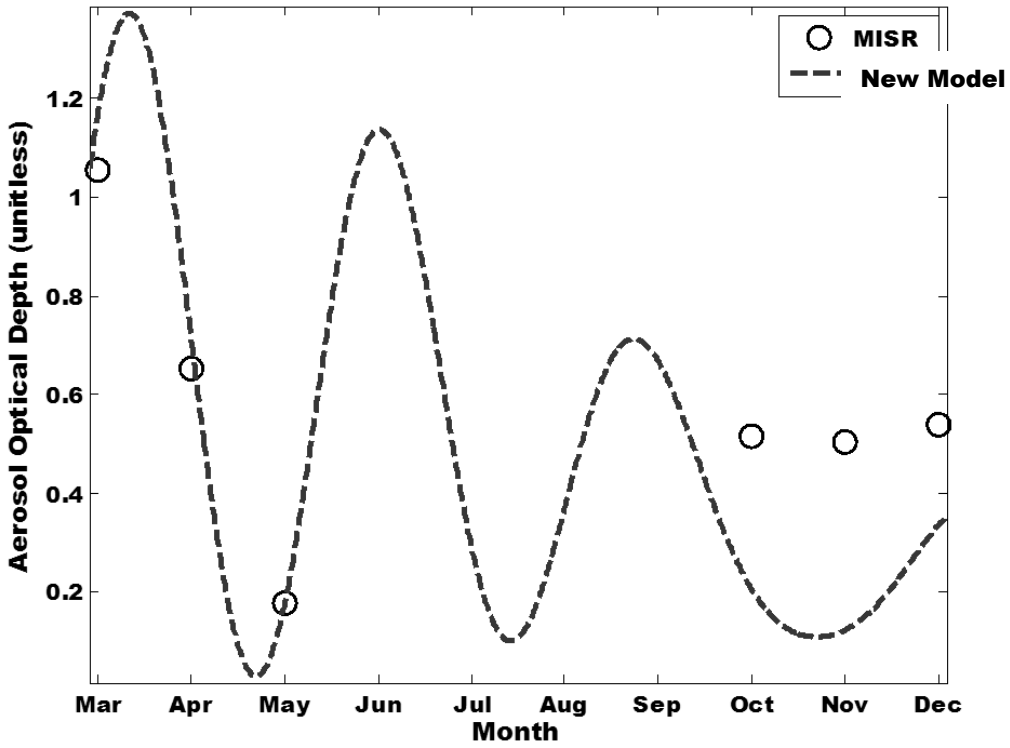

Figure 4.35a: AOD for new model and MISR for the year 2000, Ilorin

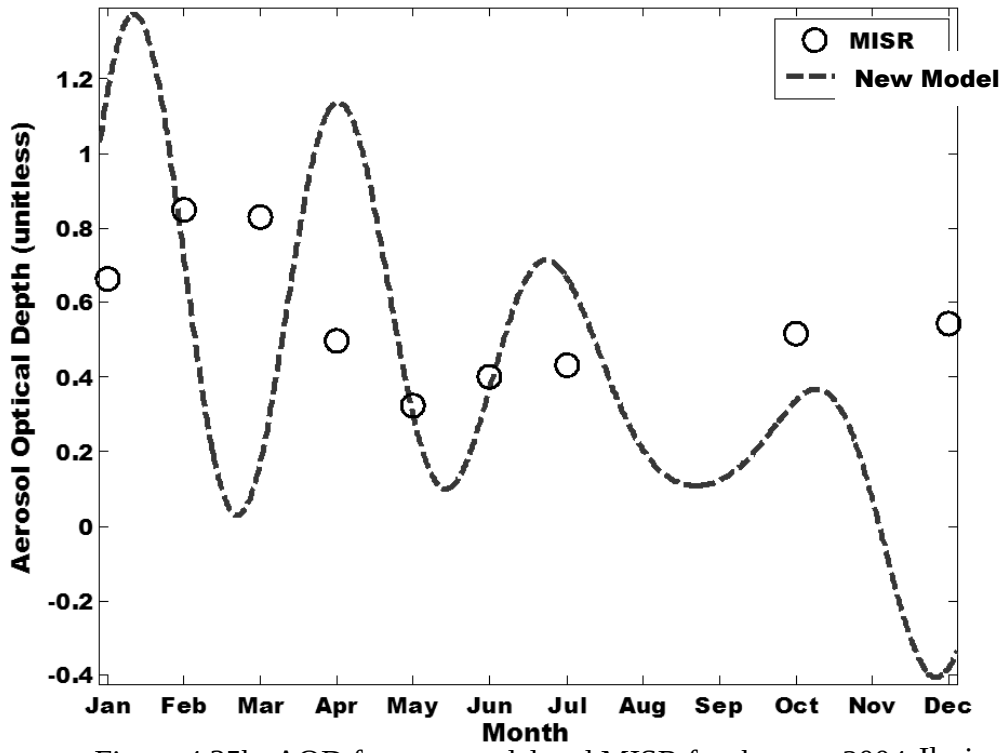

Figure 4.35b: AOD for new model and MISR for the year 2004 Ilorin

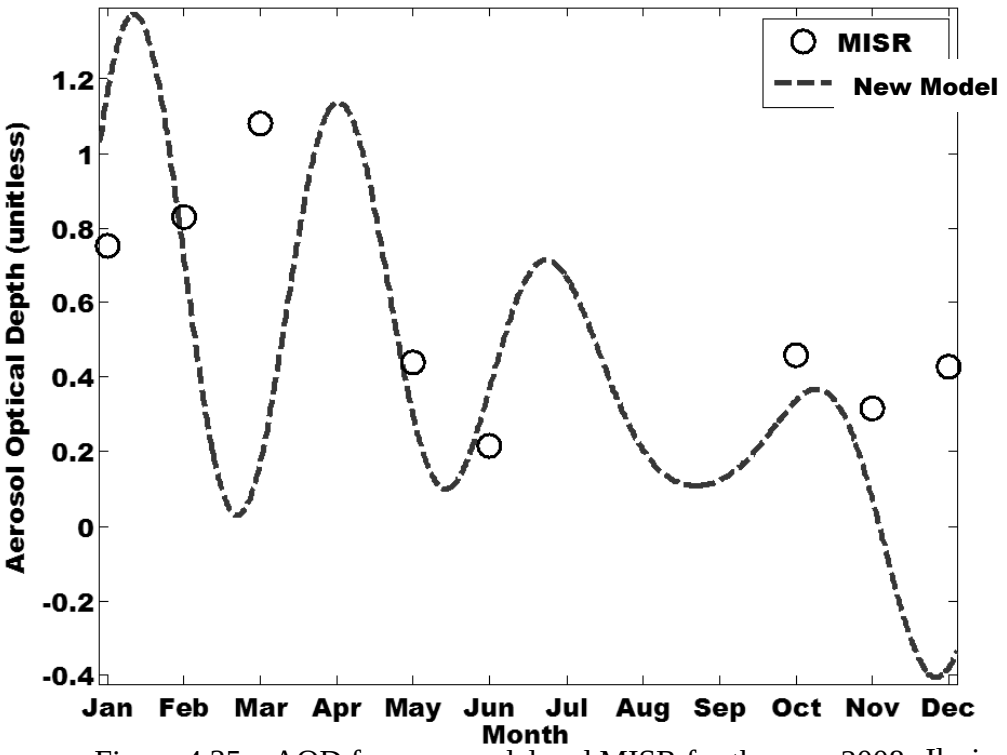

Figure 4.35c: AOD for new model and MISR for the year 2008 Ilorin

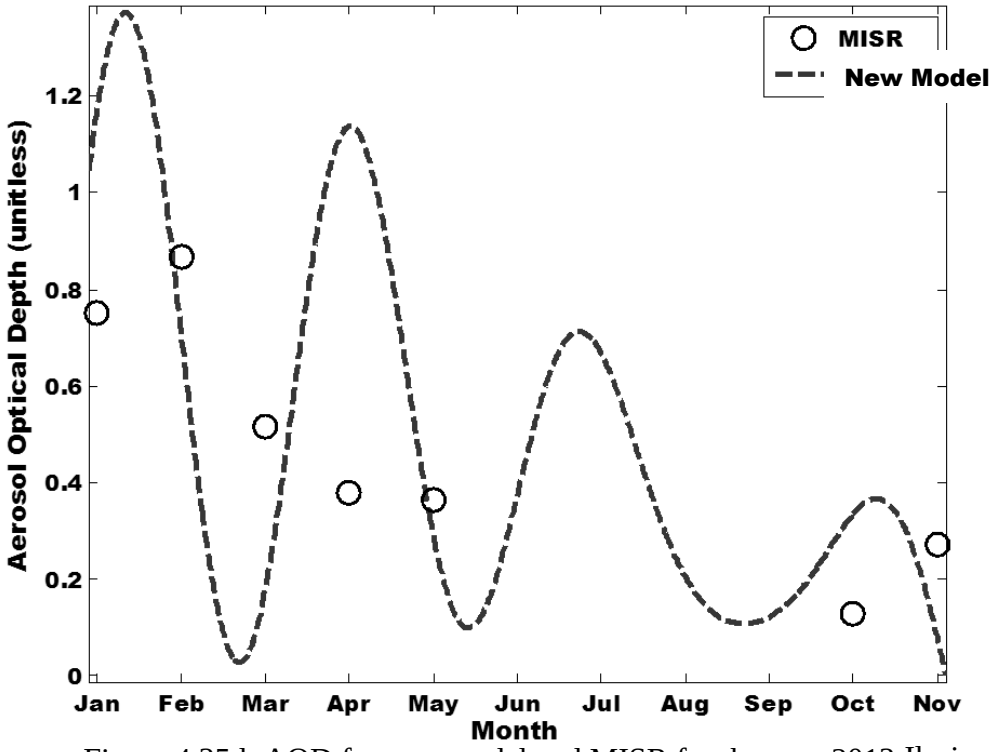

Figure 4.35d: AOD for new model and MISR for the year 2013 Ilorin

Unlike other locations discussed before now, Kano monthly AOD trend agreed perfectly with the proposed model (Figures 4.37a to 4.37d). The AOD pattern over Kano is a gamma distribution with the average maximum in March. From Figure 4.38, it can be inferred that the type of aerosols in Kano is majorly dust particulates from the northeast wind. The AOD retrieval technique by MISR is perfect over Kano. A trivial explanation is that Kano falls within the satellite orbit. Beyond the trivial reason, Accuweather (2015) showed that Kano has a more stable weather compared to other parts of the northern Nigeria.

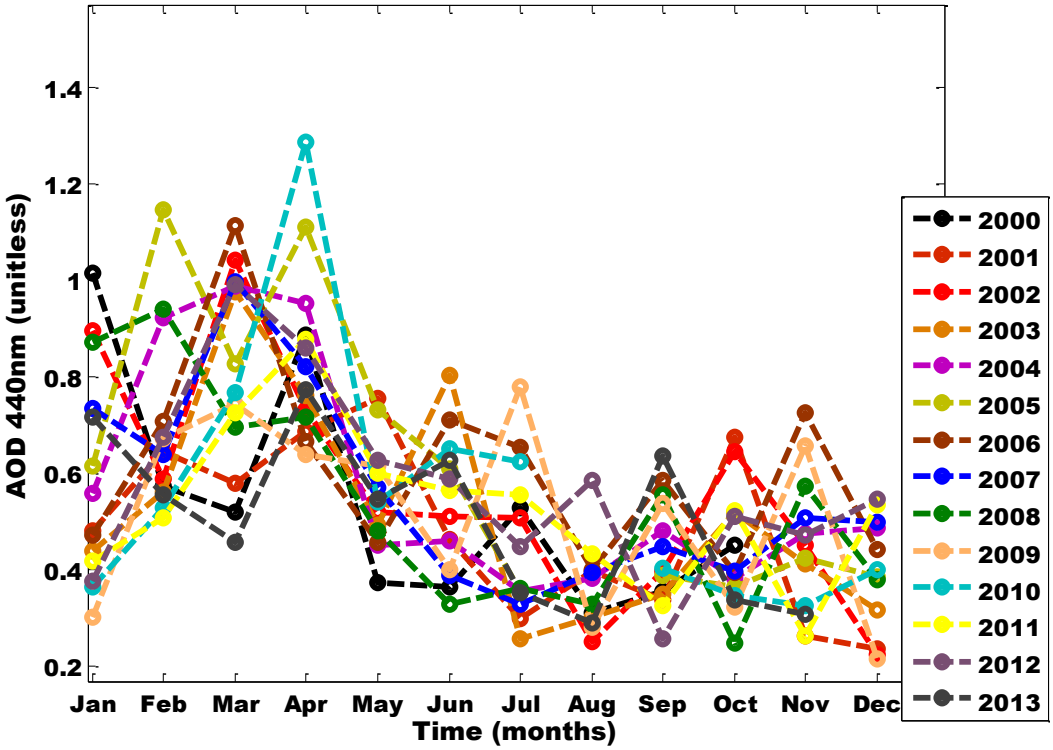

Figure 4.36: AOD pattern for Kano (2000 – 2013)

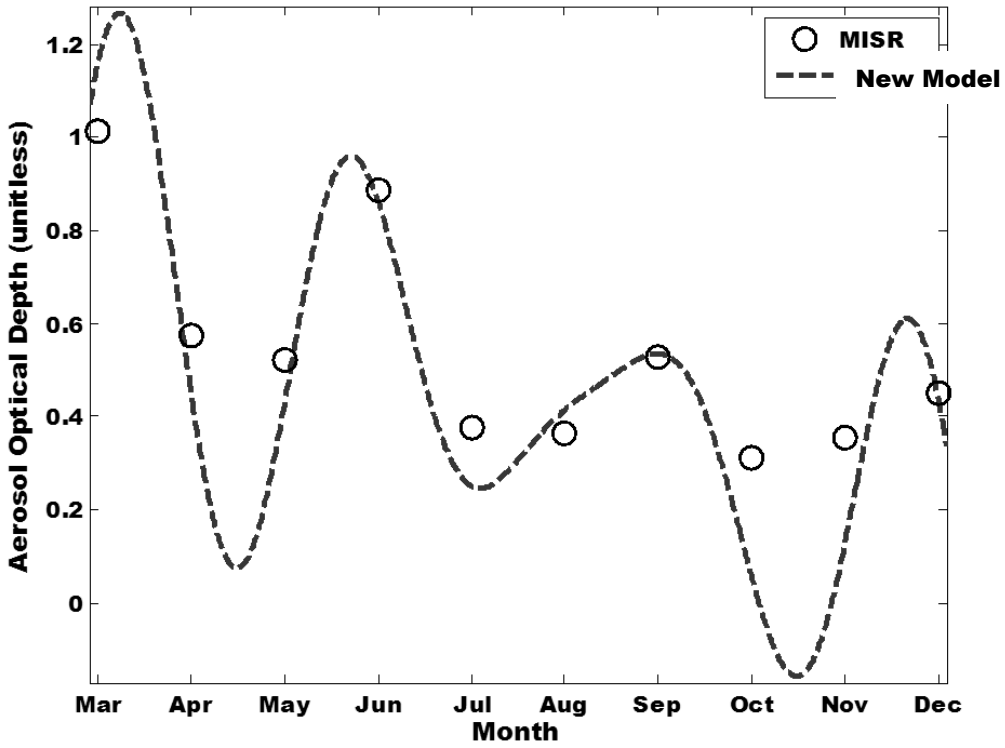

Figure 4.37a: AOD for new model and MISR for the year 2000, Kano

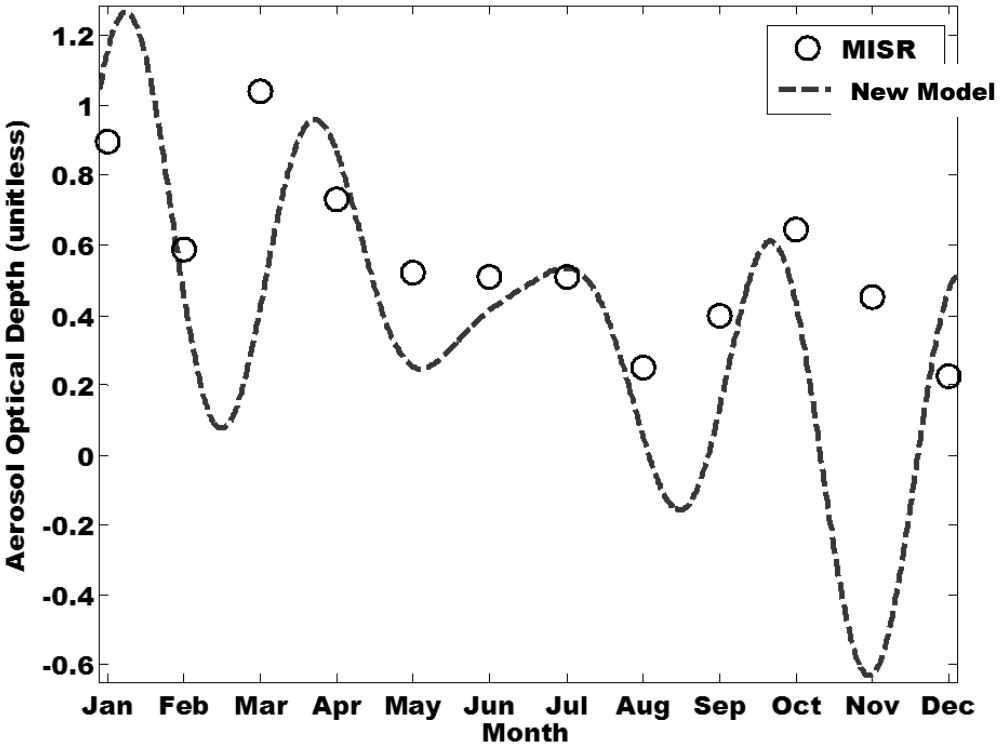

Figure 4.37b: AOD for new model and MISR for the year 2002, Kano

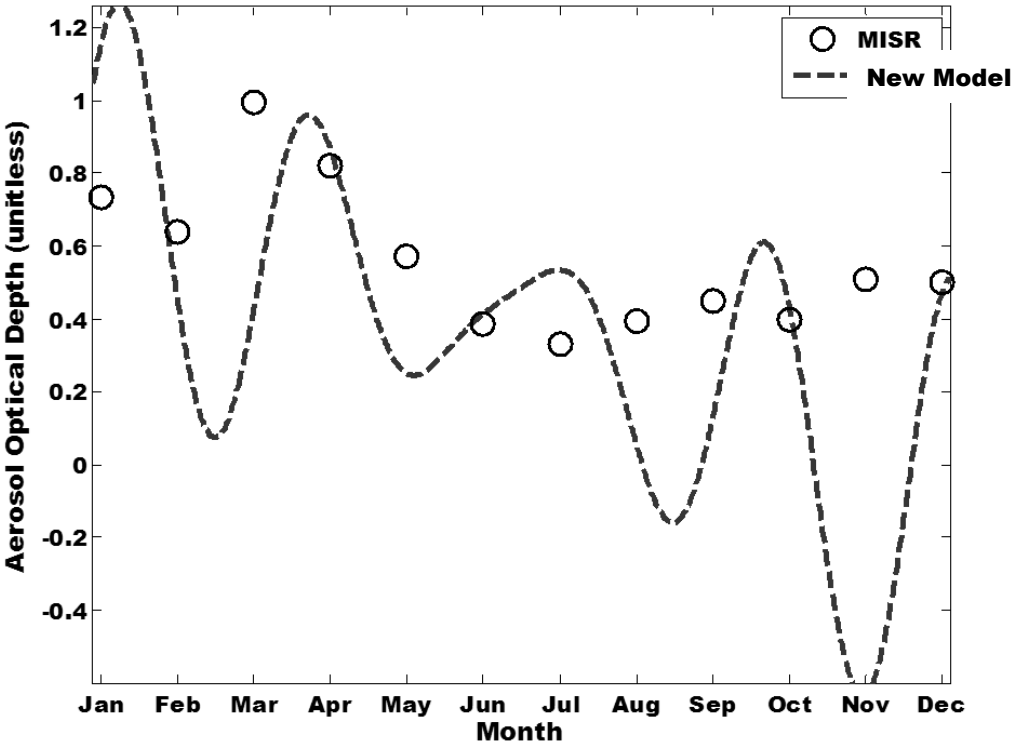

Figure 4.37c: AOD for new model and MISR for the year 2007, Kano

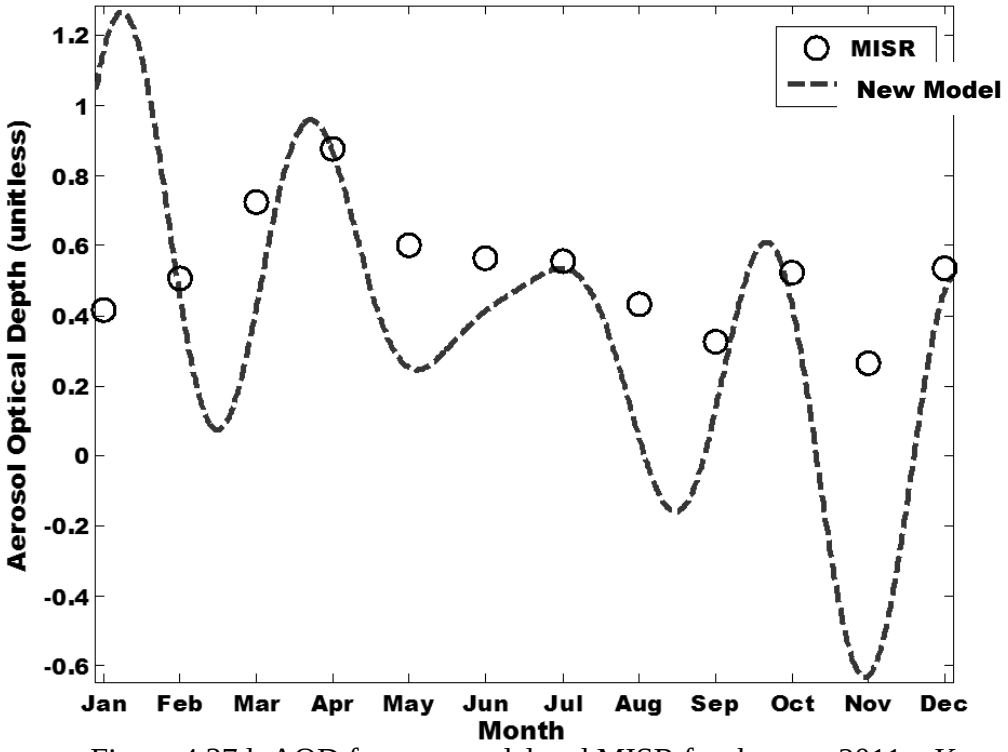

Figure 4.37d: AOD for new model and MISR for the year 2011, Kano

The monthly AOD trend in Mubi within 2000 to 2013 agrees with the proposed model in Figures 4.39a to 4.39d. This means that the proposed model can be used for nowcast and forecast purposes. The AOD pattern follows the gamma distribution with the average maximum in March. From Figure 4.38, it can be inferred that the type of aerosols in Mubi is majorly dust particulates from the northeast wind. The aerosols loading in Mubi reduced in the last four years. This may be due to a massive reduction of anthropogenic activities in the region. Also, the tropical climate of Mubi has moderate rainfall to allow for 'rain wash'. 'Rain wash' is a process of reducing the aerosol content in the lower atmosphere via rainfall.

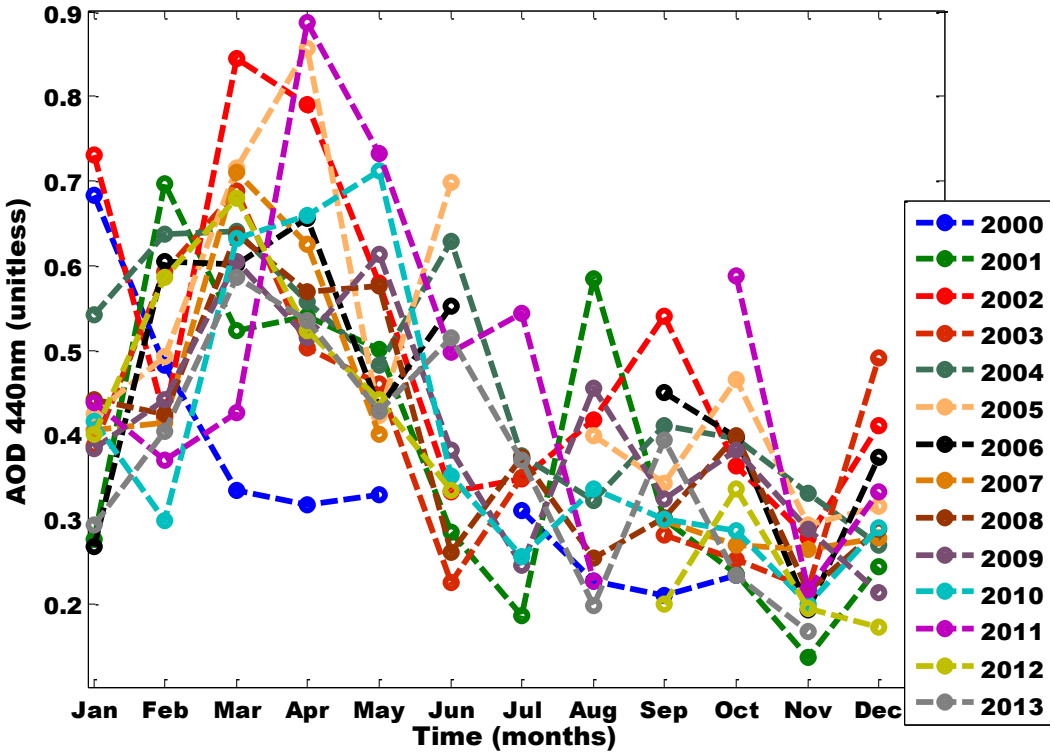

Figure 4.38: AOD pattern for Mubi (2000 – 2013)

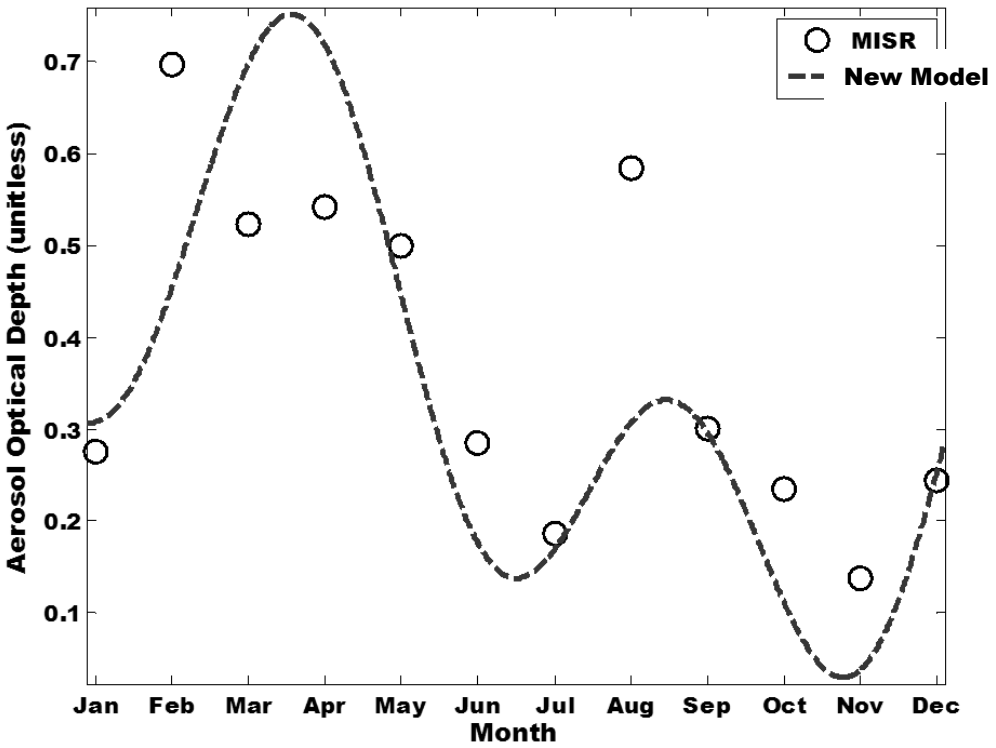

Figure 4.39a: AOD for new model and MISR for the year 2001, Mubi

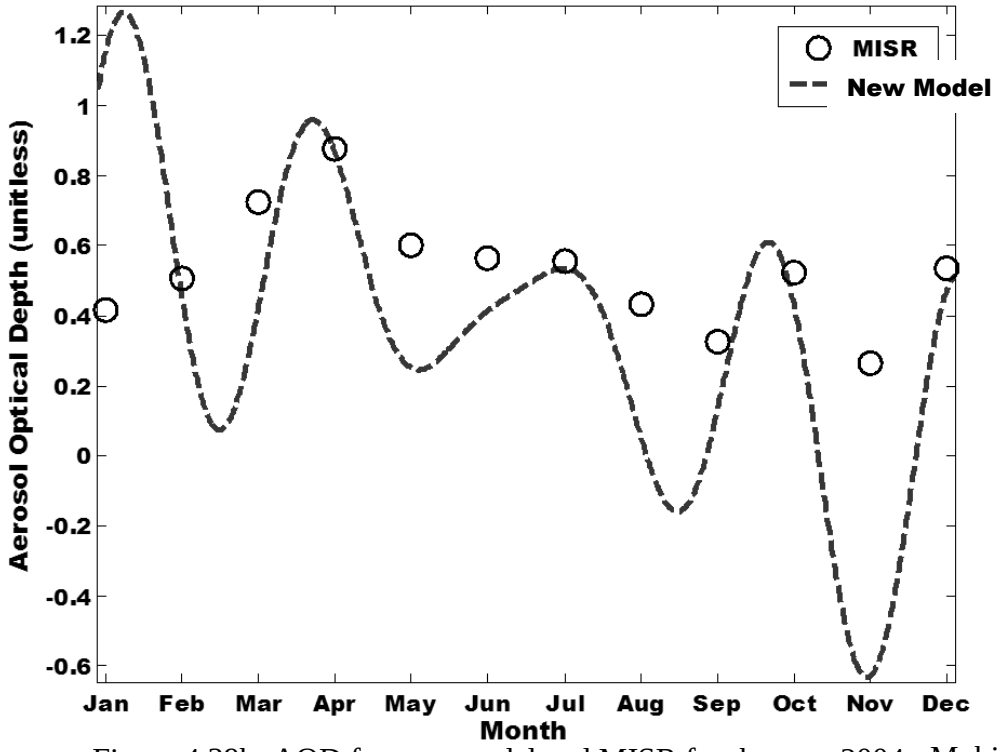

Figure 4.39b: AOD for new model and MISR for the year 2004, Mubi

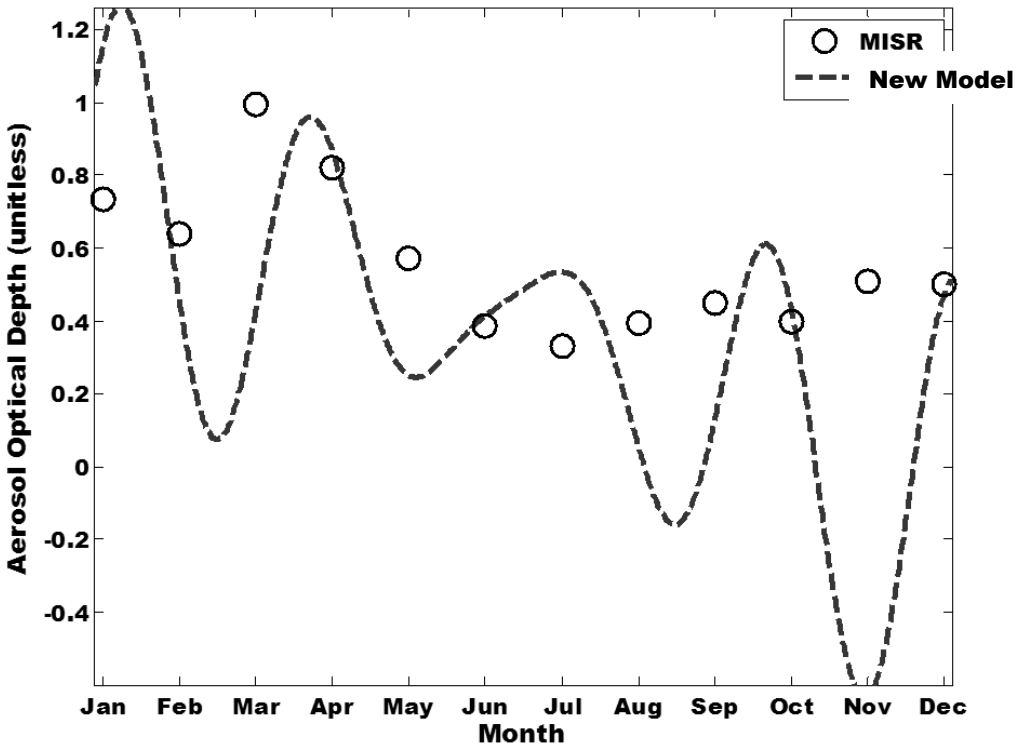

Figure 4.39c: AOD for new model and MISR for the year 2007, Mubi

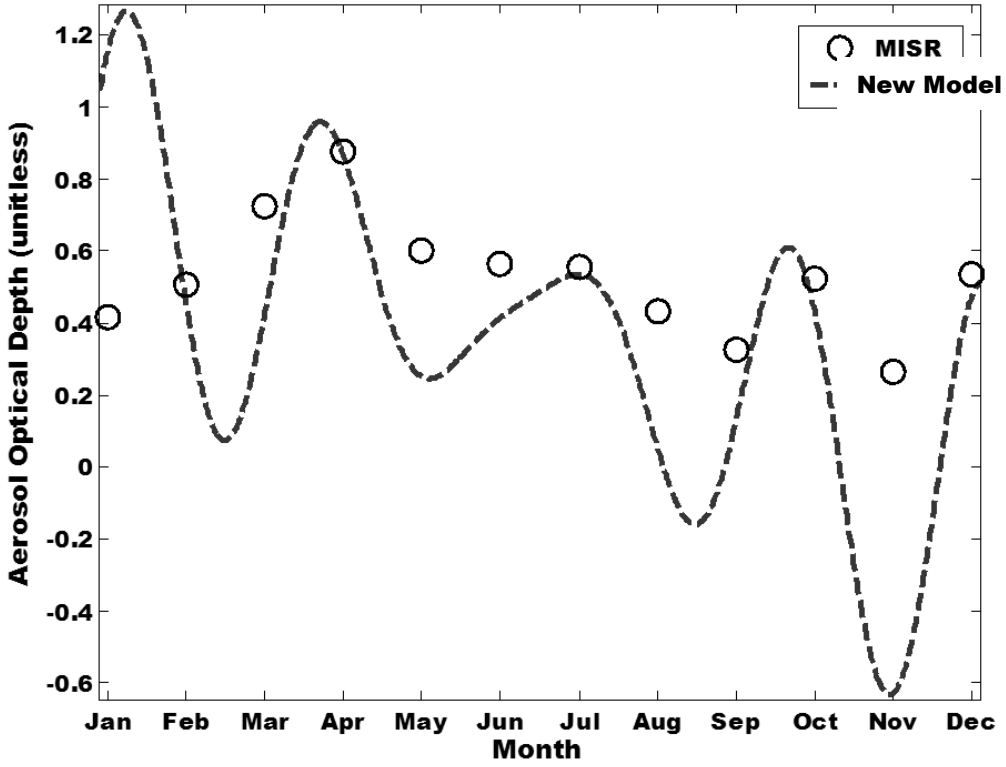

Figure 4.39d: AOD for new model and MISR for the year 2011, Mubi

The AOD retrieval data in Warri is very scanty (Figure 4.40) because of moisture content (Adebiyi et al., 2015), cloud scavenging (Dani et al., 2003), precipitable water content (Vijayakumar and Devara, 2013) and high rain drop rate (Boucher and Quaas, 2013). Adebiyi et al. (2015) reported that the moisture content in the atmosphere causes the reduction of the net maximum longwave cooling by 0.45 K day^{-1}. Moisture impact reduces the aerosols layer warming and affects AOD retrieval. Vijayakumar and Devara (2013) proposed that precipitable water content affects the concentrations of accumulation coarse mode aerosols. Boucher and Quaas (2013) propounded that rain rate affects aerosols humidification in the global circulation model. Warri is located at the coastal plain with records of massive updrafts. Unlike Lagos, the aerosols content in Warri is made up largely of tropospheric aerosols. The highest AOD data retrieval using MISR was in January (Figures 4.41a and 4.41b). No data was retrieved for the months of July and August. Therefore, it is an urgent call for the installation of ground stations in the coastal region of the South-South geopolitical zones to monitor the tropospheric aerosols. In the next section, the monitoring of aerosols using meteorological data was proposed. Also in the succeding section, the comparative performance of the proposed and MISR model was integrated into one comprehensive graph.

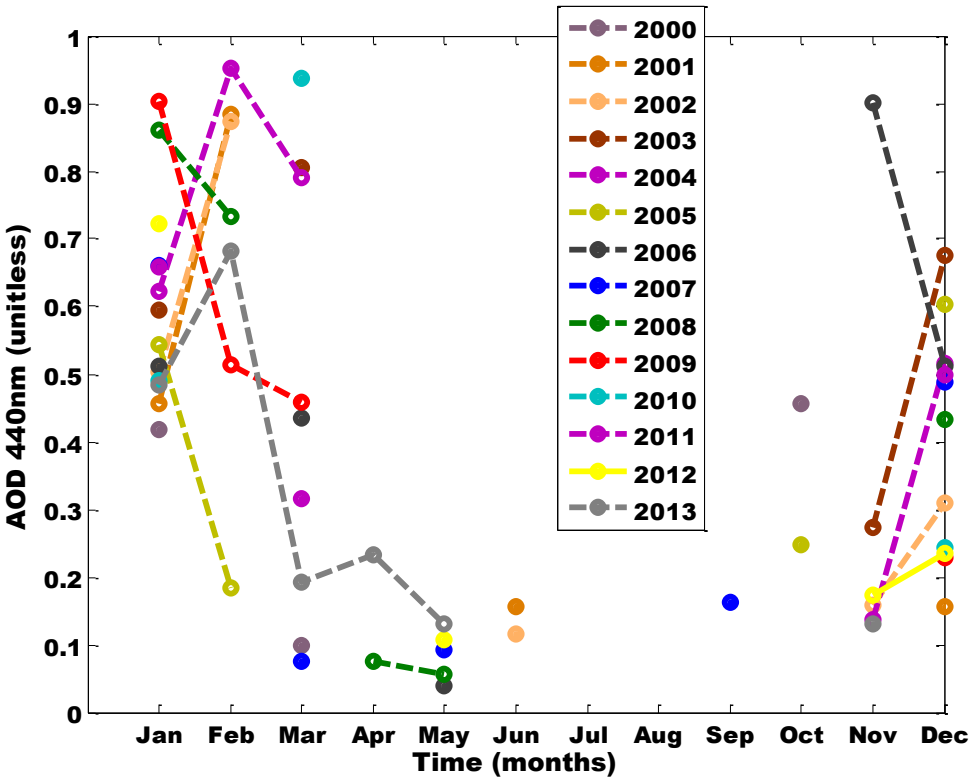

Figure 4.40: AOD pattern for Warri (2000 – 2013)

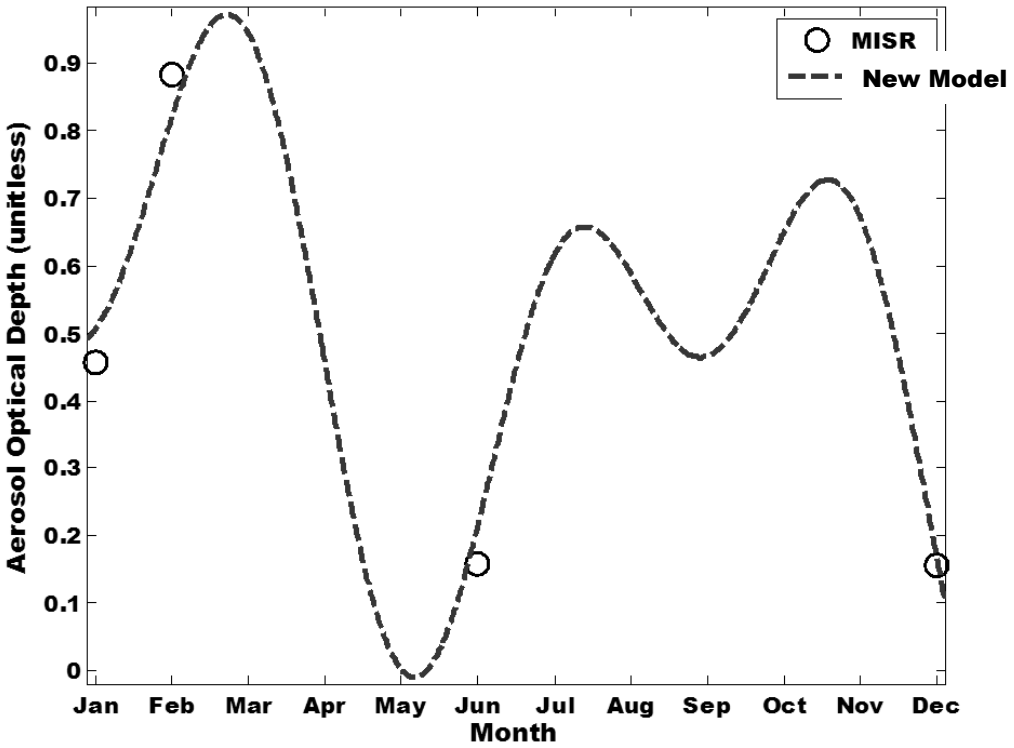

Figure 4.41a: AOD for new model and MISR for the year 2001, Warri

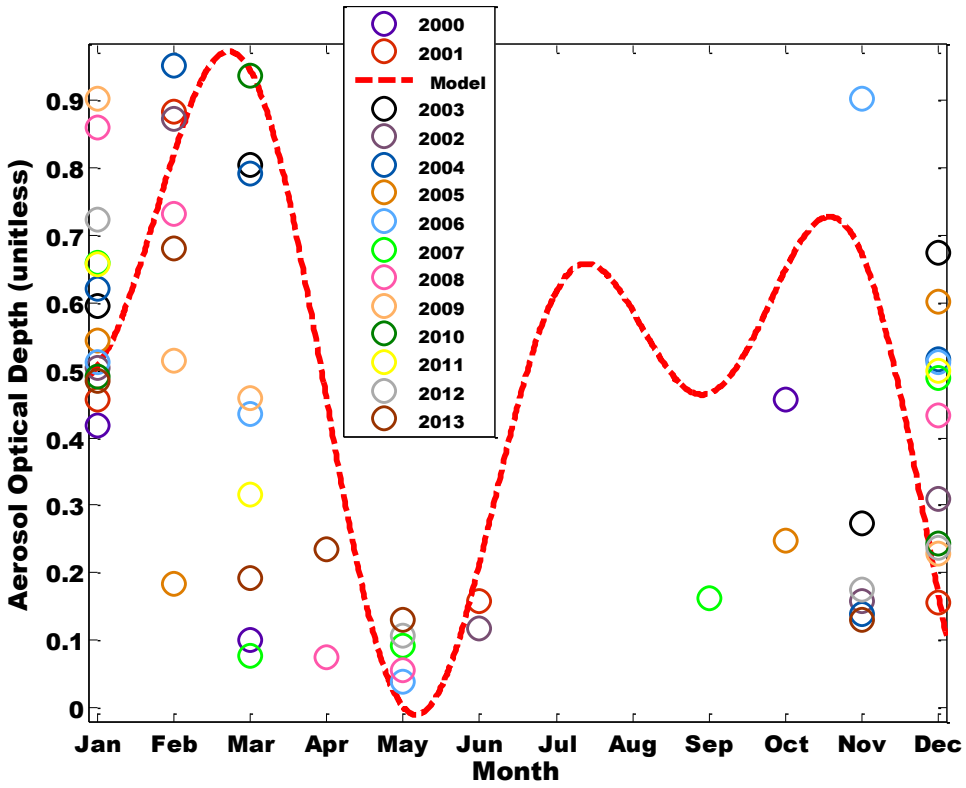

Figure 4.41b: AOD for new model and MISR for the year 2000-2013, Warri

The AOD retrieved data for Enugu is very scanty (Figure 4.42). The highest AOD retrieval was noticed in December, January and February. Like Warri, Enugu's scanty data were adduced to moisture and fog, though a theoretical approach has been proposed in this thesis towards estimating tropospheric aerosols. It is however essential to have radiosonde stations across the southern part of Nigeria. The AOD over Enugu dropped over the last five years as shown in Figures 4.43a and 4.43b. Enugu is within the humid tropical rain forest belt of Southeastern Nigeria. The statistical analysis of the proposed model in Nigeria was within 95% confidence bounds. The properties of the 'goodness of fit' for all the curves in Figure 4.43b have sum of squares due to error (SSE) of 0.006216. SSE measures the total deviation of the response values from the fit to the response values. The R-square is given as 0.9468. R-square measures how successful curve fits in explaining the variation of AOD data. From the data, it is shown that the proposed model is able to explain 94.68% of the total variation in the MISR data. This typifies that the proposed model is somewhat accurate for nowcast or forecast purposes.

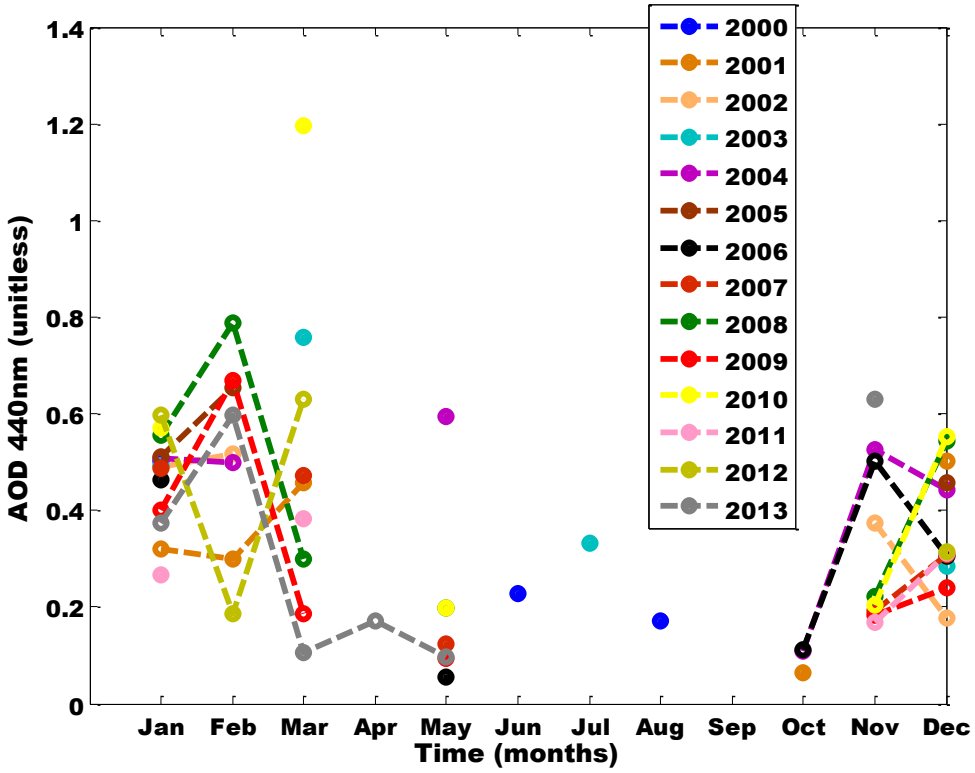

Figure 4.42: AOD pattern for Enugu (2000 – 2013)

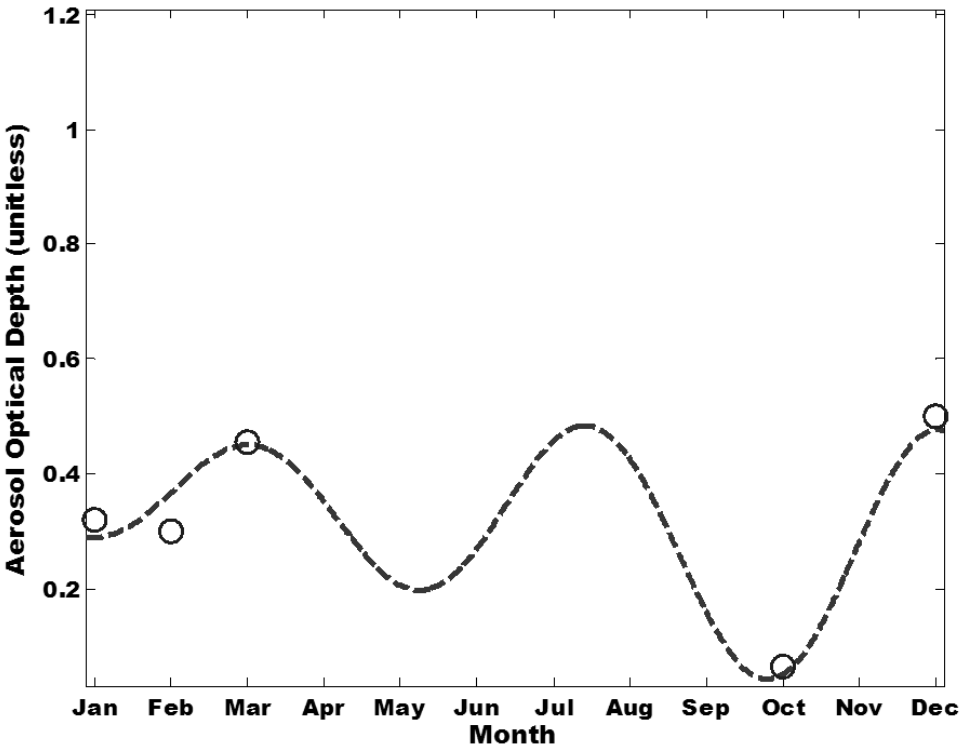

Figure 4.43a: AOD for new model and MISR for the year 2001, Enugu

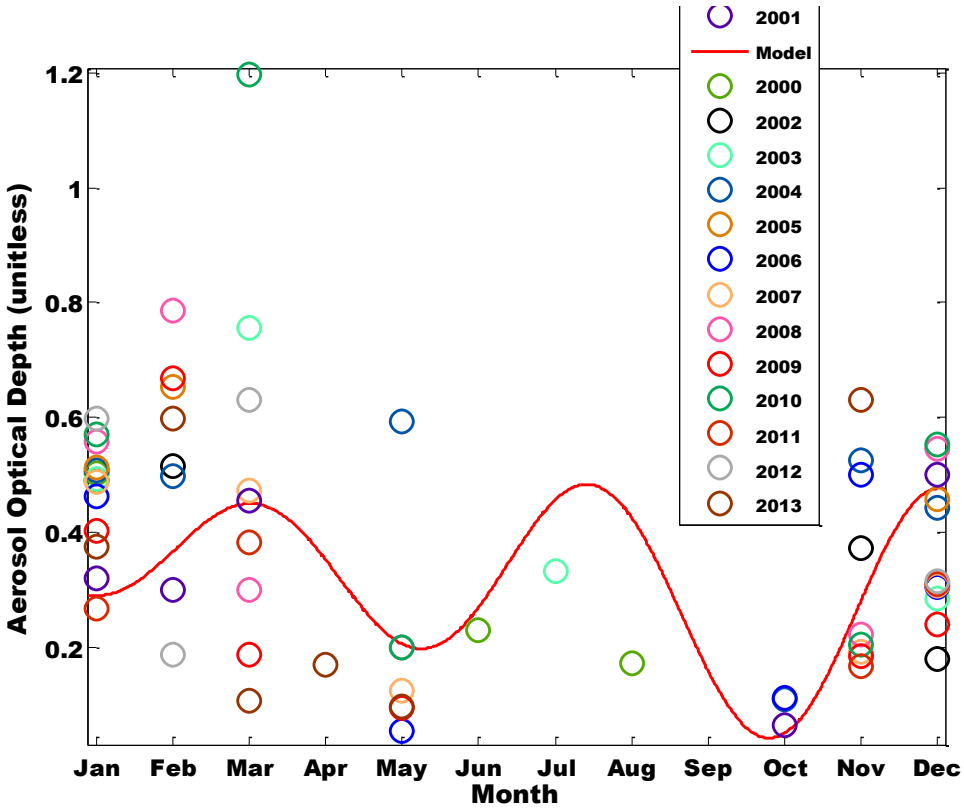

Figure 4.43b: AOD for new model and MISR for the year 2000-2013, Enugu

Ngaoundere-Cameroun has scanty data within July to September (Figure 4.44). The AOD retrieval for this period is hindered by moisture content (Adebiyi et al., 2015), cloud scavenging (Dani et al., 2003), precipitable water content (Vijayakumar and Devara, 2013) and high rain drop rate (Boucher and Quaas, 2013). The National Oceanic and Atmospheric Administration (NOAA) data set reveals that the highest precipitation over Ngaoundere is within July to September. The yearly aerosols loading is very inconsistent (Figures 4.45a and 4.45b) showing that aside the Sahara dust, the anthropogenic activities are unstable. Since Ngaoundere is located in the middle belt savannah region, its local climate and synoptic weather conditions are somewhat complex due to the north to south movement of the Intertropical Convergence Zone (Lele *et al.*, 2015).

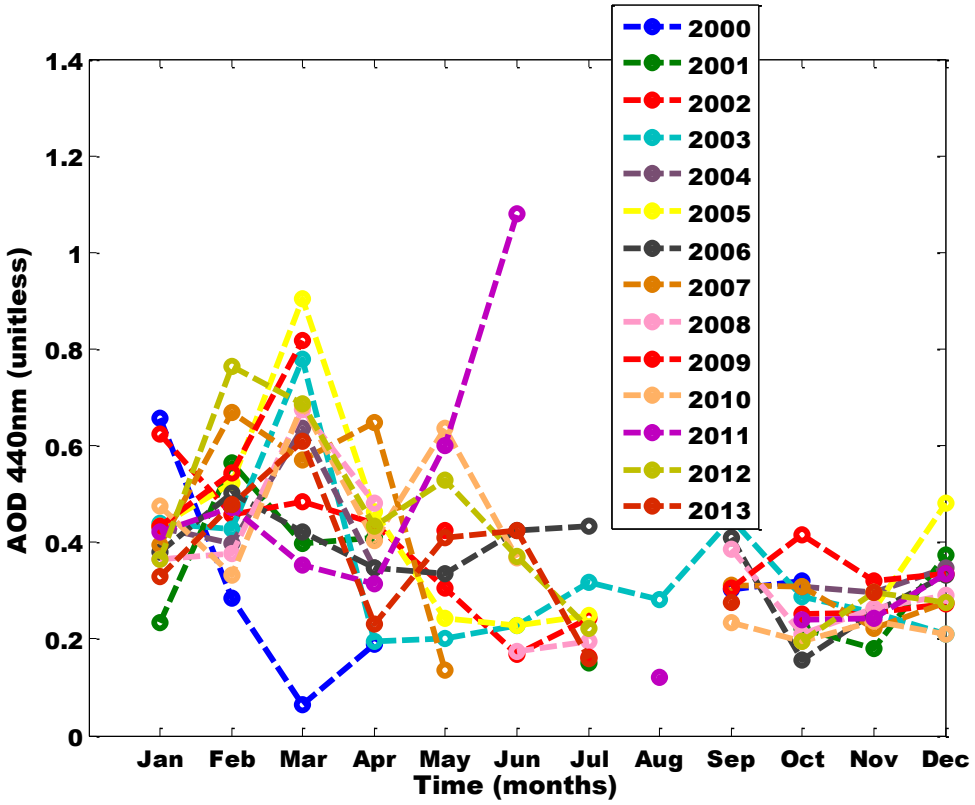

Figure 4.44: AOD pattern for Ngaoundere (2000 – 2013)

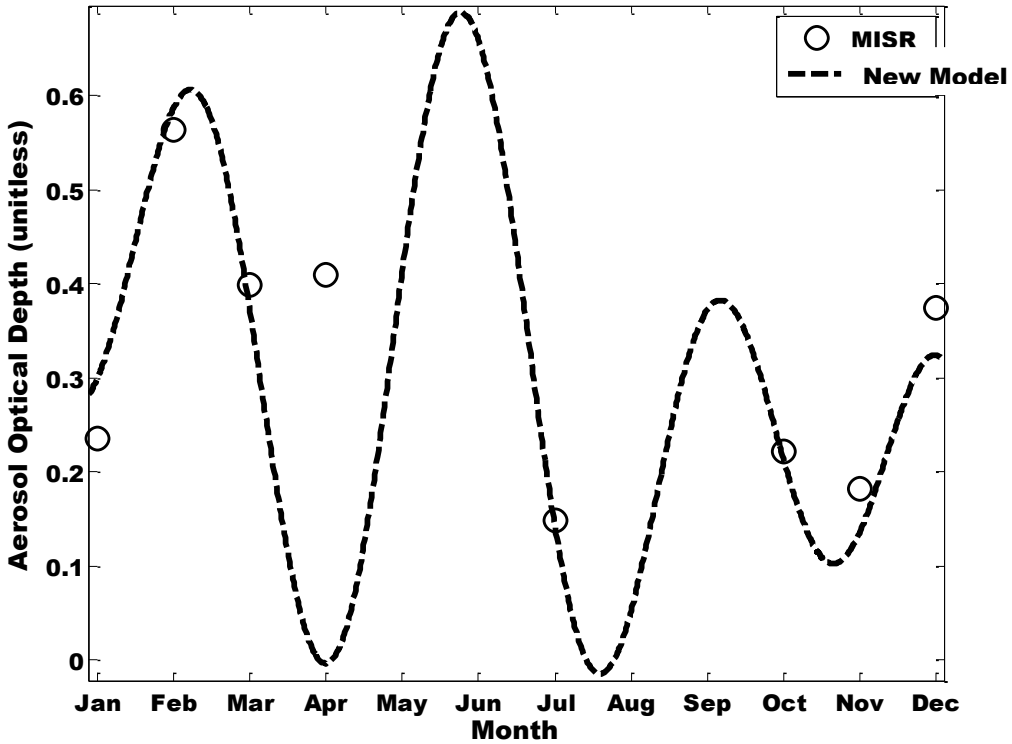

Figure 4.45a: AOD for new model and MISR for the year 2001, Ngaoundere

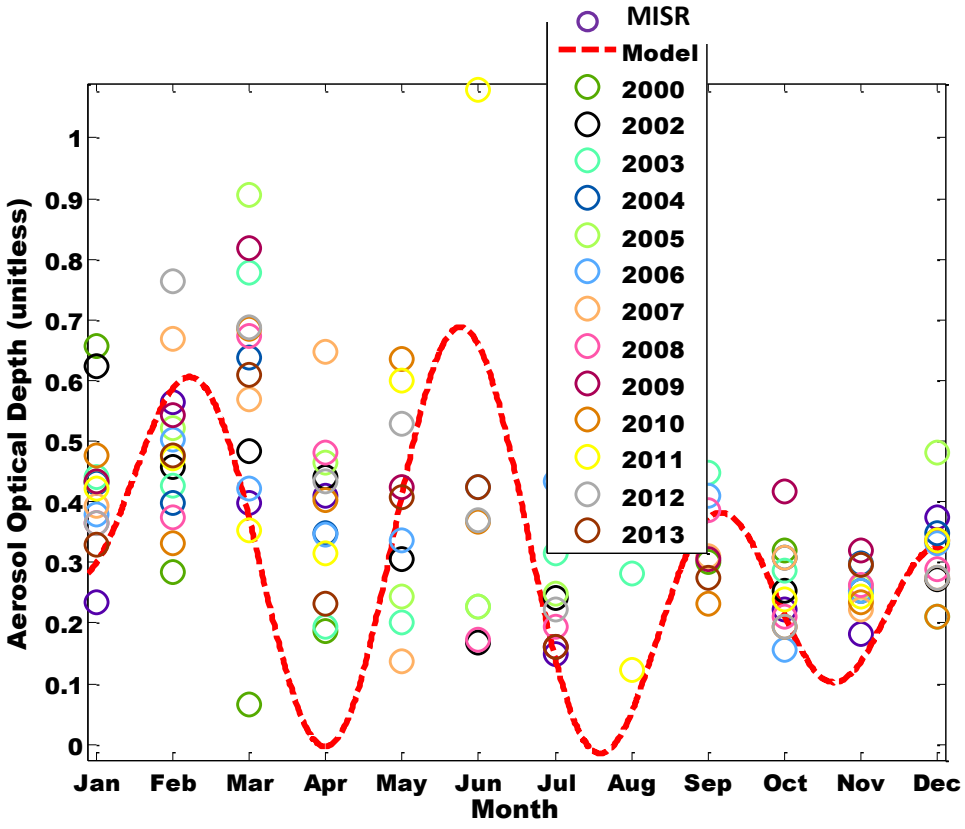

Figure 4.45b: AOD for new model and MISR for the year 2000-2013, Ngaoundere

Accra-Ghana has scanty data within June to July (Appendix II.ai). The reason may be the moisture content (Adebiyi et al., 2015), cloud scavenging (Dani et al., 2003), precipitation water content (Vijayakumar and Devara, 2013) and high rain drop rate (Boucher and Quaas, 2013). A sharp increase in aerosol loading in March, that is, leading to a decrease in succeeding months engenders a sharp decrease in October, that is, leading to an increase in aerosols loading in subsequent months. These events are very unique, that is, compared to other AOD events in other locations in West Africa. For example in 2002, the peak and low was March and October respectively, while in 2003, the peak and low was February and November. This is an evidence of aerosols accumulation in the atmosphere which results into cloud condensation nuclei (CCN) formation from the presence of Saharan dust. Bègue et al. (2015) reported the possibility of aerosols retention or accumulation in the atmosphere for a long time via a model which revealed that more than 70% of the CCN concentration observed on 30th May, 2014 can be explained by the presence of Saharan aged dust. The proposed model showed accuracy with the MISR data (Appendix II.aii and II.aii).

Bolgatanga-Ghana is located in the north of Ghana. The tendency of scanty AOD retrieval is not expected (Figure 4.46). However, there was scanty data in August when the rainfall is highest. The aerosols loading increased gradually each year due to human population until 2013 when it dropped due to rain wash in July and August (Figure 4.47a and 4.47b). The peak aerosol loading is evident in March which may have the lowest rainfall by the earlier proposition. The AOD pattern over Bolgatanga follows the gamma distribution

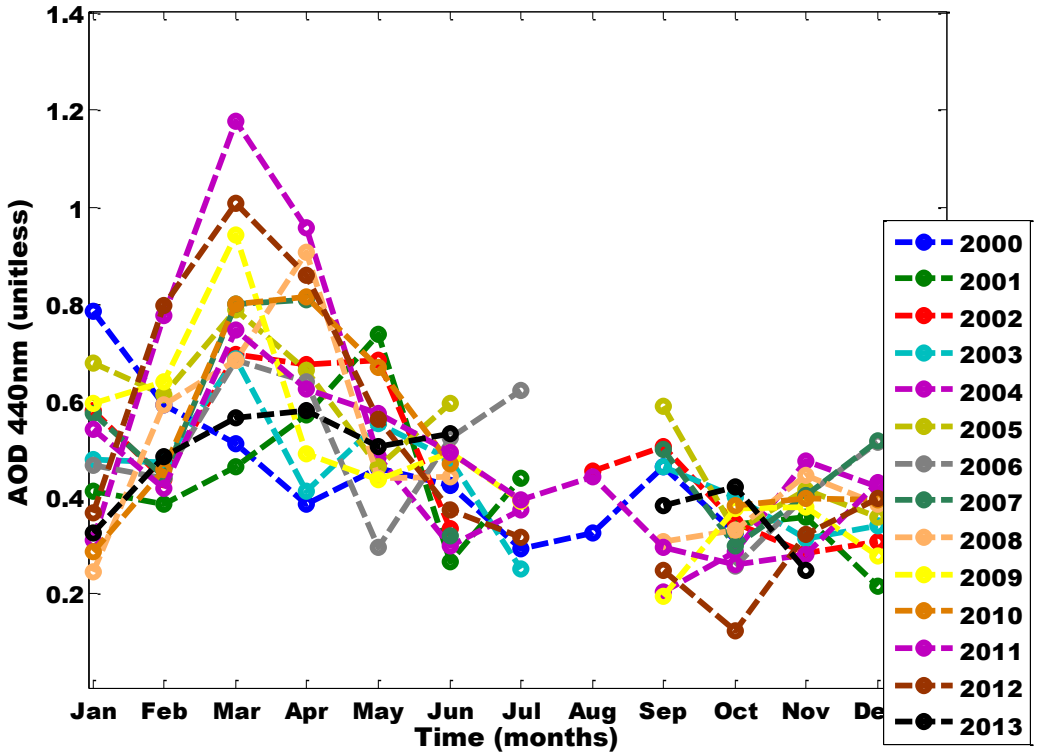

Figure 4.46: AOD pattern for Bolgatanga (2000 – 2013)

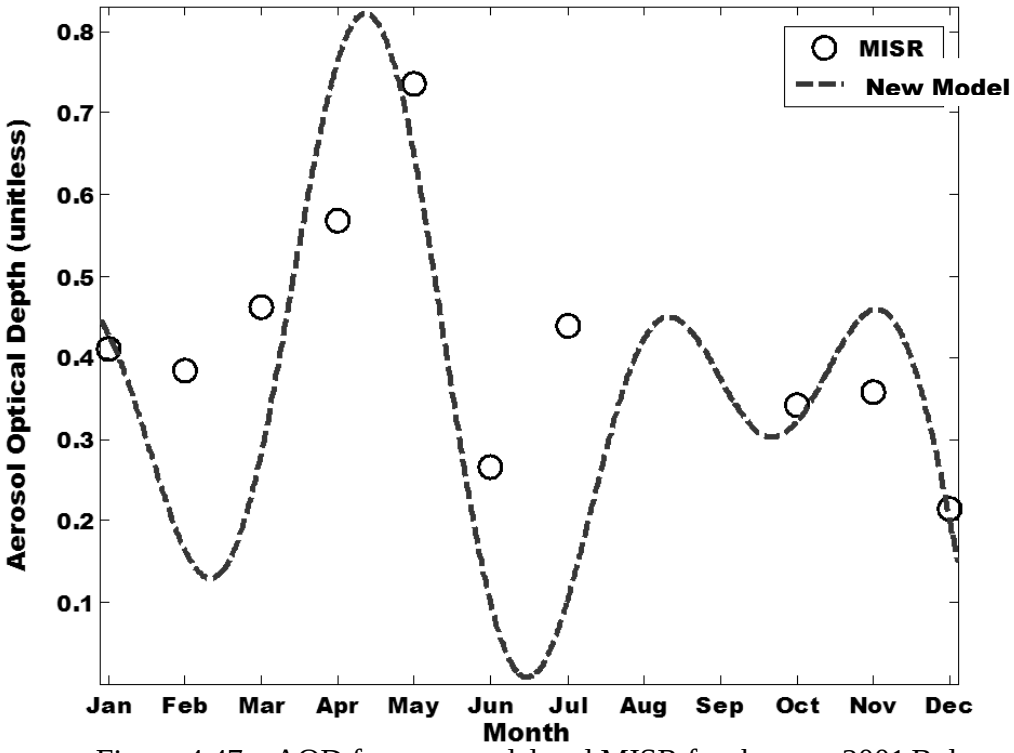

Figure 4.47a: AOD for new model and MISR for the year 2001,Bolgatanga

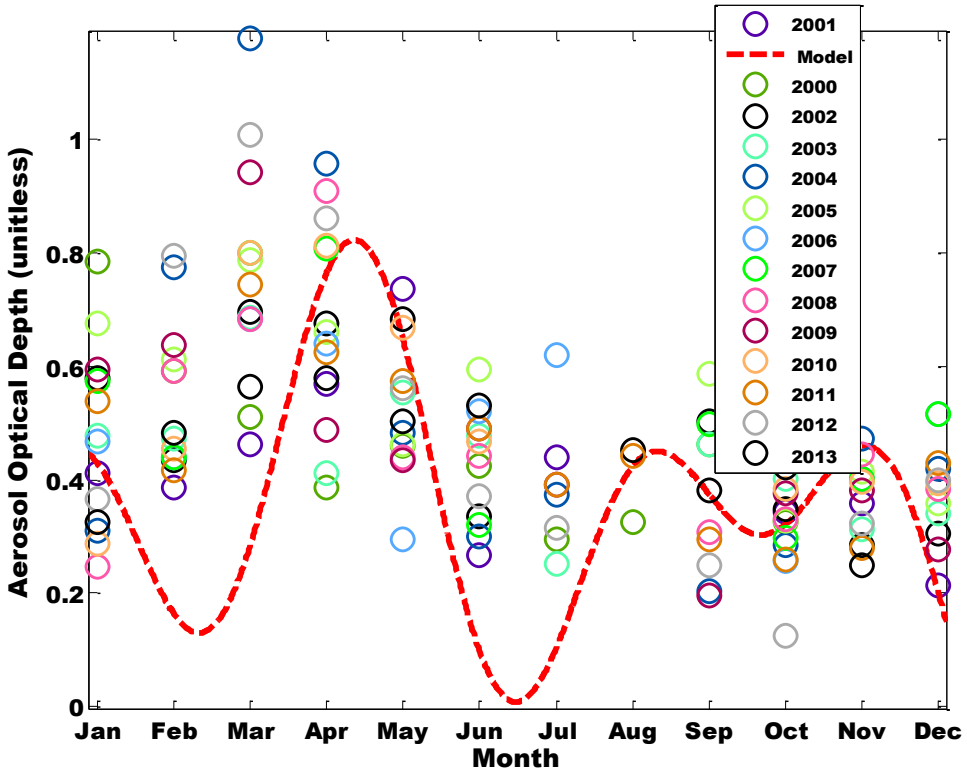

Figure 4.47b: AOD for new model and MISR for the year 2000-2013, Bolgatanga

The yearly AOD keeps dropping minutely in Ouagadougou-Burkina Faso (Appendix II.bi). Scanty AOD data was noticed in June and July due to high rainfall which led to 'rain washing'. 'Rain washing is a process where the atmosphere tries to purify itself by washing off aerosol via downpour. Since Ouagadougou is termed a hot semi-arid under Köppen-Geiger classification, it is expected that aside the anthropogenic releases from biomass, the harmattan dust from the Sahara would constantly influence its aerosols loading per year. The AOD diagram (Appendix II.bii) shows that aerosol loading kept reducing despite the increase in human activity and the constant influence of Sahara dust (Lindén et al., 2012).

The population in Ouagadougou is expected to grow from 1.9 million in 2010 to 3.4 million in 2020 (UNEP, 2011). This unique yearly reduction of AOD leads to a scientific query on the factors responsible for the reduction of the aerosols loading in 2013. There had been public awareness on preventive step towards reducing aerosols loading over the region, for example, the prevention of anthropogenic pollution in the evenings due to poor ventilation of the area (Lindén et al., 2012); the use of clean source for cooking; creating awareness on the need for populace to patronize public transport to avoid the carbon prints from automobiles. The AOD pattern perfectly agrees with the proposed model (Appendix II.biii). The only exemption was for the month of January. This feature (in January) is very unique compared to the previous locations discussed in West Africa. More preventive measures should be enforced to preserve life forms in January.

The scanty AOD data in July (Cotonou-Benin) may not be due to 'rain washing' as proposed (Appendix III.ci). UNEP (2015) clarified that there is a minor dry season from the middle of July to the middle of September. However, the minor rainy season from the middle of September to the middle of November cannot be substantiated as shown in Appendix II.cii and II.ciii. The aerosols loading in Cotonou is non-uniform because of excessive emission of anthropogenic pollution via automobiles, household generators, local cooking stoves and bush burning. Like Ouagadougou, Cotonou has poor ventilation in the evening and every particulates released into the atmosphere is localized at a particular layer. The AOD retrieval in Cotonou is very unique because despite its proximity to Atlantic Ocean and Lake Nokove, the coastal features did not influence its AOD retrieval. Secondly, like Lagos, Cotonouo is constantly influenced by oceanic trade winds, hence it can be inferred that its aerosol loadings

are majorly stratospheric (Hasebe and Noguchi, 2015). The proposed model agreed with the AOD trend in Cotonou.

In Port-Novo, the AOD trend for fourteen years follows a positive parabolic curve with minimum at the presumed raining season (Appendix II.di). Port-Novo shares the same AOD as Lagos, Nigeria. Like Cotonou, the aerosol loading in Port-Novo is unstable (Appendix II.dii and II.dii) because of excessive emission of anthropogenic pollution via automobiles, household generators, local cooking stoves and bush burning. The proposed model perfectly described the AOD over Cotonou with an accuracy of 92.69% and SSE of 1.568.

The AOD pattern in Praia-Cape Verde is normally distributed or follows a Bell curve (Appendix II.ei). It is very unique and almost similar to Sokoto-Nigeria which also has a statistical AOD gamma distribution. The maximum AOD value was found in June and July which is very different from other locations in West Africa. Also, the minimum AOD was found in January and December. From literatures, Praia has one of the strange climates globally (Unaka, 2014). For example, its rainy season can be found in May and September; and dry season at January, February, March and August. The yearly AOD output is non-uniform though it agreed with the proposed model (Appendix II.eii and II.eiii). The average aerosols loading in Praia is low compared to other locations considered. This may be because of its population

Bondokou-Cote d'ivoire has scanty AOD data from June to September (Appendix II.fi). This may be as a result of the moisture content (Adebiyi et al., 2015), cloud scavenging (Dani et al., 2003), precipitable water content (Vijayakumar and Devara, 2013) and high rain drop rate (Boucher and Quaas, 2013). The maximum AOD was found in March which is consistent with most locations in West Africa. The yearly aerosols loading is not uniform (Appendix II.fii and II.fiii) perhaps due to moderate droughts which occur frequently in Cote d'ivoire. For example, Kouadio et al. (2015) reported that the RMSE of the yearly precipitation in Bondoukou is about 80 compared to the coastal region whose value is above 100.

The AOD pattern in Abidjan has a positive parabola with the minimal in June (Figure 4.48). The yearly aerosol loading is not uniform perhaps due to moderate droughts which occur frequently in Cote d'ivoire. Hence, a percentage of the aerosol over Abidjan may be

composed of biomass burning due to the massive deforestation. It is reported that one-fifth of the land mass is cultivated (Ourafrica, 2015). The highest precipitation in Abidjan is in June (Kouadio et al., 2015) affirming the proposition made earlier. The AOD pattern over Abidjan agrees with the proposed model (Figure 4.49a and 4.49b).

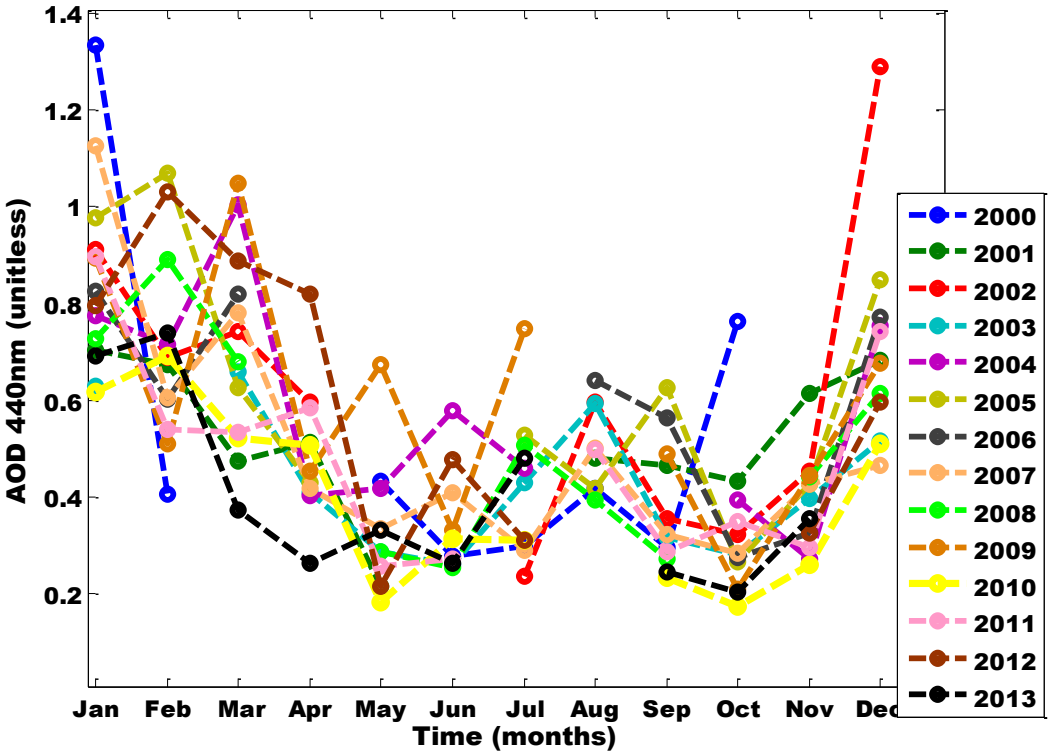

Figure 4.48: AOD pattern for Abidjan (2000 – 2013)

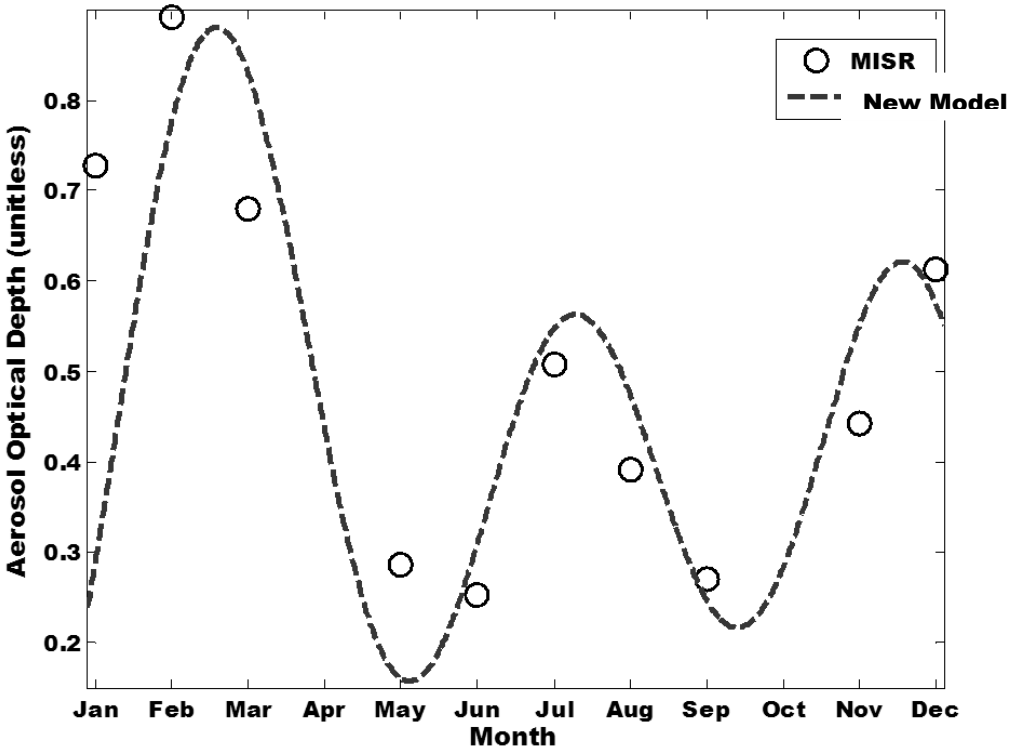

Figure 4.49a: AOD for new model and MISR for the year 2001, Abidjan

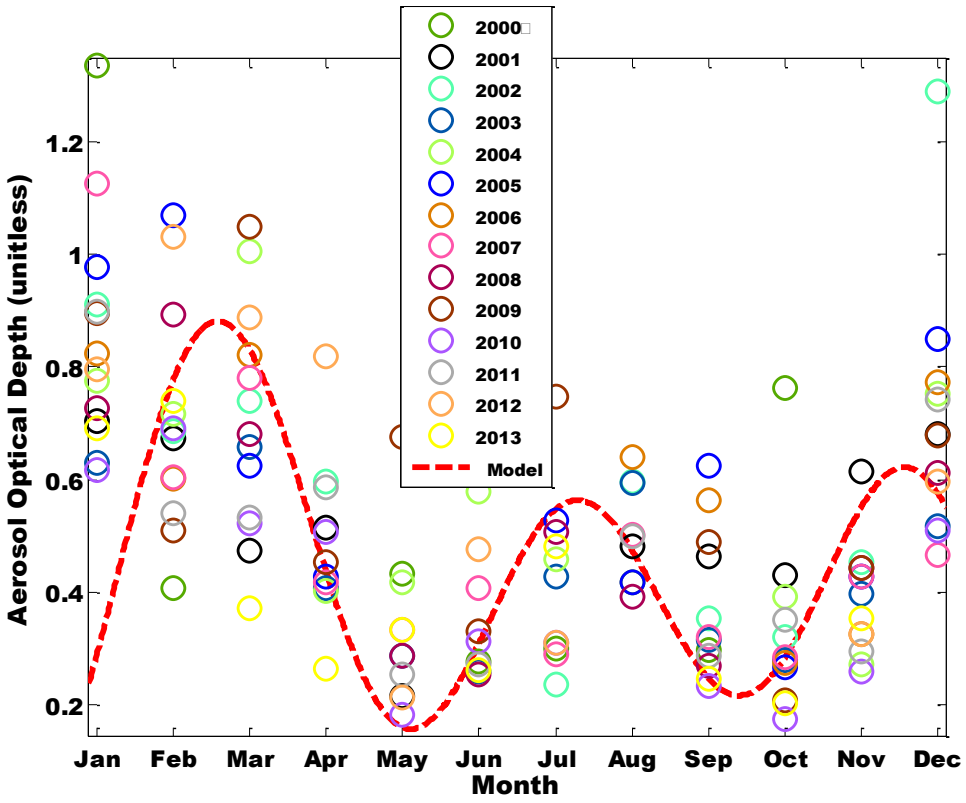

Figure 4.49b: AOD for new model and MISR for the year 2000-2013, Abidjan

The AOD pattern for Bussau was almost the same all through the year-except for the drop and scanty AOD retrieval in August (Appendix II.gi). This unusual AOD trend had brought untold hardship for the life forms, for example, a fall in agricultural, forest and grazing production as a result of no or very little rainfall from November to May every year. There are currently cases of high mortality of life forms due to malnutrition and food insecurity (UNISDR, 2007).The yearly aerosol loading is not uniform perhaps due to moderate droughts which occur frequently in Guinea Bissau and the harmattan dust which blows from Sahara. The very visible climate change influence in Bussau has attracted the aid of international community, for example, Global Environment Facility (GEF) and National Programme of Action on Adaptation to Negative Effects of Climate Changes (NAPAANECC). The AOD trend agrees with the proposed model (Appendix II.gii and II.giii).

Malabo has scanty AOD data from June to September (Appendix II.hi). This may be as a result of the moisture content (Adebiyi et al., 2015), cloud scavenging (Dani et al., 2003), precipitable water content (Vijayakumar and Devara, 2013) and high rain drop rate (Boucher and Quaas, 2013). The yearly aerosol loading is not uniform due to a lot of 'rain wash' during March, April, May, June, July, August, September and October. The driest month is February but the maximum AOD over Malabo is prominent over March. Hence, there is an evidence of aerosol accumulation in the atmosphere which encourages cloud condensation nuclei (CCN) formation of Saharan dust and an increased precipitation (Bègue et al., 2015). The AOD trend agrees with the proposed model (Appendix II.hii and II.hiii).

Like Praia and Malabo, Serekunda has almost the same AOD all through the year between 2000 and 2013 (Appendix II.i). The volume of automobiles and anthropogenic activities in Serekunda increases the carbon aerosols within its atmosphere. Since there is poor ventilation in the evening, the carbon and Sahara dust aerosols would accumulate over few months. The rainy season which runs from mid-June to October has little influence on the AOD, hence, the type of aerosols in abundance would be carbon-compound aerosols. The AOD trend agrees with the proposed model (Appendix II.ii and II.iii).

The AOD pattern in Nouakchott follows a negative parabola (Appendix II.ji). It is very unique and almost similar to Praia which has a normal AOD distribution. This type of AOD features may be because Nouakchott lies within the subtropical desert. This kind of

subtropical desert is classified as 'Köppen-Geiger' and it is characterized with low latitude arid hot climate. The maximum AOD value was found in July which is very different from other locations in West Africa. Also, the minimum AOD was found in January and December. The aerosol content of Nouakchott is constantly influenced by the harmattan dust from the Sahara. It is observed that its highest rainfall in August has little influence in reducing the aerosol content via 'rain wash'. The AOD trend perfectly agreed with the proposed model (Appendix II.jii and II.jiii).

The AOD pattern of Bamako shows a gamma distribution with the maximum in April (Appendix II.ki). The aerosol content in Bamako gradually reduced from April to December showing that almost same kind of aerosol physical properties exist in Bamako and Sokoto. Bamako and Sokoto are located on the same tropical savanna climate, so it is expected that they both possess almost the same AOD pattern. Bamako has dry winters with constant influence of harmattan dust. Out of fourteen years data, three years 2004, 2010 and 2012 had their maximum in March. The AOD pattern over Bamako agreed with the proposed model (Appendix II.kii and II.kiii).

Monrovia has the highest cases of scanty data in the locations considered (Figures 4.50 and 4.51a). There were little or no data from March to November. Since Monrovia falls within the tropical monsoonal climate, the scanty AOD data may be as a result of the moisture content (Adebiyi et al., 2015), cloud scavenging (Dani et al., 2003), precipitable water content (Vijayakumar and Devara, 2013) and high rain drop rate (Boucher and Quaas, 2013). The Tropical Rainfall Measuring Mission (TRMM) layer 3 observations in Figure 4.51b show the daily rain rate in Monrovia for the year 2012. Figure 4.51c shows a monthly rain rate analysis. Hence, it can be affirmed that the scanty AOD data was as a result of the rain rate that is higher within May and October as shown in Figure 4.51c. The AOD pattern over Monrovia agreed with proposed model (Figure 4.51a). Monrovia is constantly under the oceanic wind influence from the Atlantic oceanic. The retrieved AOD may not capture salient events in the lower atmosphere; hence, a radiosonde station is essential in Monrovia to adequately capture the inadequacies in its lower atmosphere.

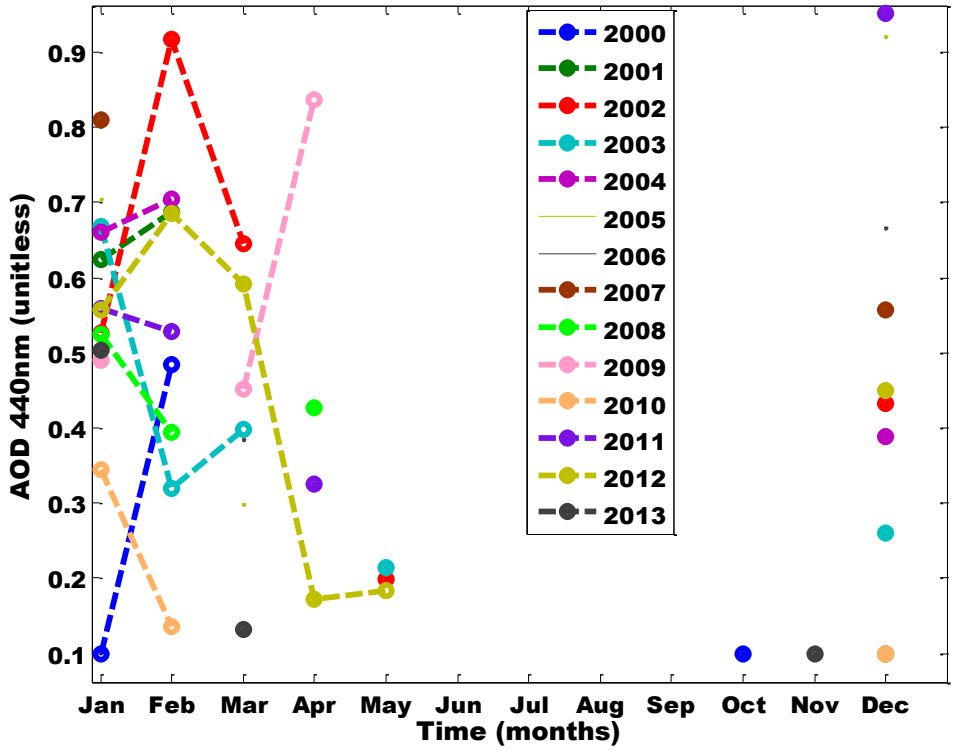

Figure 4.50: AOD pattern for Monrovia (2000 – 2013)

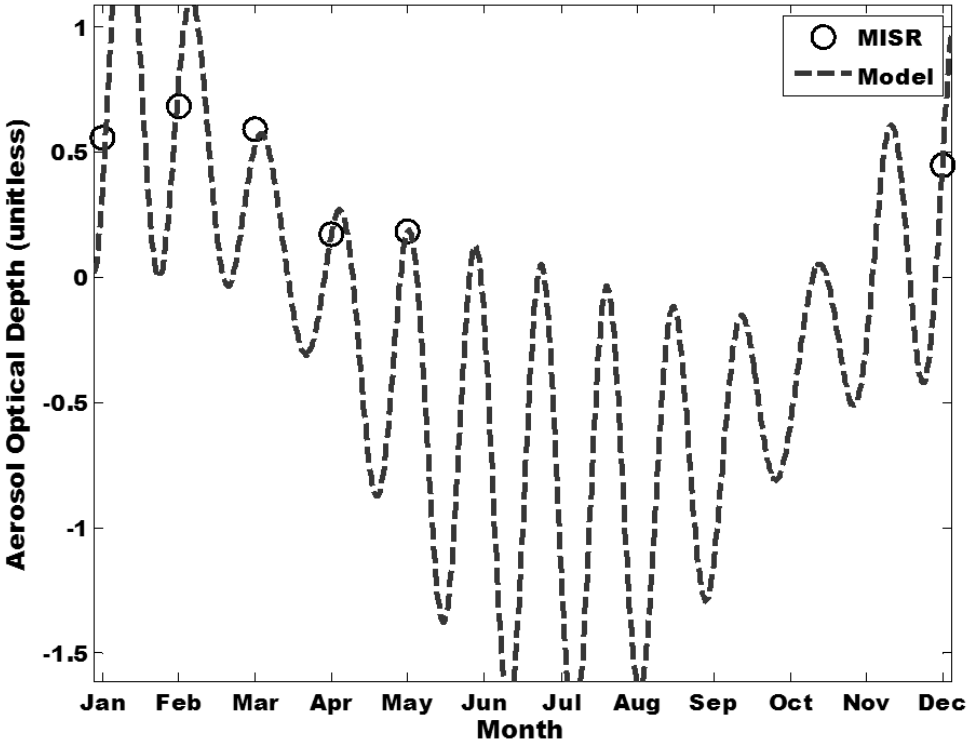

Figure 4.51a: AOD for new model and MISR for the year 2001, Monrovia

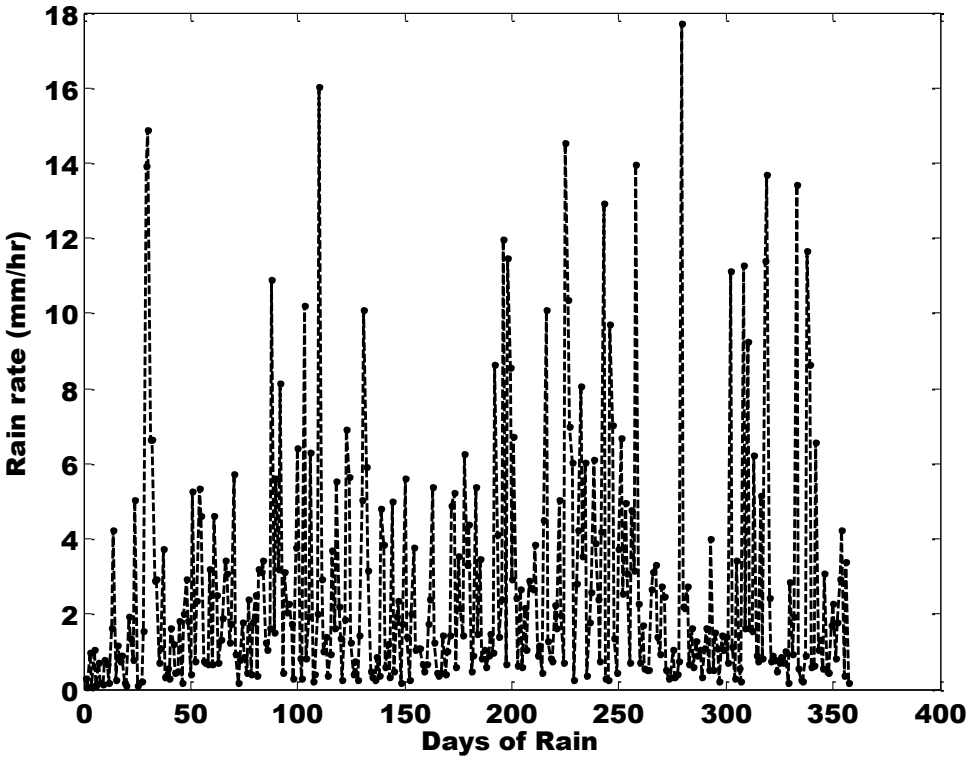

Figure 4.51b: Daily Precipitation rate over Monrovia 2012

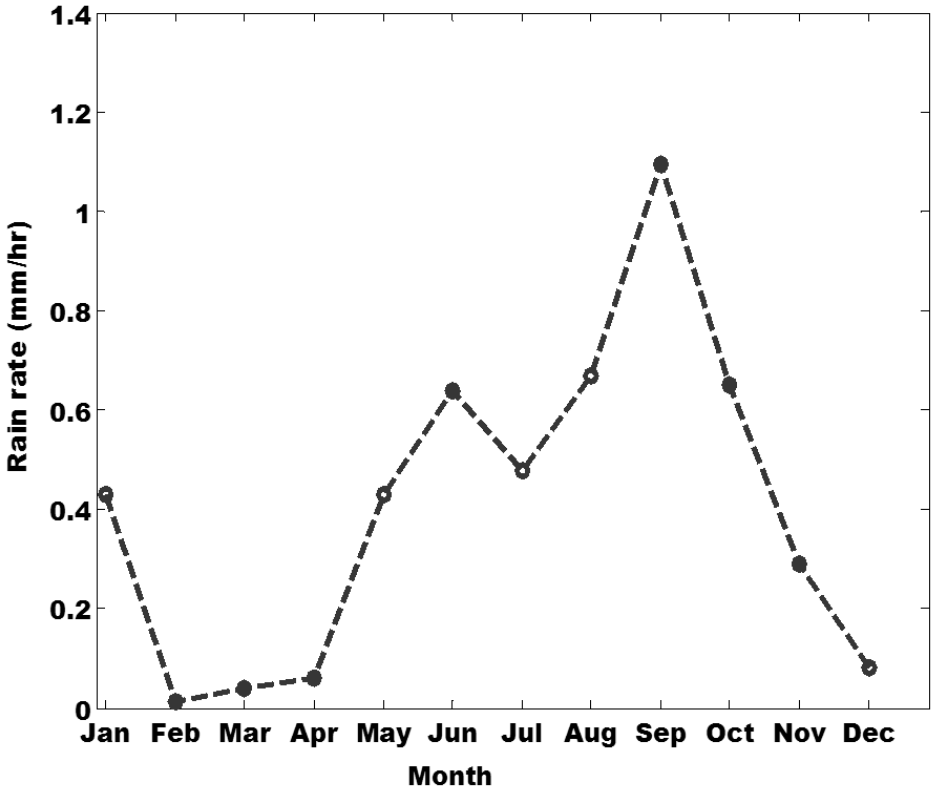

Figure 4.52c: Monthly Precipitation rate over Monrovia 2012

The aerosols loading over Conakry fluctuates on yearly bases in the last six years (Appendix II.li). For example, in 2010 and 2012 the aerosols loading was high while in 2011 and 2013 the aerosols loading was low. These results may emanate from the variation in southwesterly wind which extends from June to November and the northeasterly harmattan dusty wind that extends from December to May. There was no AOD data retrieved for the month of July. NOAA data set reveals that the highest precipitation over Conakry is found in July. Therefore, Conakry AOD feature obeys the proposition made earlier. The AOD trend in Conakry is in agreement with the proposed model (Appendix II.lii and II.liii).

The AOD pattern of Niamey shows a gamma distribution with the maximum in March (Appendix II.mi). The aerosol content in Niamey gradually reduced from March to December showing that almost same kind of aerosol physical properties exist in Niamey, Bamako and Sokoto. The three locations are within the same tropical savanna climate, so it is expected that they possess almost same AOD pattern. Niamey has hot semi-arid steppe climate with constant influence of harmattan dust. Its highest precipitation is recorded in July and August. However, this had very little influence over AOD. Hence, the volume of other types of aerosols from anthropogenic activities is high compared to the harmattan dust accumulation in the atmosphere. The AOD trend in Niamey is in agreement with the proposed model (Appendix II.mii and II.miii). However, the multi phase examination of the Niamey AOD data was used to ascertain the atmospheric constant on a yearly basis (Appendix Ia).

Lome has scanty AOD data especially from June to September (Appendix II.ni). Since Lome falls within the tropical monsoonal climate, the scanty AOD data may be as a result of the moisture content (Adebiyi et al., 2015), cloud scavenging (Dani et al., 2003), precipitable water content (Vijayakumar and Devara, 2013) and high rain drop rate (Boucher and Quaas, 2013). The scanty AOD falls within the two rainy seasons in Lome, that is, the first rainy season is from April to July while the second rainy season starts in early September to late November. Hence, the proposition holds in Lome. The AOD pattern over Lome agreed with proposed model (Appendix II.nii and II.niii). The yearly aerosols loading are unstable.

The AOD pattern in Dakar follows a negative parabola like Nouakchott (Appendix II.oi). It is very unique and almost similar to Praia which has a normal AOD distribution. This type of AOD features may be because Dakar has hot semi-arid steppe climate with a short rainy

season and a lengthy dry season. This means that Dakar's aerosol loading would constantly be under the influence of the northeast winds. The AOD pattern over Dakar agreed with the proposed model (Appendix II.oii and II.oiii) except for the month of August where an excess drop beyond the observed data was noticed. The yearly aerosols loading are unstable due to uncontrolled anthropogenic activities.

Binkolo has scanty AOD data especially from June to September (Appendix II.pi). The scanty AOD data may be as a result of the moisture content (Adebiyi et al., 2015), cloud scavenging (Dani et al., 2003), precipitable water content (Vijayakumar and Devara, 2013) and high rain drop rate (Boucher and Quaas, 2013). The AOD pattern over Binkolo agreed with proposed model (Appendix II.pii and II.piii). The yearly aerosols loading are unstable due to uncontrolled anthropogenic activities.

Younde-Cameroun has more scanty data than Ngaoundere (Appendix III.qi). Ngaoundere is at the northern part of Younde. Younde lies within a tropical wet and dry climate. Hence more moisture content (Adebiyi et al., 2015), cloud scavenging (Dani et al., 2003), precipitation water content (Vijayakumar and Devara, 2013) and high rain drop rate (Boucher and Quaas, 2013) is expected to reduce the AOD retrieval. Since the scanty AOD data is noticed from May to October (a period of highest precipitation), it is uncertain to propose from the NOAA precipitation data set that AOD is proportional to the average precipitation over an area. The proposed model perfectly described the AOD over Cameroun with an accuracy of 91.78% and SSE of 0.08422 (Appendix III.qii and III.qiii).

The cumulative atmospheric constants for locations around West Africa for fourteen years analysis are shown in Appendix Ib. The atmospheric constants can be calculated on a yearly basis. This hypothesis was carried out using Niamey-Niger as a case study because it has large volumes of ground and satellite data set (Appendix Ia). Also, Niamey was the location that had the highest volume of satellite AOD retrieval. On the average, the atmospheric constant for Niamey-Niger for fourteen years is a_1 = 0.77975, a_2 = 0.693021, n_1 = 0.140187 and n_2 = 0.759236.

It should be noted that from equation (3.99), the nth-terms ranges from a_1 to a_n and n_1 to n_n. In this study, two terms were considered out of the nth-terms, hence, a_1, a_2 and n_1, n_2. The α

and β are the same althrough the computational process. a_1, a_2 are the atmospheric constants and n_1, n_2 are the tuning constants. Both parameters are dimensionless. The significance of various constants and the role they play when their value is inserted into the compact flash of the weather station or satellite sensor is discussed. One of the constant examined in Table 4.3 is the phase difference. Phase difference is the difference in degrees or time between two or more signals having the same frequency and referenced to the same point in time. This parameter guides the installation of ground stations dedicated to examining atmospheric profiles. It may also apply to satellite sensor positioning for maximum data retrieval.

Table 4.3: Grouping of atmospheric constants for locations in West Africa

Location	a_1	a_2	n_1	n_2	α	**B**
			Nigeria			
Abuja	0.5421	0.8616	0.3271	0.5365	$\frac{\pi}{4}$	$\frac{\pi}{4}$
Lagos	1.175	0.8227	0.2926	0.3573	$\frac{\pi}{2}$	$\frac{\pi}{2}$
Sokoto	0.5754	1.027	0.4342	0.6663	$\frac{\pi}{6}$	$\frac{\pi}{6}$
Ilorin	0.9315	0.7322	0.3482	0.2994	$\pm\frac{\pi}{2}$	$\pm\frac{\pi}{2}$
Kano	0.708	0.8984	0.3173	0.3863	$\pm\frac{\pi}{2}$	$\pm\frac{\pi}{2}$
Mubi	0.6085	0.6326	0.07197	0.1748	$\pm\frac{\pi}{4}$	$\pm\frac{\pi}{4}$
Warri	0.7058	0.7633	0.1151	0.2141	$\pm\frac{\pi}{4}$	$\pm\frac{\pi}{4}$
Enugu	0.6563	0.5422	0.1711	0.1889	$\pm\frac{\pi}{4}$	$\pm\frac{\pi}{4}$
			Cameroun			
Ngaoundere	0.6782	0.542	0.1798	0.2618	$\pm\frac{\pi}{4}$	$\pm\frac{\pi}{4}$
Younde	0.8659	0.9423	0.1548	0.09207	$\pm\frac{\pi}{4}$	$\pm\frac{\pi}{4}$
			Ghana			
Accra	0.7545	0.7332	0.3224	0.1946	$\frac{\pi}{2}$	$\frac{\pi}{2}$
Bolgatanga	0.667	0.6403	0.242	0.1515	$\pm\frac{\pi}{4}$	$\pm\frac{\pi}{4}$
			Burkina Faso			
Ouagadougou	0.626	0.7999	0.09835	0.266	$\pm\frac{\pi}{4}$	$\pm\frac{\pi}{4}$
			Benin			
Cotonou	0.7602	0.81	0.185	0.1304	$\pm\frac{\pi}{2}$	$\pm\frac{\pi}{2}$
Port Novo	1.245	3.702×10^{-6}	2.096	-0.3105	$\pm\frac{\pi}{8}$	$\pm\frac{\pi}{8}$

Group 1
Group 2
Group 3
Group 4
Group 5
Group 6
Group 7
Group 8
Group 9

Cape Verde						
Praia	0.6645	0.7712	0.08138	0.3432	0	0
Cote D' ivoire						
Boundokou	0.6839	0.6842	0.2075	0.1044	$\pm\frac{\pi}{2}$	$\pm\frac{\pi}{2}$
Abidjan	0.5822	0.7758	0.1795	0.1277	$\pm\frac{\pi}{2}$	$\pm\frac{\pi}{2}$
Guinea Bissau						
Bussau	0.6135	0.6694	0.1354	0.347	$\frac{\pi}{4}$	$\frac{\pi}{4}$
Equatorial Guinea						
Malabo	0.4393	0.8158	0.1795	0.08748	$\pm\frac{\pi}{2}$	$\pm\frac{\pi}{2}$
Gambia						
Serekunda	0.6718	0.7178	0.3608	0.3009	0	0
Mauritania						
Nouakchott	0.9442	0.8131	0.4369	0.08213	$\pm\frac{\pi}{8}$	$\pm\frac{\pi}{8}$
Mali						
Bamako	0.7616	0.6676	-0.04547	0.8321	$\frac{\pi}{3}$	$\frac{\pi}{3}$
Liberia						
Monrovia	0.771	1.11	0.9534	1.08	$\pm\frac{\pi}{2}$	$\pm\frac{\pi}{2}$
Guinea						
Conakry	0.7575	0.7176	0.3618	0.2351	0	0
Niger						
Niamey	0.7082	0.8279	0.1809	0.2384	$\pm\frac{\pi}{6}$	$\pm\frac{\pi}{6}$
Togo						
Lome	0.621	0.7398	0.1997	0.2936	$\frac{\pi}{6}$	$\frac{\pi}{6}$
Senegal						
Dakar	0.6187	0.7055	0.1682	0.3639	0	0

Sierra Leone						
Binkolo	0.6378	0.7898	0.2192	0.272	$\frac{\pi}{6}$	$\frac{\pi}{6}$

From Table 4.3, it is easy to categorize the locations according to the colour codes, for instance, the phase difference in Abuja and Bussau are categorized as Group 1 $\left(\frac{\pi}{4}\right)$. This means that the configuration of the given phase difference into the flash card of the measuring instruments would enable its sensors to capture the aerosol optical depth adequately all year round. Lagos and Accra are categorized as Group 2 $\left(\frac{\pi}{2}\right)$. Ilorin, Kano, Cotonou, Bondougou, Abidjan and Malabo are categorized as Group 3 $\left(\pm\frac{\pi}{2}\right)$. Sokoto is categorized as Group 4 $\left(\frac{\pi}{6}\right)$. Mubi, Warri, Enugu, Ngaoundere, Younde, Bolgatanga and Ouagadougou are categorized as Group 5 $\left(\pm\frac{\pi}{4}\right)$. Port-Novo and Nouakchott are categorized as Group 6 $\left(\pm\frac{\pi}{8}\right)$. Praia, Serekunda and Conakry is categorized as Group 7 (0). Bamako is categorized as Group 8 $\left(\frac{\pi}{3}\right)$. Niamey, Lome and Binkolo are categorized as Group 9 $\left(\pm\frac{\pi}{6}\right)$. Out of all the groups, only Group 7 requires no phase difference adjustment.

The tuning constants n_1 and n_2 moderate the signaling angular positions. From the colour coding of n_1 and n_2 column, it can be observed that the tuning constants are dynamic for most locations except Kano, Enugu, Cotonou, Abidjan, Serekunda, Monrovia and Binkolo. The turbulence in the lower atmosphere of these locations is more stable than other locations. From the two parameters considered, which are phase difference (α, β) and tuning constants (n_1, n_2), it may be too early to infer that Serekunda is the most stable of all the West Africa locations as far as aerosols loading is concerned. Hence, it is paramount to observe the atmospheric constants for a more suitable conclusion.

The atmospheric constants a_1 and a_2 which moderates the transmitted or received signals in accordance to the actual aerosol loading over a geographical area is illustrated in Table 4.3. Also, from the colour coding of a_1 and a_2 column, it can be observed that the atmospheric constants are dynamic for most locations except Conakry, Bussau, Bondoukou, Bolgatanga, Accra and Warri. Upon the outcome of the three parameters (atmospheric constant, tuning constant and phase difference), it is logical to conclude that the lower atmosphere of West Africa is very dynamic and any measuring devices adapted should be calibrated to follow the recommended constants as suggested in this research.

4.7 A Technique of Determining AOD using Meteorological Measurement in Selected Locations of West Africa

One of the objectives of this study is that a theoretical approach would be enacted to estimate aerosols loading over an area using meteorological data set. In this section, the first supportive model was illustrated which entails retrieving aerosols data set through meteorological parameters. For this illustration, six locations were considered across the 335 × 230 km^2 area (see Table 3.2). The data for Ondo-Ondo state, Lagos-Lagos state, Ibadan-Oyo state, Abeokuta-Ogun state, Ilorin-Kwara state and Osogbo-Osun state was obtained from the Nigeria Meteorological Agency. The technique adopted for this section deals with the use of mathematical expression to compute colours generated from satellite or ground data set. However, the success of the technique depends on the parameter associated with the AOD. Another advantage of this technique is its applicability to discover other environmental force aside AOD.

In this section, it is proposed that few parameters can be used to determine AOD pattern over a geographical location. The parameters include minimum temperature, relative humidity, cloud cover and rainfall. The minimum temperature is important to this study because it is measured at the lowest temperature layer called Ramdas layer. This parameter expresses the aerosol microphysical properties and transport. Another parameter is the cloud cover. This is the portion/fraction of the sky obscured by clouds which defines the interaction of thermal radiation effects on atmospheric aerosols. Most clouds owe their existence to aerosols. Another parameter proposed is relative humidity. It is define as the measure of the amount of moisture in the air relative to the total amount of moisture the air can hold. Rainfall was also proposed as one of the parameter because aerosols have effects on clouds and precipitation. The parameters were plotted with adequate reference to the satellite AOD imagery as shown in Figures 4.31a to 4.31d.

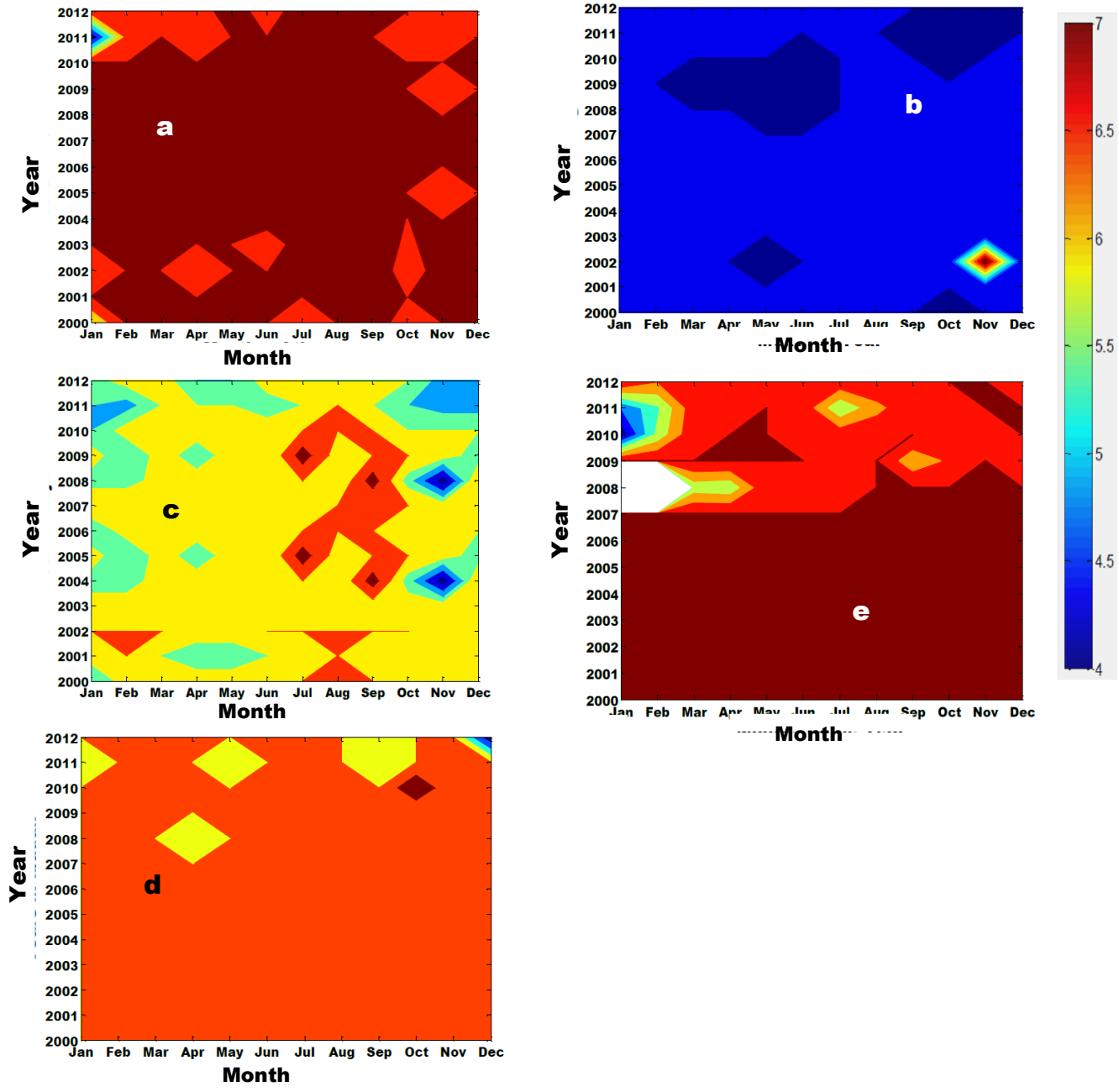

Figure 4.52: The cloud cover over five locations (a) Ilorin (b) Oshogbo (c) Lagos (d) Ibadan (e) Ondo

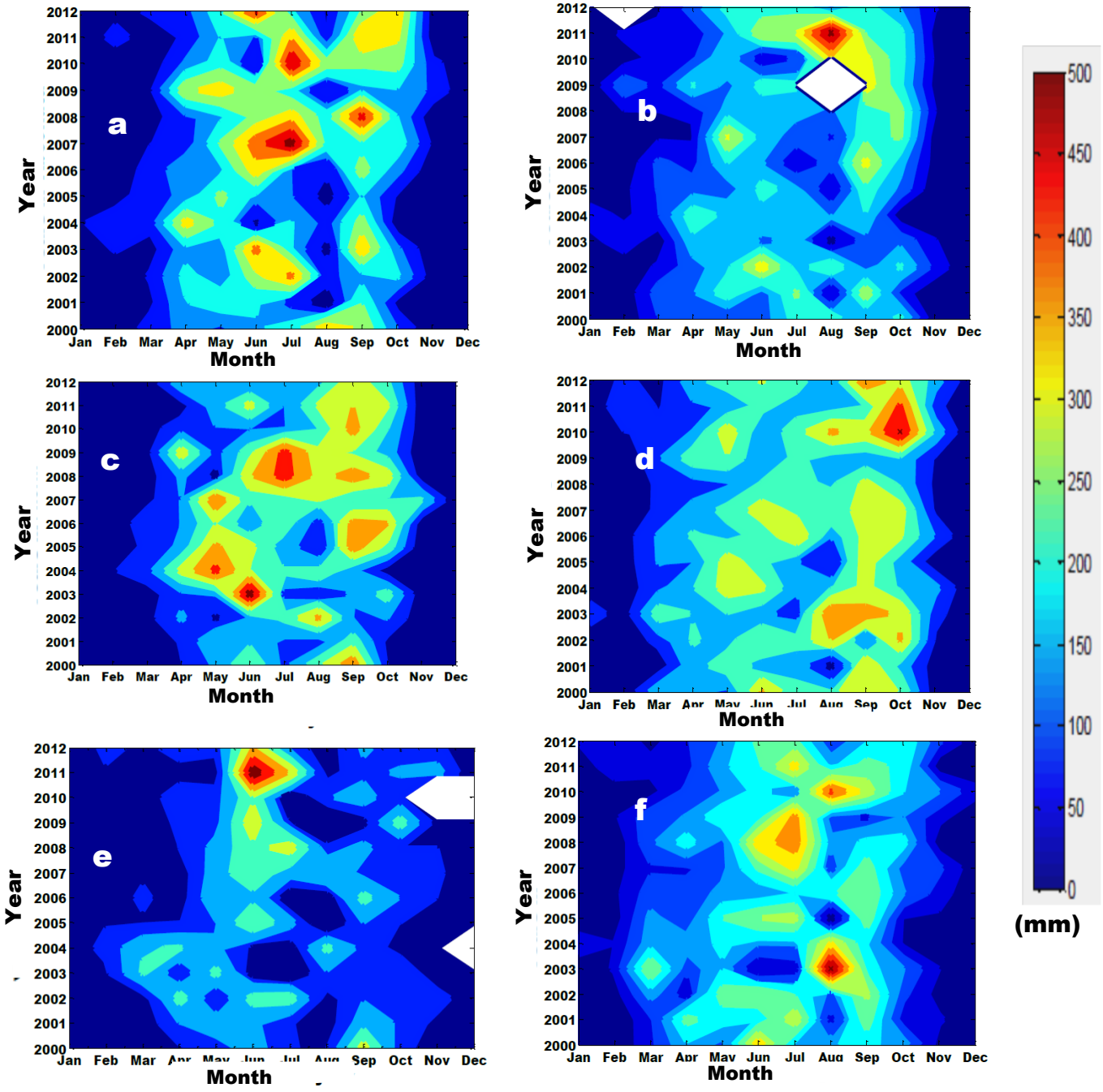

Figure 4.53: Yearly rainfall analysis for six locations (a) Abeokuta (b) Ibadan (c) Ilorin (d) Oshogbo (e) Lagos (f) Ondo

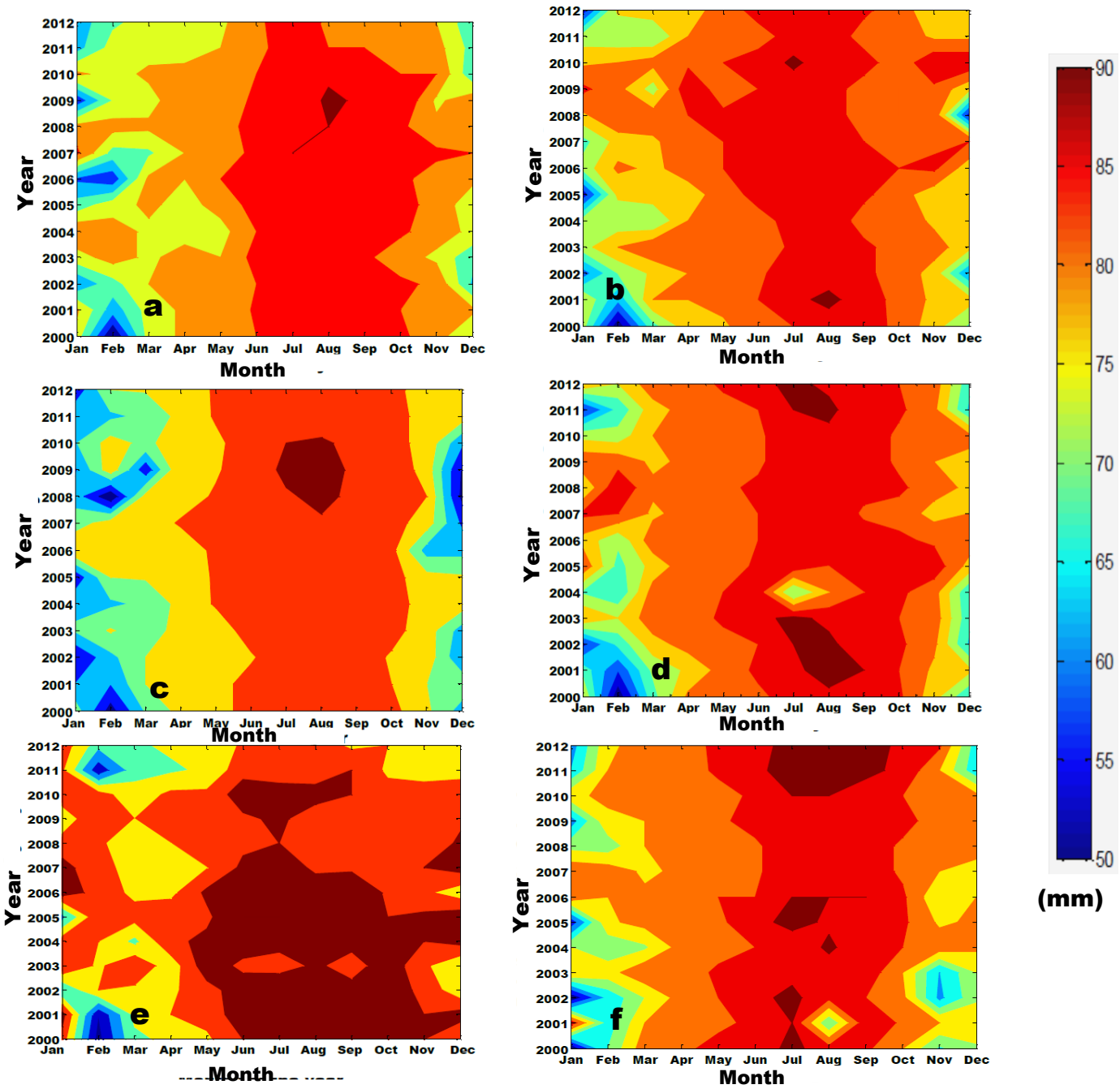

Figure 4.54: Yearly relative humidity analysis for six locations (a) Abeokuta (b) Ibadan (c) Ilorin (d) Oshogbo (e) Lagos (f) Ondo

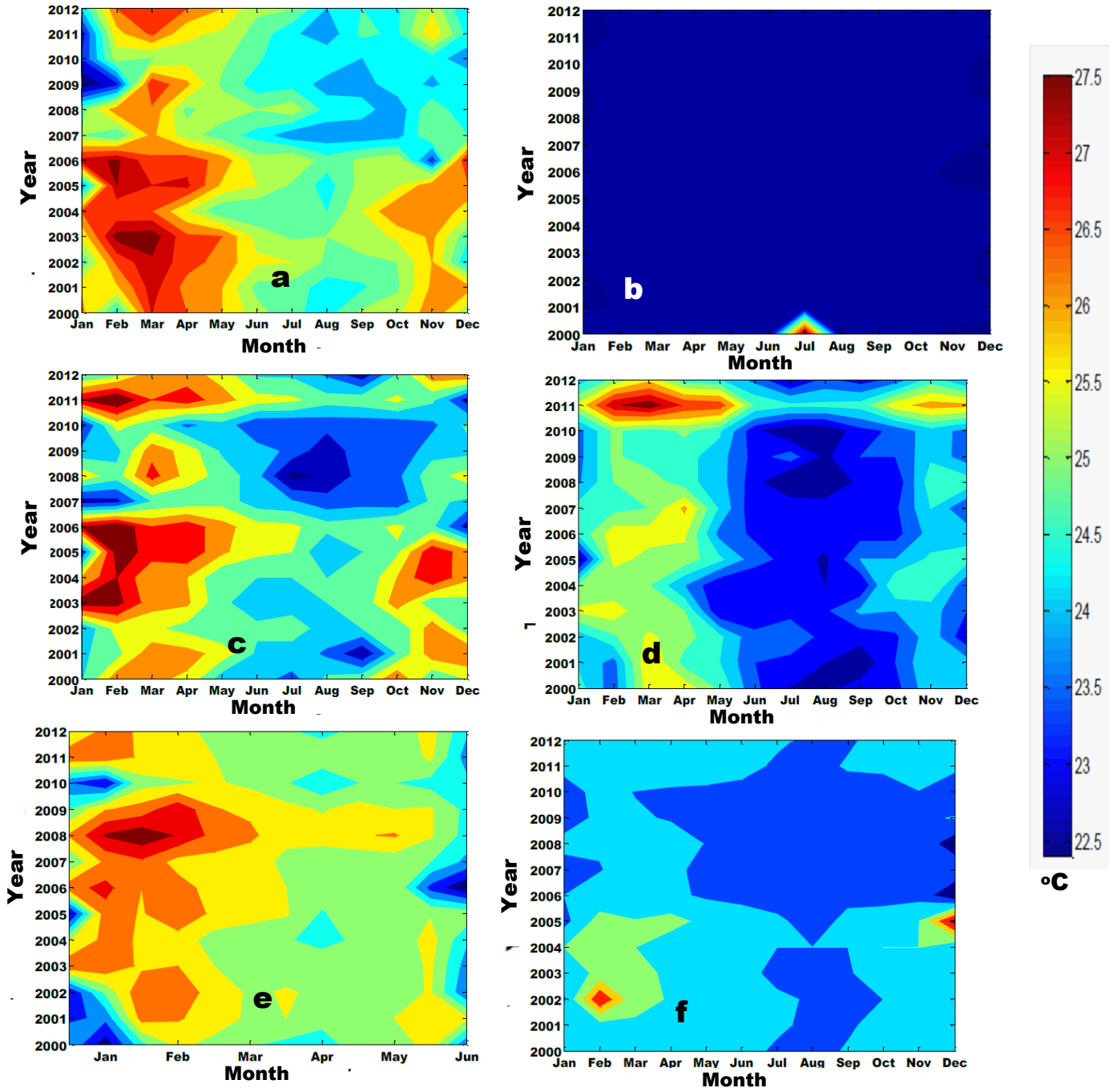

Figure 4.55: Yearly analysis of minimum temperature for six locations (a) Abeokuta (b) Ilorin (c) Ondo (d) Lagos (e) Oshogbo (f) Ibadan

The cloud cover over Ilorin is shown in Figure 4.52 (a-e). Ilorin has the highest cloud cover in the past fourteen years with its average value as 7.0 compared to Ondo whose values ranged between 5.0 and 7.0. The cloud cover data when compared with the AOD of Ilorin shows that an increase in cloud cover leads to a decrease in AOD and vice-versa. This trend extends to the observation of the cloud cover in the other locations studied and their corresponding AOD (Figure 4.30 to 4.31d). Hence, cloud cover is a valid parameter to estimate AOD in any area. The cloud cover for Abeokuta was not included in Figure 4.52 because it has a uniform cloud cover of average value of 7.0 for fourteen years studied. The rainfall trend shown in Figure 4.53 (c and e) for Ilorin and Lagos was compared to their AOD trend (Figures 4.30 and 4.34). It shows an inverse relationship, that is, an increased volume of rainfall (not frequency) leads to a decrease in the AOD output. An increased rainfall eliminates aerosol at the PBL. The relative humidity trend shown in Figure 4.54 (c and e) and AOD trend (shown in Figures 4.30 and 4.34) shows a direct relationship, that is an increased relative humidity (not frequency) results in an increase AOD output. The minimum temperature trend (Figure 4.55) showed an unstable relationship with the AOD. The stability of the relation between minimum temperature and AOD is sectionalized. For example, January to April reveals a direct relationship between the two parameters for three locations, that is, Lagos, Abeokuta and Ibadan. The minimum temperature is discarded because it is sectionalized and unpredictable. Fitzgerald (1989) related the minimum temperature to AOD. However, with the results obtained from the six locations, no mathematical assumptions can practically capture all the known and unknown forces responsible for thermal abnormality.

Upon this logical reasoning, the minimum temperature was ignored in this section because of the instability of the data set (Figure 4.55). Guzzi et al. (1987) supported the use of solar irradiance in his model. Without going through rigorous proof which is not the objective of this section, the realities of climate change should have altered the model propounded by Guzzi et al.(1987). Two parameters that were not discussed in this section are the height and wavelength.

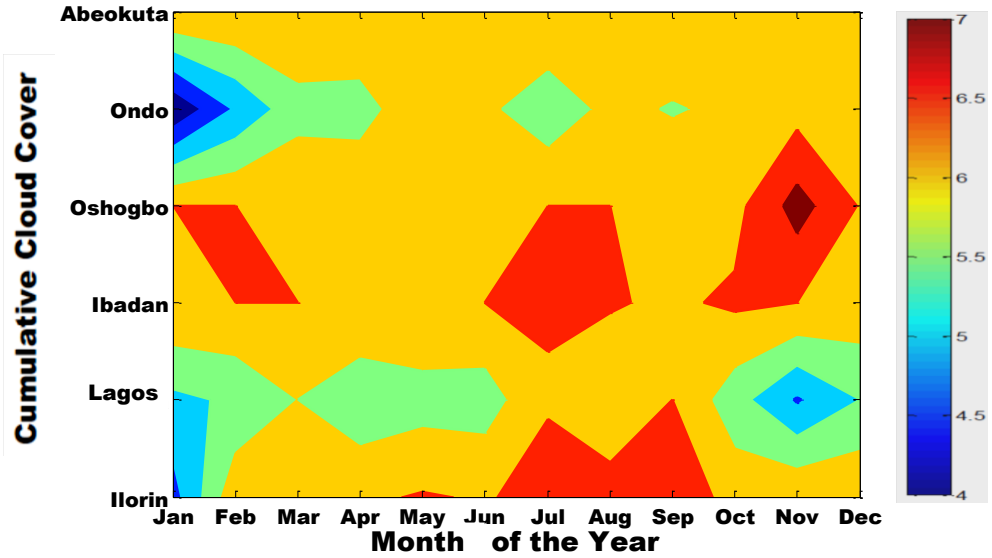

Figure 4.56: Cumulative cloud cover over the six locations

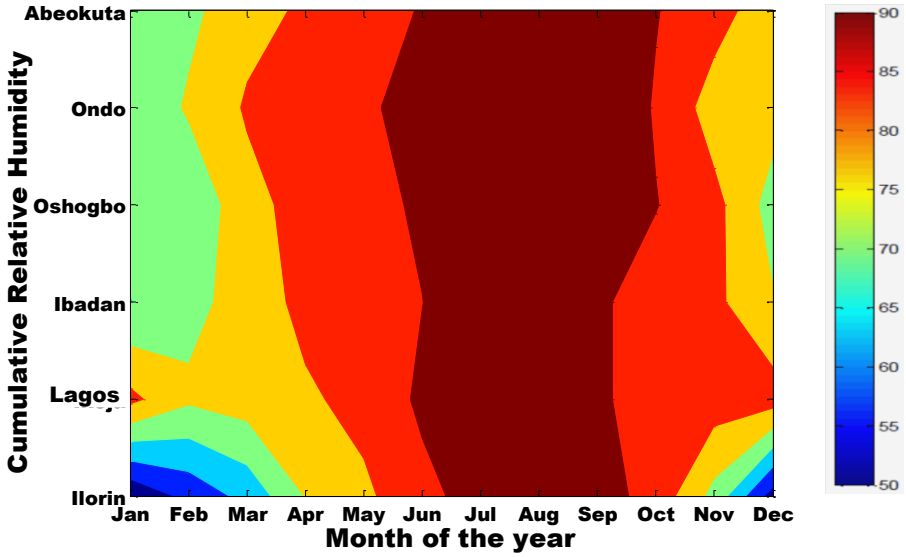

Figure 4.57: Cumulative relative humidity over the six locations

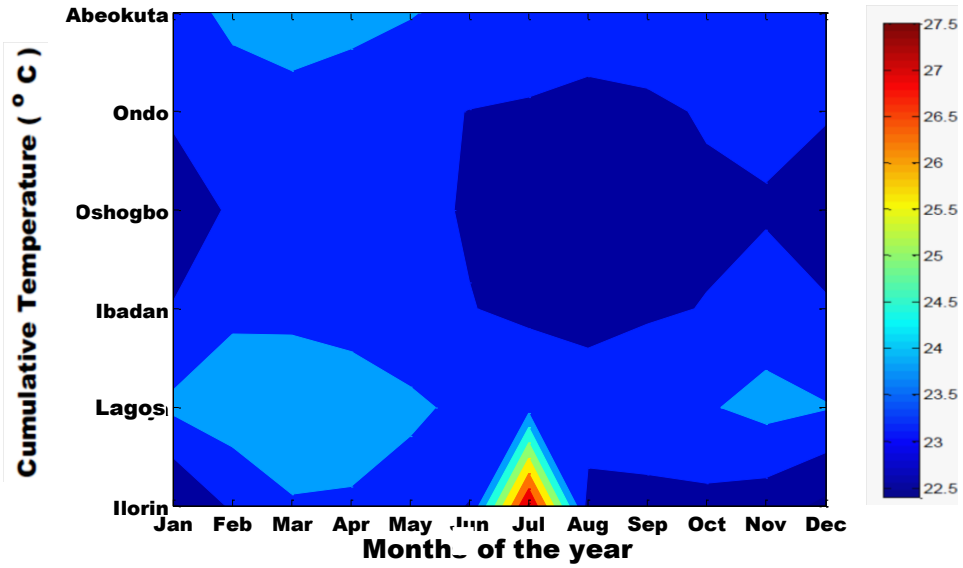

Figure 4.58: Cumulative temperature over the six locations

This is because the parametric model discussed earlier had shown the possibility to obtain ASD with single wavelength, hence, incorporating wavelength in this section is not necessary. The collective representation of fourteen years data set in each location is represented in Figures (4.56 to 4.58). The changing features in Figures 4.56 to 4.58 reveal how difficult it is to accurately estimate AOD either using satellite or ground data set. The second technique is the sectionalizing of each location via the conversion of equations (3.106 to 3.108) to a polynomial expression. The following were considered: cloud cover index at 20 m above the PBL, relative humidity index at 20m above the PBL, rainfall index at 20 m above the PBL and aerosol optical index are illustrated below in Figures 4.59 to 4.61.

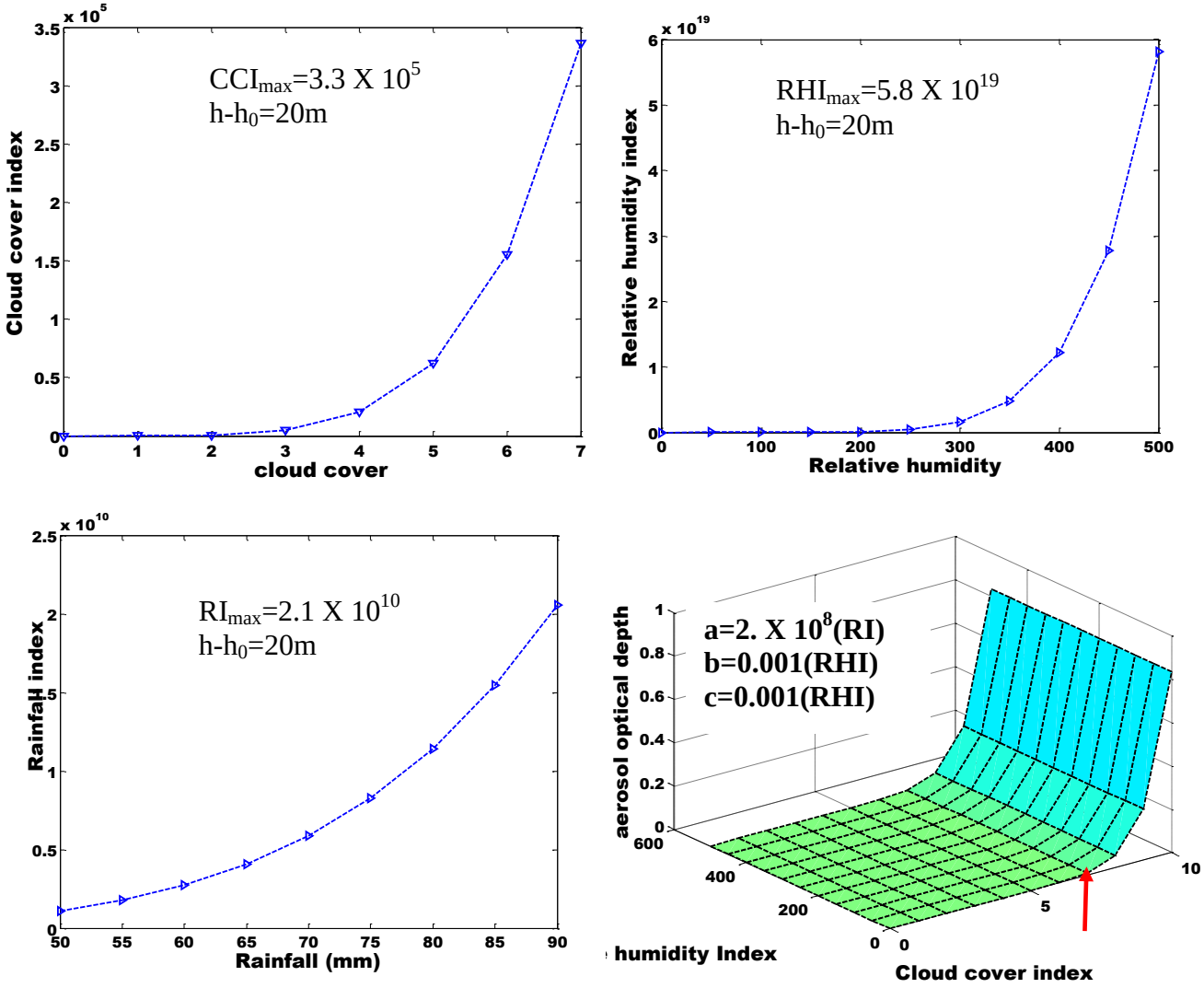

Figure 4.59: Polynomial analysis of ATOPM-Abeokuta

Symbol 'G' in equation (3.110) is referred to as the cloud cover index. Cloud cover index refers to the tendency of cloud cover growth over an area. Symbol 'H' in equation (3.110) is the relative humidity index. Relative humidity index is the degree of air saturation over an area. Symbol 'J' in equation (3.110) is referred to as rainfall index. Rainfall index is the annual description of the magnitude of rainfall over an area. The tunning constants for cloud cover, relative humidity and rainfall are represented as 'a', 'b', and 'c' respectively. The tuning constant originates from equation (3.109). The indices at a height of 20 m of the PBL were considered. As shown above, the maximum indexes are inscribed in Figure (4.59). The positive parabola features shows that the relationship between the meteorological parameter and its indexes (for example, cloud cover index and cloud cover) are directly proportional to one another. Also, the depth of relationship depends on the steepness of the parabola and the magnitude of the index.

The table of all the values generated for the six research locations are listed in Table 4.4. Ondo has the highest relative humidity index (RHI), Oshogbo has the highest cloud cover index (CCI), Ondo has the highest rainfall index (RI) and Ilorin has the highest controlling constant 'a'.

The index reveals the cumulative effect in numerical value. High index shows a region of lower activity of its corresponding parameter and vice-versa. For example, in descending order, the CCI of the listed locations (Osun, Ibadan, Ilorin, Ondo, Lagos and Abeokuta) can be inferred in Table 4.5.

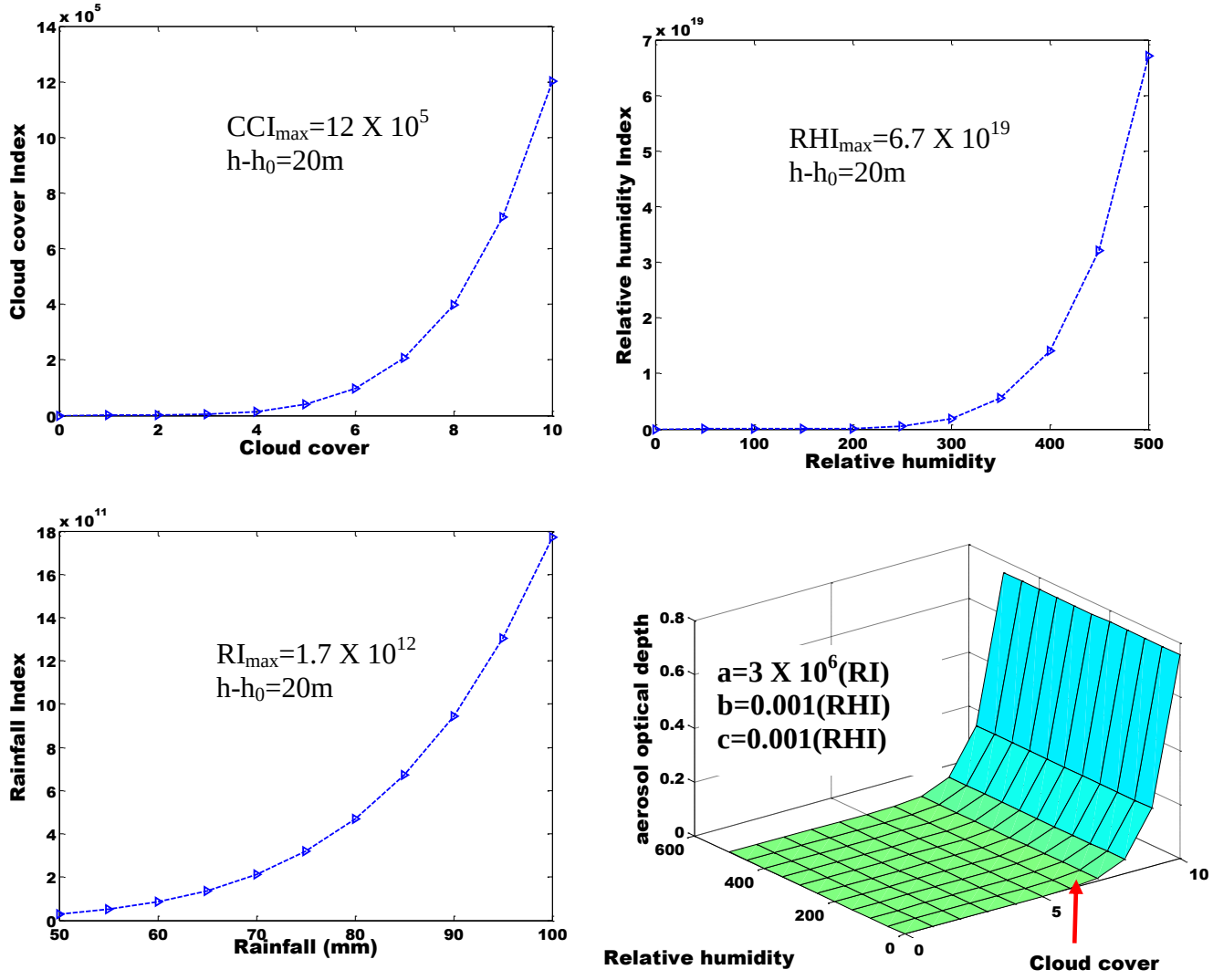

Figure 4.60: Polynomial analysis of ATOPM-Ondo

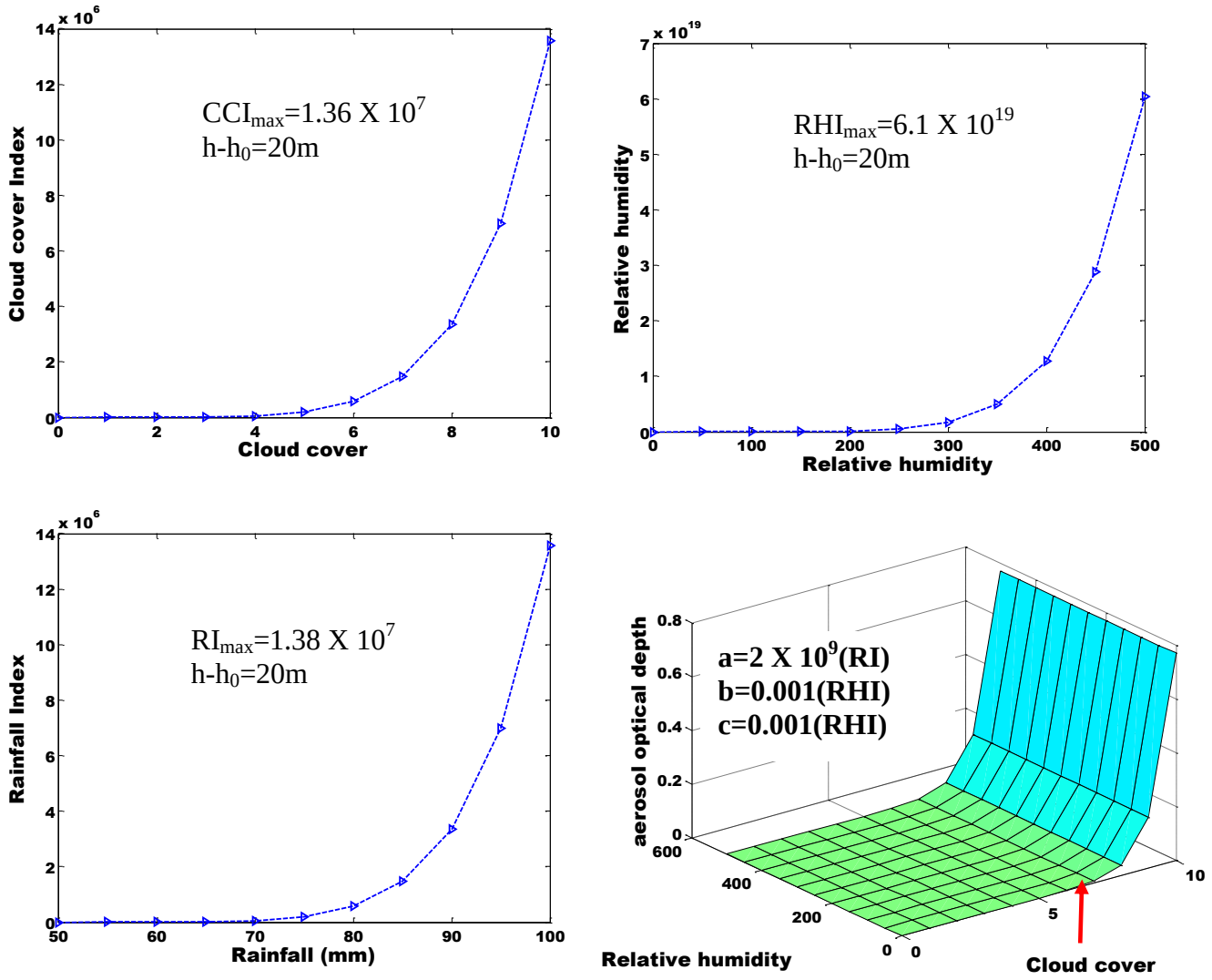

Figure 4.61: Polynomial analysis of ATOPM-Oshogbo

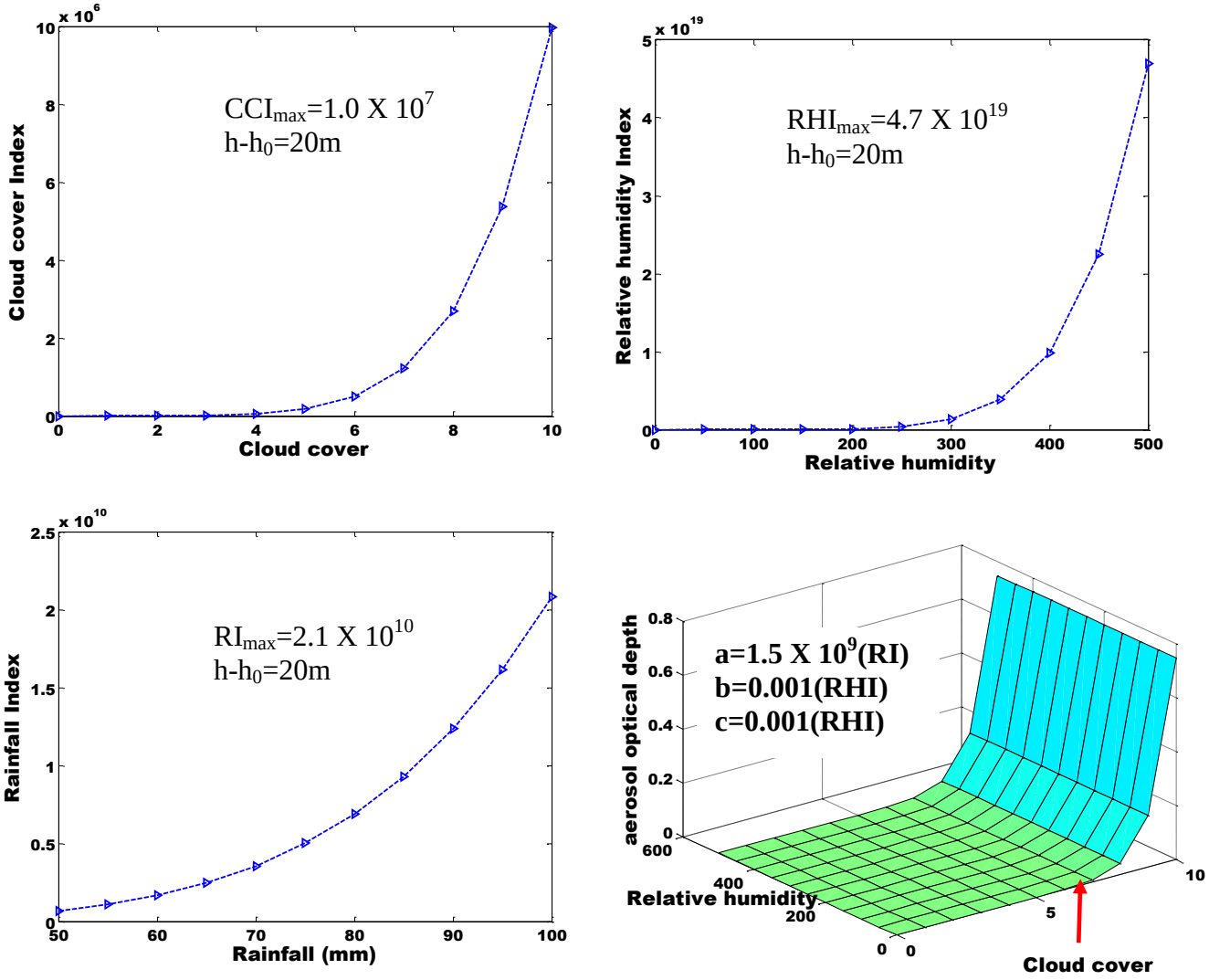

Figure 4.62: Polynomial analysis of ATOPM-Ibadan

Table 4.4: Index table of parameters

Location	CCI	RHI	RI	a
Abeokuta	3.3×10^{5}	5.8×10^{19}	2.1×10^{10}	2.0×10^{8}
Ondo	1.2×10^{6}	**6.7×10^{19}**	**1.7×10^{12}**	3.0×10^{6}
Oshogbo	**1.36×10^{7}**	6.1×10^{19}	1.38×10^{7}	2.0×10^{9}
Ibadan	1.0×10^{7}	4.7×10^{19}	2.1×10^{10}	1.5×10^{9}
Lagos	7.3×10^{5}	3.6×10^{19}	7.3×10^{5}	2.0×10^{4}
Ilorin	7.1×10^{6}	4.7×10^{19}	7.3×10^{6}	**3.0×10^{9}**

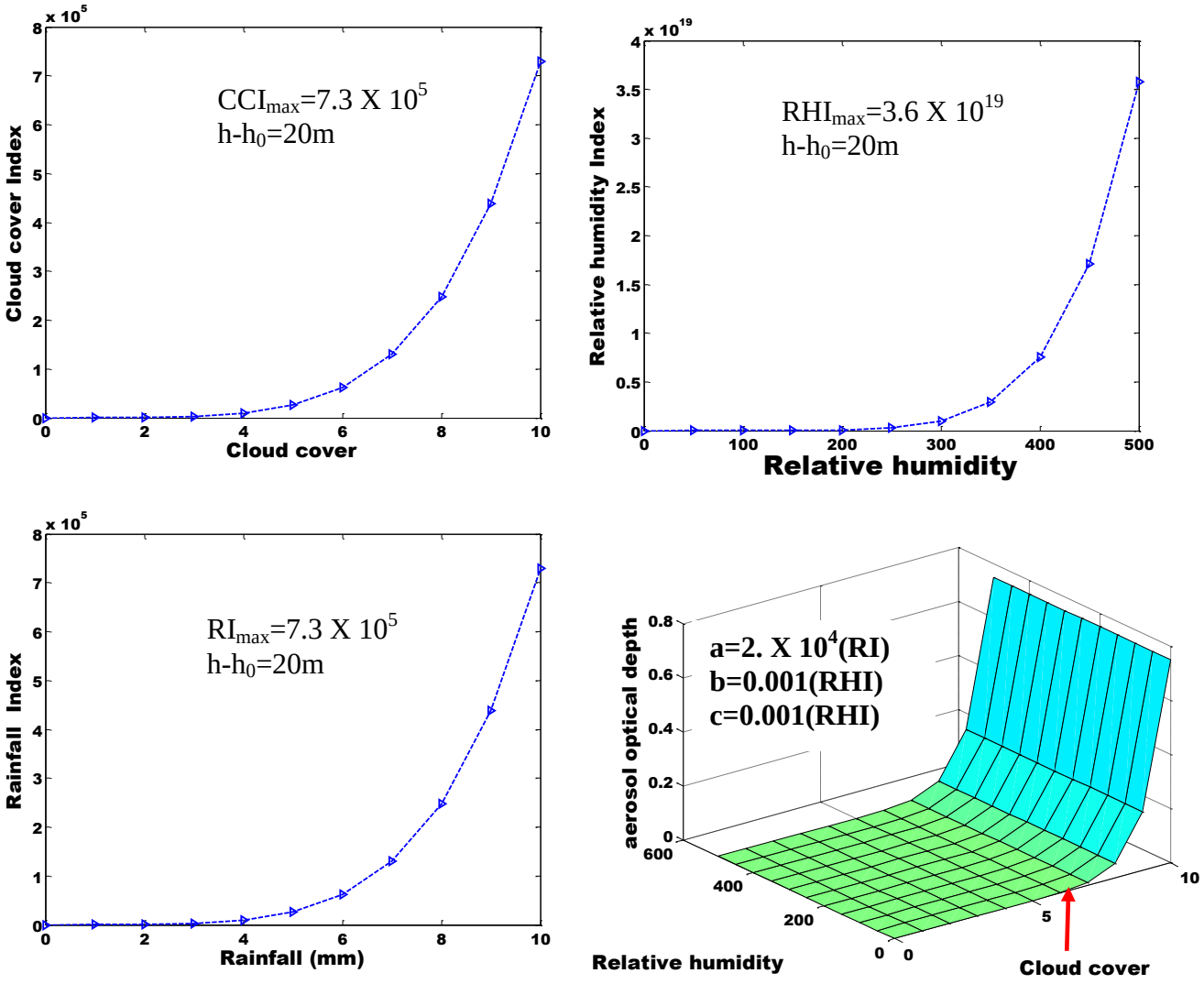

Figure 4.63: Polynomial analysis of ATOPM-Lagos

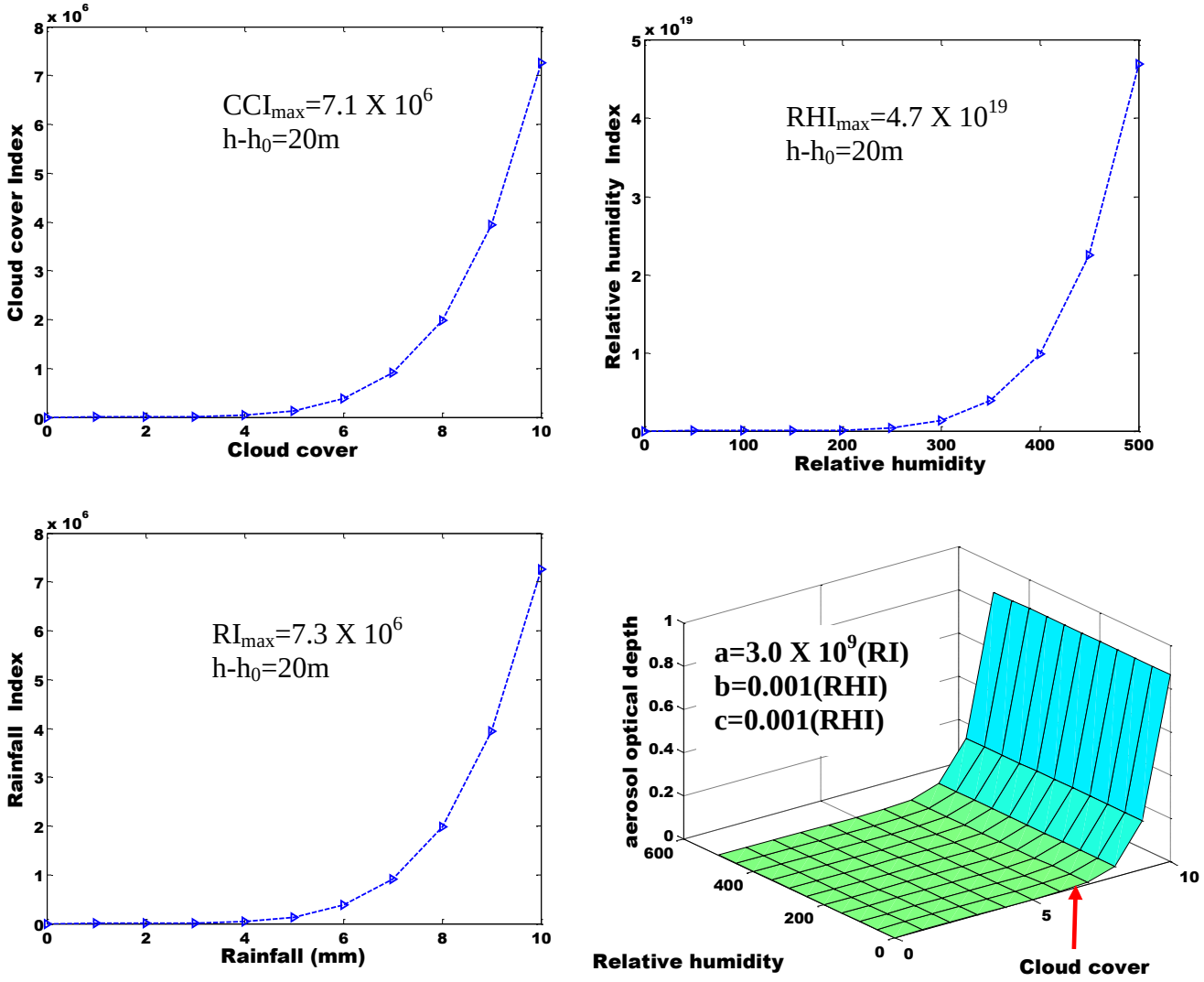

Figure 4.64: Polynomial analysis of ATOPM-Ilorin

The positioning of the indices (Table 4.5) may be used for forecast purposes as shown below. The multiplication of the positions is expressed in the column-marked 'R'. It is proposed that region of exceeding high value of 'R' (R>100) symbolizes region prone to errors, that is, using any forecast models. Therefore, Lagos and Abeokuta are highly prone to errors. Ondo and Oshogbo lies almost on the same horizon. They possess low 'R' (R<100) showing that any forecast model would be almost accurate. Ilorin and Ibadan are almost in the class of Ondo and Oshogbo. The same result is expected for any forecast model.

Table 4.5: Forecasting via index positioning

Location	**CCI** $\times 10^5$	P	**RHI** $\times 10^{19}$	P	**RI** $\times 10^5$	P	**A** $\times 10^6$	P	R
Abeokuta	3.3	**6**	5.8	**3**	210000	**3**	200	**4**	**216**
Ondo	120	**4**	6.7	**1**	1.7×10^7	**1**	3.0	**5**	**20**
Oshogbo	136	**1**	6.1	**2**	138	**5**	2000	**2**	**20**
Ibadan	100	**2**	4.7	**4**	210000	**3**	1500	**3**	**72**
Lagos	7.3	**5**	3.6	**6**	7.3	**6**	0.02	**6**	**1080**
Ilorin	71	**3**	4.7	**4**	73	**2**	3000	**1**	**24**

4.8 Comparative Analysis of the Ground and Satellite Observations over West Africa

The second supportive model (statistical model) would be illustrated in this section. The ground and satellite data set are complementary to each other especially as it relates to AOD (Figure 4.65). The main advantage of satellite observation over the ground-based observations is its tendency to provide more spatially representative measurements of AOD. Ground-based observations have the advantages of high accuracy if properly maintained. Also, it enables the study of local variability effects for tuning processes during ground truthing. However, the main challenge of not totally relying on either the satellite or ground observation is because of the climate changes effect on operational satellites and recalibration of ground-based instruments (Fioletov et al., 2002). As shown in all the Figures in this section, features of AOD are more poorly pronounced under the satellite observation (Mikhalev et al., 2003). Using statistical tool (Table 4.6), the level of reliance on the satellite data set over West Africa was illustrated. Bojanowski et al. (2014) highlighted the several sources of uncertainty when validating satellite observation. The uncertainties include; different viewing perspective, different spatial footprint and different sensitivity of a satellite. These uncertainties were investigated by comparatively validating the reliance on satellite observation via the ground observation in the West African space.

The ground data set for Lagos is more complete than the satellite data set (Figure 4.65). The ground data for 2012 has a low standard error and standard deviation. It is more convenient to align this kind of data using any aerosol dispersion models. A comparative study of the ground and satellite data set reveals an abnormal variance in April. The AOD satellite data set for April, 2012 and 2013 is 1.35 and 0.3 (Figure 4.65a). The abnormality in April shows the likely formation of recirculation region or atmospheric aerosols retention over Lagos. The AOD ground data for April, 2012 and 2013 is 0.4 and 0.96 respectively affirmed the formation of recirculation region (Figure 4.65b). The sensitivity of satellite and ground data set to capture the AOD over Lagos could be obtained from the skew analysis, that is, the measure of the asymmetry of the AOD probability distribution. The negative and positive skew analysis for 2012 and 2013 respectively shows that the atmospheric condition over Lagos is dynamic. The atmospheric condition can be determined by a minimum ten years data which has been done in the previous section. The nowcast can be inferred from the coefficient

variance, that is, normalized dispersion of probability distribution. The dynamism of the AOD over Lagos shows that the difference between the ground and satellite observation in 2012 and 2013 are 83% and 64% respectively. A close observation of 2012 and 2013 may prompt an early conclusion that atmospheric dynamism increases and may likely extend for some years. The Kolmogorov-Smirnov statistics showed that the highest AOD continuity distribution occurred in 2013.

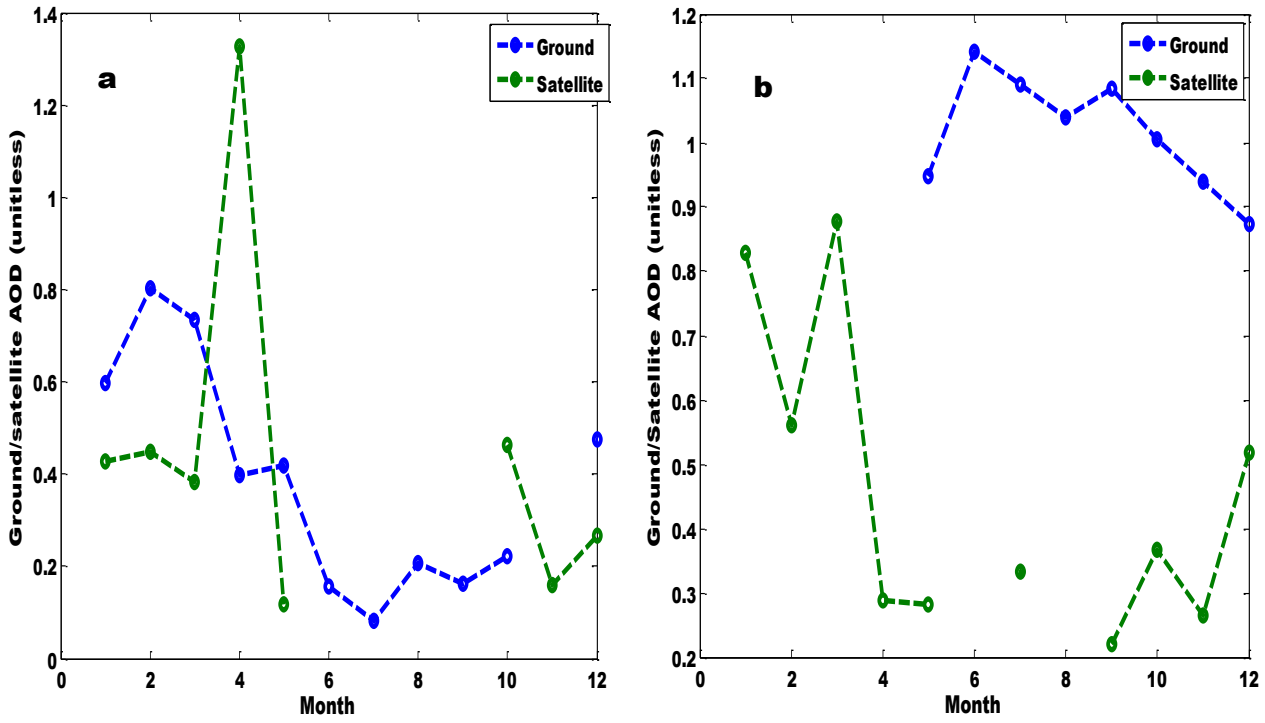

Figure 4.65a: Ground and Satellite observations over Lagos in 2012 (b) Ground and Satellite observations over Lagos in 2013

Table 4.6: Statistical analysis of ground and satellite data set, Lagos

Statistical Parameter	2012		2013	
	Ground	**Satellite**	**Ground**	**Satellite**
Standard error	0.03194	0.074879	0.049783	0.06908
95% confidence interval	0.075539	0.169377	0.10957	0.15391
Variance	0.008162	0.056069	0.02974	0.052492
Standard deviation	0.090341	0.236789	0.17245	0.229112
Coefficient of variation	0.089	0.5213	0.19466	0.54109
Skew	-0.205	1.03	0.504	0.904
Kurtosis	-1.009	-0.298	-0.975	-0.434
Kolmogorov-Smirnov stat	0.15	0.245	0.233	0.265

The ground observation in Ilorin-Nigeria for the year 2001 was more stable than the satellite observation though they have almost the same trending (Figure 4.66). However, the variations between the satellite and ground observations may be due to multiple refractive indexes from the moving aerosol layers in the atmosphere. In the previous section, the mathematical representation has been shown and tested. The comparative features between 2001 and 2002 indicate a change of formation between May and December in the year 2002. The sudden reverse in the pattern can be induced from the statistical analysis within 2001 to 2002.

The AOD pattern in the year 2002 extended to 2003 as shown by the satellite and ground observations. Generally, the ground and satellite observation over Ilorin reveals high corresponding trends. This shows that either the satellite or ground observations would give a near perfect aerosol loading state per time over Ilorin. In 2004, though the ground observations were characterized by missing data set, the satellite observation could be relied upon to see the AOD trends. Figure 4.66b showed that the occurrence in the year 2002 extend also into 2004. Since the 2002 trend extends to 2013, it may likely be the usual trend expected over Ilorin. This results calls for the extensive probe of the year 2001 observation for the purpose of nowcast and forecast. One of the likely guesses may corroborate the findings of Sauvage et al. (2005) and Haywood et al. (2008) that the aerosol emission over Ilorin-Nigeria in 2002 may be influenced by the seasonal north-to-south shift of the Inter-Tropical Convergence Zone (ITCZ). Also, another likely guess is the activities of the mesoscale convective systems (MCS) over the northern edge of the West African ITCZ (Mohr, 2004).

In more general terms, the observations in 2000 may be as a result of excessive influence of either African Easterly Jet (AEJ), Intertropical Discontinuity (ITD), associated heat low (HL), Subtropical Jet (STJ), troughs and cyclonic centers associated with African Easterly Waves (AEW) and Tropical Easterly Jet (TEJ). Year 2004 has the lowest standard error and deviations. This means that the AOD features for 2004 was the most reliable observation. Hence, it can be used as the control source to discuss the abnormality present in all the years shown in Figure 4.66a to 4.66h. From the ground observation, the peak aerosol loadings over Ilorin shifts alternatively between February and March. This shows that there is aerosol retention in the atmosphere as predicted from the satellite observations in the previous

section. The percentage of retention can be determined from the coefficient of variance for each year. Hence we propound the aerosols retention between two years as:

$$A = \left|\frac{G_P}{G_P - G_r}\right|^2 \times 100\% \quad (4.12)$$

Equation (5.12) is valid only if $G_P - G_r > G_P$ else, equation (5.13) is valid.

$$A = \left|\frac{G_P - G_r}{G_P}\right|^2 \times 100\% \quad (4.13)$$

The aerosols retention can be calculated from Tables 4.7 to 4.13. Hence the likely aerosol retention in the atmosphere over Ilorin is given in Table 4.7 below.

There was no record for 2004 and 2005 in Table 4.7 because of the scanty data in 2004.

It can be inferred from Table 4.7 that the maximum aerosol retention for Ilorin is 14.9 % between 2009 and 2010 while the minimum aerosol retention is 0.5% between 2005 and 2006. Tables 4.7 to 4.13 were analysed using colour coding. The yellow box signifies the highest value of the ground observation for Ilorin between 2001 and 2012. The blue box signifies the highest value of the satellite observation for Ilorin between 2001 and 2012. The green box signifies the lowest value of the ground observation for Ilorin between 2001 and 2012. The red box signifies the lowest value of the satellite observation for Ilorin between 2001 and 2012.

The highest statistical result for the satellite observation over Ilorin occurred in 2001. All statistical parameters shown in Table 4.8 were high. As explained earlier in this section, the satellite observations corroborate the presuppose events over Ilorin. The lowest statistical result for the satellite observation over Ilorin occurred in 2002. All statistical parameters shown in Table 4.8 were low except for the skew and Kolmogorov-Smirnov stat. The lowest standard error for the satellite observation was in 2003. This may be the best satellite observation using the statistical predictions. However, the early conclusion based on the standard error may not be scientific because the lowest 95% confidence interval was observed in the same year. The highest kurtosis for the ground data set was observed in 2003. This means that more of the variance in the AOD ground data set for the year 2003 is as a result of uncommon extreme deviations within each month of the year. The lowest kurtosis for the

ground data set was observed in 2002. The highest kurtosis for the satellite data set was observed in 2003 while the lowest in 2008. The lowest skew for the ground data set over Ilorin was observed in 2006 while the highest skew for the ground data set was in 2008. The maximum skew for the satellite data set was observed in 2003 while the minimum in 2007.

The highest 95% confidence interval for the satellite data set was observed in 2006 while the lowest in 2003. The maximum 95% confidence intervals for the ground data set was observed in 2010 while the minimum in 2002. The highest standard error for the satellite data set was observed in 2003 while the lowest in 2011. The maximum standard errors for the ground data set was observed in 2010 while the minimum in 2002. The highest Kolmogorov-Smirnov stat for the satellite data set was observed in 2003 while the lowest in 2007. The maximum Kolmogorov-Smirnov stat for the ground data set was observed in 2011 while the minimum in 2009. The highest coefficient of variance for the ground data set was observed in 2010 while the lowest in 2011. The maximum coefficients of variance for the satellite data set was observed in 2003 while the minimum in 2011. The highest variance for the ground data set was observed in 2012 while the lowest in 2002. The maximum variances for the satellite data set was observed in 2003 while the minimum in 2011. The highest standard deviation for the ground data set was observed in 2012 while the lowest in 2002. The maximum standard deviations for the satellite data set was observed in 2003 while the minimum in 2011. It is inferred from the statistical parameters that the AOD features over Ilorin is dynamic as the year of highest or lowest value varied within eight years. This shows that any AOD changes within Ilorin can be captured with a minimum of eight years data set.

Table 4.7: Aerosol retention over Ilorin

Year	2002	2003	2006	2007	2008	2009	2010	2011	2012
Aerosol Retention (%)	12	10.4	0.5	2.7	3.6	4.8	14.9	9.8	8.3

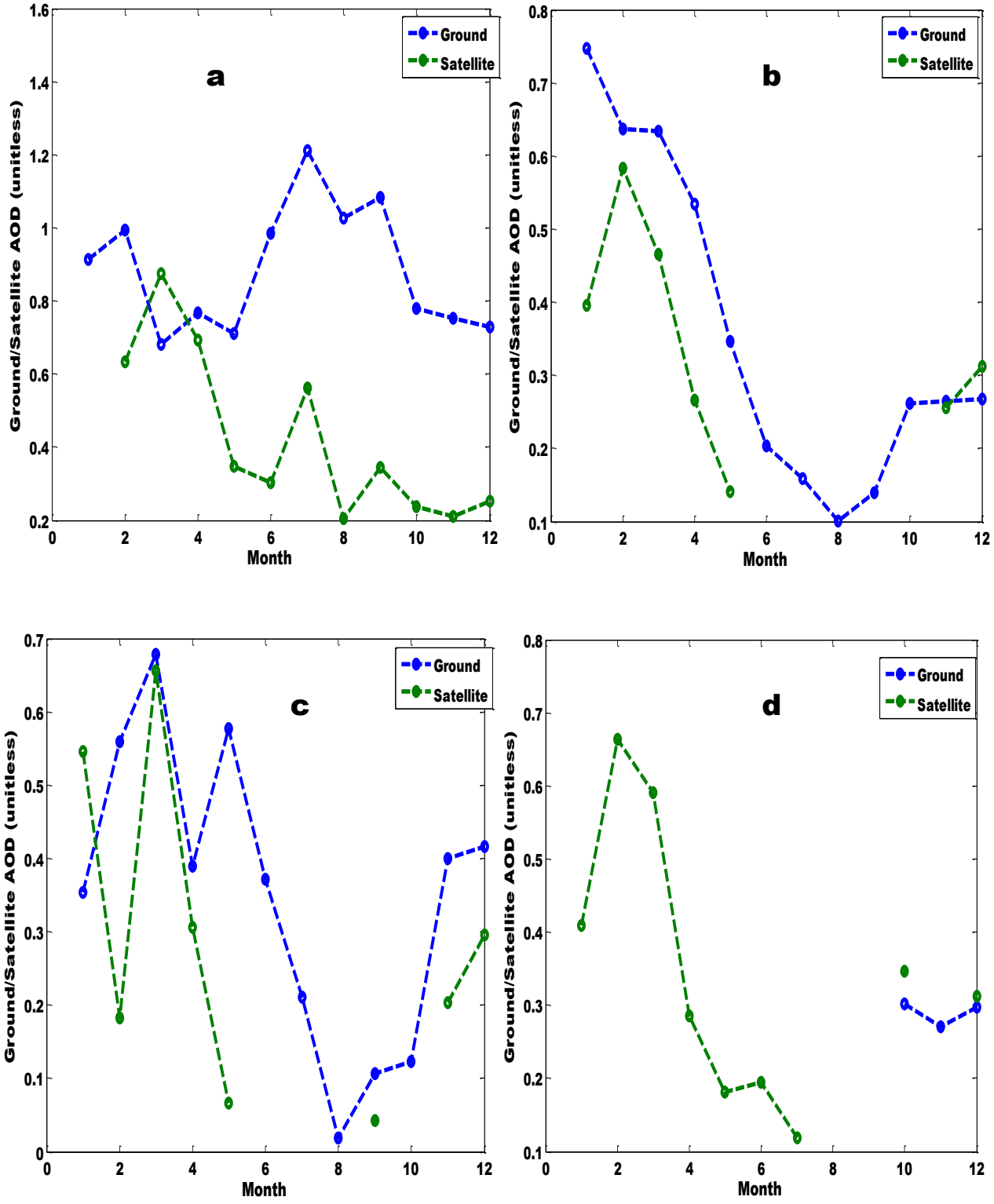

Figure 4.66 a to d: Ground and Satellite observation for (a) 2001, (b) 2002 (c) 2003 (d) 2004 (d) 2005 over Ilorin

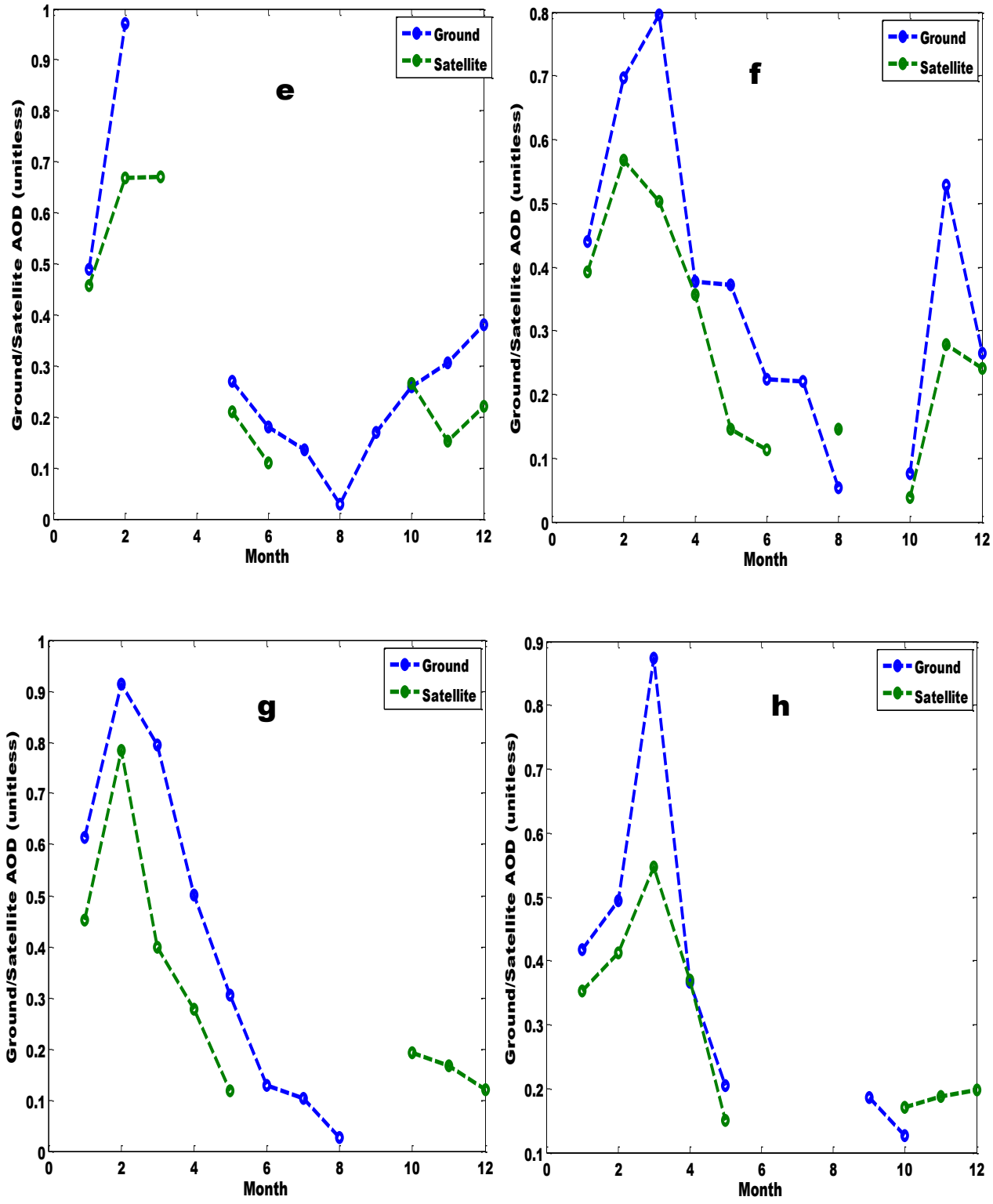

Figure 4.66e to h: Ground and Satellite observations for (e) 2006 (f) 2007 (g) 2008 (h) 2012 over Ilorin

Table 4.8: Statistical analysis of ground and satellite data sets, Ilorin

Statistical Parameters	2001		2002	
	Ground	Satellite	Ground	Satellite
Standard error	0.074	0.134	0.015	0.064
95% confidence interval	0.165	0.317	0.046	0.151
Variance	0.060	0.144	0.001	0.032
Standard deviation	0.245	0.379	0.029	0.180
Coefficient of variation	0.634	0.845	0.163	0.555
Skew	0.506	2.140	0.292	0.036
Kurtosis	-1.029	5.361	-3.360	-0.921
Kolmogorov-Smirnov stat	0.203	0.361	0.244	0.191

Table 4.9: Statistical analysis of ground and satellite data sets, Ilorin

Statistical Parameters	2003		2004	
	Ground	Satellite	Ground	Satellite
Standard error	0.096	0.050	0.010	0.061
95% confidence interval	0.236	0.119	0.043	0.141
Variance	0.065	0.020	0.000	0.034
Standard deviation	0.255	0.143	0.017	0.184
Coefficient of variation	0.670	0.478	0.060	0.534
Skew	1.278	0.622	-1.555	0.722
Kurtosis	1.798	-0.811	#N/A	-0.413
Kolmogorov-Smirnov stat	0.186	0.259	0.329	0.161

Table 4.10: Statistical analysis of ground and satellite data sets, Ilorin

Statistical Parameters	2005		2006	
	Ground	Satellite	Ground	Satellite
Standard error	0.064	0.056	0.058	0.077
95% confidence interval	0.141	0.137	0.129	0.181
Variance	0.049	0.022	0.041	0.047
Standard deviation	0.222	0.148	0.202	0.217
Coefficient of variation	0.620	0.428	0.578	0.755
Skew	0.661	0.395	-0.115	0.750
Kurtosis	-1.102	-0.237	-0.784	-0.415
Kolmogorov-Smirnov stat	0.242	0.162	0.173	0.217

Table 4.11: Statistical analysis of ground and satellite data sets, Ilorin

Statistical Parameters	2007		2008	
	Ground	Satellite	Ground	Satellite
Standard error	0.075	0.054	0.083	0.080
95% confidence interval	0.165	0.125	0.188	0.189
Variance	0.068	0.026	0.069	0.051
Standard deviation	0.260	0.162	0.263	0.225
Coefficient of variation	0.692	0.460	0.825	0.655
Skew	0.683	-0.070	1.875	0.754
Kurtosis	-0.716	-0.117	4.349	-1.250
Kolmogorov-Smirnov stat	0.188	0.115	0.220	0.263

Table 4.12: Statistical analysis of ground and satellite data sets, Ilorin

Statistical Parameters	2009		2010	
	Ground	Satellite	Ground	Satellite
Standard error	0.071	0.055	0.215	0.083
95% confidence interval	0.159	0.125	2.727	0.202
Variance	0.056	0.031	0.092	0.048
Standard deviation	0.237	0.175	0.303	0.219
Coefficient of variation	0.643	0.629	0.891	0.650
Skew	0.507	0.383	#N/A	1.048
Kurtosis	-0.420	-0.948	#N/A	-0.956
Kolmogorov-Smirnov stat	0.125	0.177	0.260	0.331

Table 4.13: Statistical analysis of ground and satellite data sets, Ilorin

Statistical Parameters	2011		2012	
	Ground	Satellite	Ground	Satellite
Standard error	0.064	0.050	0.118	0.080175
95% confidence interval	0.203	0.123	0.279	0.189615
Variance	0.016	0.018	0.111	0.051425
Standard deviation	0.128	0.133	0.334	0.22677
Coefficient of variation	0.612	0.413	0.788	0.72253
Skew	1.225	0.184	0.277	1.423
Kurtosis	1.773	-0.736	-1.565	1.92
Kolmogorov-Smirnov stat	0.265	0.130	0.186	0.205

The ground and satellite observations over Ouagadougou are represented in Figures 67a to 67g. The ground observation in Ouagadougou for 2001 represents the whole months of the years with maximum AOD in April and the minimum in August. However, the satellite observation revealed a maximum AOD in January and minimum AOD in September. In 2002, both the ground and satellite observation revealed that there was no data for July. As discussed earlier, the reason may be the moisture content (Adebiyi et al., 2015), cloud scavenging (Dani et al., 2003), precipitation water content (Vijayakumar and Devara, 2013) and high rain drop rate (Boucher and Quaas, 2013). The maximum AOD for satellite and ground observation were in the month of May while the minimum AOD were in the months of October and December respectively.

The satellite and ground observations did not follow the same trend for January to June; however, the two observations showed same trending between August and December. In 2003, both the satellite and ground observations had their maximum AOD in March, while the minimum AOD were in October and December respectively. The AOD trends for both observations were fairly related. In 2004, both the satellite and ground observations had their maximum AOD in March, while the minimum AOD were in July and August respectively. In 2005, both the satellite and ground observations had their maximum AOD in March and May respectively. The minimum AOD was found in August and September. In 2006, both the satellite and ground observations had their maximum AOD in February, while the minimum AOD were in November and May respectively.

Hence the likely aerosol retention in the atmosphere over Ouagadougou is given in Table 4.14

Table 4.14: Aerosol retention over Ouagadougou

Year	2002	2003	2004	2005	2006
Aerosol Retention (%)	79	14.1	71.2	35.4	9.3

It can be inferred that the maximum aerosol retention for Ouagadougou is 79% between 2001 and 2002 while the minimum aerosol retention is 9.3% between 2005 and 2006 (Table 4.14). This means Ilorin and Ouagadougou had the highest aerosols retention between 2001 and 2002 and was observed generally over West Africa.

From Tables 4.15 to 4.17, the yellow box signifies the highest value of the ground observation for Ouagadougou between 2001 and 2012. The blue box signifies the highest value of the satellite observation for Ouagadougou between 2001 and 2012. The green box signifies the lowest value of the ground observation for Ouagadougou between 2001 and 2012. The red box signifies the lowest value of the satellite observation for Ouagadougou between 2001 and 2012.

The lowest kurtosis for the ground data set was observed in 2003 while the highest was observed in 2006. The maximum kurtosis' for the satellite data set was observed in 2004 while the minimum in 2006. The lowest skew for the ground data set over Ouagadougou was observed in 2001 while the highest skew for the ground data set was in 2006. The maximum skew for the satellite data set was observed in 2003 while the minimum in 2005. The highest 95% confidence interval for the satellite data set was observed in 2002 while the lowest in 2006. The maximum 95% confidence interval for the ground data set was observed in 2006 while the minimum in 2001.The highest standard error for the satellite data set was observed in 2002 while the lowest in 2006. The maximum standard errors for the ground data set was observed in 2004 while the minimum in 2005. The highest Kolmogorov-Smirnov stat for the satellite data set was observed in 2003 while the lowest in 2006. The maximum Kolmogorov-Smirnov stat for the ground data set was observed in 2006 while the minimum in 2003. The highest coefficient of variance for the ground data set was observed in 2005 while the lowest in 2001. The maximum coefficients of variance for the satellite data set was observed in 2004 while the minimum in 2005.

The highest variance for the ground data set was observed in 2006 while the lowest in 2001. The highest variance for the satellite data set was observed in 2002 while the lowest in 2006. The highest standard deviation for the ground data set was observed in 2006 while the lowest in 2001. The highest standard deviation for the satellite data set was observed in 2002 while the lowest in 2006. It is inferred from the statistical results that the corresponding highest skew and Kolmogorov-Smirnov stat for the satellite data set in 2003, may not be just a coincidence with the statistical value in Ilorin. The likely guesses may be that the satellite orbited over Ilorin and Ouagadougou almost at the same time (Figure 4.67g). Also, it may be

as a result of fast moving aerosol layer which occurs in the evening time due to fast moving cold front.

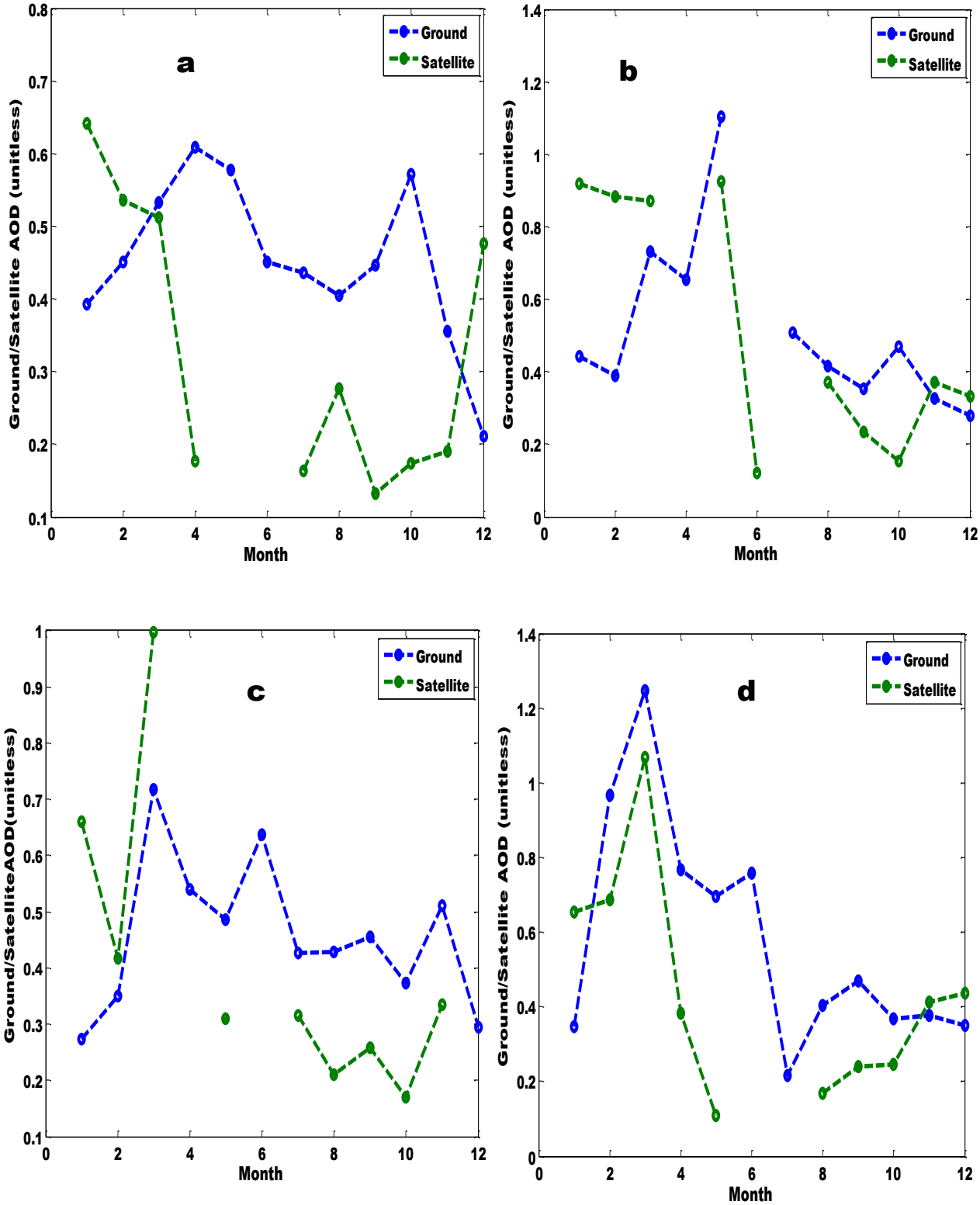

Figure 4.67 (a-d): Ground and Satellite observations for (a) 2001, (b) 2002 (c) 2003 (d) 2004 over Ouagadougou

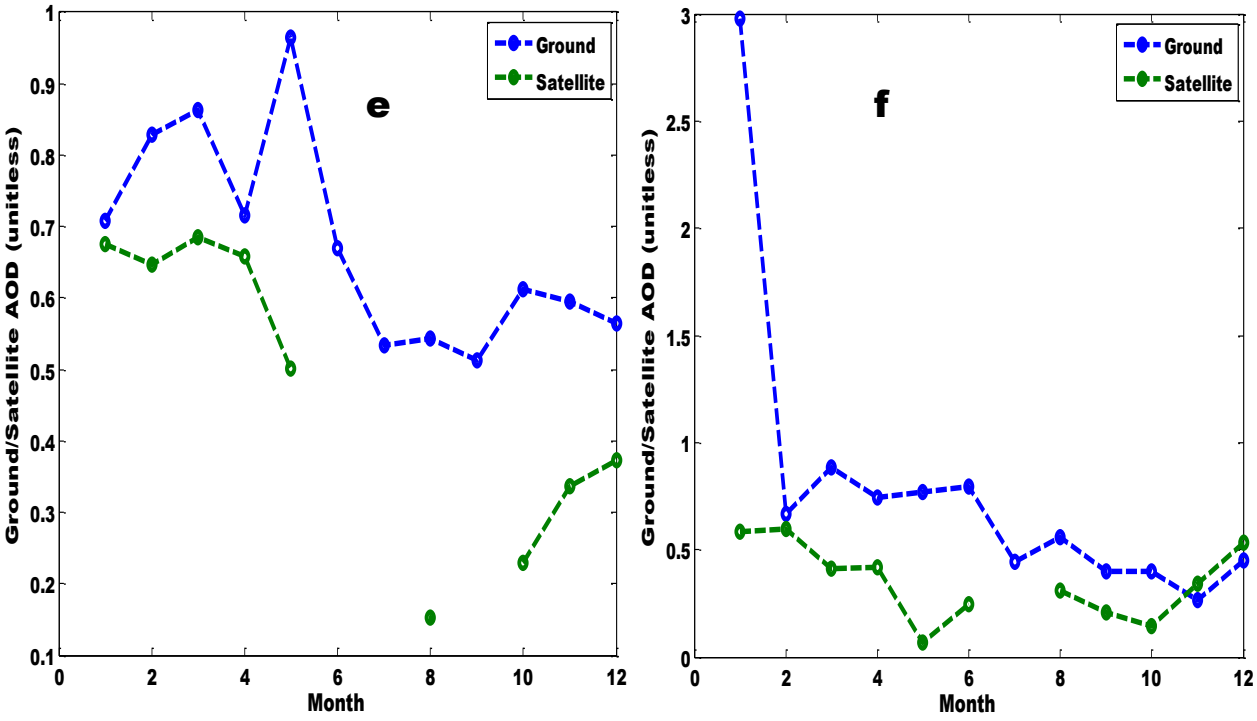

Figure 4.67(e and f): Ground and Satellite observations for (e) 2005 (f) 2006 over Ouagadougou

Figure 4.67: GPM core and TRMM Satellite Orbit Search showing passage over Ilorin and Ouagadougou

Table 4.15: Statistical analysis of ground and satellite data sets, Ouagadougou

Statistical Parameters	2001		2002	
	Ground	Satellite	Ground	Satellite
Standard error	0.032	0.061	0.072	0.107
95% confidence interval	0.070	0.137	0.160	0.242
Variance	0.012	0.037	0.057	0.115
Standard deviation	0.111	0.192	0.238	0.339
Coefficient of variation	0.244	0.585	0.461	0.654
Skew	-0.611	0.543	1.721	0.277
Kurtosis	0.808	-1.622	3.214	-2.058
Kolmogorov-Smirnov stat	0.175	0.263	0.239	0.267

Table 4.16: Statistical analysis of ground and satellite data sets, Ouagadougou

Statistical Parameters	2003		2004	
	Ground	Satellite	Ground	Satellite
Standard error	0.038	0.088	0.089	0.092
95% confidence interval	0.084	0.202	0.196	0.209
Variance	0.017	0.069	0.095	0.085
Standard deviation	0.132	0.263	0.308	0.292
Coefficient of variation	0.288	0.645	0.531	0.663
Skew	0.547	1.712	0.997	1.117
Kurtosis	-0.033	2.708	0.319	1.124
Kolmogorov-Smirnov stat	0.101	0.277	0.223	0.204

Table 4.17: Statistical analysis of ground and satellite data sets, Ouagadougou

Statistical Parameters	2005		2006	
	Ground	Satellite	Ground	Satellite
Standard error	0.042	0.069	0.207	0.053
95% confidence interval	0.092	0.159	0.456	0.118
Variance	0.021	0.043	0.516	0.031
Standard deviation	0.145	0.207	0.718	0.176
Coefficient of variation	0.215	0.437	0.921	0.502
Skew	0.808	-0.391	3.023	-0.020
Kurtosis	-0.349	-1.597	9.836	-1.066
Kolmogorov-Smirnov stat	0.171	0.245	0.359	0.120

The AOD pattern in Praia is very unique, that is, comparing the satellite and ground observations. It is observed from Figure 4.68 that both observations show sharp differences between June and October. While the ground observation follows the usual observation for the tropics, that is, a high AOD during harmattan and low AOD during raining season, the satellite observation was different. In this case, it is suggested that praia AOD pattern is dominated by the stratospheric aerosol which may araise from the influence of oceanic winds to promote the escape of the tropospheric aerosols into the stratosphere (Hommel et al., 2015). The maximum AOD for the ground observation ranges between November and December. This idea is opposed to other West African locations. The minimum AOD for the ground observation ranges between February and April. Hence the likely aerosol retention in the atmosphere over Praia is given in Table 4.18

Table 4.18: Aerosol retention over Praia

Year	2001	2002	2003	2004	2005	2006	2007	2008
Aerosol Retention (%)	10.2	0.25	10	37.3	5.6	2.9	0.07	1.7

Year	2009	2010	2011	2012	2013
Aerosol Retention (%)	6.3	39.4	23.9	35.6	10.2

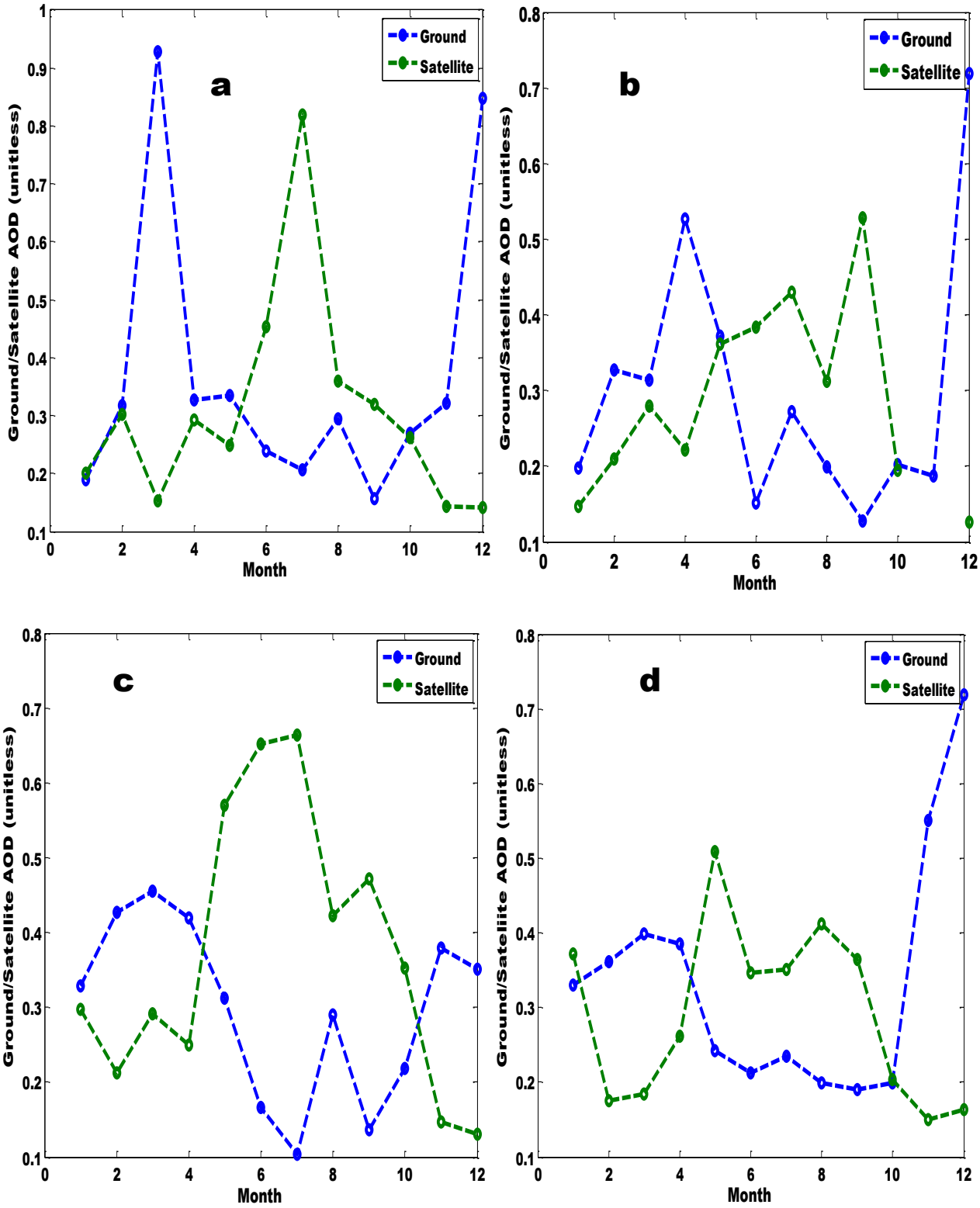

Figure 4.68(a - d): Ground and Satellite observations for (a) 2001, (b) 2002 (c) 2003 (d) 2004 (d) 2005 over Praia

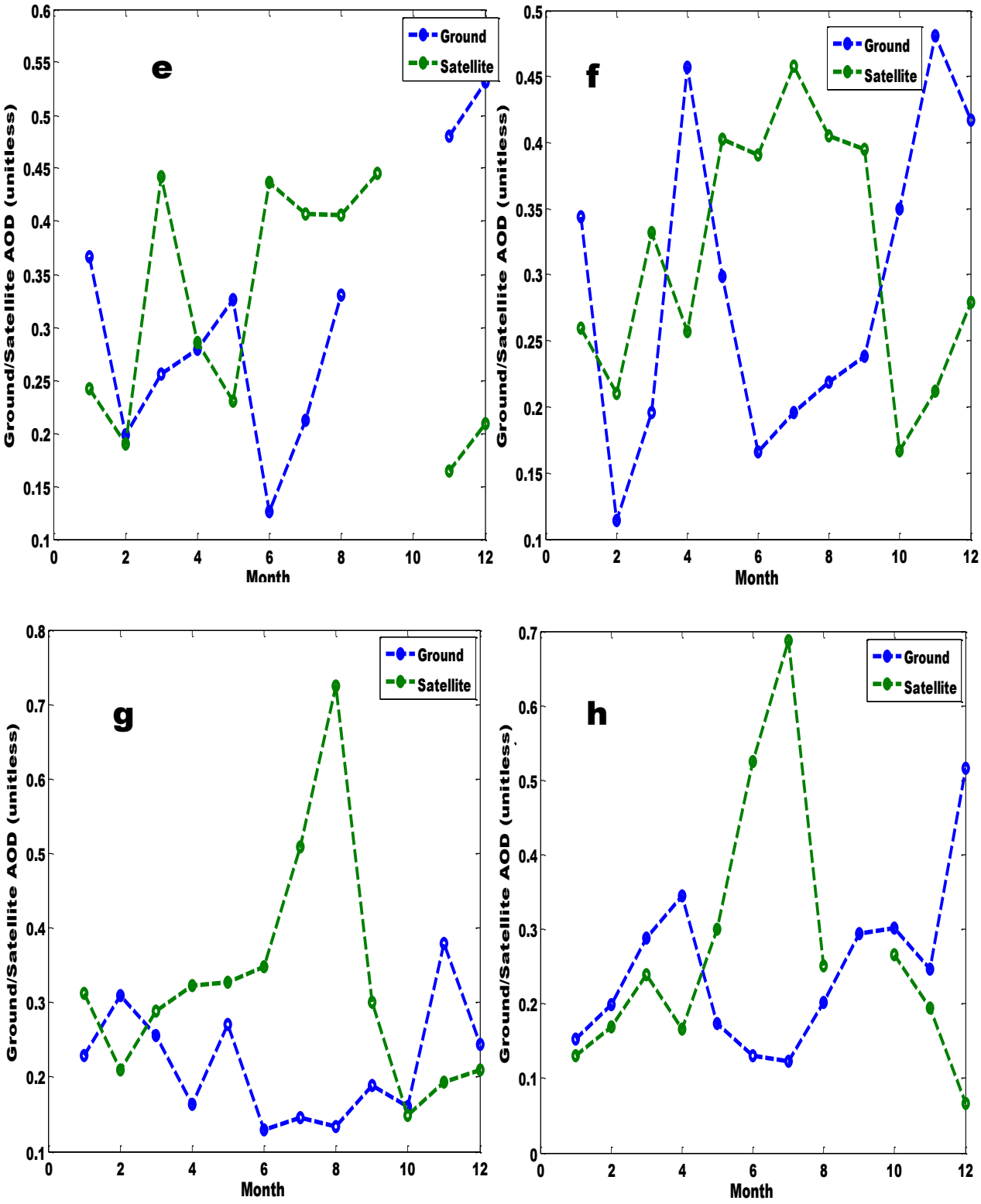

Figure 4.68(e - h): Ground and Satellite observations for (e) 2006 (f) 2007 (g) 2008 (h) 2009 over Praia

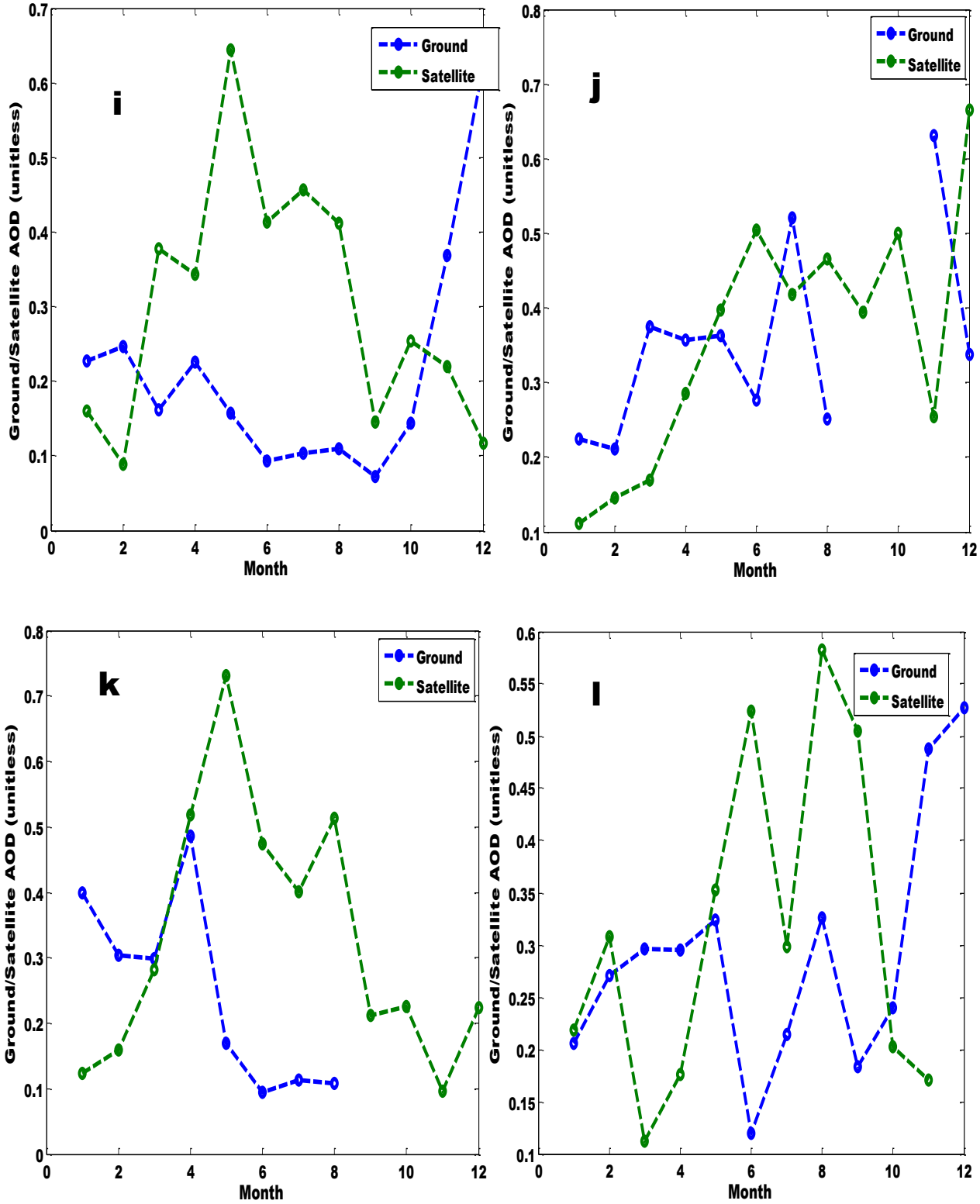

Figure 4.68(i-l): Ground and Satellite observations for (i) 2010 (j) 2011 (k) 2012 (l) 2013 over Praia

It can be inferred that most locations in West Africa had a minimum of 30% aerosol retention within its troposphere between 2003 and 2005. This shows that most aerosols in the troposphere of most locations in West Africa are made up of mainly dust and carbon particulates from biomass burning.

From Tables 4.19 to 4.25, the yellow box signifies the highest value of the ground observation for Praia between 2001 and 2012. The blue box signifies the highest value of the satellite observation for Praia between 2001 and 2012. The green box signifies the lowest value of the ground observation for Praia between 2001 and 2012. The red box signifies the lowest value of the satellite observation for Praia between 2001 and 2012.

The lowest kurtosis for the ground data set was observed in 2004 while the highest was observed in 2010. The maximum kurtoses for the satellite data set was observed in 2001 while the minimum in 2006. The lowest skew for the ground data set over Praia was observed in 2004 while the highest skew for the ground data set was in 2010. The maximum skew for the satellite data set was observed in 2001 while the minimum in 2007. The highest 95% confidence interval for the satellite data set was observed in 2012 while the lowest in 2007. The maximum 95% confidence interval for the ground data set was observed in 2004 while the minimum in 2000.The highest standard error for the satellite data set was observed in 2012 while the lowest in 2007. The maximum standard errors for the ground data set was observed in 2004 while the minimum in 2000. The highest Kolmogorov-Smirnov stat for the satellite data set was observed in 2008 while the lowest in 2010.

The maximum Kolmogorov-Smirnov stat for the ground data set was observed in 2001 while the minimum in 2004. The highest coefficient of variance for the ground data set was observed in 2010 while the lowest in 2000. The maximum coefficients of variance for the satellite data set was observed in 2009 while the minimum in 2007. The highest variance for the ground data set was observed in 2001 while the lowest in 2000. The maximum variances for the satellite data set was observed in 2012 while the minimum in 2007. The highest standard deviation for the ground data set was observed in 2001 while the lowest in 2000. The maximum standard deviations for the satellite data set was observed in 2012 while the minimum in 2007. It is inferred from the statistical results that the corresponding highest standard error for the ground data set in 2004 for Ouagadougou and Praia, may also not be

coincidence. The likely guesses may be that the anthropogenic activities in Ouagadougou and Praia were almost the same. Also, it may be as a result of fast moving aerosol layer which is induced by fast moving cold or warm front.

Table 4.19: Statistical analysis of ground and satellite data sets (Praia)

Statistical Parameters	2000		2001	
	Ground	Satellite	Ground	Satellite
Standard error	0.017	0.054	0.072	0.054
95% confidence interval	0.042	0.123	0.159	0.118
Variance	0.002	0.030	0.062	0.035
Standard deviation	0.045	0.172	0.250	0.186
Coefficient of variation	0.164	0.412	0.677	0.606
Skew	0.775	0.216	1.825	2.065
Kurtosis	-0.384	-1.759	2.219	5.243
Kolmogorov-Smirnov stat	0.194	0.169	0.390	0.226

Table 4.20: Statistical analysis of ground and satellite data sets,Praia

Statistical Parameters	2002		2003	
	Ground	Satellite	Ground	Satellite
Standard error	0.050	0.038	0.034	0.053
95% confidence interval	0.110	0.084	0.075	0.117
Variance	0.030	0.016	0.014	0.034
Standard deviation	0.173	0.126	0.118	0.185
Coefficient of variation	0.577	0.433	0.396	0.497
Skew	1.542	0.502	-0.409	0.402
Kurtosis	2.220	-0.530	-1.126	-1.083
Kolmogorov-Smirnov stat	0.213	0.162	0.134	0.155

Table 4.21: Statistical analysis of ground and satellite data sets (Praia)

Statistical Parameters	2004		2005	
	Ground	Satellite	Ground	Satellite
Standard error	0.108	0.031	0.047	0.034
95% confidence interval	0.343	0.069	0.103	0.074
Variance	0.047	0.012	0.027	0.014
Standard deviation	0.216	0.108	0.163	0.117
Coefficient of variation	0.637	0.383	0.486	0.402
Skew	-0.020	0.002	1.386	0.348
Kurtosis	-0.206	0.330	1.615	-0.992
Kolmogorov-Smirnov stat	0.133	0.160	0.215	0.190

Table 4.22: Statistical analysis of ground and satellite data sets (Praia)

Statistical Parameters	2006		2007	
	Ground	Satellite	Ground	Satellite
Standard error	0.040	0.034	0.035	0.028
95% confidence interval	0.090	0.076	0.076	0.061
Variance	0.016	0.013	0.014	0.009
Standard deviation	0.125	0.113	0.120	0.095
Coefficient of variation	0.404	0.359	0.415	0.304
Skew	0.490	0.021	0.295	-0.043
Kurtosis	-0.243	-2.057	-1.173	-1.453
Kolmogorov-Smirnov stat	0.139	0.246	0.167	0.207

Table 4.23: Statistical analysis of ground and satellite data sets,Praia

Statistical Parameters	2008		2009	
	Ground	Satellite	Ground	Satellite
Standard error	0.023	0.045	0.032	0.055
95% confidence interval	0.050	0.100	0.071	0.122
Variance	0.006	0.025	0.012	0.033
Standard deviation	0.078	0.157	0.111	0.182
Coefficient of variation	0.360	0.485	0.450	0.667
Skew	0.738	1.685	1.230	1.501
Kurtosis	-0.110	3.351	1.955	1.972
Kolmogorov-Smirnov stat	0.175	0.274	0.159	0.256

Table 4.24: Statistical analysis of ground and satellite data sets,Praia

Statistical Parameters	2010		2011	
	Ground	Satellite	Ground	Satellite
Standard error	0.045	0.048	0.042	0.049
95% confidence interval	0.098	0.106	0.095	0.107
Variance	0.024	0.028	0.018	0.028
Standard deviation	0.155	0.167	0.133	0.168
Coefficient of variation	0.732	0.552	0.375	0.468
Skew	1.999	0.537	1.116	0.061
Kurtosis	4.462	-0.210	0.868	-0.683
Kolmogorov-Smirnov stat	0.242	0.137	0.238	0.165

Table 4.25: Statistical analysis of ground and satellite data sets,Praia

Statistical Parameters	2012		2013	
	Ground	Satellite	Ground	Satellite
Standard error	0.052	0.056	0.034	0.048
95% confidence interval	0.123	0.124	0.075	0.108
Variance	0.022	0.038	0.014	0.026
Standard deviation	0.147	0.195	0.118	0.160
Coefficient of variation	0.598	0.591	0.407	0.510
Skew	0.512	0.732	0.886	0.589
Kurtosis	-1.213	-0.275	0.549	-1.049
Kolmogorov-Smirnov stat	0.201	0.204	0.215	0.179

It is inferred from the statistical parameters that the AOD features over Praia is dynamic as the year of highest or lowest value varied within five years. This shows that any changes in the AOD features over Praia can be captured with a minimum of eight years data set.

CHAPTER FIVE

CONCLUSIONS AND RECOMMENDATIONS

5.1. Conclusions

The physics of the Stokes' regime has been examined using the new dispersion model and the unified number derived to determine the aerosol transport. The model was used to examine the aerosol size distribution with a view to comparing the outcome with that of already known model - Eck's Model. The sectional technique was adopted successfully to deduce the dynamic constants which were obtained from the unified number. The proposed Un successfully derived from atmospheric forces which influence the atmospheric aerosols transport was verified. The minute analysis of the wind speed over Lagos shows that the Un captured both the westerly and easterly air masses which determine the aerosol loading or transportation over any geographical location. It was established that at least four modes of aerosol particles exist in Lagos and by extension the West African region, which are coarse mode, nucleation mode, aitken mode and accumulation mode. The coarse mode and portion of nucleation mode can be observed in the afternoon. From literature, biomass burning is a common activity during October to February, which supports the observed high concentration of aerosols in the atmosphere for this period.

In this thesis, it was confirmed that the low total concentration between October and February is due to an extensive effect of larger activity of aerosols agglomeration, coagulation and nucleation during May to July. However, the trend noticed in January to March (JFM) and August to October (ASO) shows a 15% retention of long term aerosol extension generated between October and February.

This research has established the influence of meteorological factors (cloud cover, relative humidity, rainfall) and wind speed on aerosols transport. The mass of aerosol deposited was observed to decay exponentially as the wind speed increases drastically. However, the natural instinct when layers of moving aerosols interact with each other (either chemically or

physically) creates a strange transport pattern that cannot be captured either by ground or satellite observations. This work has been able to prove that the multiple refractive indexes compromise the accuracy of the satellite sensor in determining the AOD of an area as discussed in the text. The coagulation processes of aerosols through inelastic collision do not affect the conservation of the particulate mass per time. Hence if the layer of aerosols travel at about 15 km/hr in the macro scale settings, then the 2D particulate transport derived from the aerosol model can be adjudged to be accurate.

Five evidences showing the effect of superposition on the accuracy of remotely sensed data set was proven. First, it was shown that the green band spectra of the MISR captured the wavelengths of four different bands on the MODIS. Second, it was proven analytically that the relative motion between the moving aerosol layers in the atmosphere and the moving earth creates a multiple refractive index that dictates the superposition event. Third, band superposition may be due to the differential radiation trapped amidst aerosol depth. This explanation is responsible for the inability of the passive ground sensors and satellite imagery to determine the vertical distribution of aerosol layers. Fourth, there were evidences of band superposition theory using seven years aerosol optical depth data set of the coastal region of West Africa where harsh atmospheric perturbations are expected. Fifth, there was evidence of band superposition through a comparative analysis of the ground and satellite stations. Hence, the need for the inclusion of the superposition term in form of phase difference of signals to regional climate models is essential to improve the accuracy of satellite exploration in recent times.

The atmospheric constants for studied locations had been documented for onward reconfiguration of measuring devices over West Africa. The satellite data set were used to generate the tunning constants and phase differences from the theoretical model established in this study. Fourteen years aerosol optical depth measurements were used to validate the transport mechanics and the numerical simulations of aerosols across West Africa. Twenty eight locations in West Africa were examined using the dispersion model. It showed that the estimation of the atmospheric constants over most locations in West Africa has the possibility of over 91% success. The atmospheric constants were classified into three parts; phase difference, tuning constant and atmospheric constant. This simply means that radiosonde and

other measuring instrument could achieve over eighty percent data retrieval if the atmospheric constants reported in this thesis are configured in its compact flash card. Most compact flash card require an in-depth knowledge of python computer programming to configure or recalibrate the device. It was noticed that months of high rainfall has zero or low AOD data because of irregularity in the configuration of the compact flash card inserted in the measuring instrument. It was also observed that most West Africa locations have poor ventilation towards the evening. This leads to the accumulation or retention of aerosols in the atmosphere.

One of the salient discoveries in this research was the aerosols loading and retention over selected ground stations in West Africa. The satellite and ground observation shows that Ilorin and Ouagadougou has the same aerosols loading for 2000 and 2001. This means almost the same event which occurred in Ilorin and Ouagadougou between 2001 and 2002 might have occurred generally in most locations in West Africa except Praia. The ground and satellite observation over Praia contradicts each other between June and October. In this case, it is suggested that Praia AOD pattern is dominated by the stratospheric aerosols which may engender from the influence of oceanic winds to promote the escape of the tropospheric aerosols into the stratosphere. Other locations besides Praia that showed wide variations between satellite and ground observations are Lagos and Ouagadougou. The reasons for the variations between satellite and ground observations had been discussed in the previous sections. In addition to what is already known through literatures, this thesis suggests that the reasons for the variation between satellite and ground observations is due to atmospheric aerosols retention. It was established that aerosols retention over West Africa is high because of poor ventilation in the evening and it is dependent on the type of aerosols, life-time of the aerosols, wind dynamics and aerosols size distribution.

The aerosols retention was calculated using the ground stations in West Africa region. The aerosols retention over West Africa had a minimum of 30% aerosols retention within its lower atmosphere between 2003 and 2005. It was discovered that the aerosols in most locations in West Africa are made up of mainly dust and carbon particulates from biomass burning. However, the aerosols retention was as high as 79% over some regions like Ouagadougou in 2002. This is a peculiar situation which affirmed high aerosols dispersion in

the evenings. For instance, the aerosols retention can be as low as 0.25% over some regions like Praia in 2002. Aerosols retention may distort radiosonde performance over time, such as the case of Ouagadougou. The aerosols retention over Ilorin and Praia is comparatively low due to moderate ventilations in the evenings.

It was also affirmed that aerosol loadings can be affected by rain rate over geographical regions. High rain rate influences AOD retrievals over West Africa. It is however possible for a geographical area to have high rainfall and AOD retrievals provided the rain rate is low. The first supportive model, that is, meteorological model is recommended to retrieve data under the high rain rate condition. It was discovered through the second supportive model, that is, the statistical model that the AOD features over Ilorin is dynamic, hence, the retrieval of the atmospheric constants should be captured within a minimum of eight years. It was also concluded from the statistical model that the AOD features over Ouagadougou and Praia are dynamic, hence, the atmospheric constants over Ouagadougou and Praia can be captured within a minimum of five and seven years respectively.

A theoretical model was developed upon the function of selected meteorological parameters. The model was successfully used to determine the aerosol optical depth over a geographical location. The second advantage of the first supportive model (meteorological model) is its ability to retrieve missing data over any tropical location provided the meteorological data of the geographical location is known. The study was accurate, however, due to climate change challenges; it should not be substituted for adequate provision of radiosonde station across West Africa.

The unified number was derived with the basic intention to determine the aerosols flow patterns in different atmospheric situations. The unified number captured the physics of different atmospheric forces which are dynamic in nature. The Reynolds and Knudsen numbers could account only for the inertia and viscous forces. As shown in the derivations of the unified number, the participating forces in the atmospheric fields are more than the inertia and viscous forces. The unified number to a large extent captured the chaotic nature of aerosols in the West Africa atmospheric space. Like fluids, the chaotic nature of aerosols could influence different aerosols transport by very small changes in aerosols size or shape. It was used to compliment the aerosol dispersion model to determine the aerosol size

distribution over Lagos-Nigeria. Determination of aerosol size distribution is a major challenge in atmospheric science and has been resolved using the unified number.

The height parameter in the unified number enables it to be used for calculating lift, drag, or other aerodynamic properties. Aerodynamic forces are somewhat complex to calculate because of the interaction between objects and the viscosity of the gas. Hence, the introduction of the unified number is a major contribution to knowledge because it is of great importance to the aviation industry. The efficiency of dam design and construction can now be examined and evaluated using lesser complex equations. Like the Reynolds number, the unified number can be used in the Navier-Stokes equations to determine engineering solutions. In conclusion, the incorporation of aerosols dispersion model and unified number can be used by sonde manufacturers to determine the tuning constants of measuring instruments.

Therefore, the comprehensive model which is made up of two main and two supportive models have shown high level of success using available data sets in West Africa. The models is expected to compliment each other when utilized. Meteorological centers can adopt the comprehensive model to obtain aerosols data all year round. The four models which makes up the comprehensive model was developed to withstand harsh weather conditions.

It is important to note that this thesis has significant application to the ITU model because it suggests an alteration in its formular shown in equation (5.1)

$$N = \frac{77.6P}{T} + 3.73 \times 10^5 \frac{e}{T^2} = N_{dry} + N_{wet} \ \ (N - units) \qquad (5.1)$$

where e is the water vapour pressure (hPa) , P is the atmospheric pressure (hPa) and T is the temperature (K), N is the total surface refractivity. The mathematical relationship between relative humidity and water vapour pressure is expressed as:

$$e = \frac{RH}{100} a \, exp\left[\frac{bT}{T + c}\right] \qquad (5.2)$$

Here T is the temperature in the above equation is given in ℃ and the coefficients a, b and c takes the following values: a = 6.1121, b = 17.502, and c = 240.97. Since the study proposes an inclusion of the attenuation due to moving aerosols layer into the ITU model, further

study is required for the appropriate calculation of coefficients a, b and c which are influenced by the optical state over a geographical location.

5.2: Contributions to Knowledge

The thesis proposed the following contributions:

i. Low total number of aerosols concentration between October and February over the West Africa is due to an extensive effect of larger activity of agglomeration, coagulation and nucleation during May to July;
ii. A new 2D and 3D dispersion models was enacted and tested. The 2D model showed over 95% success in all the twenty eight locations in West Africa;
iii. The unified number was derived to complement the existing Reynolds and Knudsen numbers and has wide application to the aviation and engineering fields
iv. A working model have been suggested for meteorological centers
v. A parametric analytical technique was propounded for studying aerosol size distribution;
vi. A clear aerosol transport pattern in West Africa has been suggested;
vii. The documentation of atmospheric constants for aiding measuring devices was highlighted.
viii. Parameterization of bands of either a satellite or ground sensor to individually determine the aerosol size distribution over a specific area per time.

5.3: Recommendations

i. The West African region can be regarded as the deposition site for global atmospheric influences. Though there have been significant successes in the meteorological exploration of West Africa, much need to be known about the past and present activities of the West African monsoon. The successes and challenges of the meteorological exploration in the region have been discussed to revamp the existing ground stations and possibly increase their number. Recently, meteorologically driven accidents in the world (for example, the excessive heat flux over India this year) are indication that only about 30% of information is available for nowcast or forecast

especially in the region. Hence, the urgent need to embark on a massive information driven project within the region is imminent. Active participation of the government of the West Africa countries and an uncompromised synergy of all funded projects within the region might help us avert or mitigate meteorological accidents in the future.

ii. All measuring devices imported for use in West Africa should be configured by rewriting the soft codes in the compact flash to reflect the atmospheric constants, tuning constants and phase difference. This operation would definitely improve upon the volume of data retrieved throughout the year with minimum missing data. Since, aerosols dispersion is dynamic-as shown in the main thesis; it is therefore wise for scientist to perform a re-documentation of atmospheric constant every five to ten years.

iii. In the course of the study, it was established that ventilation is poor in the evening and it leads to accumulation of atmospheric aerosols. Since the predominant source of pollution in West Africa aside the natural source is biomass burning, it is recommended that anthropogenic pollution in residential areas should be restricted to the daytime hours.

iv. Anthropogenic pollution can be curbed by adopting a national policy which encourages the use of clean or free energy source for domestic use. This includes the use of biomass stoves, solar or wind energy applications, bio-fuels, free energy sources like thermal energy generators, electromagnetic field generators.

v. Traffic congestion should be minimized by encouraging inhabitants to travel more with mass public transport.

REFERENCES

Accuweather, (2015). http://www.accuweather.com/en/ng/kano/253466/weather-forecast/253466 (Acessed 23rd June, 2015)

Adebiyi, A.A., Paquita, Z. and Steven, J.A., (2015). The convolution of dynamics and moisture with the presence of shortwave absorbing aerosols over the southeast atlantic. *Journal of Climate* **28**: 1997–2024.

Adon, M., Galy-Lacaux, C., Yoboue, V., Delon, C., Lacaux, J.P., Castera, P., Gardrat, E., Pienaar, J., Al Ourabi, H., Laouali, D., Diop, B., Sigha-Nkamdjou, L., Akpo, A., Tathy, J.P., Lavenu, F. and Mougin, E., (2010). Long term measurements of sulfur dioxide, nitrogen dioxide, ammonia, nitric acid and ozone in Africa using passive samplers. *Atmospheric Chemistry and Physics Discussion* **10**: 4407–4461

Ahmada, O.A., (2011). Modeling the dispersion of atmospheric pollutants dispersion using two dimensional advection diffusion equation, masters project submitted to University of Dar es Salaam. pp. 1-88.

Akinyemi, M.L., (2007). The influence of some atmospheric phenomena on total ozone concentration over the tropics. *Australian Journal of Basic and Applied Science*, **1 (4)**: 497-505.

Aloyan, A.E., Arutyunyan, V.O., Yermakov, A.N., Zagaynov, V.A., Mensink, C., De, K., Ridder, K. and Van de Vel, F. D., (2012). Modeling the regional dynamics of gaseous admixtures and aerosols in the areas of lake Baikal (Russia) and Antwerp (Belgium). *Aerosol and Air Quality Research* **12**: 707–721.

Antonnikova, A., Natalya, K., Olga, K., (2013). Sedimentation of superfine aerosol by means of ultrasound. *Open Journal of Acoustics* **3**: 16-20.

Asmi, E., Kondratyev, V., Brus, D., Laurila, T., Lihavainen,H., Backman, J., Vakkari, V., M. Aurela, J. Hatakka, Y. Viisanen, T. Utta, V. Ivakhov, and A. Makshtas, (2015). Aerosol size distribution seasonal characteristics measured in Tiksi, Russian Arctic, *Atmospheric Chemistry Physics Discussion* **15**: 18109–18149

Bègue, N., Tulet, P., Pelon, J., Aouizerats, B., Berger, A. and Schwarzenboeck, A., (2015). Aerosol processing and CCN formation of an intense Saharan dust plume during the EUCAARI 2008 campaign. *Atmospheric Chemistry Physics* **15**: 3497-3516.

Belen, R.F., Elsa, M., Carlos, R., Mechoso, C.C., Michela, B., Marco, Gaetani, J.G.S., Edward, K., Vizy, K.C., Yongkang, X., Irene, P., Losada, T., Druyan, T., Bernard, F., Juergen, B., Francisco, J.D.R., Goddard, L., Janicot, S., Alberto, A., William, L., Andrew, C.M., Vellinga, D.P., Rowell, F.K. and Voldoire, A., (2015). Variability and predictability of West African droughts: a review on the role of sea surface temperature anomalies, *Journal of Climate* **28**: 4034–4060.

Benson, D.A., Wheatcraft, S.W. and Meerschaert, M.M., (2000). Application of a fractional advection-dispersion equation. *Water Resources Research* **36 (6)**: 1403–1412.

Bjourn, S., (2015). Rethinking the lower bound on aerosol radiative forcing. *Journal of Climate* **28**: 4794–4819

Bock, O., Bouin, M-N, Doerflinger, E., Collard, P., Masson, F., Meynadier, R., Nahmani, S., Koit, M., Gaptia, L.B.K., Did, F., Ouedraogo, D., Pokperlaar, S., Ngamini, J.-B., Lafore, J.P., Janicot, S., Guichard, F. and Nuret, M., (2008). The West African monsoon observed with ground based GPS receivers during AMMA. *Journal of Geophysical Research* **113**: D21105.

Bojanowski, J.S., Stöckli, R., Anke, T. and Heike, K., (2014). The impact of time difference between satellite overpass and ground observation on cloud cover performance statistics. *Remote Sensing* **6**: 12866-12884.

Boucher, O. and Quaas, J., (2013). Water vapour affects both rain and aerosol optical depth, *Nature Geosciences* **6**: 4–5

Brian Everitt, (1998). The Cambridge Dictionary of Statistics. Cambridge, UK New York: Cambridge University Press. ISBN 0521593468.

Brown, A., (2012). Aerosol choices matter. *Nature Climate Change* **2**: 75-79.

Brown Stan, (2016). http://brownmath.com/stat/shape.htm (Acessed on 20th January, 2016)

Burns, E., (1996). Results of 2-dimensional sandbox experiments: longitudinal dispersivity determination and seawater intrusion of coastal aquifers, Master's Research, University of Nevada, Reno. 1-67.

Calvello, M., Esposito, F., Pavese, G. and Serio, C., (2010). Physical and optical properties of atmospheric aerosols by in-situ and radiometric measurements, *Atmospheric Chemistry Physics* **10**: 2195-2208.

Cao, J.-J., Zhu, C.-S., Tie, X.-X., Geng, F.-H., Xu, H.-M., Ho, S.S.H., Wang, G.-H., Han, Y.-M. and Ho, K.-F., (2013). Characteristics and sources of carbonaceous aerosols from Shanghai, China. *Atmospheric Chemistry Physics* **13**: 803-817.

Che, H., Xia, X., Zhu, J., Li, Z., Dubovik, O., Holben, B., Goloub, P., Chen, H., Estelles, V., Cuevas-Agulló, E., Blarel, L., Wang, H., Zhao, H., Zhang, X., Wang, Y., Sun, J., Tao, R., Zhang, X. and Shi, G., (2014). Column aerosol optical properties and aerosol radiative forcing during a serious haze-fog month over North China plain in 2013 based on ground-based sunphotometer measurements. *Atmospheric Chemistry Physics* **14**: 2125-2138

Choo-in, S., (2001). Mathematical model for determining carbon monoxide and nitrogen oxide concentration in street tunnel. M.Sc. Research, Thammasat University, Thailand. 1-67.

Daitche, A. and Tamás, T., (2014). Memory effects in chaotic advection of inertial particles. *New Journal of Physics*, **16**: 073008, 1-35.

Dani, K.K., Maheskumar, R.S., and Devara, P.C.S., (2003). Study of total column atmospheric aerosol optical depth, ozone and precipitable water content over Bay of Bengal during BOBMEX-99. *Journal of Earth System Science* **112 (2)**: 205-221.

Das, S.K., Chen, J.-P., Venkat, R.M. and Jayaraman, A., (2013). Investigation of radiative effects of the optically thick dust layer over the Indian tropical region. *Annales Geophysicae* **31**: 647-663.

Doraiswamy, P., Hoegrefe, C., Hao, W., Civerelo, K., Ku J.Y. and Sistla, G., (2010). A retrospective com-parison of model based forecasted PM2.5 concentrations with measurements. *Journal of Air and Waste Management Association* **60 (11)**: 1293-1308.

Eck, T.F., Holben, B.N., Reid, J.S., Dubovik, O., Smirnov, A., O'Neill, N.T., Slutsker, I. and Kinne, S., (1999). Wavelength dependence of the optical depth of biomass burning, urban and desert dust aerosols. *Geophysical Research Letter* **104**: 31333-31350.

Faccani, C., Rabier, F., Fourrie, N., Agust´ı-Panareda, A., Karbou, F., Moll, P., Lafore, J.P., Nuret, M., Hdidou, F.Z. and Bock, O., (2009). The impact of the AMMA radiosonde

data on the French global assimilation and forecast system. *Weather and Forecasting*, **24**: 1268–1286.

Falaiye, A.O., Babatunde, E.B. and Willoughby, A.A., (2015). Atmospheric aerosol loading at Ilorin, a tropical station. *The African Review of Physics* **9 (1)**: 527-535

Ferreira, J., Reeves, C.E., Murphy, J.G., Garcia-Carreras, L., Parker, D.J., and Oram, D.E., (2010). Isoprene emissions modelling for West Africa using MEGAN. *Atmospheric Chemistry and Physics* **10**: 6923–6953.

Feedthenation, (2015). http://www.feedthefuture.gov/country/west-africa-regional (Acessed on 20th June, 2015).

Fioletov, V.E., Bodeker, G.E., Miller, A.J., McPeters, R.D. and Stolarski, R., (2002). Global and zonal total ozone variations estimated from ground-based and satellite measurements: 1964–2000, *Journal of Geophysical Research* **107 (D22)**: 4647-4651.

Fitzgerald, J.W., (1989). Model of the aerosol extinction profile in a well-mixed marine boundary layer. *Applied Optics* **28 (15)**: 3534-3538.

Garabedian, S.P., LeBlanc, D.R., Gelhar, L.W., and Celia, M.A., (1991). Analysis of spatial moments for a nonreactive tracer, *Water Resources Research* **27 (5)**: 911–924

Gazala, H., Venkataraman, C., Isabelle C., Ramachandran, S., Olivier, B. and Shekar, M.R., (2006). Seasonal and interannual variability in absorbing aerosols over India derived from TOMS: Relationship to regional meteorology and emissions. *Atmospheric Environment* **40**: 1909–1921.

Gbadebo, A.M. and Amos, A.J., (2010). Assessment of radionuclide pollutants in bedrocks and soil Ewekoro cement factory, southwest Nigeria. *Asian Journal of Applied Sciences* **2010**: 1-10

Giglio, L., Randerson, J.T., van der Werf, G.R., Kasibhatla, P.S., Collatz, G.J., Morton, D.C. and DeFries, R.S., (2010). Assessing variability and long-term trends in burned area by merging multiple satellite fire products. *Biogeosciences* **7**: 1171-1186.

Gouw, J.A., Warneke, C., Stohl, A., Wollny, A.G., Brock, C.A., Cooper, O.R., Holloway, J.S., Trainer, M., Fehsenfeld, F.C., Atlas, E.L., Donnelly, S.G., Stroud, V. and Lueb, A., (2006). Volatile organic compounds composition of merged and aged forest fire plumes from Alaska and western Canada. *Journal of Geophysical Research* **111**: D10303, 1-8.

Guzzi, R., Rizzi, R. and Zibordi G., (1987). Atmospheric correction of data measured by a flying platform over the sea: elements of a model and its experimental validation. *Applied Optics* **26 (15)**: 3043-3051.

Gwen A. L. and Cederwall, R.T., (2004). Precipitation scavenging of atmospheric aerosols for emergency response applications: testing an updated model with new real-time data. *Atmospheric Environment* **38**: 993–1003.

Hansen, J., Sato, M. and Ruedy, R., (1997). Radiative forcing and climate response. *Journal of Geophysical Research* **102**: 6831–6864.

Hatano M., Seungjae M. and Minghong L., (2000), Excimer Laser-Induced Temperature Field in Melting and Resolidification of Silicon Thin Films, *Journal of Applied Physics* **87**: 36-43.

Hasebe, F. and Noguchi, T., (2015). A Lagrangian description on the troposphere-to-stratosphere transport changes associated with the stratospheric water drop around the year 2000. *Atmospheric Chemistry and Physics* **15**: 28037-28068.

Haywood, J.M., Pelon, J., Formenti, P., Bharmal, N.A., Brooks, M., Capes, G., Chazette, P., Chou, C., Christopher, S., Coe, H., Cuesta, J., Derimian, Y., Desboeufs, K., Greed, G., Harrison, M., Heese, B., Highwood, E.J., Johnson, B.T., Mallet, M., Marticorena, B., Marsham, J., Milton, S., Myhre, G., Osborne, S.R., Parker, D.J., Rajot, J.-L., Schulz, M., Slingo, A., Tanre, D. and Tulet, P., (2008). Overview of the dust and biomass burning experiment and African monsoon, multidisciplinary analysis special observing period-0. *Journal of Geophysical Research* **113**: D00C06, 1-12.

He, Q., Li, C., Geng, F., Yang, H., Li, P., Li, T., Liu, D. and Pei, Z. (2012). Aerosol optical properties retrieved from Sun photometer measurements over Shanghai, China. *Journal of Geophysical Research* **117**: D16204, 1-8.

Holmes, N.S. and Morawska, L., (2006). A review of dispersion modeling and its application to the dispersion of particles: an overview of different dispersion models available. *Atmospheric Environment* **40 (30)**: 5902-5928.

Hommel, R., Timmreck, C., Giorgetta, M.A. and Graf, H.F., (2015). Quasi-biennial oscillation of the tropical stratospheric aerosol layer. *Atmospheric Chemistry Physics* **15**: 5557-5584.

Huang Y. and Dejun L., (2014). Soil nitric oxide emissions from terrestrial ecosystems in China: a synthesis of modeling and measurements. *Scientific Reports* **4**: 7406, 1-8.

Hussein T., Puustinen, A., Aalto, P. P., Makela, J. M., Hameri, K. and Kulmala, M. (2004). Urban aerosol number size distributions. *Atmospheric Chemistry and Physics* **4**: 391–411.

IPCC, (2007). Summary for policymakers, fourth assessment report of the intergovernmental panel on climate change, Cambridge University Press, Cambridge, United Kingdom and New York, NY, USA. pp. 78

Jackson, L.S., Crook, J.A., Jarvis, A., Leedal, D., Ridgwell, A., Vaughan, N. and Forster, P.M., (2015). Assessing the controllability of Arctic sea ice extent by sulphate aerosol geoengineering. *Geophysical Research Letters*, **42**: 1223–1231.

Janicot, S., Caniaux, G., Chauvin, F., de Coëtlogon, G., Fontaine, B., Hall, N. and Kiladis, G., (2011). Intraseasonal variability of the West African monsoon. *Atmospheric Science Letters*, **12**: 58–66.

Jewtoukoff, V., Plougonven, R. and Hertzog, A., (2013). Gravity waves generated by deep tropical convection: estimates from balloon observations and mesoscale simulations. *Journal of Geophysical Research Atmospheric*, **118**: 9690–9707.

Kouadio, K., Konare, A., Diawara, A., Dje, B.K., Ajayi, V.O. and Diedhiou, A., (2015). Assessment of regional climate models over Côte D'Ivoire and analysis of future projections over West Africa. *Atmospheric and Climate Sciences*, **5**: 63-81.

Kumar, D., Kumar, A., Kumar, V., Rao, K.S. and Kumar, J., (2011) Study of atmospheric stagnation, recirculation, and ventilation potential at Narora Atomic Power Station site. *Radiation Protection Environment*, **34**: 104-109.

Kumierczyk-Michulec, J., (1993). The aerosol optical thickness of the atmosphere over the Norwegian Sea obtained from different experimental data. *Oceanologia*, **34**: 27-37.

Lélé, M.I., Lance M.L., and Peter J.L., (2015). Analysis of Low-Level Atmospheric Moisture Transport Associated with the West African Monsoon. Journal of Climate, **28**: 4414–4430.

Libault, M., (2014). The carbon-nitrogen balance of the nodule and its regulation under elevated carbon dioxide concentration. *BioMed Research International*, **2014**: 507946, 1-7.

Li, J., Min, Q., Peng, Y., Sun, Z. and Zhao, J.-Q., (2015). Accounting for dust aerosol size distribution in radiative transfer. *Journal of Geophysical Research Atmosphere*, **120**: 6537–6550.

Lindén, J., Thorsson, S., Boman, R. and Holmer, B., (2012). Urban climate and air pollution in Ouagadougou, Burkina Faso: an overview of results from five field studies, University of Gothenburg, http://hdl.handle.net/2077/34289, 1-88.

Liu, Y., Wang, Z., Wang, J., Ferrare, R., Newsom, R. and Welton, E., (2011). The effect of aerosol vertical profiles on satellite-estimated surface particle sulphate concentrations. *Remote Sensing of Environment,* **115 (2)**: 508-513.

Liu, J. and Zhanqing, L., (2014). Estimation of cloud condensation nuclei concentration from aerosol optical quantities: influential factors and uncertainties. *Atmospheric Chemistry Physics*, 14: 471–483.

Lohmann, U., Feichter, J., Penner, J. and Leaitch, R., (2000). Indirect effect of sulphate and carbonaceous aerosols: A mechanistic treatment. *Journal Geophysical Research*, **105 (12)**: 193–206

Lovejoy E.R., Curtius J. and Froyd K.D., (2004). Atmospheric ion-induced nucleation of sulphuric acid and water. *Journal of Geophysical Research*, **109**: D08204, 1-8.

Mansel, E. and Ziegler, C. L., (2013). Aerosol effects on simulated storm electrification and precipitation in a two-moment bulk microphysics model. *Journal of Atmospheric Science*, **70**: 2032–2050

Mari C´eline H., Claire E. Reeves, Katherine S. Law, G´erard Ancellet, Maria Dolores Andr´es-Hern´andez, Brice Barret, Joelle Bechara, Agn`es Borbon, Idir Bouarar, Francesco Cairo, Roisin Commane, Claire Delon, Matthew J. Evans, Federico Fierli, C´edric Floquet, Corinne Galy-Lacaux,1 Dwayne E. Heard, Carine D. Homan, Trevor Ingham, Niels Larsen, Alastair C. Lewis, Catherine Liousse, Jennifer G. Murphy, Emiliano Orlandi, David E. Oram, Marielle Saunois, Dominique Serca, David J. Stewart, Daniel Stone,Valerie Thouret, Peter van Velthoven and Jason E. W., (2011). Atmospheric composition of West Africa: highlights from the AMMA international program. *Atmospheric Science Letters*, **12**: 13–18.

Marsham, J.H., Dixon, N., Garcia-Carreras, L., Lister, G.M.S., Parker, D.J., Knippertz, P., and Birch, C., (2013). The role of moist convection in the West African monsoon

system: insights from continental-scale convection-permitting simulations. *Geophysical Research Letter*, **40**: 1843–1849.

Madhu, V., (2014). Variation of zonal winds in the upper troposphere and lower stratosphere in association with deficient and excess Indian summer monsoon scenario. *Atmospheric and Climate Sciences*, **4**: 685-695.

Marticorena, B., Haywood, J., Coe, H., Formenti, P., Liousse, C., Mallet, M. and Pelon, J., (2011). Tropospheric aerosols over West Africa: highlights from the AMMA international program. *Atmospheric Science Letter*, **12**: 19–23.

McKibbin, R., (2008). Mathematical modeling of aerosol transport and deposition: Analytic formulae for fast computation, *Proceedings of International Congress On Environmental Modeling*, pp 1420-1430.

Mikhalev, A.V., Mikhail A.T., Chernigovskaya, M.A. and Yu, A., (2003). Erythemal ultraviolet radiation as deduced from data of ground-based and satellite measurements, Ninth Joint International Symposium on Atmospheric and Ocean Optics/Atmospheric Physics: Part II. *Proceedings of SPIE*, **5027**: 258-266.

Mohr, K. I., (2004). Interannual, Monthly, and Regional Variability in the Wet Season Diurnal Cycle of Precipitation in Sub-Saharan Africa. *Journal of Climate*, **17**: 2441–2453.

Moroni, B., Becagli, S., Bolzacchini, E., Busetto, M., Cappelletti, D., Crocchianti, S., Ferrero, L., Frosini, D., Lanconelli, C., Lupi, A., Maturilli, M., Mazzola, M., Perrone, M.G., Sangiorgi, G., Traversi, R., Udisti, R., Viola, A. and Vitale, V., (2015). Vertical profiles and chemical properties of aerosol particles upon Ny-Ålesund (Svalbard Islands). *Advances in Meteorology*, **2015**: 292081, 1-11.

Nabat, P., Somot, S., Mallet, M., Michou, M., Sevault, F., Driouech, F., Meloni, D., di Sarra, A., Di Biagio, C., Formenti, P., Sicard, M., Léon, J.-F. and Bouin, M.-N., (2015). Dust aerosol radiative effects during summer 2012 simulated with a coupled regional aerosol–atmosphere–ocean model over the Mediterranean. *Atmospheric Chemistry and Physics*, **15**: 3303-3326.

NASA (2015). http://visibleearth.nasa.gov/view.php?id=1043 (Acessed 23rd June, 2015)

Nicholson Sharon E., (2013). The West African sahel: a review of recent studies on the rainfall regime and its interannual variability. *ISRN Meteorology*, **2013**: 453521, 1-32.

Nnaemeka, D.C., Okechukwu, K.N., Theo, C.C., Ezekiel, O.E. and Victor, N.D., (2015). Implications of MODIS impression of aerosol loading over urban and rural settlements in Nigeria: possible links to energy consumption patterns in the country. *Atmospheric Pollution Research* **6 (1)**: 484-494.

NOAA, (2015). http://www.esrl.noaa.gov/gmd/outreach/lesson_plans/ (Acessed 23rd June, 2015)

Norris, S.J., Ian, M.B. and Dominic, J.S., (2013). A wave roughness Reynolds number parameterization of the sea spray source flux. *Geophysical Research Letters*, **40**: 4415–4419.

Nuret, M., Lafore, J.P., Bock, O., Guichard, F., Agust´ı-Panareda, A., Ngamini, J.B. and Redelsperger, J.L., (2008). Correction of humidity bias for Vaısala RS80 sondes during AMMA 2006 Observing Period. *Journal of Atmospheric and Oceanic Technology* **25**: 2152–2158.

Ogungbenro, S.B., and Tobi, E.M., (2014). Rainfall distribution and change detection across climatic zones in Nigeria, *Weather and Climate Extremes*, **5–6**: 1–6

Okonkwo, C., (2014). An advanced review of the relationships between Sahel precipitation and climate indices: a wavelet approach. *International Journal of Atmospheric Sciences*, **2014**: 759067, 1-11

Oluwole, O.S.A., (2015). Climate regimes, El Niño-Southern oscillation and konzo epidemics. *Frontiers in Environmental Sciences*, **3**: 40, 1-9

Ourafrica, (2015). Ivory Coast, http://www.our-africa.org/ivory-coast/climate-agriculture (Acessed 23rd May, 2015)

Palluconi, F.D. and Meeks, G.R., (1985). Thermal infrared multispectral scanner (TIMS): an investigator's guide to TIMS data, Jet Propulsion Laboratory publication, pp 85–92.

Polcher, J., Parker, D.J., and Gaye, A.T., (2011). African Monsoon Multidisciplinary Analysis: an integrated project for understanding of the West African climate system and its human dimension. *Atmospheric Science Letter*, **12**: 1-8.

Rajeev, K., Ramanathan,V. and Meywerk, J., (2000). Regional aerosol distribution and its long-range transport over the Indian Ocean. *Journal of Geophysical Research*, **105 (2)**: 2029–2043.

Reeves, C. E., Formenti, P., Afif, C., Ancellet, G., Attie, J.L., Bechara, J., Borbon, A., Cairo, F., Coe, H., Crumeyrolle, S., Fierli, F., Flamant, C., Gomes, L., Hamburger, T., Lambert, C., Law, K.S., Mari, C., Matsuki, A., Methven, J., Mills, G.P., Minikin, A., Murphy, J.G., Nielsen, J.K., Oram, D.E., Parker, D.J., Richter, A., Schlager, H., Schwarzenboeck, A. and Thouret, V., (2010). Chemical and aerosol characterisation of the troposphere over West Africa during the monsoon period as part of AMMA. *Atmospheric Chemistry and Physics*, **10**: 7115–7183.

Sagert, I., Jim, H., Alec, S., Terrance, S., Dirk, C. and Wolfgang, B., (2015). Knudsen-number dependence of two-dimensional single-mode Rayleigh-Taylor fluid instabilities. *Physical Review E* **92**: 013009.

Samko, S.G., Kilbas, A.A. and Marichev, O.I., (1993). Fractional integrals and derivatives: theory and applications, Gordon and Breach Science Publisher, Yverdon, pp. 376-388.

Sanusi, Y.K. and Abisoye, S.G., (2011). Estimation of wind energy potential in Southwestern Nigeria. *The Pacific Journal of Science and Technology*, **12(2)**: 160-166.

Sauvage, B., Thouret, V., Cammas, J.-P., Gheusi, F., Athier, G. and Nedelec, P., (2005). Tropospheric ozone over Equatorial Africa: regional aspects from the MOZAIC data. *Atmospheric Chemistry Physics*, **5**: 311– 335.

Schotland, R.M. and Lea, T.K., (1986). Bias in a solar constant determination by the Langley method due to structured atmospheric aerosol. *Applied Optics*, **25**: 2486-2492.

Segele, Z.T., Leslie, L.M. and Tarhule, A.A., (2015). Sensitivity of Horn of Africa rainfall to regional sea surface temperature forcing. *Climate*, **3**: 365-390.

Seinfeld, J.H. and Pandis, S.N., (1998). Atmospheric chemistry and physics: from air pollution to climate change, 1st edition, J. Wiley, New York., pp. 101-141.

Shunsuke, N., (2004). http://chem.atmos.colostate.edu/shun/research.htm (Acessed 11th September, 2015)

Sicard, M., D'Amico, G., Comerón, A., Mona, L., Alados-Arboledas, L., Amodeo, A., Baars, H., Belegante, L., Binietoglou, I., Bravo-Aranda, J. A., Fernández, A. J., Fréville, P., García-Vizcaíno, D., Giunta, A., Granados-Muñoz, M. J., Guerrero-Rascado, J. L., Hadjimitsis, D., Haefele, A., Hervo, M., Iarlori, M., Kokkalis, P., Lange, D., Mamouri, R. E., Mattis, I., Molero, F., Montoux, N., Muñoz, A., Muñoz Porcar, C., Navas-Guzmán, F., Nicolae, D., Nisantzi, A., Papagiannopoulos, N., Papayannis, A., Pereira,

S., Preibler, J., Pujadas, M., Rizi, V., Rocadenbosch, F., Sellegri, K., Simeonov, V., Tsaknakis, G., Wagner, F. and Pappalardo, G., (2015). EARLINET: potential operationality of a research network. *Atmospheric Measurement and Technology*, **8**: 6599-6659.

Spada, M., Jorba, O., Perez García-Pando, C., Janjic, Z. and Baldasano, J.M., (2015). On the evaluation of global sea-salt aerosol models at coastal/orographic sites. *Atmospheric Environment*, **101**: 41-48.

Srivastava, P.K., Majumdar, T.J. and Bhattacharya, A.K., (2010). Study of land surface temperature and spectral emissivity using multi-sensor satellite data. *Journal of Earth Systemic Science*, **119 (1)**; 67–74.

Sun, W.Y., Yang, K.J.S. and Lin, N.H., (2013). Numerical simulations of asian dust-aerosols and regional impacts on weather and climate- Part II: PRCM-dust model simulation. *Aerosol and Air Quality Research*, **13**: 1641–1654.

Tageo, (2015). countries, http://www.tageo.com/index-e-gh-cities-GH.htm(Acessed 3rd October, 2015)

Thongmoon, M., McKibbin, R., and Tangmanee, S., (2007). Numerical solution of a 3-D advection-dispersion model for pollutant transport. *Thai Journal of Mathematics*, **5 (1)**: 91-108.

Unaka, J.N., (2014).The Cape Verde Project: teaching ecologically sensitive and socially responsive design, A Ph.D thesis submitted to University of Wisconsin Milwaukee, pp.1-459.

UNEP, (2015). Benin Summary Project Site, www.unep.org/.../Eng-BENIN(Acessed 3rd October, 2015)

UNEP, (2011). Nairobi UN Habitat, State of African Cities 2010, Governance, Inequalities and Urban Land Markets pp. 122.

UNISDR, (2007). Guinea-Bissau: National programme of action of adaptation to climate changes, http://www.preventionweb.net/english/professional/policies/v.php?id=21647 (Acessed 3rd October, 2015)

Uno, I., Wang, Z., Chiba, M., Chun, Y.S., Gong, S.L., Hara, Y., Jung, E., Lee, S.S., Liu, M. and Mikami, M., (2006). Dust model intercomparison (DMIP) study over Asia: overview. *Journal of Geophysical Research*, **111**: D12213, 1-8.

Uno, E.U., Kasssim, I. and Adelabu, J.S.A., (2012). Analysing the Impact of Soil Parameters on the Sensible Heat Flux Using Simulated Temperature Curve Model. *International Journal of Physics and Research* **2 (4)**: 1-9.

Vijayakumar, K. and Devara, P.C.S., (2013). Study of aerosol optical depth, ozone, and precipitable water vapour content over Sinhagad, a high-altitude station in the Western Ghats. *International Journal of Remote Sensing*, **34 (2)**: 613-630.

Vladutescu, D.V., Bomidi, L.M., Barry, M.G., Qi, Z. and Shan, Z., (2013). Aerosol transport and source attribution using sunphotometers, models and in-situ chemical composition measurements. *IEEE Transactions On Geoscience And Remote Sensing*, **51 (7)**: 3803 – 3811.

Wang, L.C., Gong, W., Xia, X.A., Zhu, J., Li, J. and Zhu, Z.M., (2015). Long-term observations of aerosol optical properties at Wuhan, an urban site in Central China. *Atmospheric Environment*, **101**: 94-102.

Wang, Y., Sartelet, K. N., Bocquet, M., Chazette, P., Sicard, M., D'Amico, G., Léon, J. F., Alados-Arboledas, L., Amodeo, A., Augustin, P., Bach, J., Belegante, L., Binietoglou, I., Bush, X., Comerón, A., Delbarre, H., García-Vízcaino, D., Guerrero-Rascado, J. L., Hervo, M., Iarlori, M., Kokkalis, P., Lange, D., Molero, F., Montoux, N., Muñoz, A., Muñoz, C., Nicolae, D., Papayannis, A., Pappalardo, G., Preissler, J., Rizi, V., Rocadenbosch, F., Sellegri, K., Wagner, F. and Dulac, F., (2014). Assimilation of lidar signals: application to aerosol forecasting in the western Mediterranean basin, *Atmospheric Chemistry and Physics*, **14**: 12031–12053.

Welton, E.J., Kenneth J.V., Patricia, K.Q., Piotr, J.F., Krzyszt, M. and James , E.J., (2002). Measurements of aerosol vertical profiles and optical properties during INDOEX 1999 using micropulse lidars. *Journal Geophysical Research*, **107 (D1)**: 8019, 1-9.

Wen-Yih, S., Kate, J.-S.Y. and Neng-Huei, L., (2013). Numerical simulations of Asian dust-aerosols and regional impact on weather and climate- part I: control case-PRCM simulation without dust-aerosols. *Aerosol and Air Quality Research*, **13**: 1630–1640.

Wu, Y., Hao, J., Fu, L., Wang, Z. and Tang, U., (2002). Vertical and horizontal profiles of airborne particulate matter near major roads in Macao, China. *Atmospheric Environment*, **36**: 4907–4918.

Yang, Y., Liao, H. and Lou, S.-J., (2014). Simulated impacts of sulphate and nitrate aerosol formation on surface-layer ozone concentrations in China. *Atmospheric and Oceanic Science Letters*, **7 (5)**: 441-446.

Yermakov, A.N., Larin, I.K., Ugarova, A.A. and Purmal, A.P., (2003). Catalyst of SO2 oxidation by iron ions in the atmosphere. *Kinematics and Catalysis*, **44 (4)**: 524-537.

Yuan, T., Remer, L.A., Pickering, K.E. and Yu, H., (2011). Observational evidence of aerosol enhancement of lightning activity and convective invigoration. *Geophysical Research Letter*, **38**: L0470, 1-6.

Zahra, B., Gail, P. and Box, M.A., (2010). Seasonal variability of aerosol optical properties in Darwin, Australia. *Journal of Atmospheric and Solar Terrestrial Physics*,**72**: 726–739.

Zhao, D.F., Buchhol, A., Kortner, B., Schlag, P., Rubach, F., Fuchs, H., Kiendler-Scharr, A., Tillmann, R., Wahner, A., Watne, Å.K., Hallquist, M., Flores, J.M., Rudich, Y., Kristensen, K., Hansen, A.M.K., Glasius, M., Kourtchev, I., Kalberer, M. and Mentel, T.F., (2015). Cloud condensation nuclei activity, droplet growth kinetics and hygroscopicity of biogenic and anthropogenic Secondary Organic Aerosol (SOA). *Atmospheric Chemistry and Physics Discussion*, **15**: 19903-19945.

Zhang, T., Ning, Xu, L., Guo, Y.H. and Yong, B., (2014). A global atmospheric contaminant transport model based on 3D advection-diffusion equation. *Journal of Clean Energy Technologies*, **2 (1)**: 43-47.

Ziemke, J.R., Douglass, A.R., Oman, L.D., Strahan, S.E. and Duncan, B.N., (2015). Tropospheric ozone variability in the tropics from ENSO to MJO and shorter timescales. *Atmospheric Chemistry Physics*, **15**: 8037-8049.

Appendix 1

List of published ISI/SCOPUS conferences/Articles

1. **Emetere, M.E**., and Akinyemi M.L., (2015). First Kind Plume Analysis of Volcanic Blast: Application of an Indigenous Model, IEEE Proceedings 2015 International Conference on Space Science & Communication pp. 136 - 140
2. **Emetere, M.E.,** Akinyemi M.L. and Uno U.E., (2015). Computational Analysis of Aerosol Dispersion Trends From Cement Factory, IEEE Proceedings 2015 International Conference on Space Science & Communication pp. 288 - 291
3. **Emetere, M.E**., Akinyemi M.L. and Akinojo O., (2015). A Novel Technique for Estimating Aerosol Optical Thickness Trends Using Meteorological Parameters, AIP Conference Proceedings 1705, 020037; doi: 10.1063/1.4940285
4. **Emetere, M.E**., Akinyemi M.L., and Akinojo O., (2016) Theoretical Aid for Improving Measuring Instruments Efficiency within the Meteorological Space of Lagos-Nigeria, AIP Conference Proceedings 1705, 020054; doi: 10.1063/1.4940302.
5. **Emetere, M.E**., Akinyemi M.L. and Akinojo O., (2015). Effects Of Band Superposition On The Satellite Imagery Of Aerosol Optical Depth Over West Africa, Journal of Engineering and Applied Sciences, **10 (24)**: 44278-44282
6. **Emetere, M.E.** and Akin-Ojo, O., (2015). Computerized Modeling of Aerosol Effects on the Thermal Comfort in the Urban Climate of Ilorin-Nigeria International Journal of Applied Environmental Sciences, **10(2)**: 665-672
7. **Emetere, M.E**., Akinyemi M.L., and Akinojo O., (2015). Parametric retrieval model for estimating aerosol size distribution via the AERONET, LAGOS station, Elsevier: Environmental Pollution, **207 (C)**: 381-390
8. **Emetere, M.E.,** Akinyemi M.L. and Akin-Ojo O., (2015). Aerosol Optical Depth Trends over Different Regions of Nigeria: Thirteen years Analysis, *Modern Applied Science*. **9 (9)**: 267-279
9. **Emetere, M.E**., Akinyemi M. L. and Akinojo O., (2015). Effects Of Band Superposition On The Satellite Imagery Of Aerosol Optical Depth Over West Africa, Journal of Engineering and Applied Sciences, **10 (24)**: 44278-44282

Appendix Ia: Atmospheric constants for Niamey-Niger

Year	a_1	a_2	n_1	n_2
2000	0.8394	1.357	0.1129	0.8819
2001	0.8667	1.137	0.1074	0.9848
2002	0.7035	0.7578	0.2388	0.7797
2003	0.9213	0	0	0.4746
2004	0.6092	1.192	0.01576	0.8934
2005	0.4084	1.114	0.01346	0.7647
2006	0.7145	0.7876	0.2596	0.8587
2007	0.7145	0.7876	0.2596	0.8587
2008	0.6525	0.7952	0.3604	0.7569
2009	0.8764	0	0	0.4747
2010	1.092	0	0	0.5551
2011	1.092	0	0	0.5551
2012	0.7373	0.9673	0.3062	0.8871
2013	0.6888	0.8068	0.2885	0.9039

Appendix Ib: Atmospheric constants for locations in West Africa

Location	a_1	a_2	n_1	n_2	α	**β**
Nigeria						
Abuja	0.5421	0.8616	0.3271	0.5365	$\frac{\pi}{4}$	$\frac{\pi}{4}$
Lagos	1.175	0.8227	0.2926	0.3573	$\frac{\pi}{2}$	$\frac{\pi}{2}$
Sokoto	0.5754	1.027	0.4342	0.6663	$\frac{\pi}{6}$	$\frac{\pi}{6}$
Ilorin	0.9315	0.7322	0.3482	0.2994	$\pm\frac{\pi}{2}$	$\pm\frac{\pi}{2}$
Kano	0.708	0.8984	0.3173	0.3863	$\pm\frac{\pi}{2}$	$\pm\frac{\pi}{2}$
Mubi	0.6085	0.6326	0.07197	0.1748	$\pm\frac{\pi}{4}$	$\pm\frac{\pi}{4}$
Warri	0.7058	0.7633	0.1151	0.2141	$\pm\frac{\pi}{4}$	$\pm\frac{\pi}{4}$
Enugu	0.6563	0.5422	0.1711	0.1889	$\pm\frac{\pi}{4}$	$\pm\frac{\pi}{4}$
Cameroun						
Ngaoundere	0.6782	0.542	0.1798	0.2618	$\pm\frac{\pi}{4}$	$\pm\frac{\pi}{4}$
Younde	0.8659	0.9423	0.1548	0.09207	$\pm\frac{\pi}{4}$	$\pm\frac{\pi}{4}$
Ghana						
Accra	0.7545	0.7332	0.3224	0.1946	$\frac{\pi}{2}$	$\frac{\pi}{2}$
Bolgatanga	0.667	0.6403	0.242	0.1515	$\pm\frac{\pi}{4}$	$\pm\frac{\pi}{4}$
Burkina Faso						
Ouagadougou	0.626	0.7999	0.09835	0.266	$\pm\frac{\pi}{4}$	$\pm\frac{\pi}{4}$

Benin						
Cotonou	0.7602	0.81	0.185	0.1304	$\pm\frac{\pi}{2}$	$\pm\frac{\pi}{2}$
Port Novo	1.245	3.702×10^{-6}	2.096	-0.3105	$\pm\frac{\pi}{8}$	$\pm\frac{\pi}{8}$
Cape Verde						
Praia	0.6645	0.7712	0.08138	0.3432	0	0
Cote D' ivoire						
Boundokou	0.6839	0.6842	0.2075	0.1044	$\pm\frac{\pi}{2}$	$\pm\frac{\pi}{2}$
Abidjan	0.5822	0.7758	0.1795	0.1277	$\pm\frac{\pi}{2}$	$\pm\frac{\pi}{2}$
Guinea Bissau						
Bussau	0.6135	0.6694	0.1354	0.347	$\frac{\pi}{4}$	$\frac{\pi}{4}$
Equatorial Guinea						
Malabo	0.4393	0.8158	0.1795	0.08748	$\pm\frac{\pi}{2}$	$\pm\frac{\pi}{2}$
Gambia						
Serekunda	0.6718	0.7178	0.3608	0.3009	0	0
Mauritania						
Nouakchott	0.9442	0.8131	0.4369	0.08213	$\pm\frac{\pi}{8}$	$\pm\frac{\pi}{8}$
Mali						
Bamako	0.7616	0.6676	-0.04547	0.8321	$\frac{\pi}{3}$	$\frac{\pi}{3}$
Liberia						
Monrovia	0.771	1.11	0.9534	1.08	$\pm\frac{\pi}{2}$	$\pm\frac{\pi}{2}$
Guinea						
Conakry	0.7575	0.7176	0.3618	0.2351	0	0

Niger						
Niamey	0.7082	0.8279	0.1809	0.2384	$\frac{\pi}{6}$	$\frac{\pi}{6}$
Togo						
Lome	0.621	0.7398	0.1997	0.2936	$\frac{\pi}{6}$	$\frac{\pi}{6}$
Senegal						
Dakar	0.6187	0.7055	0.1682	0.3639	0	0
Sierra Leone						
Binkolo	0.6378	0.7898	0.2192	0.272	$\frac{\pi}{6}$	$\frac{\pi}{6}$

Appendix II

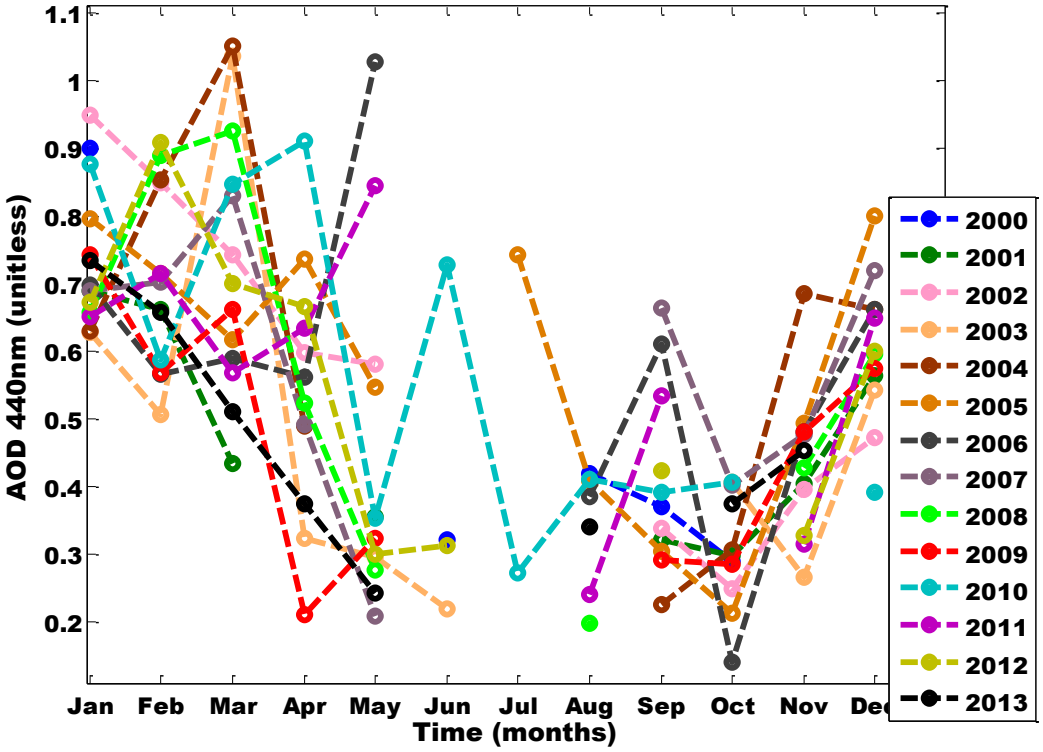

Figure II.ai: AOD pattern for Accra 2000 - 2013

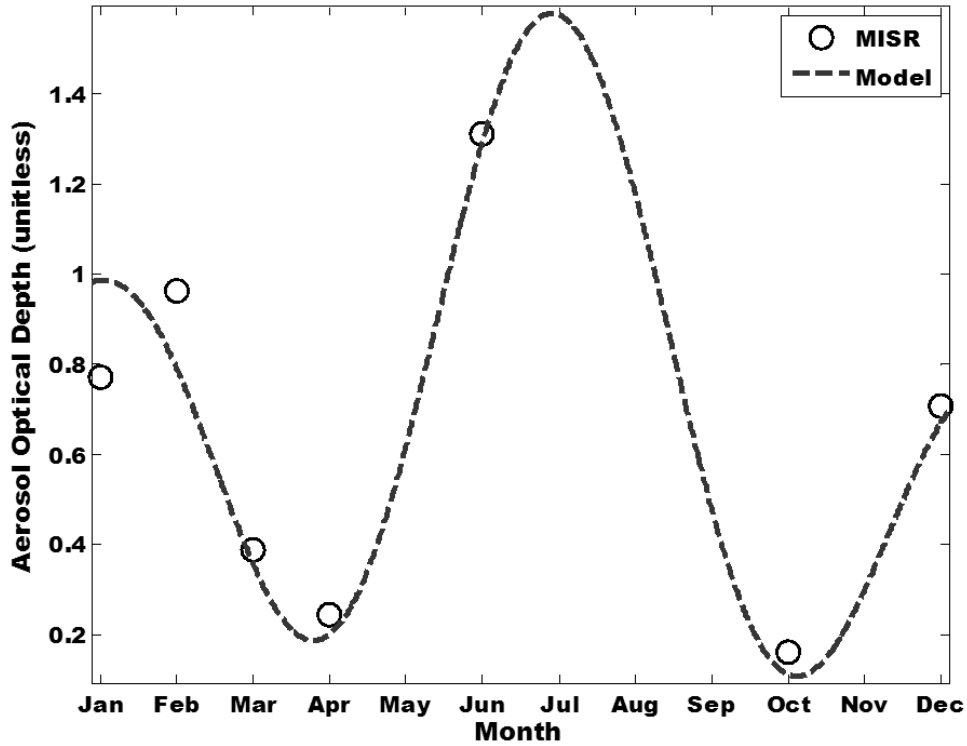

Figure II.aii: AOD for new model and MISR (Accra, 2001)

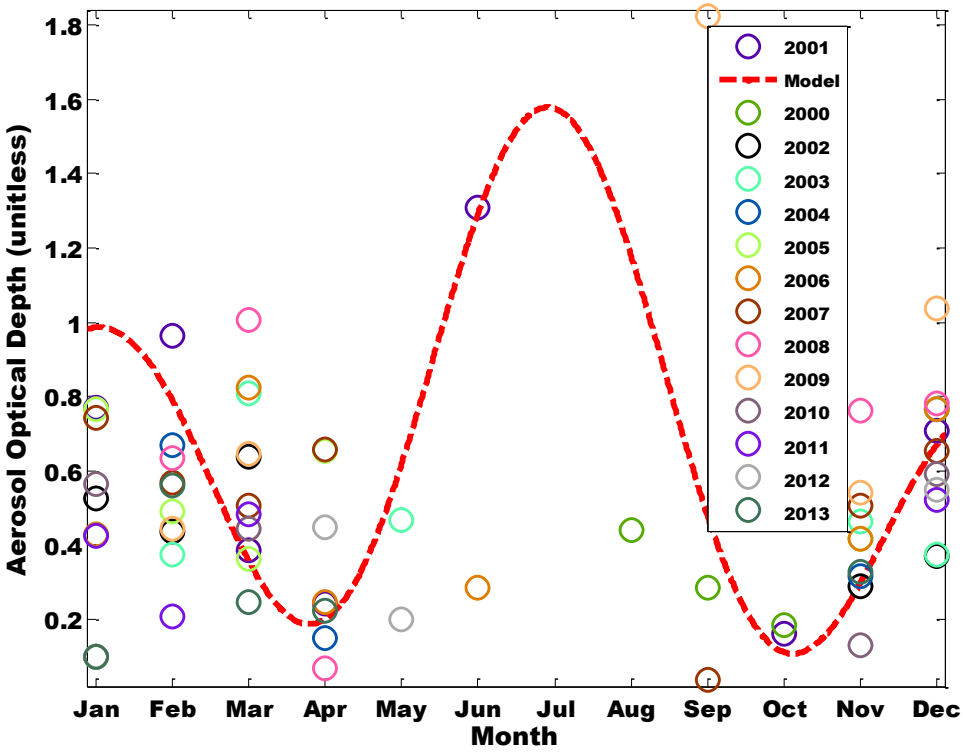

Figure II.aiii: AOD for new model and MISR (Accra, 2000-2013)

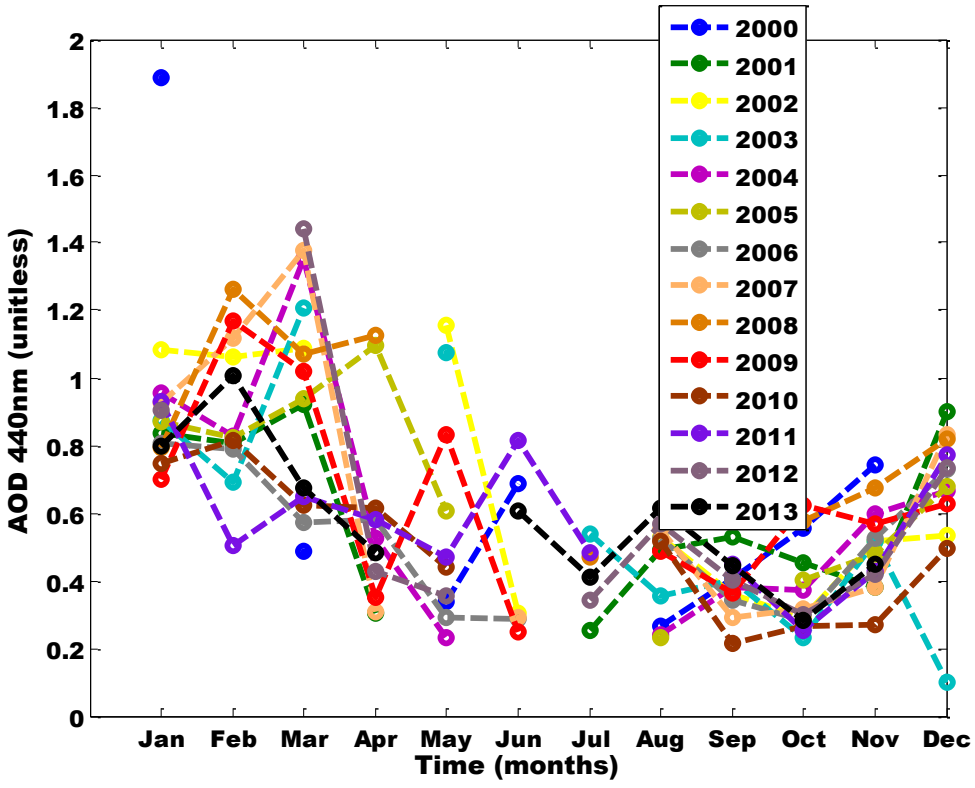

Figure II.bii: AOD pattern for Ouagadougou 2000 - 2013

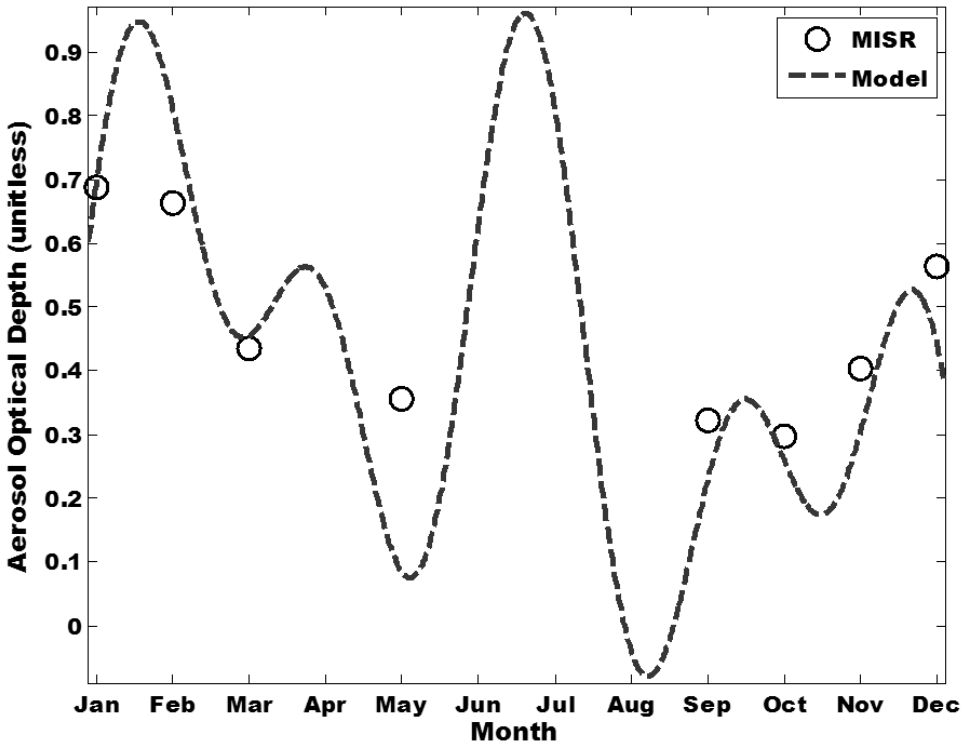

Figure II.bii: AOD for new model and MISR (Ouagadougou, 2001)

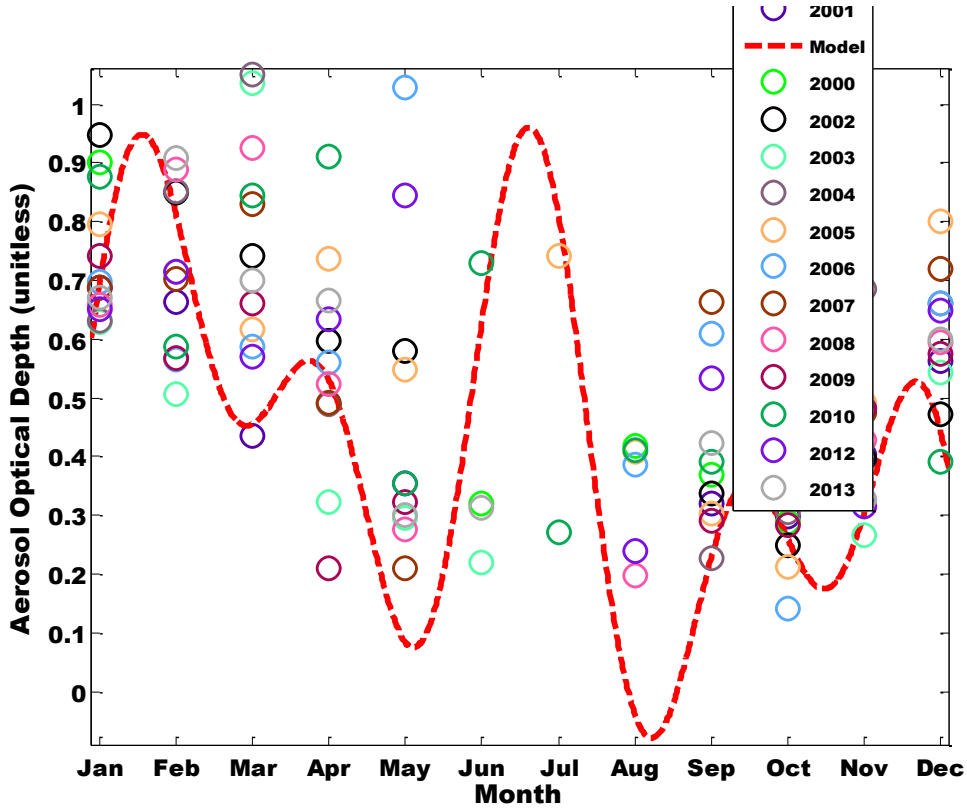

Figure II.biii: AOD for new model and MISR (Ouagadougou, 2000-2013)

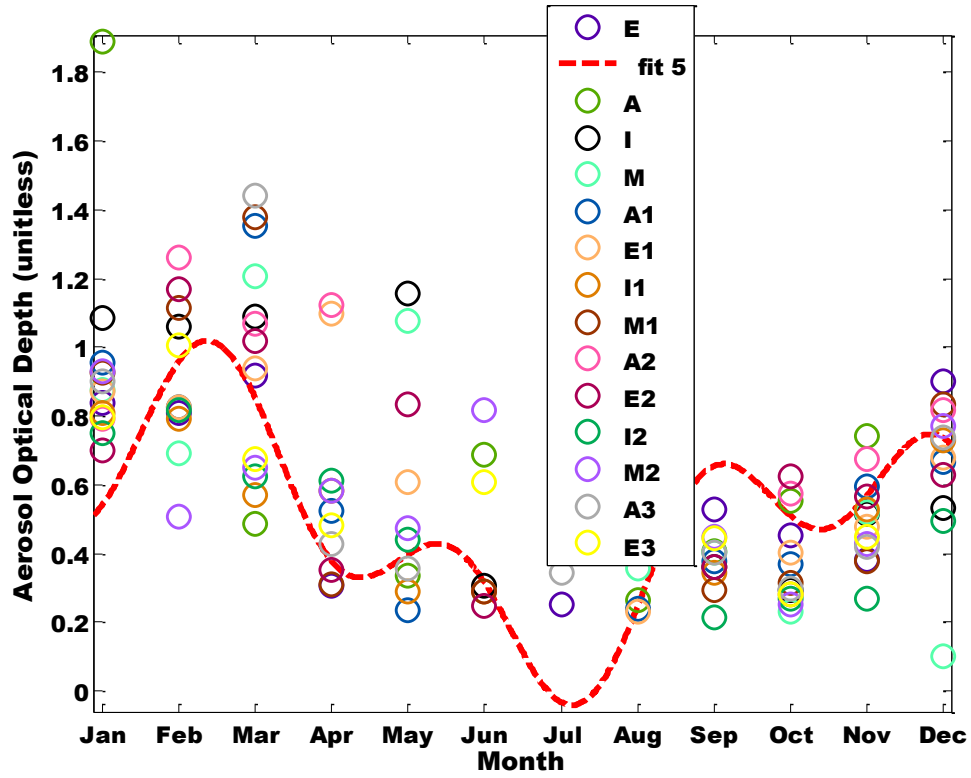

Figure II.ci: AOD for new model and MISR (Cotonou, 2000-2013)

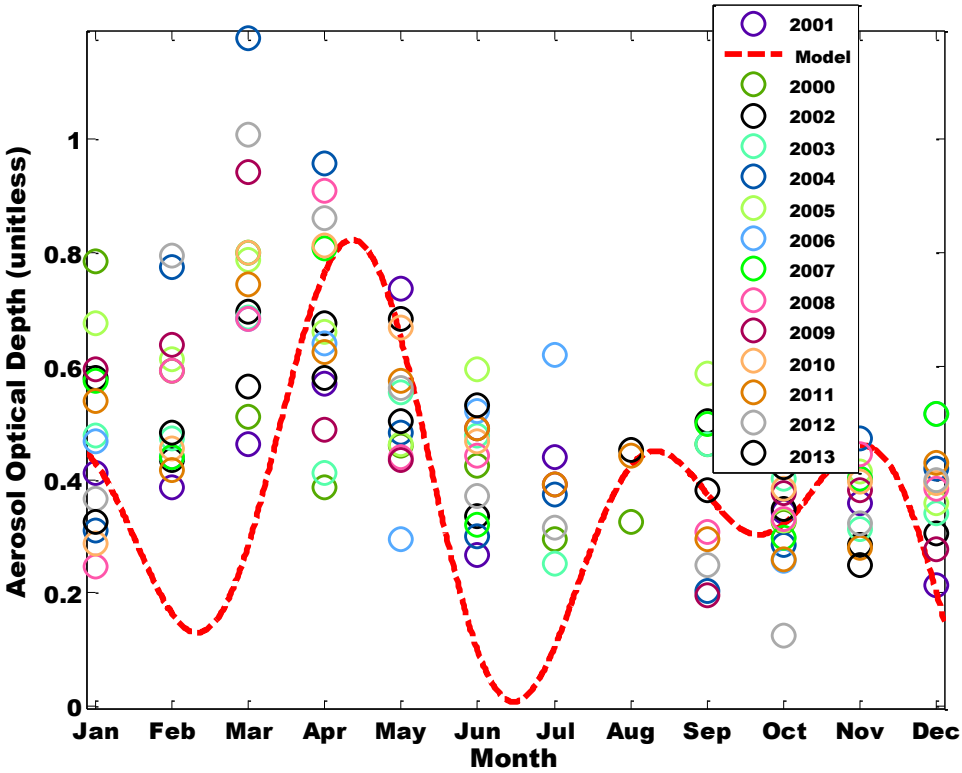

Figure II.cii: AOD pattern for new model and MISR (Cotonou 2000-2013)

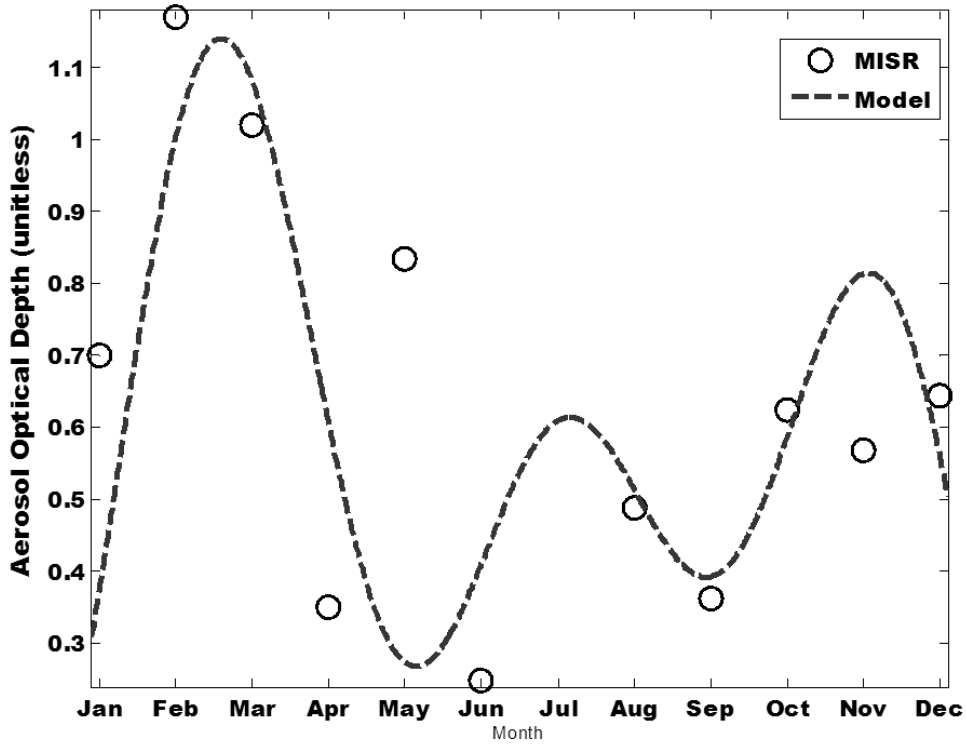

Figure II.ciii: AOD for new model and MISR (Cotonou, 2001)

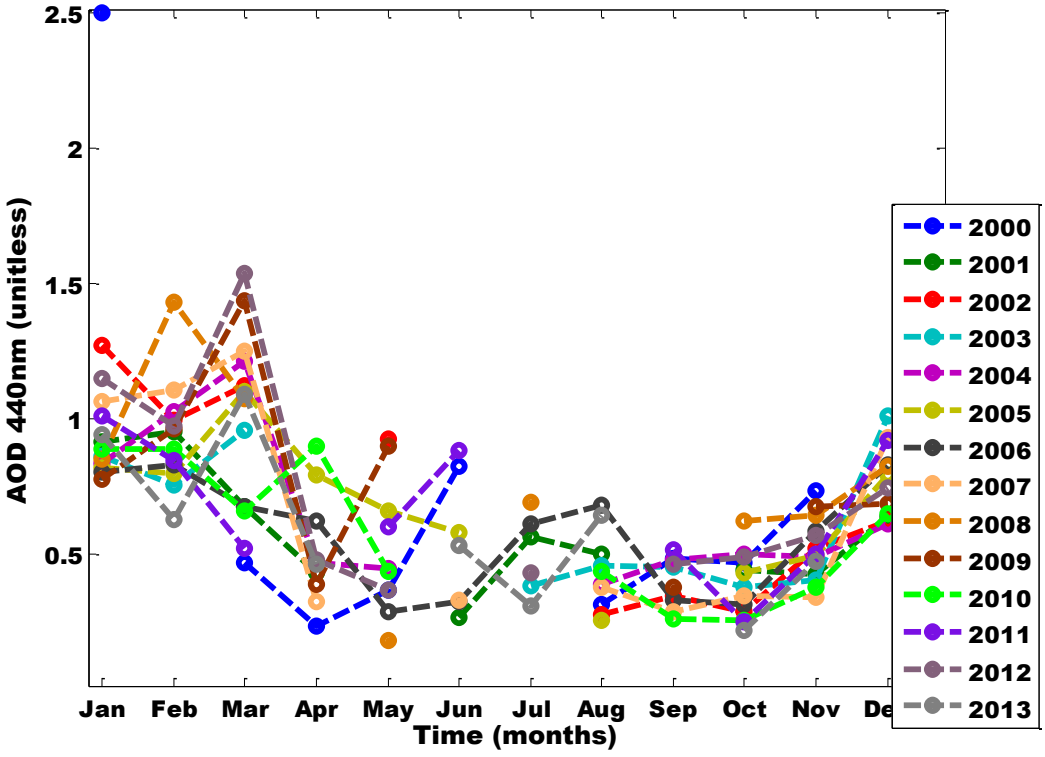

Figure II.di: AOD pattern for Port-Novo 2000 - 2013

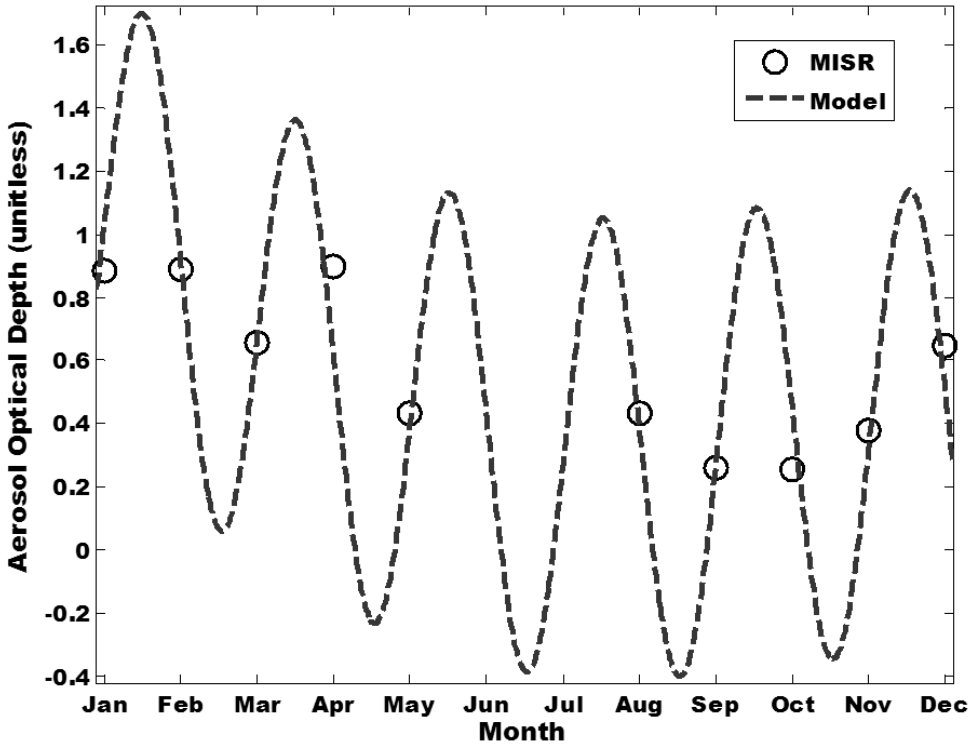

Figure II.dii: AOD for new model and MISR (Port-Novo, 2001)

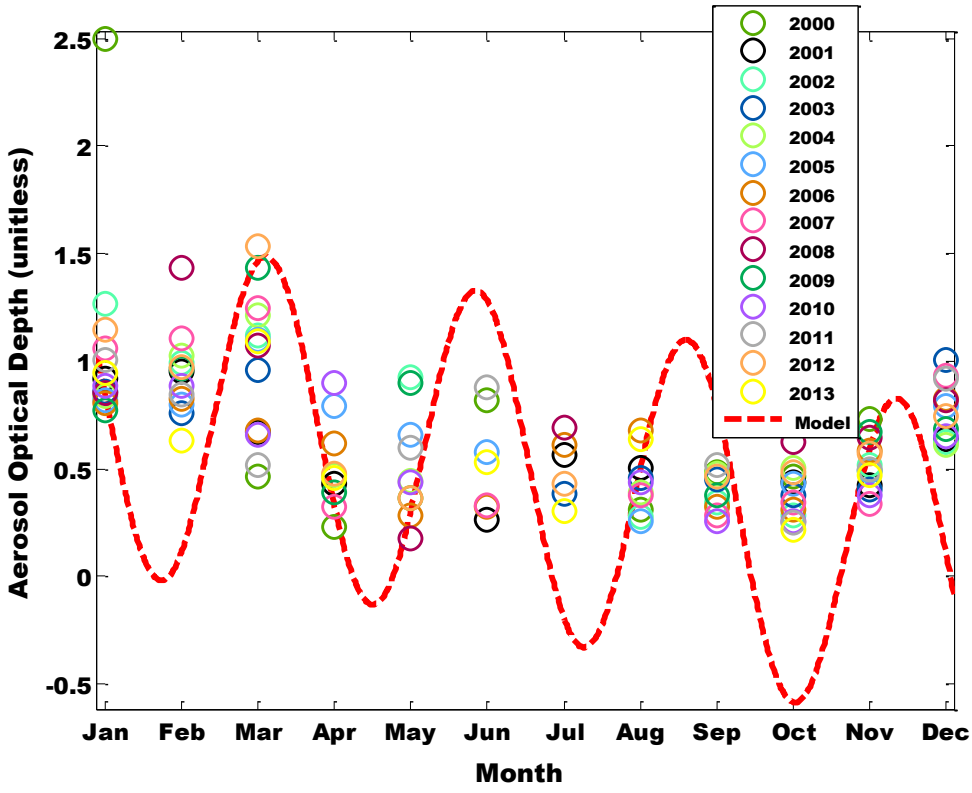

Figure II.diii: AOD for new model and MISR (Port-Novo, 2000-2013)

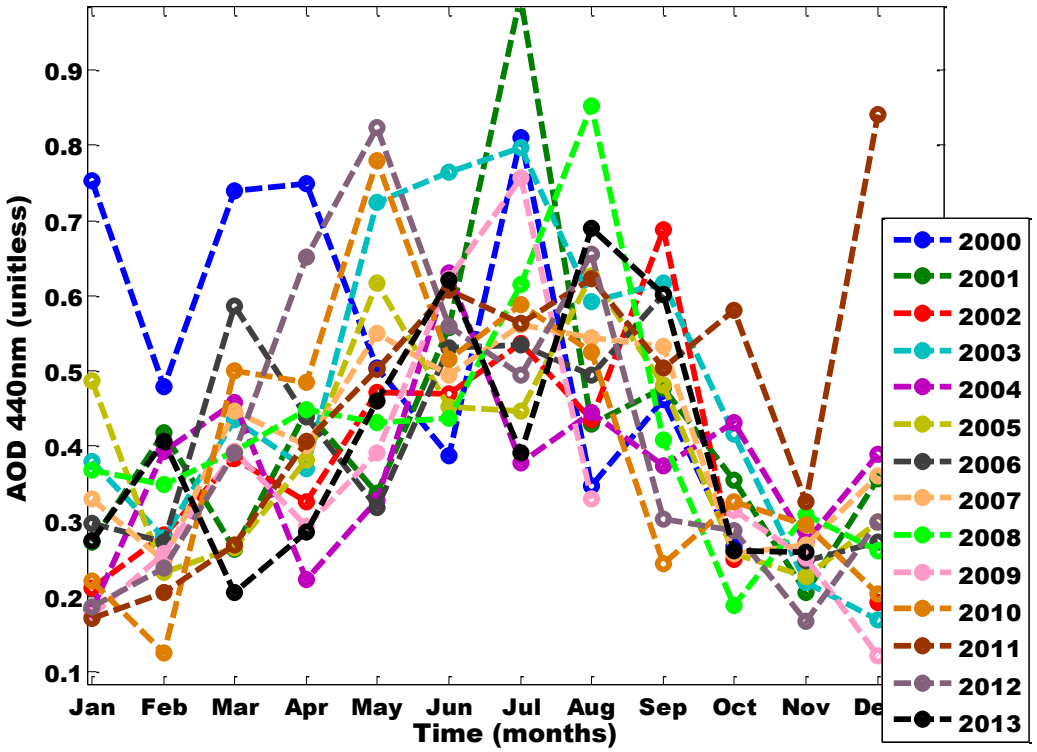

Figure II.ei: AOD pattern for Praia 2000 - 2013

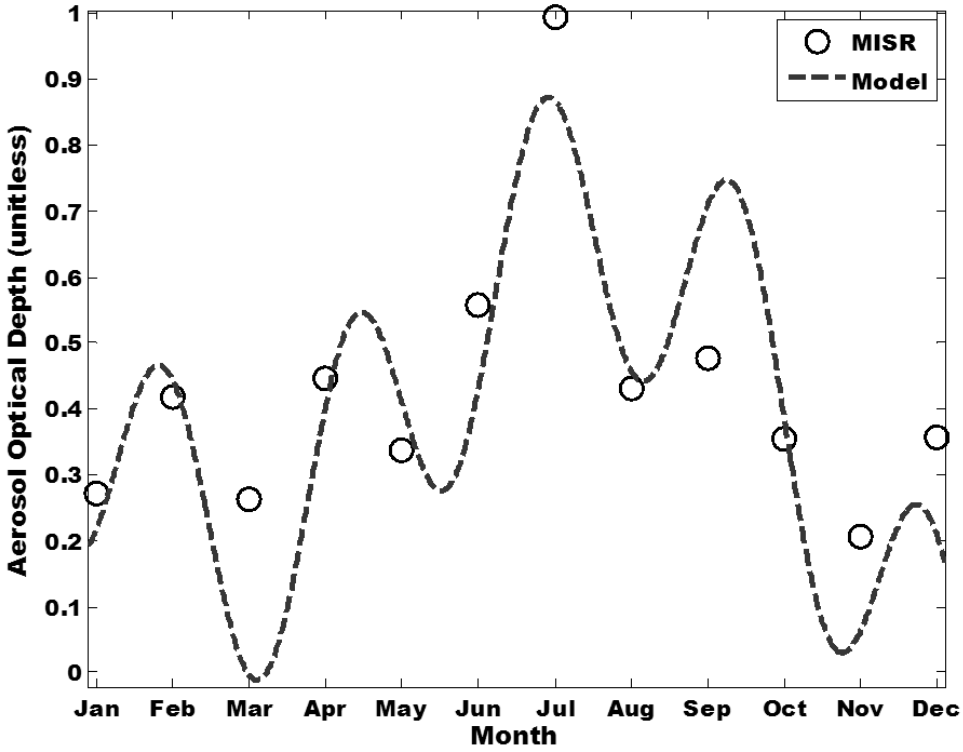

Figure II.eii: AOD for new model and MISR (Praia, 2001)

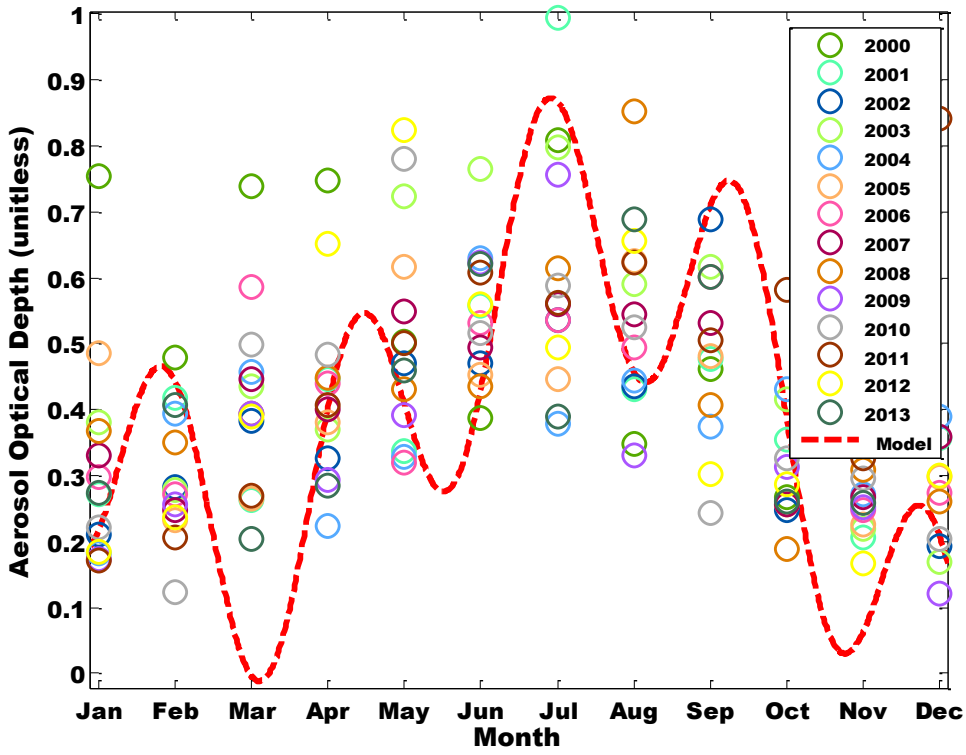

Figure II.eiii: AOD for new model and MISR (Praia, 2000-2013)

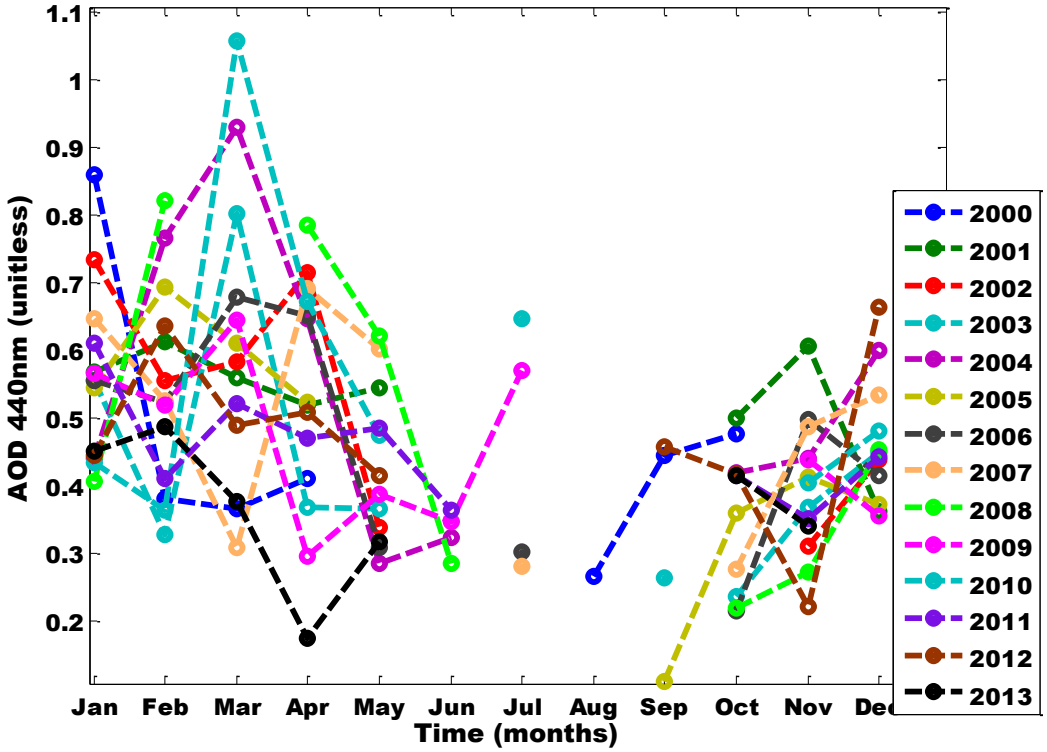

Figure II.fi: AOD pattern for Bondoukou 2000 - 2013

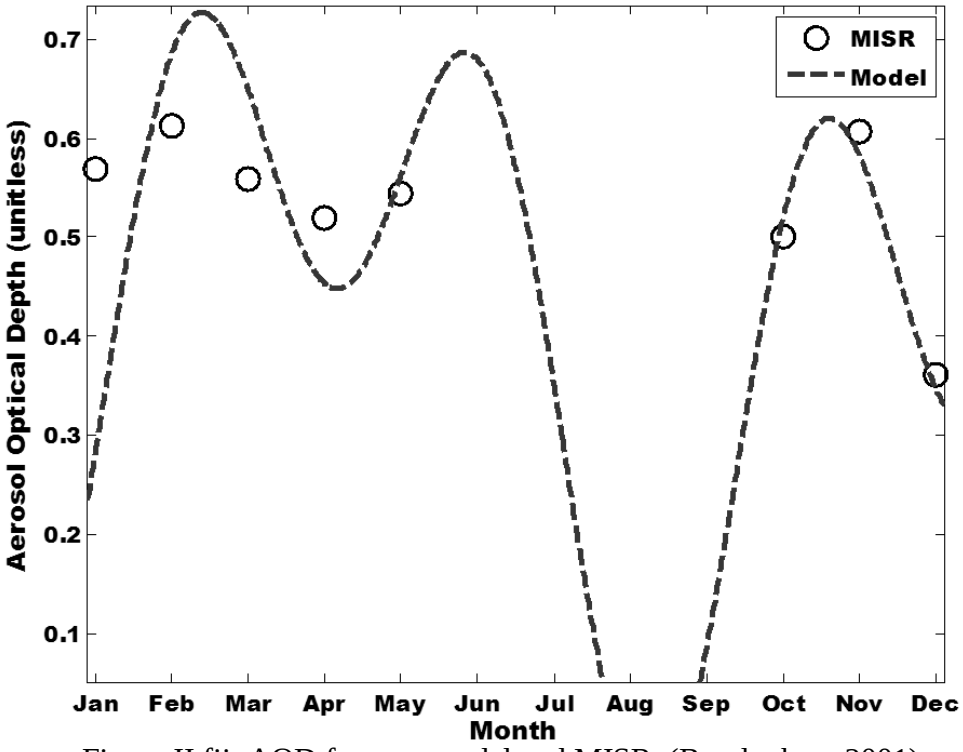

Figure II.fii: AOD for new model and MISR (Bondoukou, 2001)

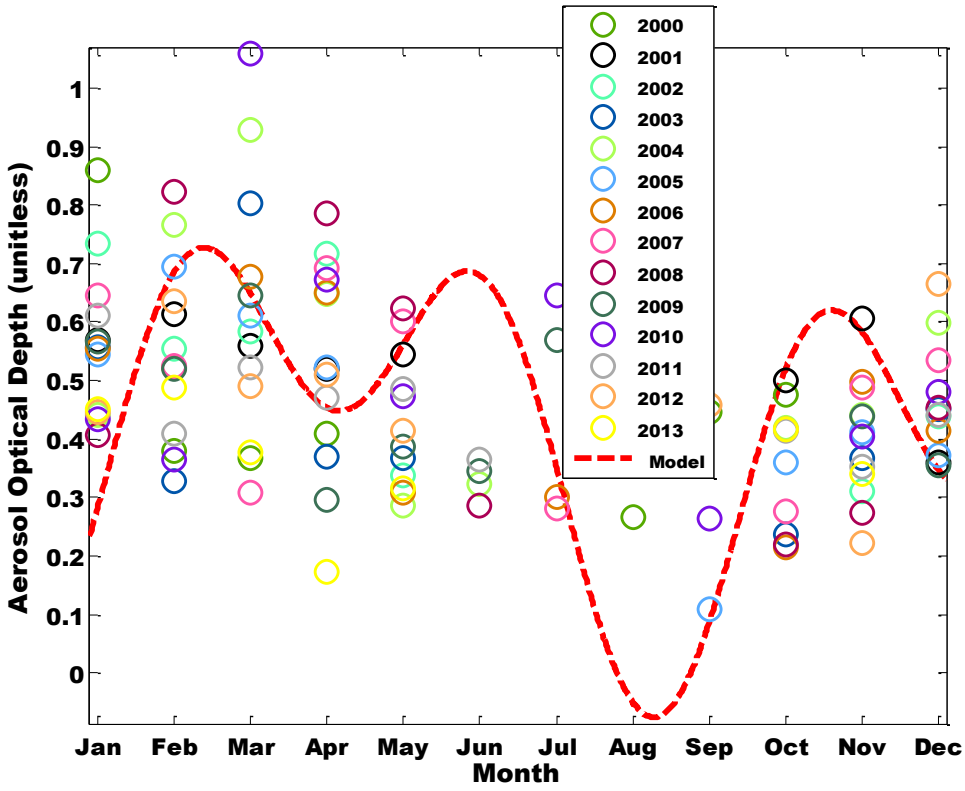

Figure II.fiii: AOD for new model and MISR (Bondoukou, 2000-2013)

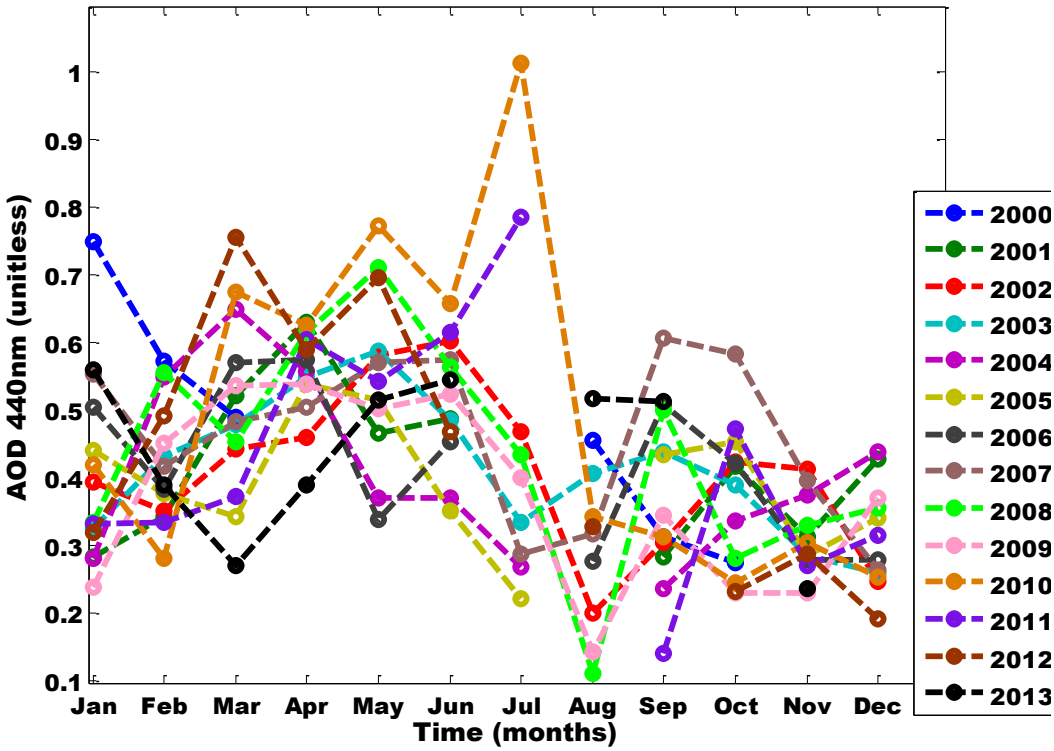

Figure II.gi: AOD pattern for Bussau 2000 - 2013

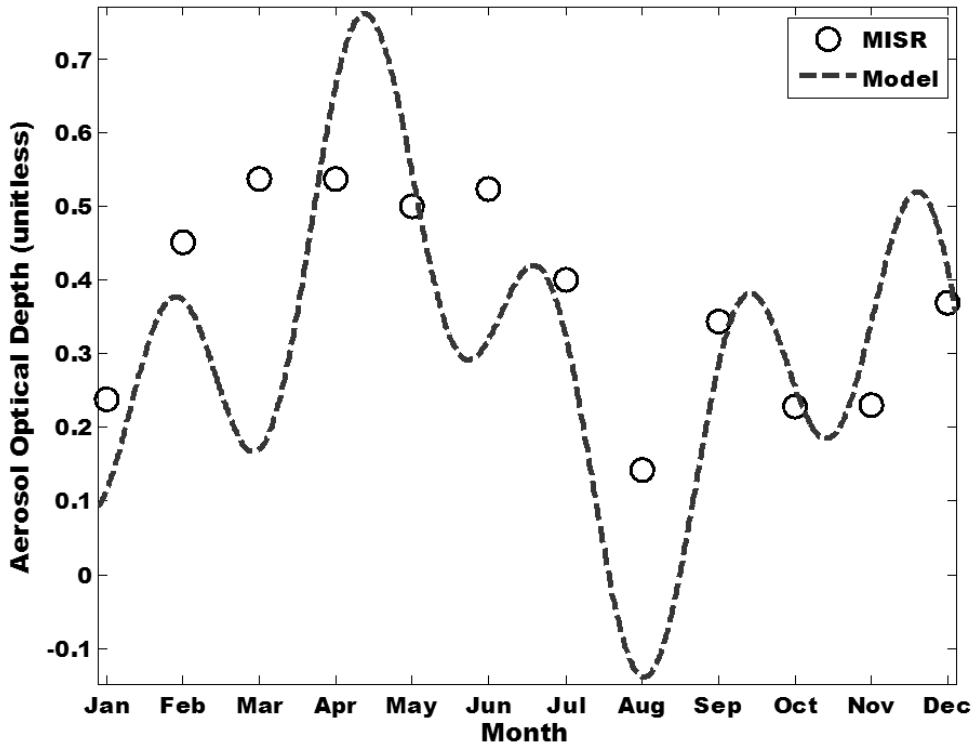

Figure II.gii: AOD for new model and MISR (Bussau, 2001)

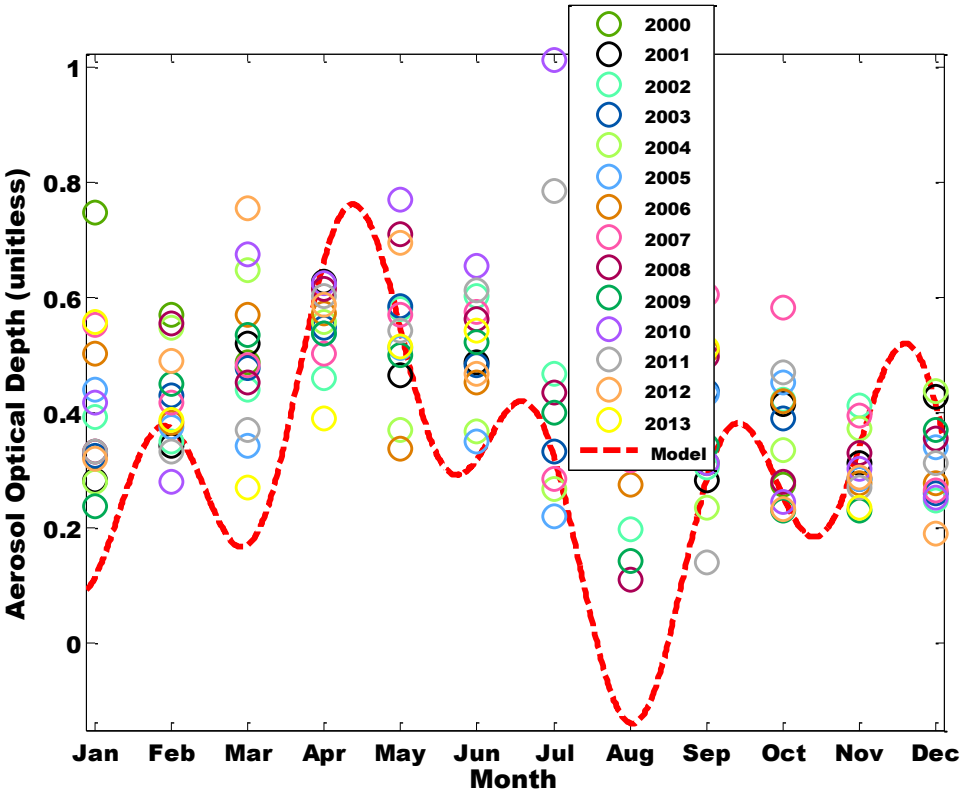

Figure II.giii: AOD for new model and MISR (Bussau, 2000-2013)

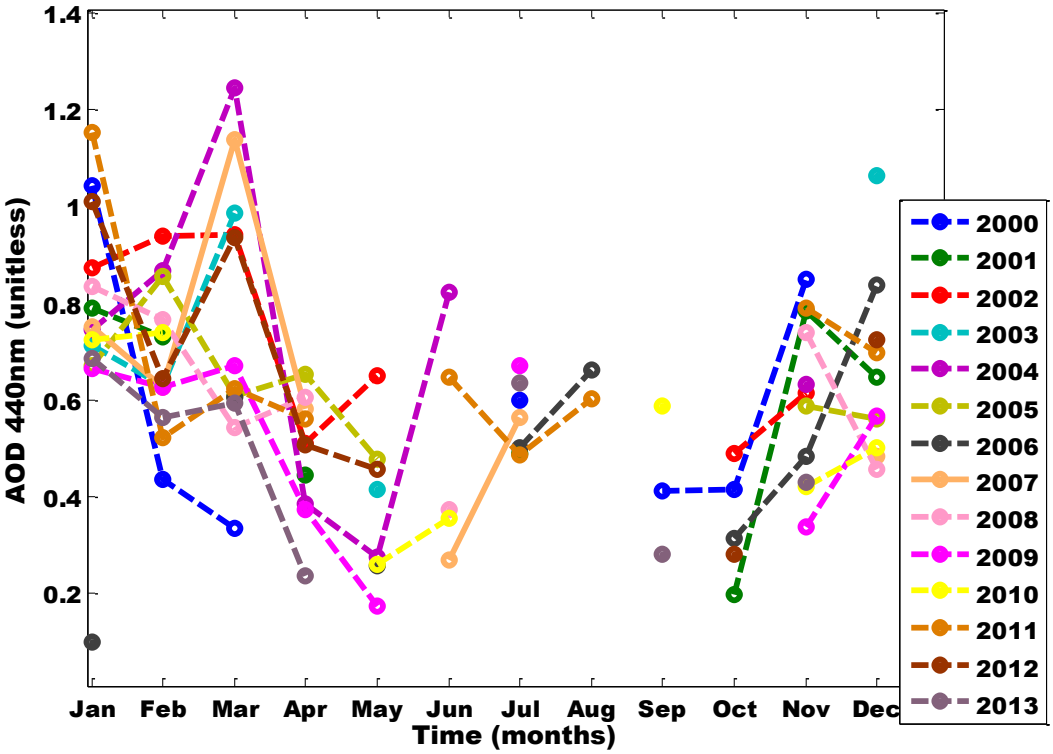

Figure II.hi: AOD pattern for Malabo 2000 - 2013

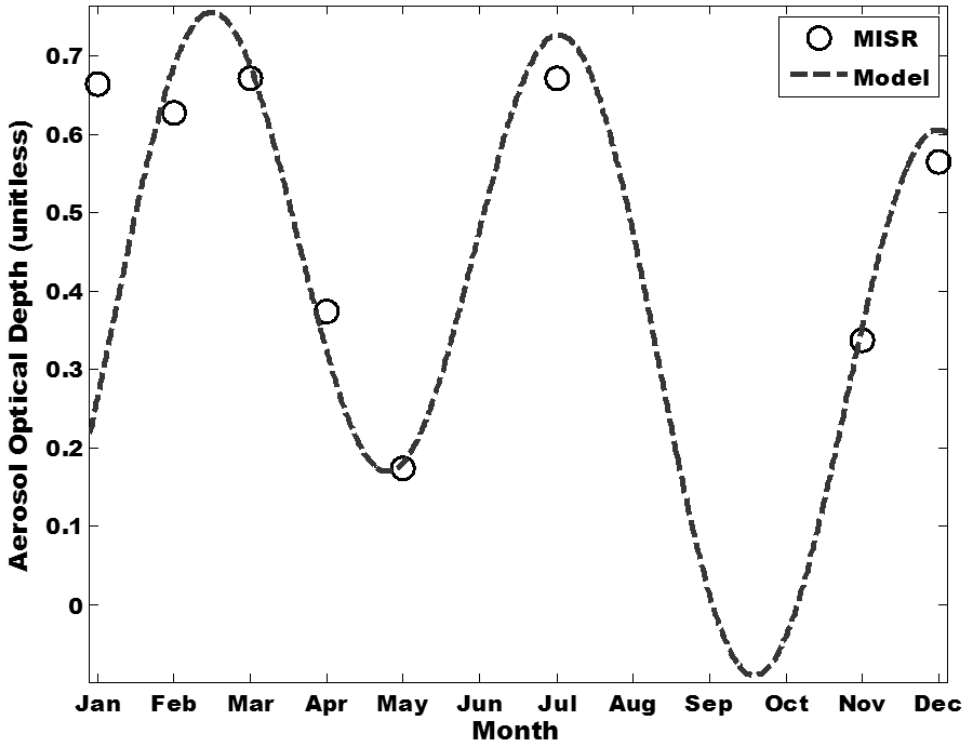

Figure II.hii: AOD for new model and MISR (Malabo, 2001)

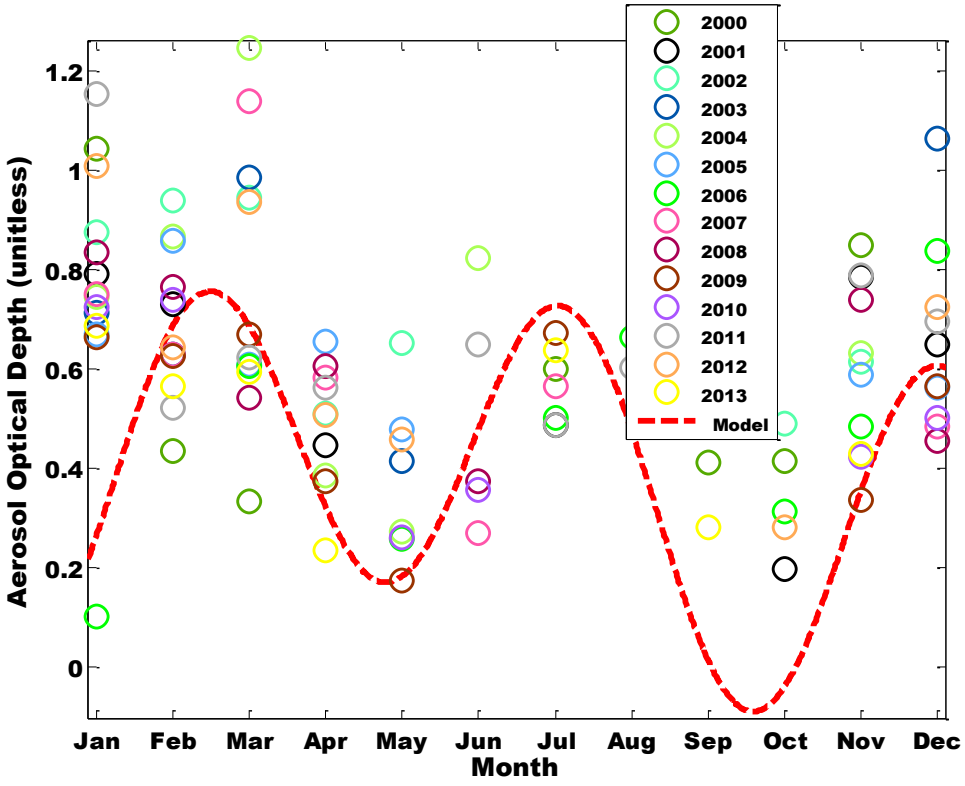

Figure II.hiii: AOD for new model and MISR (Malabo, 2000-2013)

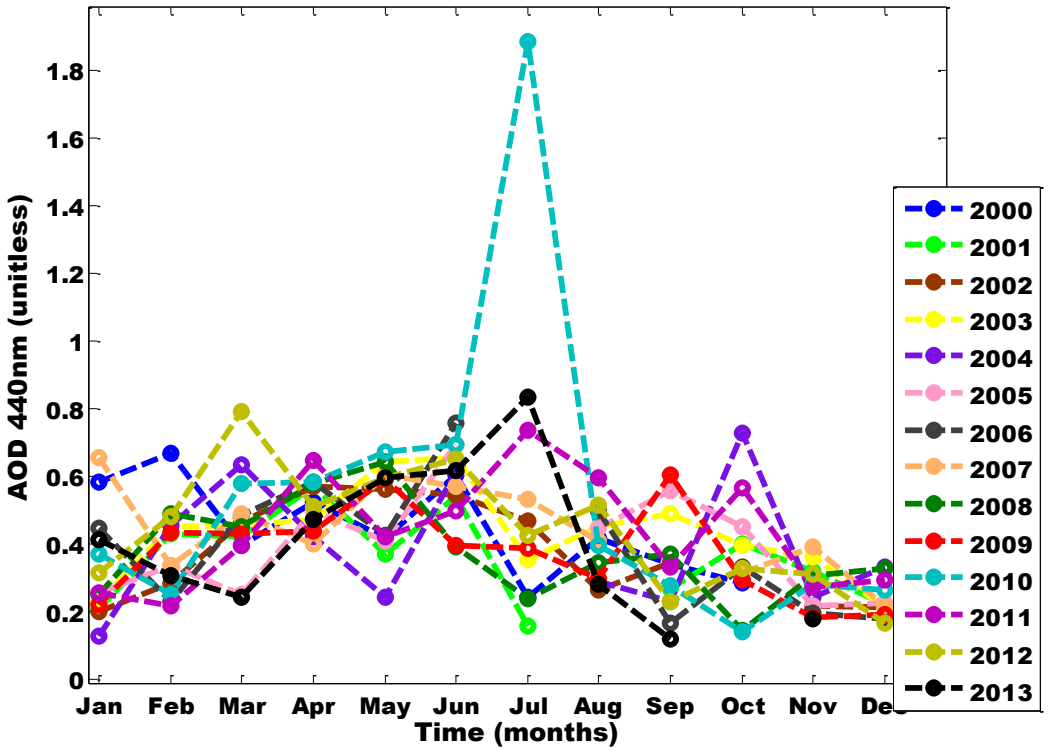

Figure II.i: AOD pattern for Serekunda 2000 - 2013

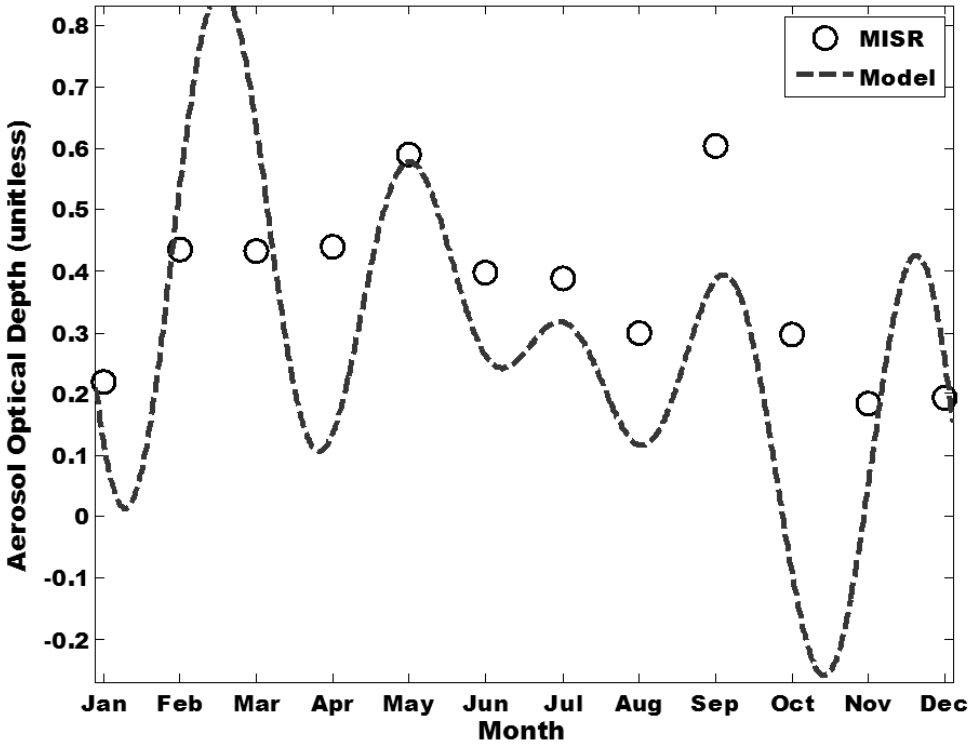

Figure II.ii: AOD for new model and MISR (Serekunda, 2001)

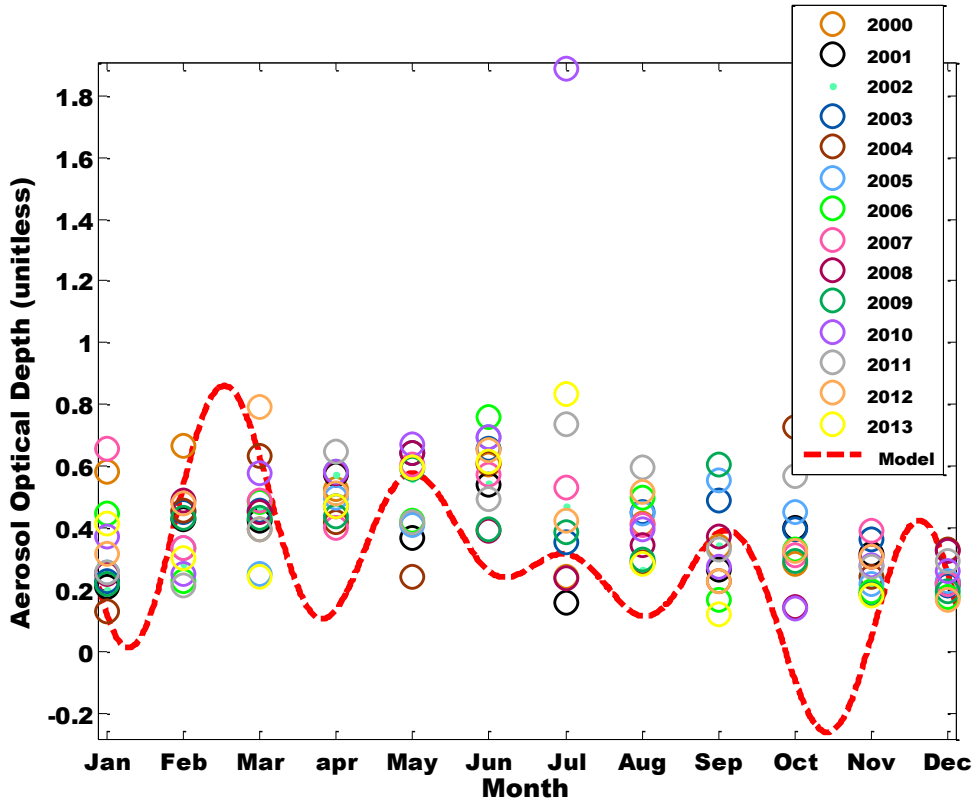

Figure II.iii: AOD for new model and MISR (Serekunda, 2000-2013)

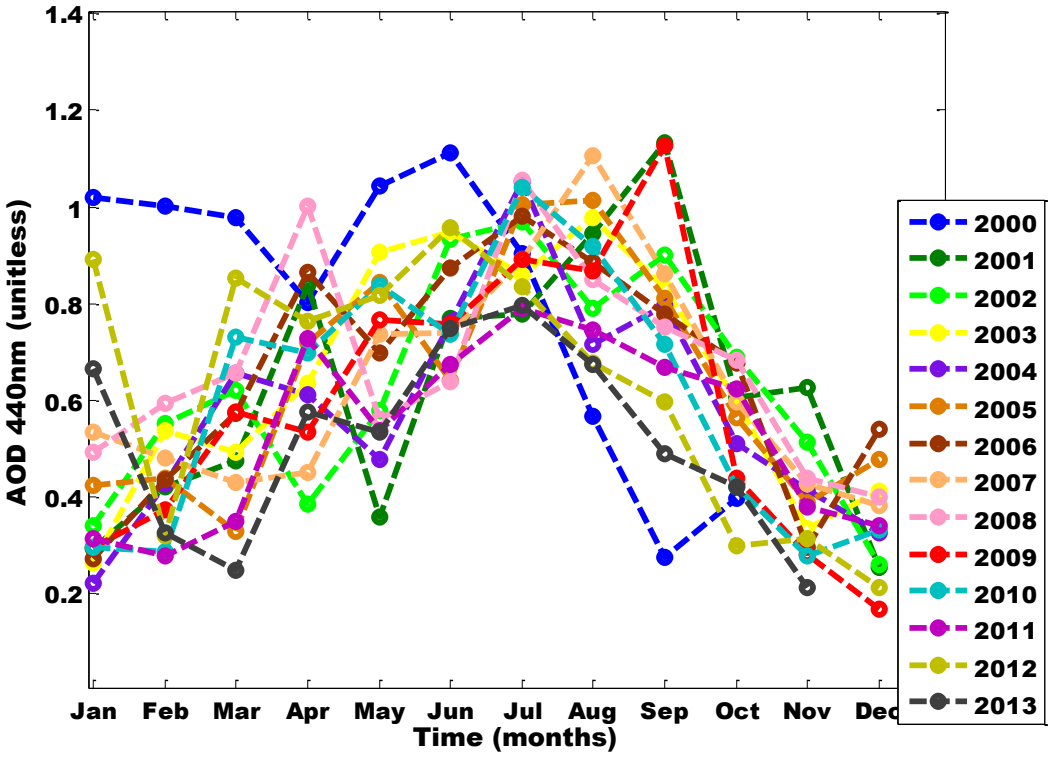

Figure II.ji: AOD pattern for Nouakchott 2000 - 2013

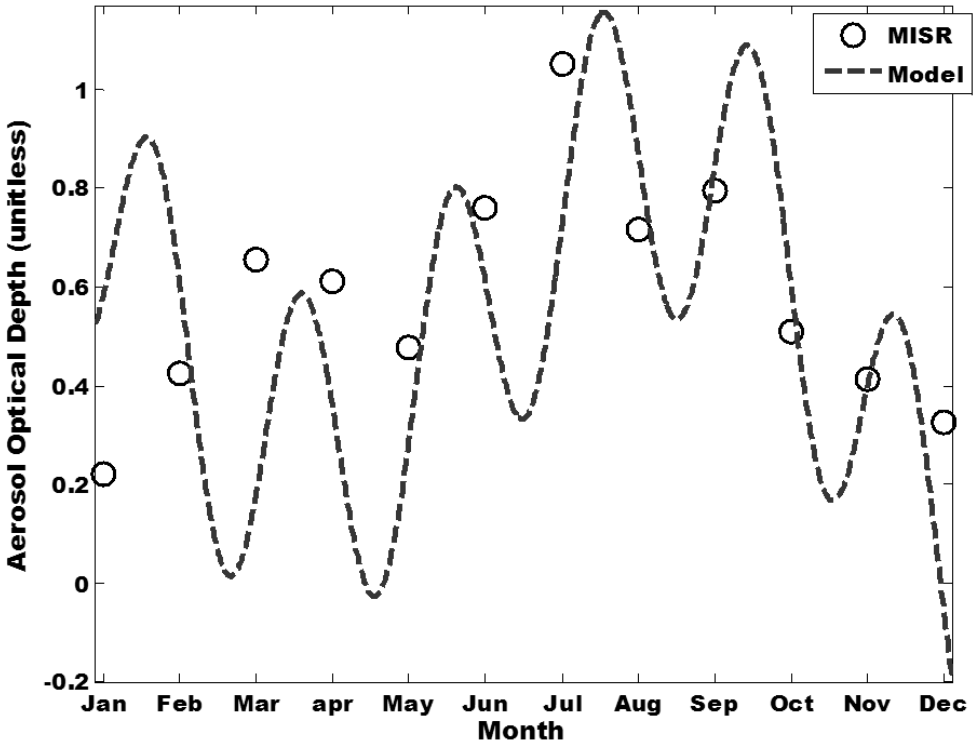

Figure II.jii: AOD for new model and MISR (Nouakchott, 2001)

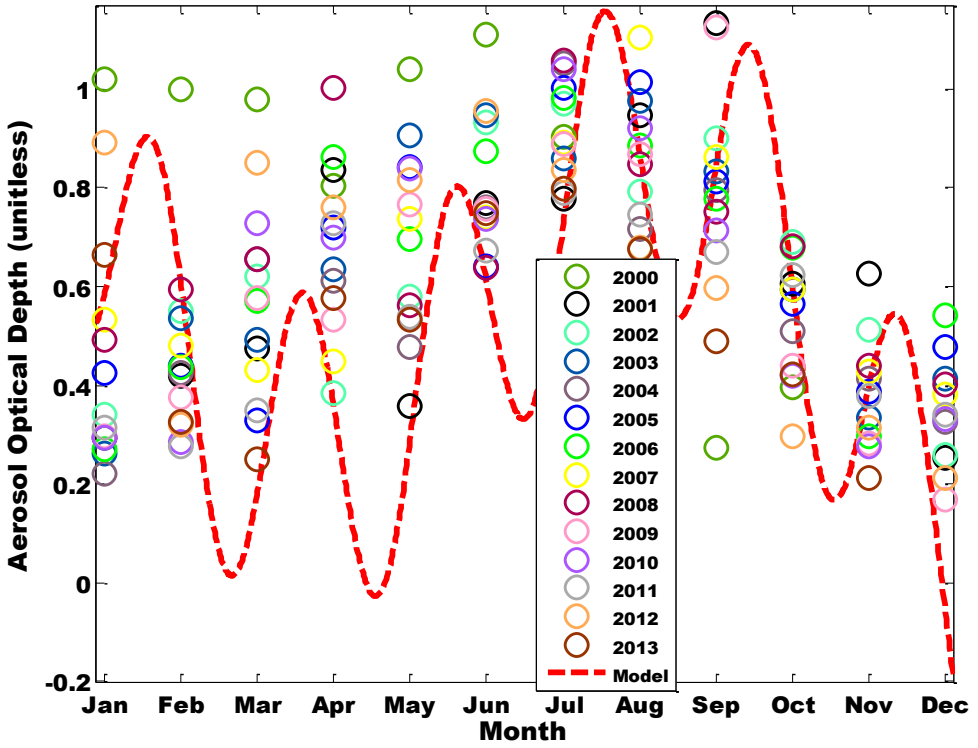

Figure II.jiii: AOD for new model and MISR (Nouakchott, 2000-2013)

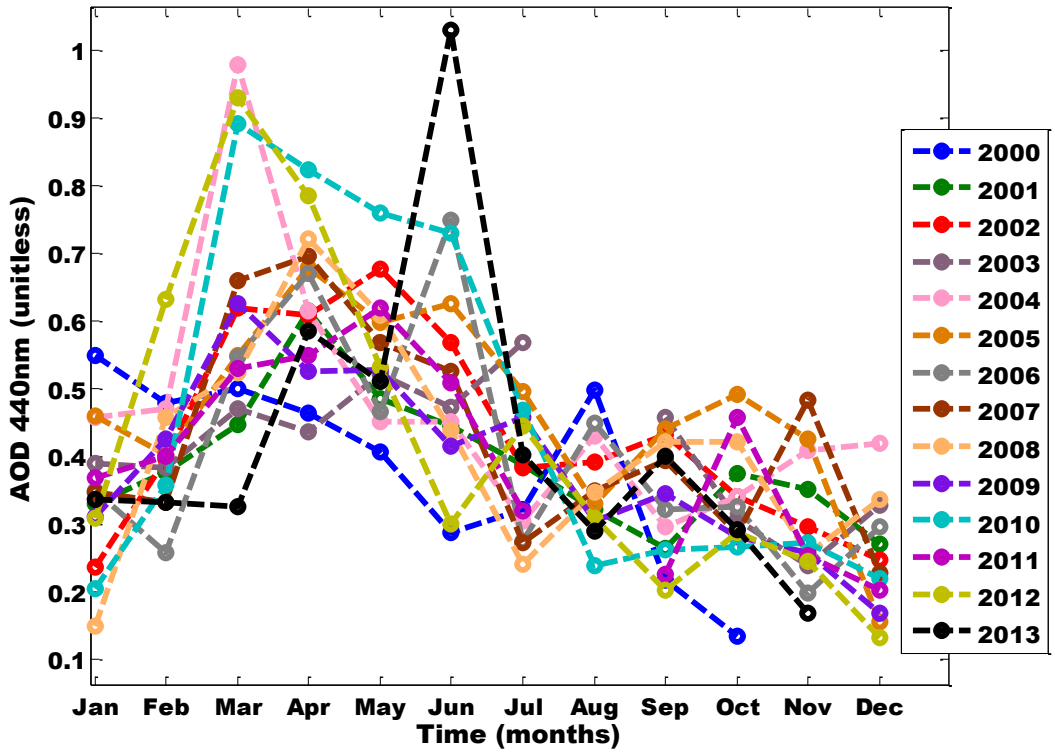

Figure II.ki: AOD pattern for Bamako 2000 - 2013

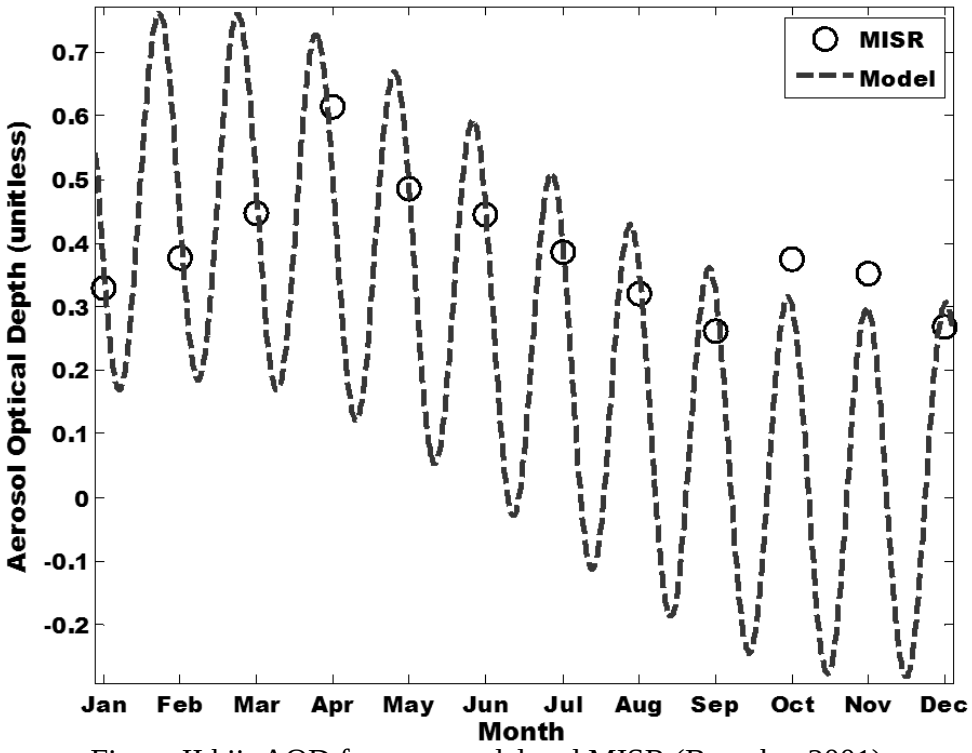

Figure II.kii: AOD for new model and MISR (Bamako, 2001)

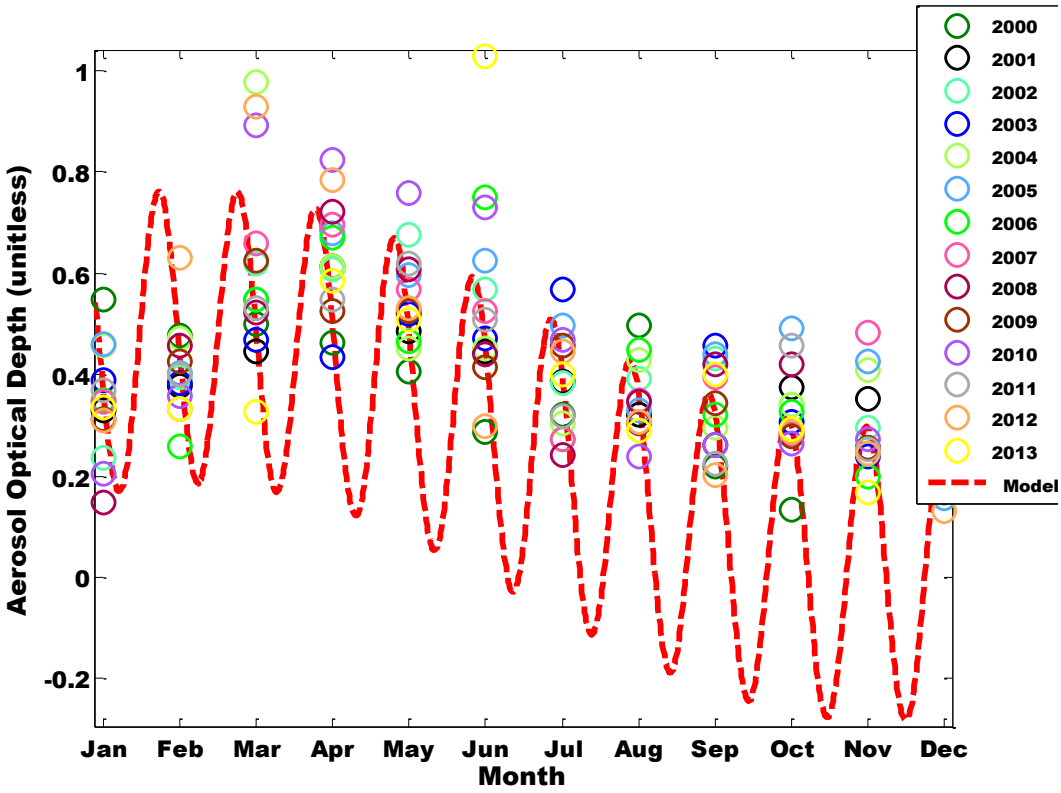

Figure II.kiii: AOD for new model and MISR (Bamako, 2000-2013)

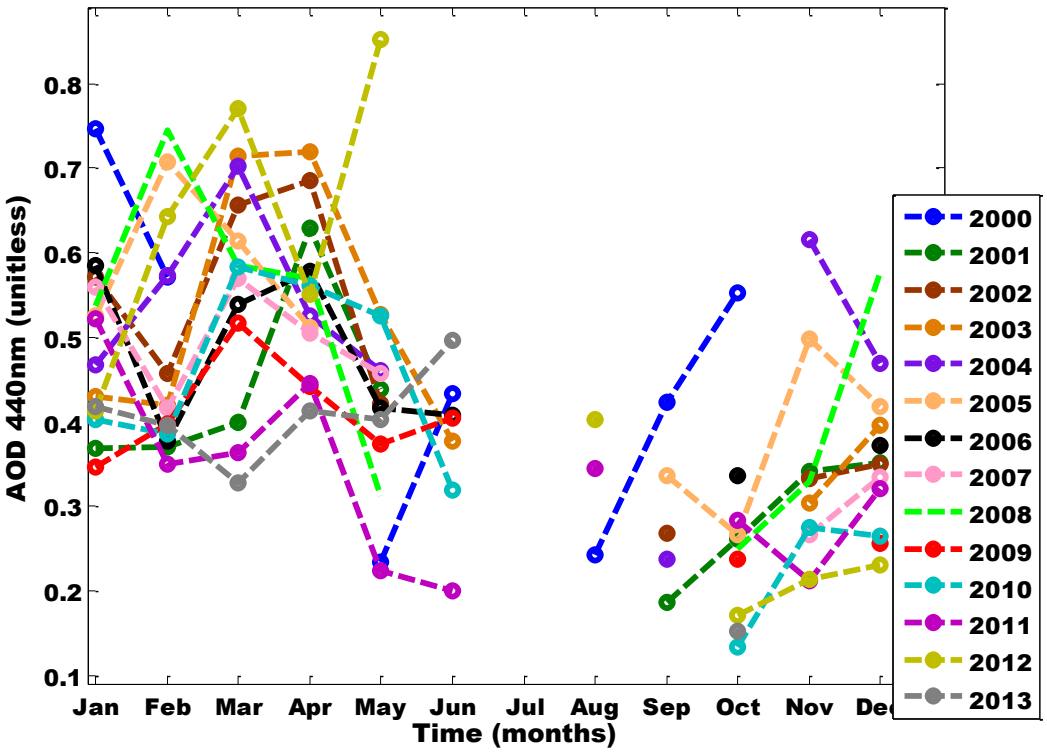

Figure II.li: AOD pattern for Conakry 2000 - 2013

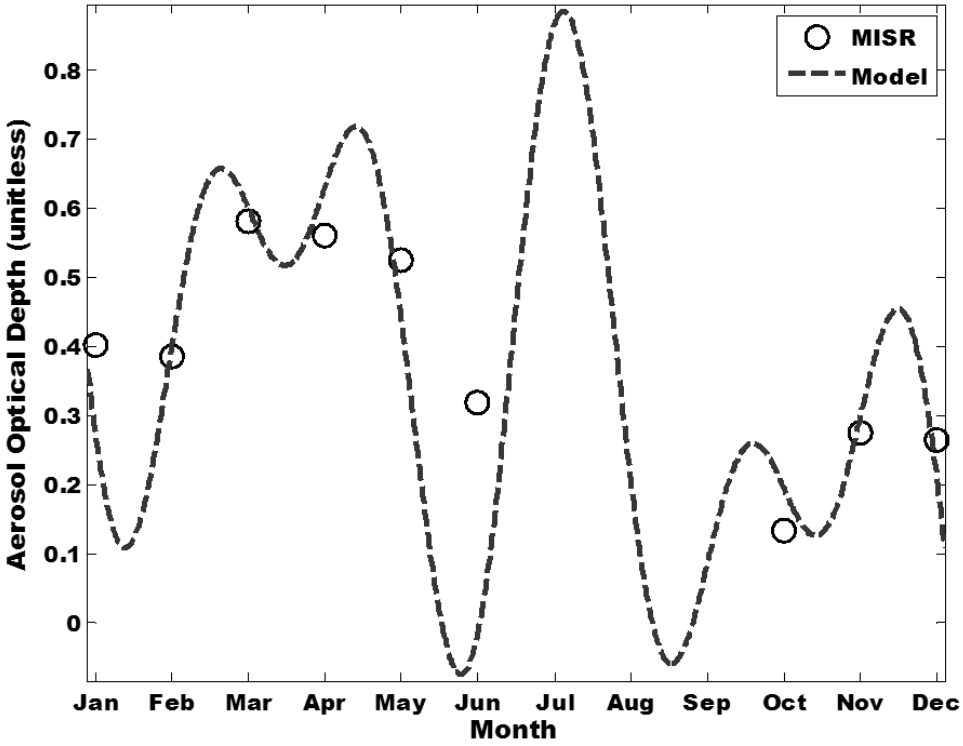

Figure II.lii: AOD for new model and MISR (Conakry, 2001)

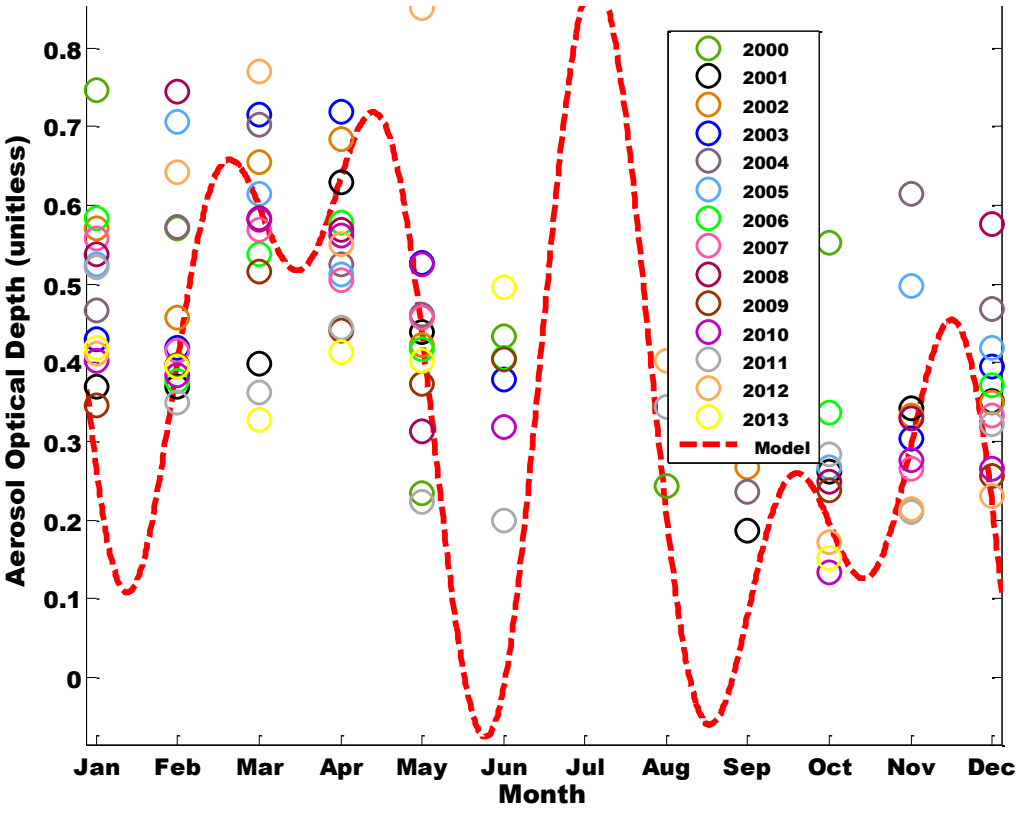

Figure II.liii: AOD for new model and MISR (Conakry, 2000-2013)

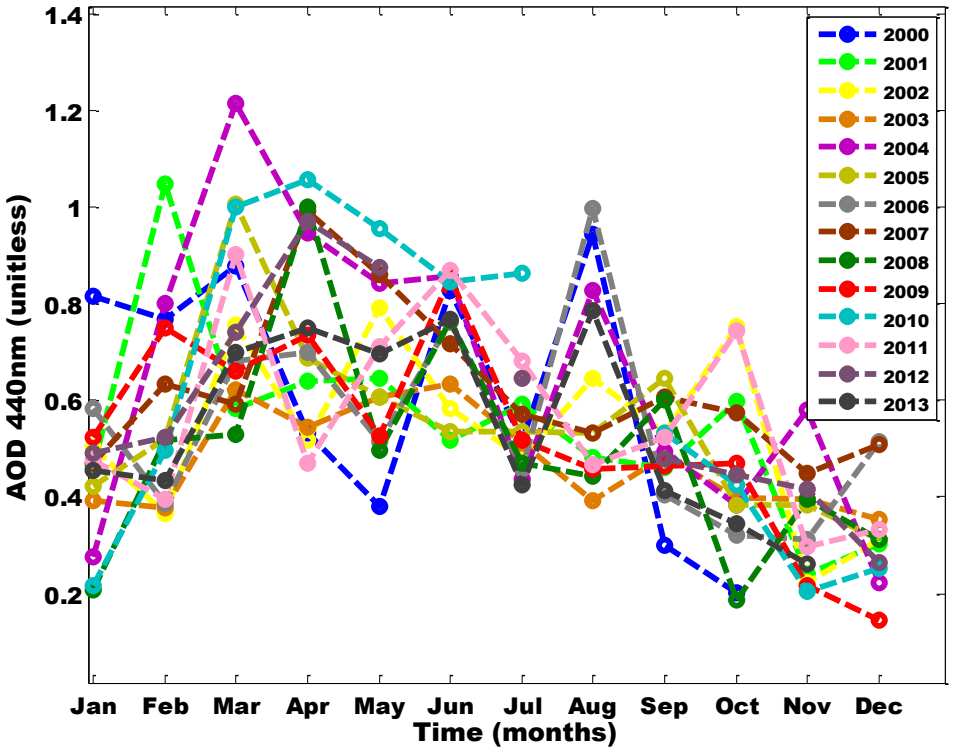

Figure II.mi: AOD pattern for Niamey 2000 - 2013

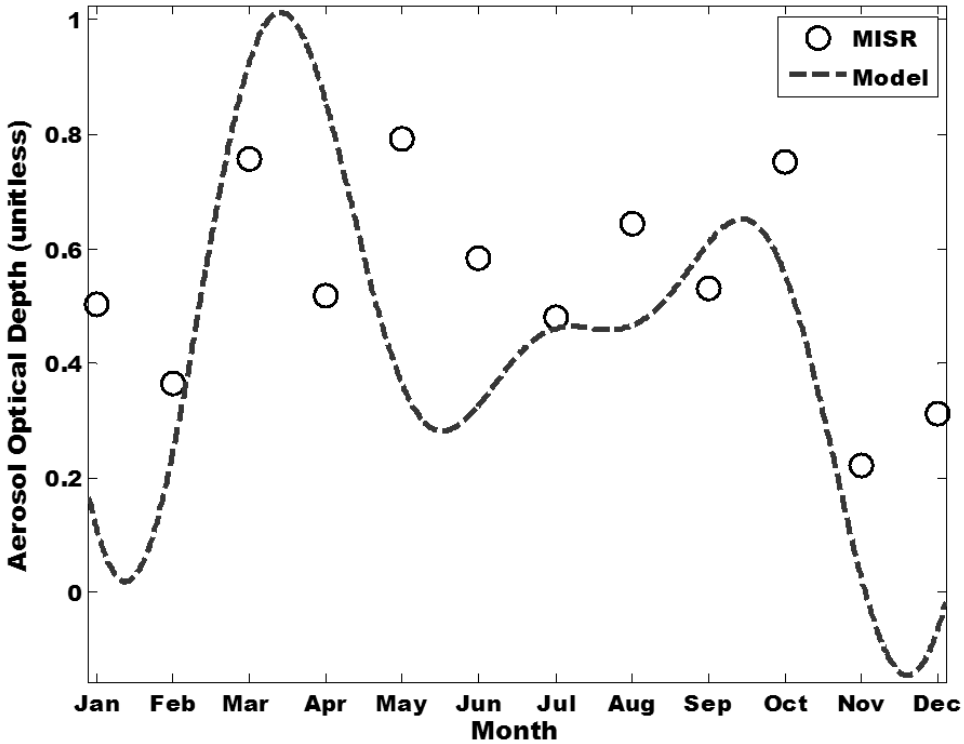

Figure II.mii: AOD for new model and MISR (Niamey, 2001)

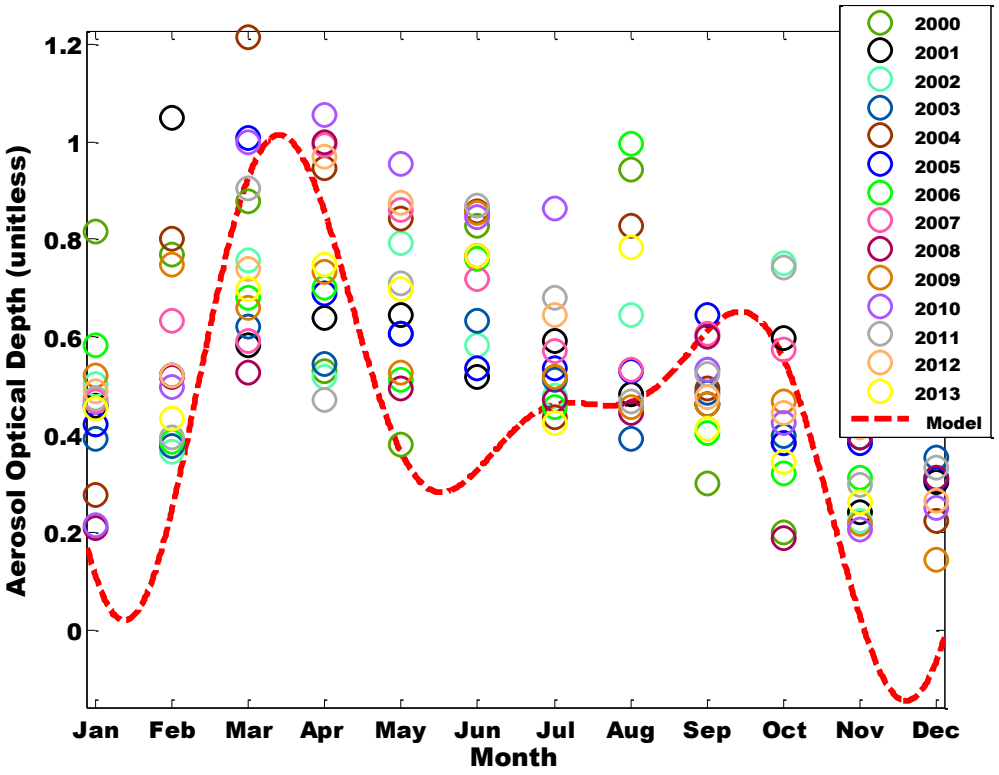

Figure II.miii: AOD for new model and MISR (Niamey, 2000-2013)

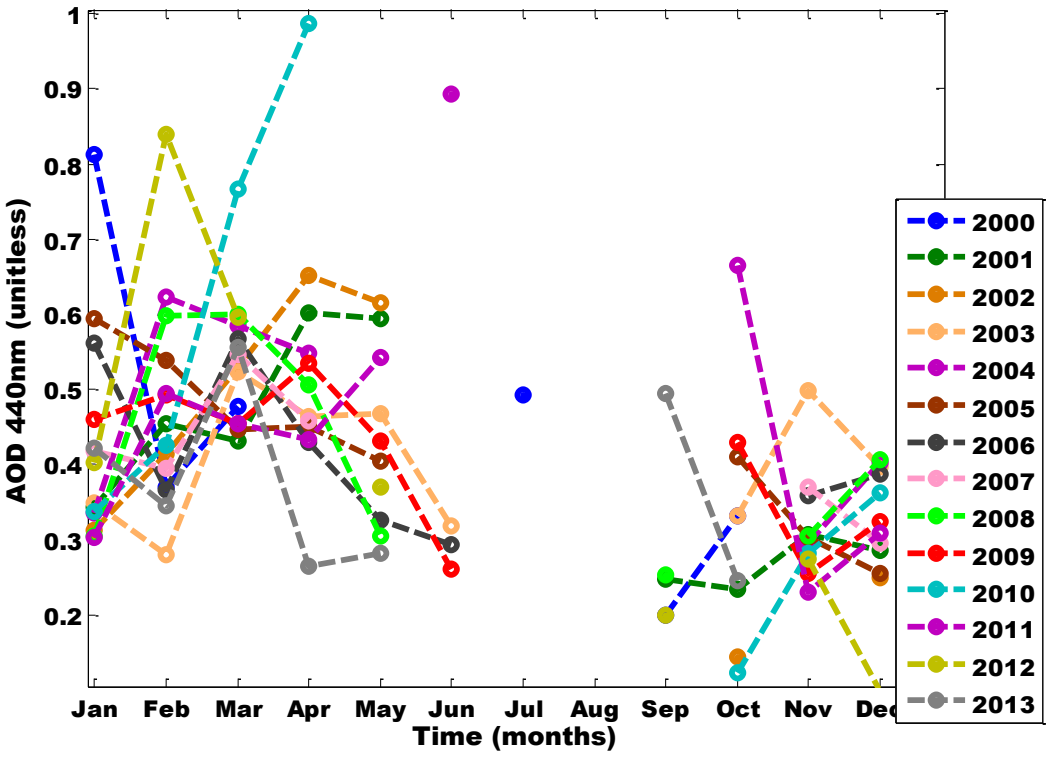

Figure II.ni: AOD pattern for Lome 2000 - 2013

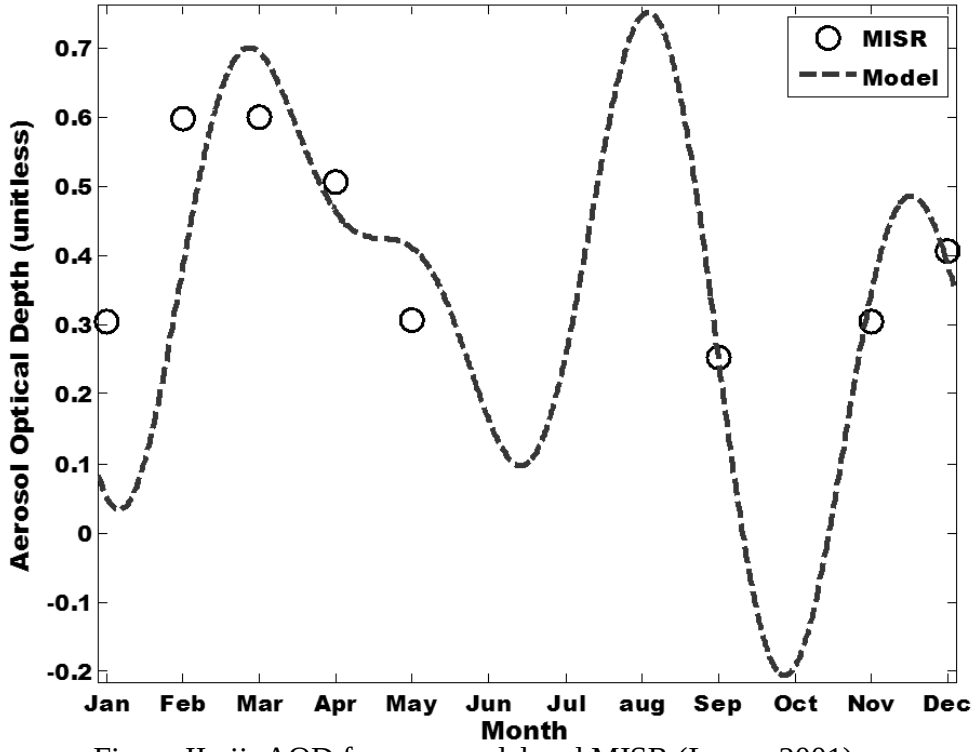

Figure II.nii: AOD for new model and MISR (Lome, 2001)

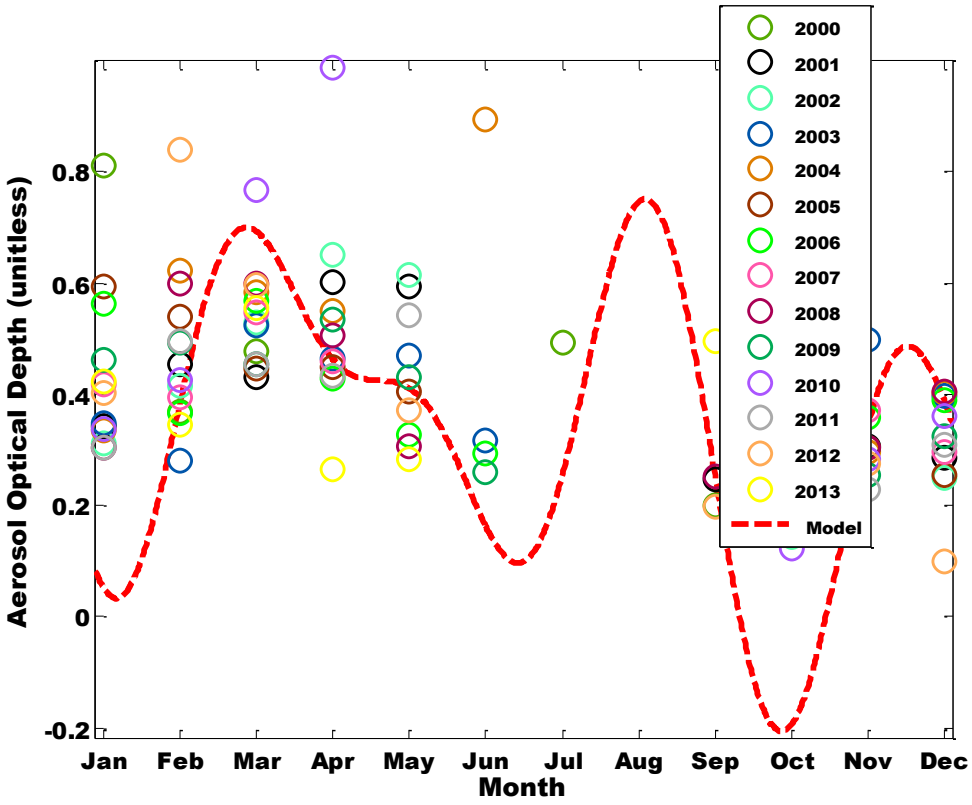

Figure II.niii: AOD for new model and MISR (Lome, 2000-2013)

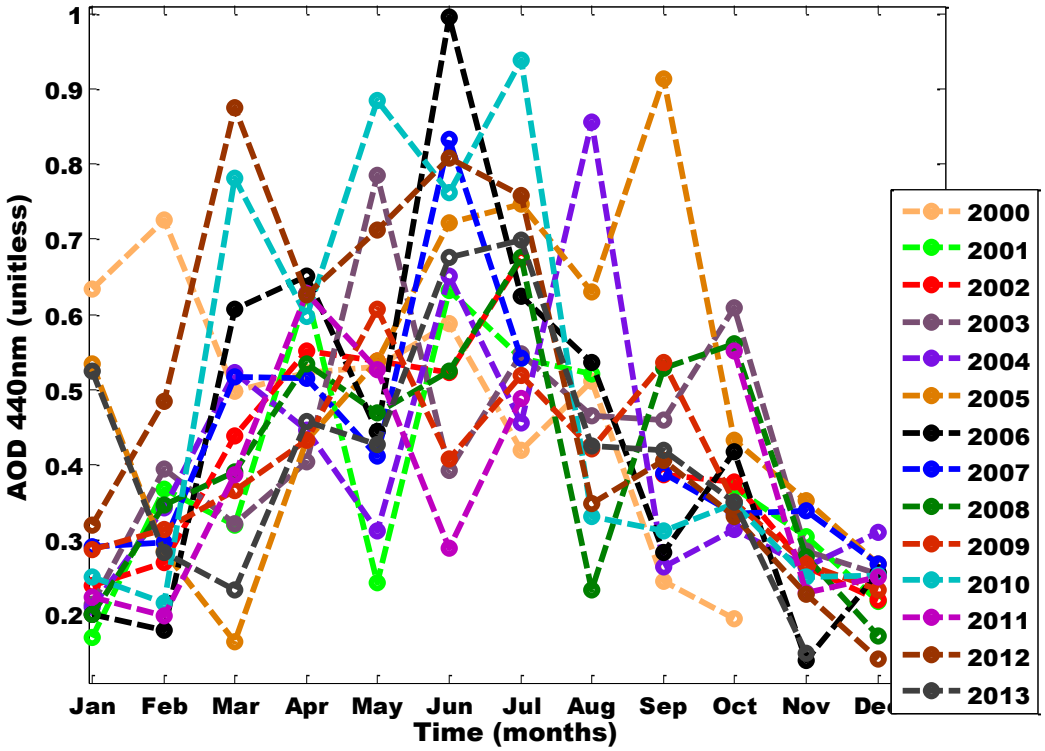

Figure II.oi: AOD pattern for Dakar 2000 - 2013

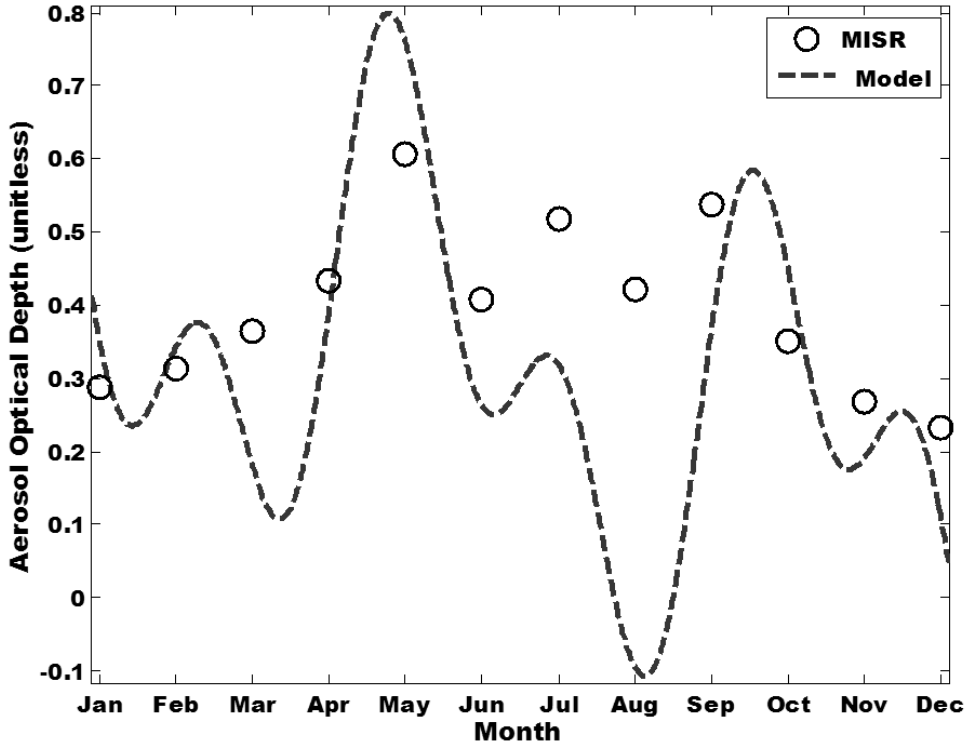

Figure II.oii: AOD for new model and MISR (Dakar, 2001)

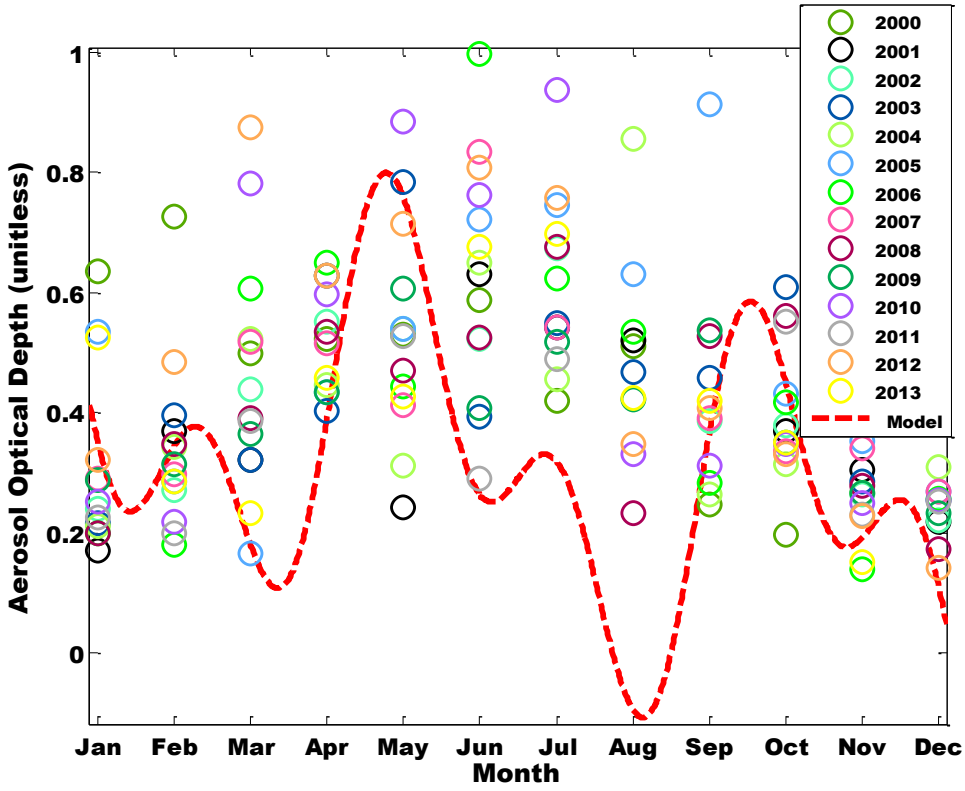

Figure II.oiii: AOD for new model and MISR (Dakar, 2000-2013)

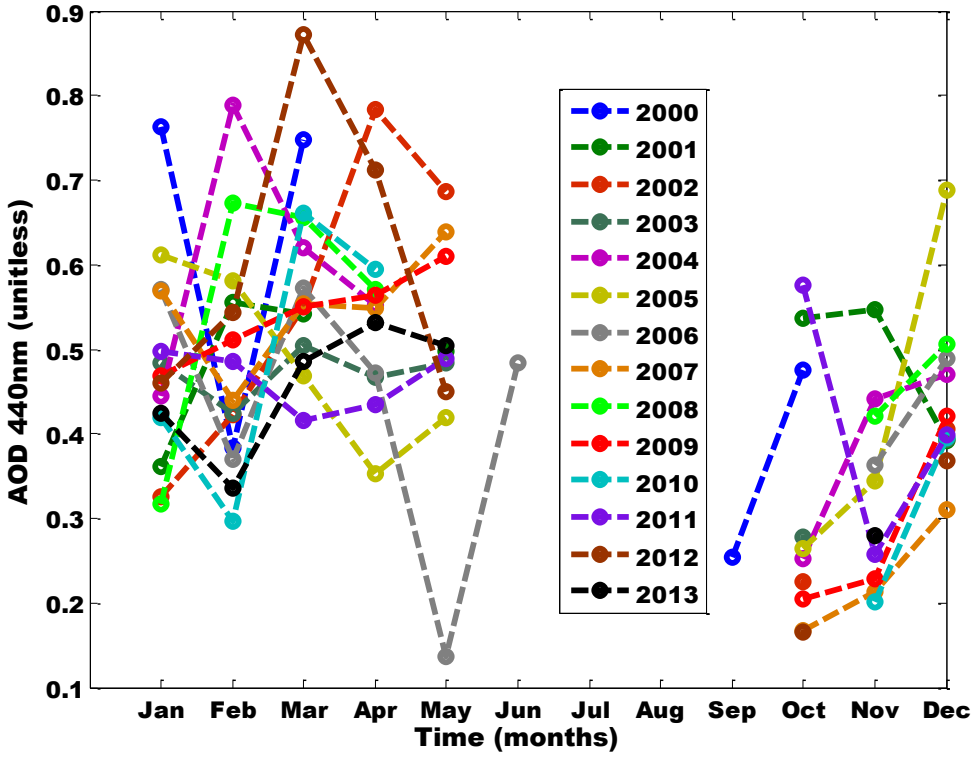

Figure II.pi: AOD pattern for Binkolo 2000 - 2013

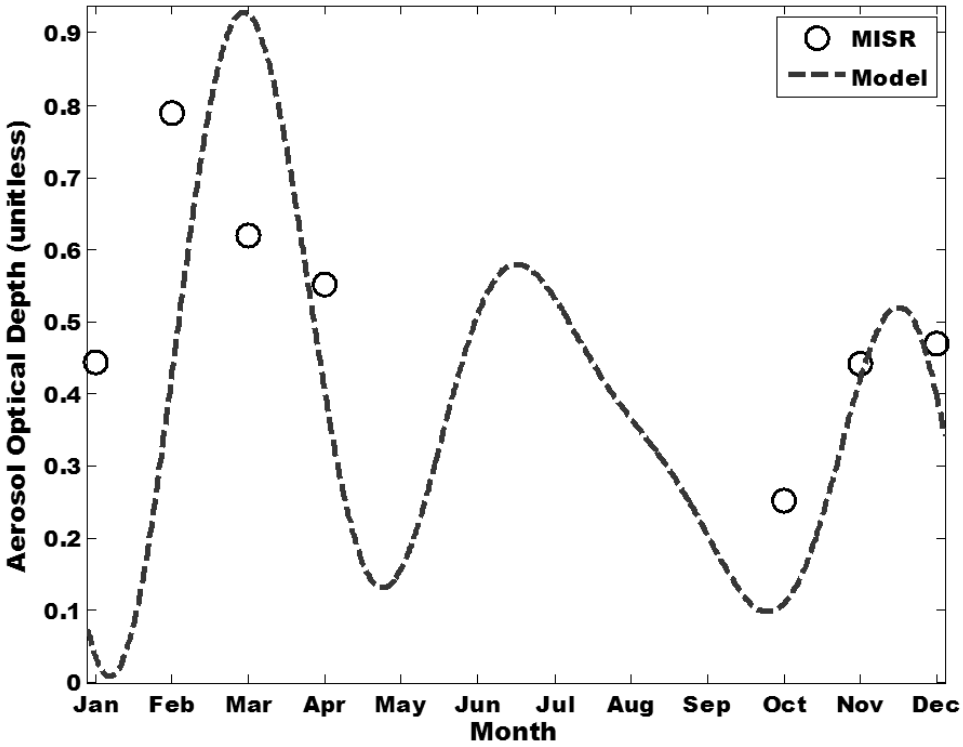

Figure II.pii: AOD for new model and MISR (Binkolo, 2001)

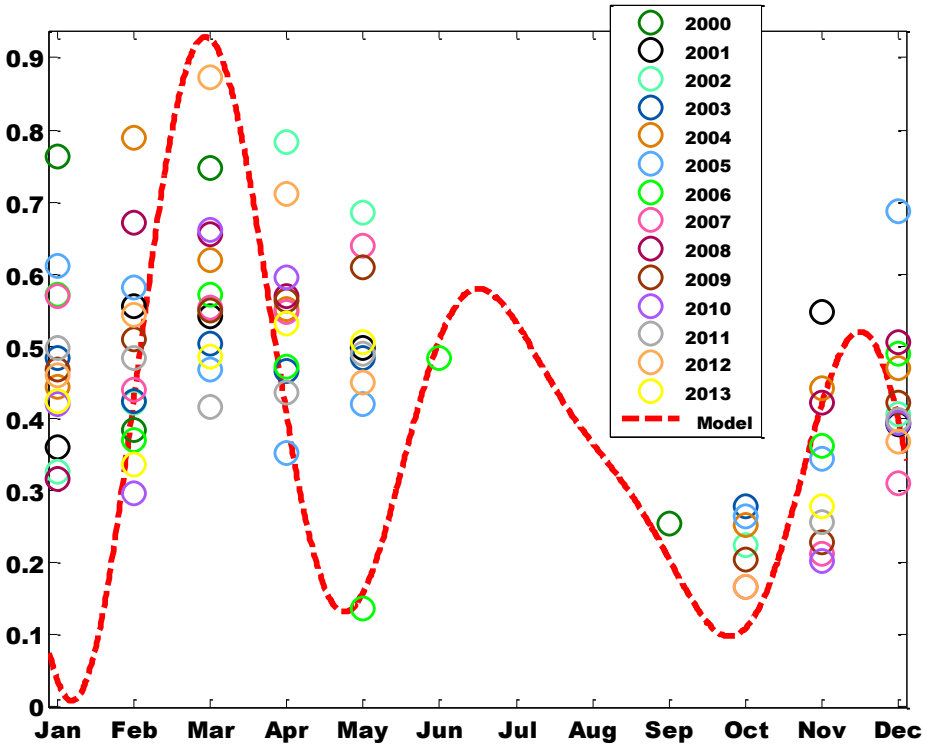

Figure II.piii: AOD for new model and MISR (Binkolo, 2000-2013)

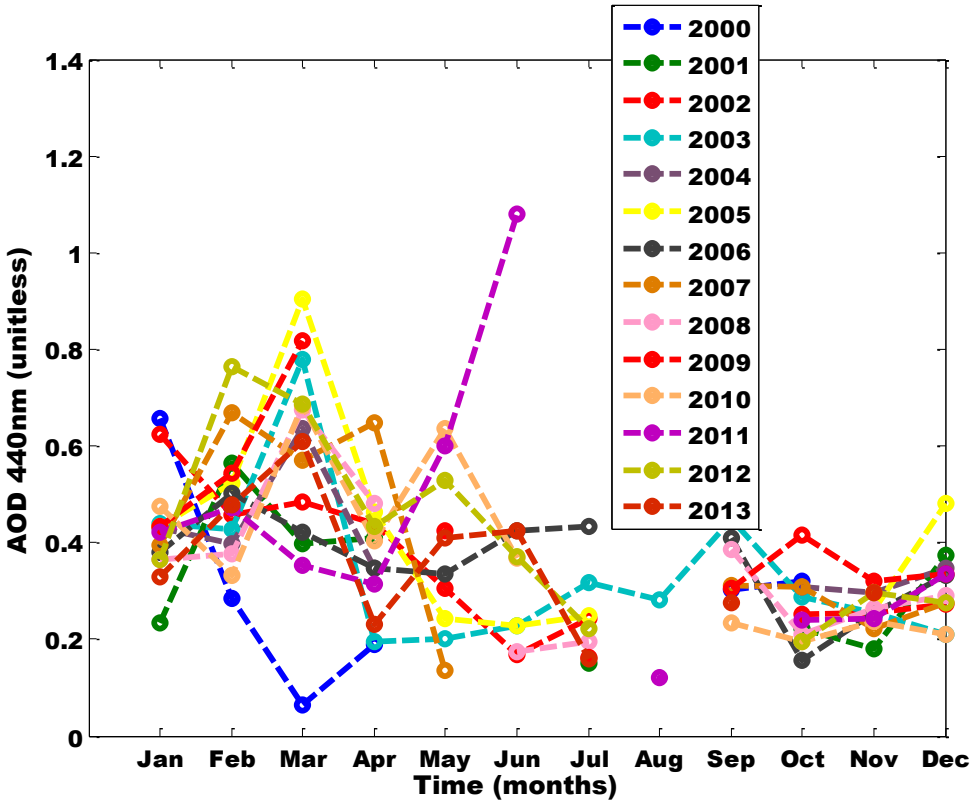

Figure II.qi: AOD pattern for Younde (2000 – 2013)

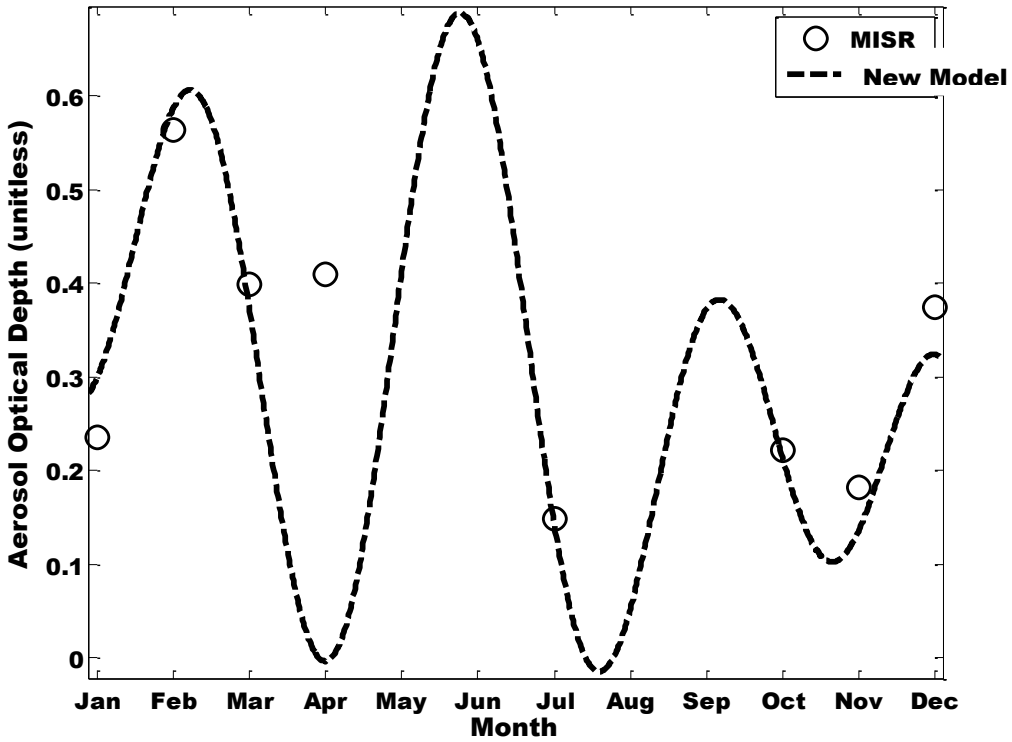

Figure II.qii: AOD for new model and MISR for the year 2001 Younde

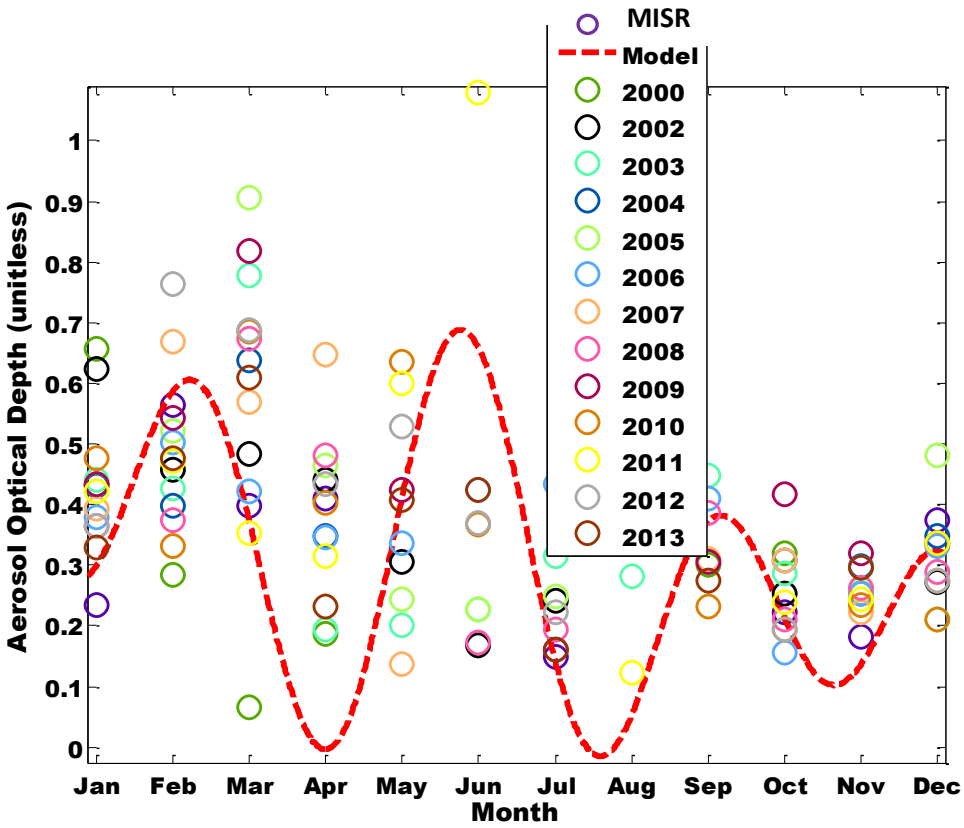

Figure II.qiii: AOD for new model and MISR for the year 2000-2013 Younde

Appendix III

Matlab programme for aerosol size distribution

MATLAB File for Unified Number (I)

```
</style></head><body><div class="content"><pre class="codeinput">filename=<span
class="string">'Davispaper.xls'</span>;
sheet=1;
a=<span class="string">'B1:B14'</span>;
b=<span class="string">'C1:C14'</span>;
c=<span class="string">'D1:D14'</span>;
d=<span class="string">'G1:G14'</span>;
e=<span class="string">'J1:J14'</span>;
f=<span class="string">'K1:K14'</span>;
g=<span class="string">'L1:L14'</span>;
h=<span class="string">'O1:O14'</span>;
i=<span class="string">'R1:R14'</span>;
j=<span class="string">'S1:S14'</span>;
k=<span class="string">'T1:T14'</span>;
l=<span class="string">'W1:W14'</span>;
n=xlsread(filename,1,a);
o=xlsread(filename,1,b);
p=xlsread(filename,1,c);
q=xlsread(filename,1,d);
r=xlsread(filename,1,e);
s=xlsread(filename,1,f);
t=xlsread(filename,1,g);
u=xlsread(filename,1,h);
v=xlsread(filename,1,i);
w=xlsread(filename,1,j);
x=xlsread(filename,1,k);
```

```
y=xlsread(filename,1,l);
A=n/o;
B=r/s;
C=v/w;
D=0.5;
E=D.*A(:,1).*q.*p;
F=D.*B(:,1).*u.*t;
M=D.*C(:,3).*y.*x;
G=0.001;
H=D.*G.*q.*p;
I=D.*G.*u.*t;
J=D.*G.*y.*x;
K=[1,2,3,4,5,6,7,8,9,10,11,12,13];
plot(K,H,K,I,K,J);
xlabel(<span class="string">'Time (minutes)'</span>);ylabel(<span class="string">'Unified
number (unitless)'</span>);
legend(<span class="string">'Reynold-Night'</span>,<span class="string">'Reynold-
Morning'</span>,<span class="string">'Reynold-Afternoon'</span>);
</pre><img vspace="5" hspace="5" src="aerosol_01.png" alt=""> <p class="footer"><br>
    Published with MATLAB&reg; 7.9<br></p></div><!--
##### SOURCE BEGIN #####
filename='Davispaper.xls';
sheet=1;
a='B1:B14';
b='C1:C14';
c='D1:D14';
d='G1:G14';
e='J1:J14';
f='K1:K14';
g='L1:L14';
h='O1:O14';
```

```
i='R1:R14';
j='S1:S14';
k='T1:T14';
l='W1:W14';
n=xlsread(filename,1,a);
o=xlsread(filename,1,b);
p=xlsread(filename,1,c);
q=xlsread(filename,1,d);
r=xlsread(filename,1,e);
s=xlsread(filename,1,f);
t=xlsread(filename,1,g);
u=xlsread(filename,1,h);
v=xlsread(filename,1,i);
w=xlsread(filename,1,j);
x=xlsread(filename,1,k);
y=xlsread(filename,1,l);
A=n/o;
B=r/s;
C=v/w;
D=0.5;
E=D.*A(:,1).*q.*p;
F=D.*B(:,1).*u.*t;
M=D.*C(:,3).*y.*x;
G=0.001;
H=D.*G.*q.*p;
I=D.*G.*u.*t;
J=D.*G.*y.*x;
K=[1,2,3,4,5,6,7,8,9,10,11,12,13];
plot(K,H,K,I,K,J);
xlabel('Time (minutes)');ylabel('Unified number (unitless)');
legend('Reynold-Night','Reynold-Morning','Reynold-Afternoon');
```

SOURCE END
--></body></html>

MATLAB File for Air density

</style></head><body> <pre class="codeinput">filename='Davispaper.xls';
sheet=1;
a='B1:B14';
b='C1:C14';
c='D1:D14';
d='G1:G14';
e='J1:J14';
f='K1:K14';
g='L1:L14';
h='O1:O14';
i='R1:R14';
j='S1:S14';
k='T1:T14';
l='W1:W14';
n=xlsread(filename,1,a);
o=xlsread(filename,1,b);
p=xlsread(filename,1,c);
q=xlsread(filename,1,d);
r=xlsread(filename,1,e);
s=xlsread(filename,1,f);
t=xlsread(filename,1,g);
u=xlsread(filename,1,h);
v=xlsread(filename,1,i);
w=xlsread(filename,1,j);

```
x=xlsread(filename,1,k);
y=xlsread(filename,1,l);
A=n/o;
B=r/s;
C=v/w;
D=0.1;
E=0.3;
F=0.5;
M=0.9;
G=D.*A(:,1).*q.*p;
H=E.*A(:,1).*q.*p;
I=F.*A(:,1).*q.*p;
J=M.*A(:,1).*q.*p;
K=[1,2,3,4,5,6,7,8,9,10,11,12,13];
plot(K,q,K,u,K,y);
xlabel(<span class="string">'Time (minutes)'</span>);ylabel(<span class="string">'Air
density (Kg/m^3)'</span>);
legend(<span class="string">'Air density-Night'</span>,<span class="string">'Air density-
Morning'</span>,<span class="string">'Air density-Afternoon'</span>);
</pre><img vspace="5" hspace="5" src="Aerosoll_01.png" alt=""> <p class="footer"><br>
    Published with MATLAB&reg; 7.9<br></p></div><!--
##### SOURCE BEGIN #####
filename='Davispaper.xls';
sheet=1;
a='B1:B14';
b='C1:C14';
c='D1:D14';
d='G1:G14';
e='J1:J14';
f='K1:K14';
g='L1:L14';
```

```
h='O1:O14';
i='R1:R14';
j='S1:S14';
k='T1:T14';
l='W1:W14';
n=xlsread(filename,1,a);
o=xlsread(filename,1,b);
p=xlsread(filename,1,c);
q=xlsread(filename,1,d);
r=xlsread(filename,1,e);
s=xlsread(filename,1,f);
t=xlsread(filename,1,g);
u=xlsread(filename,1,h);
v=xlsread(filename,1,i);
w=xlsread(filename,1,j);
x=xlsread(filename,1,k);
y=xlsread(filename,1,l);
A=n/o;
B=r/s;
C=v/w;
D=0.1;
E=0.3;
F=0.5;
M=0.9;
G=D.*A(:,1).*q.*p;
H=E.*A(:,1).*q.*p;
I=F.*A(:,1).*q.*p;
J=M.*A(:,1).*q.*p;
K=[1,2,3,4,5,6,7,8,9,10,11,12,13];
plot(K,q,K,u,K,y);
xlabel('Time (minutes)');ylabel('Air density (Kg/m^3)');
```

legend('Air density-Night','Air density-Morning','Air density-Afternoon');
SOURCE END
--></body></html>

MATLAB File Aerosol Size Distribution

</style></head><body> <pre class="codeinput">filename='aerosol.xlsx';
sheet=1;
a='A1:A9';
b='B1:B9';
c='C1:C9';
d='D1:D9';
e='F1:F13';
f='G1:G13';
g='H1:H13';
h='I1:I13';
i='K1:K6';
j='L1:L6';
k='M1:M6';
l='N1:N6';
m=xlsread(filename,1,a);
n=xlsread(filename,1,b);
o=xlsread(filename,1,c);
p=xlsread(filename,1,d);
q=xlsread(filename,1,e);
r=xlsread(filename,1,f);
s=xlsread(filename,1,g);
u=xlsread(filename,1,h);
v=xlsread(filename,1,i);
w=xlsread(filename,1,j);

```
x=xlsread(filename,1,k);
y=xlsread(filename,1,l);
z=0.003;
A=0.076;
B=1.36;
C=2.73;
D=7.57;
E=14.8;
F=30.3;
E=((C-1)./m).^-1;
F=((C-1)./n).^-1;
G=((C-1)./o).^-1;
H=((C-1)./p).^-1;
I=((B-1)./q).^-1;
J=((B-1)./r).^-1;
K=((B-1)./s).^-1;
L=((B-1)./u).^-1;
M=(C-1)./v;
N=(C-1)./w;
O=(C-1)./x;
P=(C-1)./y;
Q=[1,2,3,4,5,6,7,8];
R=[1,2,3,4,5,6,7,8,9,10,11,12];
S=[1,2,3,4,5];
plot(R,I,R,J,R,K,R,L);
xlabel(<span class="string">'Time (months)'</span>);ylabel(<span class="string">'Aerosol
size distribution (unitless)'</span>);
legend(<span class="string">'Wavelength(442nm)'</span>,<span
class="string">'Wavelength(555nm)'</span>,<span
class="string">'Wavelength(670nm)'</span>,<span
class="string">'Wavelength(865nm)'</span>);
```

</pre><img vspace="5" hspace="5" src="aerolagoss_01.png" alt="">
Published with MATLAB® 7.9
 <!--
SOURCE BEGIN

```
filename='aerosol.xlsx';
sheet=1;
a='A1:A9';
b='B1:B9';
c='C1:C9';
d='D1:D9';
e='F1:F13';
f='G1:G13';
g='H1:H13';
h='I1:I13';
i='K1:K6';
j='L1:L6';
k='M1:M6';
l='N1:N6';
m=xlsread(filename,1,a);
n=xlsread(filename,1,b);
o=xlsread(filename,1,c);
p=xlsread(filename,1,d);
q=xlsread(filename,1,e);
r=xlsread(filename,1,f);
s=xlsread(filename,1,g);
u=xlsread(filename,1,h);
v=xlsread(filename,1,i);
w=xlsread(filename,1,j);
x=xlsread(filename,1,k);
y=xlsread(filename,1,l);
z=0.003;
```

```
A=0.076;
B=1.36;
C=2.73;
D=7.57;
E=14.8;
F=30.3;
E=((C-1)./m).^-1;
F=((C-1)./n).^-1;
G=((C-1)./o).^-1;
H=((C-1)./p).^-1;
I=((B-1)./q).^-1;
J=((B-1)./r).^-1;
K=((B-1)./s).^-1;
L=((B-1)./u).^-1;
M=(C-1)./v;
N=(C-1)./w;
O=(C-1)./x;
P=(C-1)./y;
Q=[1,2,3,4,5,6,7,8];
R=[1,2,3,4,5,6,7,8,9,10,11,12];
S=[1,2,3,4,5];
plot(R,I,R,J,R,K,R,L);
xlabel('Time (months)');ylabel('Aerosol size distribution (unitless)');
legend('Wavelength(442nm)','Wavelength(555nm)','Wavelength(670nm)','Wavelength(865n
m)');
##### SOURCE END #####
--></body></html>
```

MATLAB File Aerosol Size Distribution 2

```
filename='aerosol.xlsx';
sheet=1;
a='A1:A9';
b='B1:B9';
c='C1:C9';
d='D1:D9';
e='F1:F13';
f='G1:G13';
g='H1:H13';
h='I1:I13';
i='K1:K6';
j='L1:L6';
k='M1:M6';
l='N1:N6';
m=xlsread(filename,1,a);
n=xlsread(filename,1,b);
o=xlsread(filename,1,c);
p=xlsread(filename,1,d);
q=xlsread(filename,1,e);
r=xlsread(filename,1,f);
s=xlsread(filename,1,g);
u=xlsread(filename,1,h);
v=xlsread(filename,1,i);
w=xlsread(filename,1,j);
x=xlsread(filename,1,k);
y=xlsread(filename,1,l);
z=log(q/r);
A=log(q/s);
B=log(q/u);
C=log(r/s);
```

```
D=log(r/u);
E=log(s/u);
F=-z(:,7)/(log(440/555));
G=-A(:,7)/(log(440/670));
H=-B(:,7)/(log(440/865));
I=-C(:,7)/(log(555/670));
J=-D(:,7)/(log(555/865));
K=-E(:,7)/(log(670/865));
Q=[1,2,3,4,5,6,7,8];
R=[1,2,3,4,5,6,7,8,9,10,11,12];
S=[1,2,3,4,5];
plot(R,F,R,G,R,H,R,I,R,J,R,K);
xlabel(<span class="string">'Time (months)'</span>);ylabel(<span class="string">'Aerosol
Size Distribution (unitless)'</span>);
legend(<span class="string">'ASD(440nm/555nm)'</span>,<span
class="string">'ASD(440nm/670nm)'</span>,<span
class="string">'ASD(440nm/865nm)'</span>,<span
class="string">'ASD(555nm/670nm)'</span>,<span
class="string">'ASD(555/865)'</span>,<span class="string">'ASD(670/865)'</span>);
</pre><img vspace="5" hspace="5" src="aerolagsizee_01.png" alt=""> <p
class="footer"><br>
    Published with MATLAB&reg; 7.9<br></p></div><!--
##### SOURCE BEGIN #####
filename='aerosol.xlsx';
sheet=1;
a='A1:A9';
b='B1:B9';
c='C1:C9';
d='D1:D9';
e='F1:F13';
f='G1:G13';
```

```
g='H1:H13';
h='I1:I13';
i='K1:K6';
j='L1:L6';
k='M1:M6';
l='N1:N6';
m=xlsread(filename,1,a);
n=xlsread(filename,1,b);
o=xlsread(filename,1,c);
p=xlsread(filename,1,d);
q=xlsread(filename,1,e);
r=xlsread(filename,1,f);
s=xlsread(filename,1,g);
u=xlsread(filename,1,h);
v=xlsread(filename,1,i);
w=xlsread(filename,1,j);
x=xlsread(filename,1,k);
y=xlsread(filename,1,l);
z=log(q/r);
A=log(q/s);
B=log(q/u);
C=log(r/s);
D=log(r/u);
E=log(s/u);
F=-z(:,7)/(log(440/555));
G=-A(:,7)/(log(440/670));
H=-B(:,7)/(log(440/865));
I=-C(:,7)/(log(555/670));
J=-D(:,7)/(log(555/865));
K=-E(:,7)/(log(670/865));
Q=[1,2,3,4,5,6,7,8];
```

R=[1,2,3,4,5,6,7,8,9,10,11,12];
S=[1,2,3,4,5];
plot(R,F,R,G,R,H,R,I,R,J,R,K);
xlabel('Time (months)');ylabel('Aerosol Size Distribution (unitless)');
legend('ASD(440nm/555nm)','ASD(440nm/670nm)','ASD(440nm/865nm)','ASD(555nm/670 nm)','ASD(555/865)','ASD(670/865)');
SOURCE END
--></body></html>

MATLAB File for Knudsen Number

</style></head><body> <pre class="codeinput">filename='Davispaper.xls';
sheet=1;
a='F1:F14';
b='N1:N14';
c='V1:V14';
d='D1:D14';
e='L1:L14';
f='T1:T14';
g=xlsread(filename,1,a);
h=xlsread(filename,1,b);
i=xlsread(filename,1,c);
j=xlsread(filename,1,d);
k=xlsread(filename,1,e);
l=xlsread(filename,1,f);
x=0.001;
m=1.8*10.^-5;
n=(8/(j.^2*pi.^2)).^0.5;
o=0.499*g*n;
p=m./(o(:,2)*x);

```
q=(8/(k.^2*pi.^2)).^0.5;
r=0.499*h*q;
s=m./(r(:,4)*x);
t=(8/(l.^2*pi.^2)).^0.5;
u=0.499*i*t;
v=m./(u(:,5)*x);
w=[1,2,3,4,5,6,7,8,9,10,11,12,13];
plot(w,v);
xlabel(<span class="string">'Time (minutes)'</span>);ylabel(<span class="string">'Knudsen
number (unitless)'</span>);
legend(<span class="string">'Knudsen number-Afternoon'</span>);
</pre><img vspace="5" hspace="5" src="Aerosolll_01.png" alt=""> <p class="footer"><br>
    Published with MATLAB&reg; 7.9<br></p></div><!--
##### SOURCE BEGIN #####
filename='Davispaper.xls';
sheet=1;
a='F1:F14';
b='N1:N14';
c='V1:V14';
d='D1:D14';
e='L1:L14';
f='T1:T14';
g=xlsread(filename,1,a);
h=xlsread(filename,1,b);
i=xlsread(filename,1,c);
j=xlsread(filename,1,d);
k=xlsread(filename,1,e);
l=xlsread(filename,1,f);
x=0.001;
m=1.8*10.^-5;
n=(8/(j.^2*pi.^2)).^0.5;
```

```
o=0.499*g*n;
p=m./(o(:,2)*x);
q=(8/(k.^2*pi.^2)).^0.5;
r=0.499*h*q;
s=m./(r(:,4)*x);
t=(8/(l.^2*pi.^2)).^0.5;
u=0.499*i*t;
v=m./(u(:,5)*x);
w=[1,2,3,4,5,6,7,8,9,10,11,12,13];
plot(w,v);
xlabel('Time (minutes)');ylabel('Knudsen number (unitless)');
legend('Knudsen number-Afternoon');
##### SOURCE END #####
--></body></html>
```

MATLAB File for Rate of mass transfer

```
  </style></head><body><div class="content"><pre class="codeinput">filename=<span
class="string">'aerosol.xlsx'</span>;
sheet=1;
a=<span class="string">'A1:A9'</span>;
b=<span class="string">'B1:B9'</span>;
c=<span class="string">'C1:C9'</span>;
d=<span class="string">'D1:D9'</span>;
e=<span class="string">'F1:F13'</span>;
f=<span class="string">'G1:G13'</span>;
g=<span class="string">'H1:H13'</span>;
h=<span class="string">'I1:I13'</span>;
i=<span class="string">'K1:K6'</span>;
j=<span class="string">'L1:L6'</span>;
k=<span class="string">'M1:M6'</span>;
```

l='N1:N6';

m=xlsread(filename,1,a);

n=xlsread(filename,1,b);

o=xlsread(filename,1,c);

p=xlsread(filename,1,d);

q=xlsread(filename,1,e);

r=xlsread(filename,1,f);

s=xlsread(filename,1,g);

u=xlsread(filename,1,h);

v=xlsread(filename,1,i);

w=xlsread(filename,1,j);

x=xlsread(filename,1,k);

y=xlsread(filename,1,l);

z=0.003;

A=0.076;

B=0.3;

C=2.73;

D=7.57;

E=14.8;

F=30.3;

E=((C-1)./m).^1;

F=((C-1)./n).^1;

G=((C-1)./o).^1;

H=((C-1)./p).^1;

I=(C-1)./q;

J=(C-1)./r;

K=(C-1)./s;

L=(C-1)./u;

M=(C-1)./v;

N=(C-1)./w;

O=(C-1)./x;

```
P=(C-1)./y;
Q=[1,2,3,4,5,6,7,8];
R=[1,2,3,4,5,6,7,8,9,10,11,12];
S=[1,2,3,4,5];
plot(Q,E,Q,F,Q,G,Q,H);
xlabel(<span class="string">'Month'</span>);ylabel(<span class="string">'Rate of mass
transfer (unitless)'</span>);
legend(<span class="string">'Wavelength(442nm)'</span>,<span
class="string">'Wavelength(555nm)'</span>,<span
class="string">'Wavelength(670nm)'</span>,<span
class="string">'Wavelength(865nm)'</span>);
</pre><img vspace="5" hspace="5" src="aerosolmass_01.png" alt=""> <p
class="footer"><br>
    Published with MATLAB&reg; 7.9<br></p></div><!--
##### SOURCE BEGIN #####
filename='aerosol.xlsx';
sheet=1;
a='A1:A9';
b='B1:B9';
c='C1:C9';
d='D1:D9';
e='F1:F13';
f='G1:G13';
g='H1:H13';
h='I1:I13';
i='K1:K6';
j='L1:L6';
k='M1:M6';
l='N1:N6';
m=xlsread(filename,1,a);
n=xlsread(filename,1,b);
```

```
o=xlsread(filename,1,c);
p=xlsread(filename,1,d);
q=xlsread(filename,1,e);
r=xlsread(filename,1,f);
s=xlsread(filename,1,g);
u=xlsread(filename,1,h);
v=xlsread(filename,1,i);
w=xlsread(filename,1,j);
x=xlsread(filename,1,k);
y=xlsread(filename,1,l);
z=0.003;
A=0.076;
B=0.3;
C=2.73;
D=7.57;
E=14.8;
F=30.3;
E=((C-1)./m).^1;
F=((C-1)./n).^1;
G=((C-1)./o).^1;
H=((C-1)./p).^1;
I=(C-1)./q;
J=(C-1)./r;
K=(C-1)./s;
L=(C-1)./u;
M=(C-1)./v;
N=(C-1)./w;
O=(C-1)./x;
P=(C-1)./y;
Q=[1,2,3,4,5,6,7,8];
R=[1,2,3,4,5,6,7,8,9,10,11,12];
```

S=[1,2,3,4,5];
plot(Q,E,Q,F,Q,G,Q,H);
xlabel('Month');ylabel('Rate of mass transfer (unitless)');
legend('Wavelength(442nm)','Wavelength(555nm)','Wavelength(670nm)','Wavelength(865nm)');
SOURCE END
--></body></html>

MATLAB File Reynold vs Unified number

</style></head><body> <pre class="codeinput">filename='Davispaper.xls';
sheet=1;
a='B1:B14';
b='C1:C14';
c='D1:D14';
d='G1:G14';
e='J1:J14';
f='K1:K14';
g='L1:L14';
h='O1:O14';
i='R1:R14';
j='S1:S14';
k='T1:T14';
l='W1:W14';
n=xlsread(filename,1,a);
o=xlsread(filename,1,b);
p=xlsread(filename,1,c);
q=xlsread(filename,1,d);
r=xlsread(filename,1,e);
s=xlsread(filename,1,f);

t=xlsread(filename,1,g);
u=xlsread(filename,1,h);
v=xlsread(filename,1,i);
w=xlsread(filename,1,j);
x=xlsread(filename,1,k);
y=xlsread(filename,1,l);
A=n/o;
B=r/s;
C=v/w;
D=0.5;
E=D*A*q*p;
F=D*B*u*t;
M=D*C*y*x;
G=0.001;
H=D*G*q*p;
I=D*G*u*t;
J=D*C*y*x;
K=[1,2,3,4,5,6,7,8,9,10,11,12,13,14];
plot(K,E,K,F,K,M,K,H,K,I,K,J);
xlabel('Time (minutes)');ylabel('Unified number & Reynolds number (unitless)');
legend('Unified-Night','Unified=Morning','Unified-Afternoon','Reynold-Night','Reynold-Morning','Reynold-Afternoon');
</pre><pre class="codeoutput">Error using ==> evalin
Undefined function or method 'unified' for input arguments of type 'char'.
</pre>
Published with MATLAB® 7.9
 <!--
SOURCE BEGIN

```
filename='Davispaper.xls';
sheet=1;
a='B1:B14';
b='C1:C14';
c='D1:D14';
d='G1:G14';
e='J1:J14';
f='K1:K14';
g='L1:L14';
h='O1:O14';
i='R1:R14';
j='S1:S14';
k='T1:T14';
l='W1:W14';
n=xlsread(filename,1,a);
o=xlsread(filename,1,b);
p=xlsread(filename,1,c);
q=xlsread(filename,1,d);
r=xlsread(filename,1,e);
s=xlsread(filename,1,f);
t=xlsread(filename,1,g);
u=xlsread(filename,1,h);
v=xlsread(filename,1,i);
w=xlsread(filename,1,j);
x=xlsread(filename,1,k);
y=xlsread(filename,1,l);
A=n/o;
B=r/s;
C=v/w;
D=0.5;
E=D*A*q*p;
```

```
F=D*B*u*t;
M=D*C*y*x;
G=0.001;
H=D*G*q*p;
I=D*G*u*t;
J=D*C*y*x;
K=[1,2,3,4,5,6,7,8,9,10,11,12,13,14];
plot(K,E,K,F,K,M,K,H,K,I,K,J);
xlabel('Time (minutes)');ylabel('Unified number & Reynolds number (unitless)');
legend('Unified-Night','Unified=Morning','Unified-Afternoon','Reynold-Night','Reynold-
Morning','Reynold-Afternoon');
##### SOURCE END #####
--></body></html>
```

MATLAB File Wind Investigation

```
  </style></head><body><div class="content"><pre
class="codeinput">x=0:pi/192:(5*pi)/16;
y=0:40:2400;
<span class="keyword">for</span> i=1:length(x)
<span class="keyword">for</span> j=1:length(y)
<span class="keyword">if</span> x(i)&lt;pi/16 &amp; y(j)&lt;480
F(i,j)=0.078*y(j)*sin(x(i));
<span class="keyword">elseif</span> x(i)&gt;pi/16 &amp; x(i)&lt;=pi/8, y(j)&gt;480
&amp; y(j)&lt;=960
F(i,j)=0.078*y(j)*cos(x(i));
<span class="keyword">elseif</span> x(i)&gt;pi/8 &amp; x(i)&lt;=3*pi/16, y(j)&gt;960
&amp; y(j)&lt;=1440
   F(i,j)=0.078*y(j)*(sin(x(i))+cos(x(i)));
   <span class="keyword">elseif</span> x(i)&gt;3*pi/16 &amp; x(i)&lt;=pi/4, y(j)&gt;1440
&amp; y(j)&lt;=1920
```

```
   F(i,j)=0.078*y(j)*sin(x(i)).^2;
<span class="keyword">else</span>
 F(i,j)=0.078*y(j)*cos(x(i)).^2;
<span class="keyword">end</span>
<span class="keyword">end</span>
<span class="keyword">end</span>
plot(F,y)
xlabel(<span class="string">'turbulence kinetic energy (J/Kg)'</span>);ylabel(<span
class="string">'Altitude (m)'</span>);
</pre><pre class="codeoutput">
 </pre><img vspace="5" hspace="5" src="windrainfall1_01.png" alt=""> <p
class="footer"><br>
     Published with MATLAB&reg; 7.9<br></p></div><!--
##### SOURCE BEGIN #####
x=0:pi/192:(5*pi)/16;
y=0:40:2400;
for i=1:length(x)
for j=1:length(y)
if x(i)<pi/16 & y(j)<480
F(i,j)=0.078*y(j)*sin(x(i));
elseif x(i)>pi/16 & x(i)<=pi/8, y(j)>480 & y(j)<=960
F(i,j)=0.078*y(j)*cos(x(i));
elseif x(i)>pi/8 & x(i)<=3*pi/16, y(j)>960 & y(j)<=1440
   F(i,j)=0.078*y(j)*(sin(x(i))+cos(x(i)));
   elseif x(i)>3*pi/16 & x(i)<=pi/4, y(j)>1440 & y(j)<=1920
   F(i,j)=0.078*y(j)*sin(x(i)).^2;
else
 F(i,j)=0.078*y(j)*cos(x(i)).^2;
end
end
end
```

```
plot(F,y)
xlabel('turbulence kinetic energy (J/Kg)');ylabel('Altitude (m)');
##### SOURCE END #####
--></body></html>
```

MATLAB File for numerical Analysis of wind

```
  </style></head><body><div class="content"><pre class="codeinput"><span
class="keyword">function</span> u = wind(v, x, t, init, bdry)
J = length(x);
N = length(t);
dx = mean(diff(x));
dt = mean(diff(t));
s = v*dt/dx;
u = zeros(N,J);
u(1, :) = init;
<span class="keyword">for</span> n = 1:N-1
u(n+1, 1:J-1) = (1 + s)*u(n, 1:J-1)-s*u(n+1,1:J-1);
u(n+1, 1) = bdry(1);
u(n+1, J) = bdry(2);
<span class="keyword">end</span>
</pre><pre class="codeoutput">Attempt to execute SCRIPT wind as a function:
C:\Users\Moses\Desktop\Desktop\wind.m
</pre><p class="footer"><br>
    Published with MATLAB&reg; 7.9<br></p></div><!--
##### SOURCE BEGIN #####
function u = wind(v, x, t, init, bdry)
J = length(x);
N = length(t);
dx = mean(diff(x));
dt = mean(diff(t));
```

```
s = v*dt/dx;
u = zeros(N,J);
u(1, :) = init;
for n = 1:N-1
u(n+1, 1:J-1) = (1 + s)*u(n, 1:J-1)-s*u(n+1,1:J-1);
u(n+1, 1) = bdry(1);
u(n+1, J) = bdry(2);
end

##### SOURCE END #####
--></body></html>
```

MATLAB File Aerosol vertical Profile

```
  </style></head><body><div class="content"><pre class="codeinput">a=10^5:10^5:10^6;

b=5;
c=3*10^5;
d=a*b-c;
e=1-(d.^2)/2+(d.^4)/12-(d.^6)/240;
plot(a,e);
xlabel(<span class="string">'frequency (Hz)'</span>);ylabel(<span class="string">'vertical
profile of aerosol content (&micro;gm^3)'</span>);
</pre><img vspace="5" hspace="5" src="plume_01.png" alt=""> <p class="footer"><br>
    Published with MATLAB&reg; 7.9<br></p></div><!--
##### SOURCE BEGIN #####
a=10^5:10^5:10^6;
b=5;
c=3*10^5;
d=a*b-c;
e=1-(d.^2)/2+(d.^4)/12-(d.^6)/240;
plot(a,e);
```

xlabel('frequency (Hz)');ylabel('vertical profile of aerosol content (Âµgm^3)');
SOURCE END
--></body></html>

MATLAB File Aerosol content dynamics

</style></head><body> <pre
class="codeinput">a=meshgrid(19:0.2:25);
d=meshgrid(4:0.2:10);
e=cos(d);
b=1./a;
c=e.*(1+b+(b.^2)./2);
surf(c)
xlabel('Wind Speed');ylabel('Mass
aerosol deposited (log)');zlabel('Aerosol content
dynamics');
</pre><img vspace="5" hspace="5" src="ewekoro_01.png" alt="">
Published with MATLAB® 7.9
 <!--
SOURCE BEGIN
a=meshgrid(19:0.2:25);
d=meshgrid(4:0.2:10);
e=cos(d);
b=1./a;
c=e.*(1+b+(b.^2)./2);
surf(c)
xlabel('Wind Speed');ylabel('Mass aerosol deposited (log)');zlabel('Aerosol content
dynamics');
SOURCE END
--></body></html>

MATLAB File Ground AOD

</style></head><body> <pre class="codeinput">filename='groundsatellite.xls';
sheet=1;
a='A1:A13';
b='B1:B13';
c=xlsread(filename,1,a);
d=xlsread(filename,1,b);
e=[1,2,3,4,5,6,7,8,9,10,11,12];
plot(e,c,e,d)
xlabel ('Time (month)'); ylabel ('AOD (unitless)'); legend ('ground AOD','satellite AOD');
</pre><img vspace="5" hspace="5" src="aod_01.png" alt="">
Published with MATLAB® 7.9
 <!--
SOURCE BEGIN
filename='groundsatellite.xls';
sheet=1;
a='A1:A13';
b='B1:B13';
c=xlsread(filename,1,a);
d=xlsread(filename,1,b);
e=[1,2,3,4,5,6,7,8,9,10,11,12];
plot(e,c,e,d)
xlabel ('Time (month)'); ylabel ('AOD (unitless)'); legend ('ground AOD','satellite AOD');

SOURCE END
--></body></html>

MATLAB File Atmospheric Constants Malabo

```
filename='Eguinea Malabo.xlsx';
sheet=1;
a='A1:A12';
b='B1:B12';
c='C1:C12';
d='D1:D12';
e='F1:F12';
f='G1:G12';
g='H1:H12';
h='I1:I12';
i='K1:K12';
j='L1:L12';
k='M1:N12';
l='N1:O12';
m='P1:P12';
n='Q1:Q12';
o='R1:R12';
p='S1:S12';
A=xlsread(filename,1,a);
B=xlsread(filename,1,b);
C=xlsread(filename,1,c);
D=xlsread(filename,1,d);
E=xlsread(filename,1,e);
F=xlsread(filename,1,f);
G=xlsread(filename,1,g);
H=xlsread(filename,1,h);
I=xlsread(filename,1,i);
J=xlsread(filename,1,j);
K=xlsread(filename,1,k);
L=xlsread(filename,1,l);
```

```
M=xlsread(filename,1,m);
N=xlsread(filename,1,n);
O=xlsread(filename,1,o);
P=xlsread(filename,1,p);
sheet=2;
a1=<span class="string">'A1:A12'</span>;
b1=<span class="string">'B1:B12'</span>;
c1=<span class="string">'C1:C12'</span>;
d1=<span class="string">'D1:D12'</span>;
e1=<span class="string">'F1:F12'</span>;
f1=<span class="string">'G1:G12'</span>;
g1=<span class="string">'H1:H12'</span>;
h1=<span class="string">'I1:I12'</span>;
i1=<span class="string">'K1:K12'</span>;
j1=<span class="string">'L1:L12'</span>;
k1=<span class="string">'M1:N12'</span>;
l1=<span class="string">'N1:O12'</span>;
m1=<span class="string">'P1:P12'</span>;
n1=<span class="string">'Q1:Q12'</span>;
o1=<span class="string">'R1:R12'</span>;
p1=<span class="string">'S1:S12'</span>;
A1=xlsread(filename,2,a1);
B1=xlsread(filename,2,b1);
C1=xlsread(filename,2,c1);
D1=xlsread(filename,2,d1);
E1=xlsread(filename,2,e1);
F1=xlsread(filename,2,f1);
G1=xlsread(filename,2,g1);
H1=xlsread(filename,2,h1);
I1=xlsread(filename,2,i1);
J1=xlsread(filename,2,j1);
```

```
K1=xlsread(filename,2,k1);
L1=xlsread(filename,2,l1);
M1=xlsread(filename,2,m1);
N1=xlsread(filename,2,n1);
O1=xlsread(filename,2,o1);
P1=xlsread(filename,2,p1);
sheet=3;
a2=<span class="string">'A1:A12'</span>;
b2=<span class="string">'B1:B12'</span>;
c2=<span class="string">'C1:C12'</span>;
d2=<span class="string">'D1:D12'</span>;
e2=<span class="string">'F1:F12'</span>;
f2=<span class="string">'G1:G12'</span>;
g2=<span class="string">'H1:H12'</span>;
h2=<span class="string">'I1:I12'</span>;
i2=<span class="string">'K1:K12'</span>;
j2=<span class="string">'L1:L12'</span>;
k2=<span class="string">'M1:N12'</span>;
l2=<span class="string">'N1:O12'</span>;
m2=<span class="string">'P1:P12'</span>;
n2=<span class="string">'Q1:Q12'</span>;
o2=<span class="string">'R1:R12'</span>;
p2=<span class="string">'S1:S12'</span>;
A2=xlsread(filename,3,a2);
B2=xlsread(filename,3,b2);
C2=xlsread(filename,3,c2);
D2=xlsread(filename,3,d2);
E2=xlsread(filename,3,e2);
F2=xlsread(filename,3,f2);
G2=xlsread(filename,3,g2);
H2=xlsread(filename,3,h2);
```

```
I2=xlsread(filename,3,i2);
J2=xlsread(filename,3,j2);
K2=xlsread(filename,3,k2);
L2=xlsread(filename,3,l2);
M2=xlsread(filename,3,m2);
N2=xlsread(filename,3,n2);
O2=xlsread(filename,3,o2);
P2=xlsread(filename,3,p2);
sheet=4;
a3=<span class="string">'A1:A12'</span>;
b3=<span class="string">'B1:B12'</span>;
c3=<span class="string">'C1:C12'</span>;
d3=<span class="string">'D1:D12'</span>;
e3=<span class="string">'F1:F12'</span>;
f3=<span class="string">'G1:G12'</span>;
g3=<span class="string">'H1:H12'</span>;
h3=<span class="string">'I1:I12'</span>;
A3=xlsread(filename,4,a3);
B3=xlsread(filename,4,b3);
C3=xlsread(filename,4,c3);
D3=xlsread(filename,4,d3);
E3=xlsread(filename,4,e3);
F3=xlsread(filename,4,f3);
G3=xlsread(filename,4,g3);
H3=xlsread(filename,4,h3);
x=[1,2,3,4,5,6,7,8,9,10,11];
y=[1,2,3,4,5,6,7,8,9,10];
z=[1,2,3,4,5,6,7,8,9,10,11,12];
plot(x,A,z,E,x,I,z,M,x,A1,z,E1,z,I1,z,M1,z,A2,z,E2,z,I2,z,M2,z,A3,x,E3);
xlabel(<span class="string">'Time (months)'</span>);ylabel(<span class="string">'AOD
440nm (unitless)'</span>);
```

legend('2000','2001','2002','2003','2004','2005','2006','2007','2008','2009','2010','2011','2012','2013')
</pre><img vspace="5" hspace="5" src="proeguineamalabo_01.png" alt="">
Published with MATLAB® 7.9
 <!--
SOURCE BEGIN
filename='Eguinea Malabo.xlsx';
sheet=1;
a='A1:A12';
b='B1:B12';
c='C1:C12';
d='D1:D12';
e='F1:F12';
f='G1:G12';
g='H1:H12';
h='I1:I12';
i='K1:K12';
j='L1:L12';
k='M1:N12';
l='N1:O12';
m='P1:P12';
n='Q1:Q12';
o='R1:R12';
p='S1:S12';
A=xlsread(filename,1,a);
B=xlsread(filename,1,b);

```
C=xlsread(filename,1,c);
D=xlsread(filename,1,d);
E=xlsread(filename,1,e);
F=xlsread(filename,1,f);
G=xlsread(filename,1,g);
H=xlsread(filename,1,h);
I=xlsread(filename,1,i);
J=xlsread(filename,1,j);
K=xlsread(filename,1,k);
L=xlsread(filename,1,l);
M=xlsread(filename,1,m);
N=xlsread(filename,1,n);
O=xlsread(filename,1,o);
P=xlsread(filename,1,p);
sheet=2;
a1='A1:A12';
b1='B1:B12';
c1='C1:C12';
d1='D1:D12';
e1='F1:F12';
f1='G1:G12';
g1='H1:H12';
h1='I1:I12';
i1='K1:K12';
j1='L1:L12';
k1='M1:N12';
l1='N1:O12';
m1='P1:P12';
n1='Q1:Q12';
o1='R1:R12';
p1='S1:S12';
```

```
A1=xlsread(filename,2,a1);
B1=xlsread(filename,2,b1);
C1=xlsread(filename,2,c1);
D1=xlsread(filename,2,d1);
E1=xlsread(filename,2,e1);
F1=xlsread(filename,2,f1);
G1=xlsread(filename,2,g1);
H1=xlsread(filename,2,h1);
I1=xlsread(filename,2,i1);
J1=xlsread(filename,2,j1);
K1=xlsread(filename,2,k1);
L1=xlsread(filename,2,l1);
M1=xlsread(filename,2,m1);
N1=xlsread(filename,2,n1);
O1=xlsread(filename,2,o1);
P1=xlsread(filename,2,p1);
sheet=3;
a2='A1:A12';
b2='B1:B12';
c2='C1:C12';
d2='D1:D12';
e2='F1:F12';
f2='G1:G12';
g2='H1:H12';
h2='I1:I12';
i2='K1:K12';
j2='L1:L12';
k2='M1:N12';
l2='N1:O12';
m2='P1:P12';
n2='Q1:Q12';
```

```
o2='R1:R12';
p2='S1:S12';
A2=xlsread(filename,3,a2);
B2=xlsread(filename,3,b2);
C2=xlsread(filename,3,c2);
D2=xlsread(filename,3,d2);
E2=xlsread(filename,3,e2);
F2=xlsread(filename,3,f2);
G2=xlsread(filename,3,g2);
H2=xlsread(filename,3,h2);
I2=xlsread(filename,3,i2);
J2=xlsread(filename,3,j2);
K2=xlsread(filename,3,k2);
L2=xlsread(filename,3,l2);
M2=xlsread(filename,3,m2);
N2=xlsread(filename,3,n2);
O2=xlsread(filename,3,o2);
P2=xlsread(filename,3,p2);
sheet=4;
a3='A1:A12';
b3='B1:B12';
c3='C1:C12';
d3='D1:D12';
e3='F1:F12';
f3='G1:G12';
g3='H1:H12';
h3='I1:I12';
A3=xlsread(filename,4,a3);
B3=xlsread(filename,4,b3);
C3=xlsread(filename,4,c3);
D3=xlsread(filename,4,d3);
```

```
E3=xlsread(filename,4,e3);
F3=xlsread(filename,4,f3);
G3=xlsread(filename,4,g3);
H3=xlsread(filename,4,h3);
x=[1,2,3,4,5,6,7,8,9,10,11];
y=[1,2,3,4,5,6,7,8,9,10];
z=[1,2,3,4,5,6,7,8,9,10,11,12];
plot(x,A,z,E,x,I,z,M,x,A1,z,E1,z,I1,z,M1,z,A2,z,E2,z,I2,z,M2,z,A3,x,E3);
xlabel('Time (months)');ylabel('AOD 440nm (unitless)');
legend('2000','2001','2002','2003','2004','2005','2006','2007','2008','2009','2010','2011','2012','2
013')

##### SOURCE END #####
--></body></html>
```

MATLAB File Atmospheric Constants Abidjan

```
  </style></head><body><div class="content"><pre class="codeinput">filename=<span
class="string">'Cotedvoire Abidjan.xlsx'</span>;
sheet=1;
a=<span class="string">'A1:A12'</span>;
b=<span class="string">'B1:B12'</span>;
c=<span class="string">'C1:C12'</span>;
d=<span class="string">'D1:D12'</span>;
e=<span class="string">'F1:F12'</span>;
f=<span class="string">'G1:G12'</span>;
g=<span class="string">'H1:H12'</span>;
h=<span class="string">'I1:I12'</span>;
i=<span class="string">'K1:K12'</span>;
j=<span class="string">'L1:L12'</span>;
k=<span class="string">'M1:N12'</span>;
```

```
l='N1:O12';
m='P1:P12';
n='Q1:Q12';
o='R1:R12';
p='S1:S12';
A=xlsread(filename,1,a);
B=xlsread(filename,1,b);
C=xlsread(filename,1,c);
D=xlsread(filename,1,d);
E=xlsread(filename,1,e);
F=xlsread(filename,1,f);
G=xlsread(filename,1,g);
H=xlsread(filename,1,h);
I=xlsread(filename,1,i);
J=xlsread(filename,1,j);
K=xlsread(filename,1,k);
L=xlsread(filename,1,l);
M=xlsread(filename,1,m);
N=xlsread(filename,1,n);
O=xlsread(filename,1,o);
P=xlsread(filename,1,p);
sheet=2;
a1='A1:A12';
b1='B1:B12';
c1='C1:C12';
d1='D1:D12';
e1='F1:F12';
f1='G1:G12';
g1='H1:H12';
h1='I1:I12';
i1='K1:K12';
```

```
j1=<span class="string">'L1:L12'</span>;
k1=<span class="string">'M1:N12'</span>;
l1=<span class="string">'N1:O12'</span>;
m1=<span class="string">'P1:P12'</span>;
n1=<span class="string">'Q1:Q12'</span>;
o1=<span class="string">'R1:R12'</span>;
p1=<span class="string">'S1:S12'</span>;
A1=xlsread(filename,2,a1);
B1=xlsread(filename,2,b1);
C1=xlsread(filename,2,c1);
D1=xlsread(filename,2,d1);
E1=xlsread(filename,2,e1);
F1=xlsread(filename,2,f1);
G1=xlsread(filename,2,g1);
H1=xlsread(filename,2,h1);
I1=xlsread(filename,2,i1);
J1=xlsread(filename,2,j1);
K1=xlsread(filename,2,k1);
L1=xlsread(filename,2,l1);
M1=xlsread(filename,2,m1);
N1=xlsread(filename,2,n1);
O1=xlsread(filename,2,o1);
P1=xlsread(filename,2,p1);
sheet=3;
a2=<span class="string">'A1:A12'</span>;
b2=<span class="string">'B1:B12'</span>;
c2=<span class="string">'C1:C12'</span>;
d2=<span class="string">'D1:D12'</span>;
e2=<span class="string">'F1:F12'</span>;
f2=<span class="string">'G1:G12'</span>;
g2=<span class="string">'H1:H12'</span>;
```

h2='I1:I12';
i2='K1:K12';
j2='L1:L12';
k2='M1:N12';
l2='N1:O12';
m2='P1:P12';
n2='Q1:Q12';
o2='R1:R12';
p2='S1:S12';
A2=xlsread(filename,3,a2);
B2=xlsread(filename,3,b2);
C2=xlsread(filename,3,c2);
D2=xlsread(filename,3,d2);
E2=xlsread(filename,3,e2);
F2=xlsread(filename,3,f2);
G2=xlsread(filename,3,g2);
H2=xlsread(filename,3,h2);
I2=xlsread(filename,3,i2);
J2=xlsread(filename,3,j2);
K2=xlsread(filename,3,k2);
L2=xlsread(filename,3,l2);
M2=xlsread(filename,3,m2);
N2=xlsread(filename,3,n2);
O2=xlsread(filename,3,o2);
P2=xlsread(filename,3,p2);
sheet=4;
a3='A1:A12';
b3='B1:B12';
c3='C1:C12';
d3='D1:D12';
e3='F1:F12';

f3='G1:G12';
g3='H1:H12';
h3='I1:I12';
A3=xlsread(filename,4,a3);
B3=xlsread(filename,4,b3);
C3=xlsread(filename,4,c3);
D3=xlsread(filename,4,d3);
E3=xlsread(filename,4,e3);
F3=xlsread(filename,4,f3);
G3=xlsread(filename,4,g3);
H3=xlsread(filename,4,h3);
x=[1,2,3,4,5,6,7,8,9,10,11];
y=[1,2,3,4,5,6,7,8,9,10];
z=[1,2,3,4,5,6,7,8,9,10,11,12];
plot(y,A,z,E,z,I,z,M,z,A1,z,E1,z,I1,z,M1,z,A2,z,E2,z,I2,z,M2,z,A3,x,E3);
xlabel('Time (months)');ylabel('AOD
440nm (unitless)');
legend('2000','2001',<span
class="string">'2002','2003',<span
class="string">'2004','2005',<span
class="string">'2006','2007',<span
class="string">'2008','2009',<span
class="string">'2010','2011',<span
class="string">'2012','2013')
</pre><img vspace="5" hspace="5" src="procotediovreabidjan_01.png" alt=""> <p
class="footer">
Published with MATLAB® 7.9
</p> <!--
SOURCE BEGIN
filename='Cotedvoire Abidjan.xlsx';
sheet=1;
a='A1:A12';

```
b='B1:B12';
c='C1:C12';
d='D1:D12';
e='F1:F12';
f='G1:G12';
g='H1:H12';
h='I1:I12';
i='K1:K12';
j='L1:L12';
k='M1:N12';
l='N1:O12';
m='P1:P12';
n='Q1:Q12';
o='R1:R12';
p='S1:S12';
A=xlsread(filename,1,a);
B=xlsread(filename,1,b);
C=xlsread(filename,1,c);
D=xlsread(filename,1,d);
E=xlsread(filename,1,e);
F=xlsread(filename,1,f);
G=xlsread(filename,1,g);
H=xlsread(filename,1,h);
I=xlsread(filename,1,i);
J=xlsread(filename,1,j);
K=xlsread(filename,1,k);
L=xlsread(filename,1,l);
M=xlsread(filename,1,m);
N=xlsread(filename,1,n);
O=xlsread(filename,1,o);
P=xlsread(filename,1,p);
```

```
sheet=2;
a1='A1:A12';
b1='B1:B12';
c1='C1:C12';
d1='D1:D12';
e1='F1:F12';
f1='G1:G12';
g1='H1:H12';
h1='I1:I12';
i1='K1:K12';
j1='L1:L12';
k1='M1:N12';
l1='N1:O12';
m1='P1:P12';
n1='Q1:Q12';
o1='R1:R12';
p1='S1:S12';
A1=xlsread(filename,2,a1);
B1=xlsread(filename,2,b1);
C1=xlsread(filename,2,c1);
D1=xlsread(filename,2,d1);
E1=xlsread(filename,2,e1);
F1=xlsread(filename,2,f1);
G1=xlsread(filename,2,g1);
H1=xlsread(filename,2,h1);
I1=xlsread(filename,2,i1);
J1=xlsread(filename,2,j1);
K1=xlsread(filename,2,k1);
L1=xlsread(filename,2,l1);
M1=xlsread(filename,2,m1);
N1=xlsread(filename,2,n1);
```

```
O1=xlsread(filename,2,o1);
P1=xlsread(filename,2,p1);
sheet=3;
a2='A1:A12';
b2='B1:B12';
c2='C1:C12';
d2='D1:D12';
e2='F1:F12';
f2='G1:G12';
g2='H1:H12';
h2='I1:I12';
i2='K1:K12';
j2='L1:L12';
k2='M1:N12';
l2='N1:O12';
m2='P1:P12';
n2='Q1:Q12';
o2='R1:R12';
p2='S1:S12';
A2=xlsread(filename,3,a2);
B2=xlsread(filename,3,b2);
C2=xlsread(filename,3,c2);
D2=xlsread(filename,3,d2);
E2=xlsread(filename,3,e2);
F2=xlsread(filename,3,f2);
G2=xlsread(filename,3,g2);
H2=xlsread(filename,3,h2);
I2=xlsread(filename,3,i2);
J2=xlsread(filename,3,j2);
K2=xlsread(filename,3,k2);
L2=xlsread(filename,3,l2);
```

```
M2=xlsread(filename,3,m2);
N2=xlsread(filename,3,n2);
O2=xlsread(filename,3,o2);
P2=xlsread(filename,3,p2);
sheet=4;
a3='A1:A12';
b3='B1:B12';
c3='C1:C12';
d3='D1:D12';
e3='F1:F12';
f3='G1:G12';
g3='H1:H12';
h3='I1:I12';
A3=xlsread(filename,4,a3);
B3=xlsread(filename,4,b3);
C3=xlsread(filename,4,c3);
D3=xlsread(filename,4,d3);
E3=xlsread(filename,4,e3);
F3=xlsread(filename,4,f3);
G3=xlsread(filename,4,g3);
H3=xlsread(filename,4,h3);
x=[1,2,3,4,5,6,7,8,9,10,11];
y=[1,2,3,4,5,6,7,8,9,10];
z=[1,2,3,4,5,6,7,8,9,10,11,12];
plot(y,A,z,E,z,I,z,M,z,A1,z,E1,z,I1,z,M1,z,A2,z,E2,z,I2,z,M2,z,A3,x,E3);
xlabel('Time (months)');ylabel('AOD 440nm (unitless)');
legend('2000','2001','2002','2003','2004','2005','2006','2007','2008','2009','2010','2011','2012','2
013')

##### SOURCE END #####
--></body></html>
```

MATLAB File Atmospheric Constants Boundougou

</style></head><body> <pre class="codeinput">filename='Cotedevoire Bondougou.xlsx';
sheet=1;
a='A1:A12';
b='B1:B12';
c='C1:C12';
d='D1:D12';
e='F1:F12';
f='G1:G12';
g='H1:H12';
h='I1:I12';
i='K1:K12';
j='L1:L12';
k='M1:N12';
l='N1:O12';
m='P1:P12';
n='Q1:Q12';
o='R1:R12';
p='S1:S12';
A=xlsread(filename,1,a);
B=xlsread(filename,1,b);
C=xlsread(filename,1,c);
D=xlsread(filename,1,d);
E=xlsread(filename,1,e);
F=xlsread(filename,1,f);
G=xlsread(filename,1,g);
H=xlsread(filename,1,h);
I=xlsread(filename,1,i);

```
J=xlsread(filename,1,j);
K=xlsread(filename,1,k);
L=xlsread(filename,1,l);
M=xlsread(filename,1,m);
N=xlsread(filename,1,n);
O=xlsread(filename,1,o);
P=xlsread(filename,1,p);
sheet=2;
a1=<span class="string">'A1:A12'</span>;
b1=<span class="string">'B1:B12'</span>;
c1=<span class="string">'C1:C12'</span>;
d1=<span class="string">'D1:D12'</span>;
e1=<span class="string">'F1:F12'</span>;
f1=<span class="string">'G1:G12'</span>;
g1=<span class="string">'H1:H12'</span>;
h1=<span class="string">'I1:I12'</span>;
i1=<span class="string">'K1:K12'</span>;
j1=<span class="string">'L1:L12'</span>;
k1=<span class="string">'M1:N12'</span>;
l1=<span class="string">'N1:O12'</span>;
m1=<span class="string">'P1:P12'</span>;
n1=<span class="string">'Q1:Q12'</span>;
o1=<span class="string">'R1:R12'</span>;
p1=<span class="string">'S1:S12'</span>;
A1=xlsread(filename,2,a1);
B1=xlsread(filename,2,b1);
C1=xlsread(filename,2,c1);
D1=xlsread(filename,2,d1);
E1=xlsread(filename,2,e1);
F1=xlsread(filename,2,f1);
G1=xlsread(filename,2,g1);
```

```
H1=xlsread(filename,2,h1);
I1=xlsread(filename,2,i1);
J1=xlsread(filename,2,j1);
K1=xlsread(filename,2,k1);
L1=xlsread(filename,2,l1);
M1=xlsread(filename,2,m1);
N1=xlsread(filename,2,n1);
O1=xlsread(filename,2,o1);
P1=xlsread(filename,2,p1);
sheet=3;
a2=<span class="string">'A1:A12'</span>;
b2=<span class="string">'B1:B12'</span>;
c2=<span class="string">'C1:C12'</span>;
d2=<span class="string">'D1:D12'</span>;
e2=<span class="string">'F1:F12'</span>;
f2=<span class="string">'G1:G12'</span>;
g2=<span class="string">'H1:H12'</span>;
h2=<span class="string">'I1:I12'</span>;
i2=<span class="string">'K1:K12'</span>;
j2=<span class="string">'L1:L12'</span>;
k2=<span class="string">'M1:N12'</span>;
l2=<span class="string">'N1:O12'</span>;
m2=<span class="string">'P1:P12'</span>;
n2=<span class="string">'Q1:Q12'</span>;
o2=<span class="string">'R1:R12'</span>;
p2=<span class="string">'S1:S12'</span>;
A2=xlsread(filename,3,a2);
B2=xlsread(filename,3,b2);
C2=xlsread(filename,3,c2);
D2=xlsread(filename,3,d2);
E2=xlsread(filename,3,e2);
```

```
F2=xlsread(filename,3,f2);
G2=xlsread(filename,3,g2);
H2=xlsread(filename,3,h2);
I2=xlsread(filename,3,i2);
J2=xlsread(filename,3,j2);
K2=xlsread(filename,3,k2);
L2=xlsread(filename,3,l2);
M2=xlsread(filename,3,m2);
N2=xlsread(filename,3,n2);
O2=xlsread(filename,3,o2);
P2=xlsread(filename,3,p2);
sheet=4;
a3=<span class="string">'A1:A12'</span>;
b3=<span class="string">'B1:B12'</span>;
c3=<span class="string">'C1:C12'</span>;
d3=<span class="string">'D1:D12'</span>;
e3=<span class="string">'F1:F12'</span>;
f3=<span class="string">'G1:G12'</span>;
g3=<span class="string">'H1:H12'</span>;
h3=<span class="string">'I1:I12'</span>;
A3=xlsread(filename,4,a3);
B3=xlsread(filename,4,b3);
C3=xlsread(filename,4,c3);
D3=xlsread(filename,4,d3);
E3=xlsread(filename,4,e3);
F3=xlsread(filename,4,f3);
G3=xlsread(filename,4,g3);
H3=xlsread(filename,4,h3);
x=[1,2,3,4,5,6,7,8,9,10,11];
y=[1,2,3,4,5,6,7,8,9,10];
z=[1,2,3,4,5,6,7,8,9,10,11,12];
```

plot(y,A,z,E,z,I,z,M,z,A1,z,E1,z,I1,z,M1,z,A2,z,E2,z,I2,z,M2,z,A3,x,E3);
xlabel('Time (months)');ylabel('AOD 440nm (unitless)');
legend('2000','2001','2002','2003','2004','2005','2006','2007','2008','2009','2010','2011','2012','2013')
</pre><img vspace="5" hspace="5" src="procotedevoirbondogo_01.png" alt="">
Published with MATLAB® 7.9
 <!--
SOURCE BEGIN
filename='Cotedevoire Bondougou.xlsx';
sheet=1;
a='A1:A12';
b='B1:B12';
c='C1:C12';
d='D1:D12';
e='F1:F12';
f='G1:G12';
g='H1:H12';
h='I1:I12';
i='K1:K12';
j='L1:L12';
k='M1:N12';
l='N1:O12';
m='P1:P12';
n='Q1:Q12';
o='R1:R12';

```
p='S1:S12';
A=xlsread(filename,1,a);
B=xlsread(filename,1,b);
C=xlsread(filename,1,c);
D=xlsread(filename,1,d);
E=xlsread(filename,1,e);
F=xlsread(filename,1,f);
G=xlsread(filename,1,g);
H=xlsread(filename,1,h);
I=xlsread(filename,1,i);
J=xlsread(filename,1,j);
K=xlsread(filename,1,k);
L=xlsread(filename,1,l);
M=xlsread(filename,1,m);
N=xlsread(filename,1,n);
O=xlsread(filename,1,o);
P=xlsread(filename,1,p);
sheet=2;
a1='A1:A12';
b1='B1:B12';
c1='C1:C12';
d1='D1:D12';
e1='F1:F12';
f1='G1:G12';
g1='H1:H12';
h1='I1:I12';
i1='K1:K12';
j1='L1:L12';
k1='M1:N12';
l1='N1:O12';
m1='P1:P12';
```

```
n1='Q1:Q12';
o1='R1:R12';
p1='S1:S12';
A1=xlsread(filename,2,a1);
B1=xlsread(filename,2,b1);
C1=xlsread(filename,2,c1);
D1=xlsread(filename,2,d1);
E1=xlsread(filename,2,e1);
F1=xlsread(filename,2,f1);
G1=xlsread(filename,2,g1);
H1=xlsread(filename,2,h1);
I1=xlsread(filename,2,i1);
J1=xlsread(filename,2,j1);
K1=xlsread(filename,2,k1);
L1=xlsread(filename,2,l1);
M1=xlsread(filename,2,m1);
N1=xlsread(filename,2,n1);
O1=xlsread(filename,2,o1);
P1=xlsread(filename,2,p1);
sheet=3;
a2='A1:A12';
b2='B1:B12';
c2='C1:C12';
d2='D1:D12';
e2='F1:F12';
f2='G1:G12';
g2='H1:H12';
h2='I1:I12';
i2='K1:K12';
j2='L1:L12';
k2='M1:N12';
```

```
l2='N1:O12';
m2='P1:P12';
n2='Q1:Q12';
o2='R1:R12';
p2='S1:S12';
A2=xlsread(filename,3,a2);
B2=xlsread(filename,3,b2);
C2=xlsread(filename,3,c2);
D2=xlsread(filename,3,d2);
E2=xlsread(filename,3,e2);
F2=xlsread(filename,3,f2);
G2=xlsread(filename,3,g2);
H2=xlsread(filename,3,h2);
I2=xlsread(filename,3,i2);
J2=xlsread(filename,3,j2);
K2=xlsread(filename,3,k2);
L2=xlsread(filename,3,l2);
M2=xlsread(filename,3,m2);
N2=xlsread(filename,3,n2);
O2=xlsread(filename,3,o2);
P2=xlsread(filename,3,p2);
sheet=4;
a3='A1:A12';
b3='B1:B12';
c3='C1:C12';
d3='D1:D12';
e3='F1:F12';
f3='G1:G12';
g3='H1:H12';
h3='I1:I12';
A3=xlsread(filename,4,a3);
```

```
B3=xlsread(filename,4,b3);
C3=xlsread(filename,4,c3);
D3=xlsread(filename,4,d3);
E3=xlsread(filename,4,e3);
F3=xlsread(filename,4,f3);
G3=xlsread(filename,4,g3);
H3=xlsread(filename,4,h3);
x=[1,2,3,4,5,6,7,8,9,10,11];
y=[1,2,3,4,5,6,7,8,9,10];
z=[1,2,3,4,5,6,7,8,9,10,11,12];
plot(y,A,z,E,z,I,z,M,z,A1,z,E1,z,I1,z,M1,z,A2,z,E2,z,I2,z,M2,z,A3,x,E3);
xlabel('Time (months)');ylabel('AOD 440nm (unitless)');
legend('2000','2001','2002','2003','2004','2005','2006','2007','2008','2009','2010','2011','2012','2
013')

##### SOURCE END #####
--></body></html>
```

MATLAB File Atmospheric Constants Praia

```
  </style></head><body><div class="content"><pre class="codeinput">filename=<span
class="string">'Capeverde Praia2.xlsx'</span>;
sheet=1;
a=<span class="string">'A1:A12'</span>;
b=<span class="string">'B1:B12'</span>;
c=<span class="string">'C1:C12'</span>;
d=<span class="string">'D1:D12'</span>;
e=<span class="string">'F1:F12'</span>;
f=<span class="string">'G1:G12'</span>;
g=<span class="string">'H1:H12'</span>;
h=<span class="string">'I1:I12'</span>;
```

i='K1:K12';
j='L1:L12';
k='M1:N12';
l='N1:O12';
m='P1:P12';
n='Q1:Q12';
o='R1:R12';
p='S1:S12';
A=xlsread(filename,1,a);
B=xlsread(filename,1,b);
C=xlsread(filename,1,c);
D=xlsread(filename,1,d);
E=xlsread(filename,1,e);
F=xlsread(filename,1,f);
G=xlsread(filename,1,g);
H=xlsread(filename,1,h);
I=xlsread(filename,1,i);
J=xlsread(filename,1,j);
K=xlsread(filename,1,k);
L=xlsread(filename,1,l);
M=xlsread(filename,1,m);
N=xlsread(filename,1,n);
O=xlsread(filename,1,o);
P=xlsread(filename,1,p);
sheet=2;
a1='A1:A12';
b1='B1:B12';
c1='C1:C12';
d1='D1:D12';
e1='F1:F12';
f1='G1:G12';

g1='H1:H12';
h1='I1:I12';
i1='K1:K12';
j1='L1:L12';
k1='M1:N12';
l1='N1:O12';
m1='P1:P12';
n1='Q1:Q12';
o1='R1:R12';
p1='S1:S12';
A1=xlsread(filename,2,a1);
B1=xlsread(filename,2,b1);
C1=xlsread(filename,2,c1);
D1=xlsread(filename,2,d1);
E1=xlsread(filename,2,e1);
F1=xlsread(filename,2,f1);
G1=xlsread(filename,2,g1);
H1=xlsread(filename,2,h1);
I1=xlsread(filename,2,i1);
J1=xlsread(filename,2,j1);
K1=xlsread(filename,2,k1);
L1=xlsread(filename,2,l1);
M1=xlsread(filename,2,m1);
N1=xlsread(filename,2,n1);
O1=xlsread(filename,2,o1);
P1=xlsread(filename,2,p1);
sheet=3;
a2='A1:A12';
b2='B1:B12';
c2='C1:C12';
d2='D1:D12';

e2='F1:F12';
f2='G1:G12';
g2='H1:H12';
h2='I1:I12';
i2='K1:K12';
j2='L1:L12';
k2='M1:N12';
l2='N1:O12';
m2='P1:P12';
n2='Q1:Q12';
o2='R1:R12';
p2='S1:S12';
A2=xlsread(filename,3,a2);
B2=xlsread(filename,3,b2);
C2=xlsread(filename,3,c2);
D2=xlsread(filename,3,d2);
E2=xlsread(filename,3,e2);
F2=xlsread(filename,3,f2);
G2=xlsread(filename,3,g2);
H2=xlsread(filename,3,h2);
I2=xlsread(filename,3,i2);
J2=xlsread(filename,3,j2);
K2=xlsread(filename,3,k2);
L2=xlsread(filename,3,l2);
M2=xlsread(filename,3,m2);
N2=xlsread(filename,3,n2);
O2=xlsread(filename,3,o2);
P2=xlsread(filename,3,p2);
sheet=4;
a3='A1:A12';
b3='B1:B12';

c3='C1:C12';
d3='D1:D12';
e3='F1:F12';
f3='G1:G12';
g3='H1:H12';
h3='I1:I12';
A3=xlsread(filename,4,a3);
B3=xlsread(filename,4,b3);
C3=xlsread(filename,4,c3);
D3=xlsread(filename,4,d3);
E3=xlsread(filename,4,e3);
F3=xlsread(filename,4,f3);
G3=xlsread(filename,4,g3);
H3=xlsread(filename,4,h3);
x=[1,2,3,4,5,6,7,8,9,10,11];
y=[1,2,3,4,5,6,7,8,9,10];
z=[1,2,3,4,5,6,7,8,9,10,11,12];
plot(y,A,z,E,z,I,z,M,z,A1,z,E1,z,I1,z,M1,z,A2,z,E2,z,I2,z,M2,z,A3,x,E3);
xlabel('Time (months)');ylabel('AOD 440nm (unitless)');
legend('2000','2001','2002','2003','2004','2005','2006','2007','2008','2009','2010','2011','2012','2013')
</pre><img vspace="5" hspace="5" src="procapeverdepraia_01.png" alt="">
Published with MATLAB® 7.9
 <!--
SOURCE BEGIN

```
filename='Capeverde Praia2.xlsx';
sheet=1;
a='A1:A12';
b='B1:B12';
c='C1:C12';
d='D1:D12';
e='F1:F12';
f='G1:G12';
g='H1:H12';
h='I1:I12';
i='K1:K12';
j='L1:L12';
k='M1:N12';
l='N1:O12';
m='P1:P12';
n='Q1:Q12';
o='R1:R12';
p='S1:S12';
A=xlsread(filename,1,a);
B=xlsread(filename,1,b);
C=xlsread(filename,1,c);
D=xlsread(filename,1,d);
E=xlsread(filename,1,e);
F=xlsread(filename,1,f);
G=xlsread(filename,1,g);
H=xlsread(filename,1,h);
I=xlsread(filename,1,i);
J=xlsread(filename,1,j);
K=xlsread(filename,1,k);
L=xlsread(filename,1,l);
M=xlsread(filename,1,m);
```

```
N=xlsread(filename,1,n);
O=xlsread(filename,1,o);
P=xlsread(filename,1,p);
sheet=2;
a1='A1:A12';
b1='B1:B12';
c1='C1:C12';
d1='D1:D12';
e1='F1:F12';
f1='G1:G12';
g1='H1:H12';
h1='I1:I12';
i1='K1:K12';
j1='L1:L12';
k1='M1:N12';
l1='N1:O12';
m1='P1:P12';
n1='Q1:Q12';
o1='R1:R12';
p1='S1:S12';
A1=xlsread(filename,2,a1);
B1=xlsread(filename,2,b1);
C1=xlsread(filename,2,c1);
D1=xlsread(filename,2,d1);
E1=xlsread(filename,2,e1);
F1=xlsread(filename,2,f1);
G1=xlsread(filename,2,g1);
H1=xlsread(filename,2,h1);
I1=xlsread(filename,2,i1);
J1=xlsread(filename,2,j1);
K1=xlsread(filename,2,k1);
```

```
L1=xlsread(filename,2,l1);
M1=xlsread(filename,2,m1);
N1=xlsread(filename,2,n1);
O1=xlsread(filename,2,o1);
P1=xlsread(filename,2,p1);
sheet=3;
a2='A1:A12';
b2='B1:B12';
c2='C1:C12';
d2='D1:D12';
e2='F1:F12';
f2='G1:G12';
g2='H1:H12';
h2='I1:I12';
i2='K1:K12';
j2='L1:L12';
k2='M1:N12';
l2='N1:O12';
m2='P1:P12';
n2='Q1:Q12';
o2='R1:R12';
p2='S1:S12';
A2=xlsread(filename,3,a2);
B2=xlsread(filename,3,b2);
C2=xlsread(filename,3,c2);
D2=xlsread(filename,3,d2);
E2=xlsread(filename,3,e2);
F2=xlsread(filename,3,f2);
G2=xlsread(filename,3,g2);
H2=xlsread(filename,3,h2);
I2=xlsread(filename,3,i2);
```

```
J2=xlsread(filename,3,j2);
K2=xlsread(filename,3,k2);
L2=xlsread(filename,3,l2);
M2=xlsread(filename,3,m2);
N2=xlsread(filename,3,n2);
O2=xlsread(filename,3,o2);
P2=xlsread(filename,3,p2);
sheet=4;
a3='A1:A12';
b3='B1:B12';
c3='C1:C12';
d3='D1:D12';
e3='F1:F12';
f3='G1:G12';
g3='H1:H12';
h3='I1:I12';
A3=xlsread(filename,4,a3);
B3=xlsread(filename,4,b3);
C3=xlsread(filename,4,c3);
D3=xlsread(filename,4,d3);
E3=xlsread(filename,4,e3);
F3=xlsread(filename,4,f3);
G3=xlsread(filename,4,g3);
H3=xlsread(filename,4,h3);
x=[1,2,3,4,5,6,7,8,9,10,11];
y=[1,2,3,4,5,6,7,8,9,10];
z=[1,2,3,4,5,6,7,8,9,10,11,12];
plot(y,A,z,E,z,I,z,M,z,A1,z,E1,z,I1,z,M1,z,A2,z,E2,z,I2,z,M2,z,A3,x,E3);
xlabel('Time (months)');ylabel('AOD 440nm (unitless)');
legend('2000','2001','2002','2003','2004','2005','2006','2007','2008','2009','2010','2011','2012','2
013')
```

SOURCE END
--></body></html>

</style></head><body> <pre class="codeinput">filename='Niamey.xlsx';
sheet=1;
a='A1:A12';
b='B1:B12';
c='C1:C12';
d='D1:D12';
e='E1:E12';
f='F1:F12';
g='G1:G12';
h='H1:H12';
i='I1:I12';
j='JL1:J12';
k='K1:K12';
l='L1:L12';
A=xlsread(filename,1,a);
B=xlsread(filename,1,b);
C=xlsread(filename,1,c);
D=xlsread(filename,1,d);
E=xlsread(filename,1,e);
F=xlsread(filename,1,f);
G=xlsread(filename,1,g);
H=xlsread(filename,1,h);
I=xlsread(filename,1,i);
J=xlsread(filename,1,j);
K=xlsread(filename,1,k);
L=xlsread(filename,1,l);

```
z=[1,2,3,4,5,6,7,8,9,10,11,12];
plot(z,A,z,B,z,C,z,D,z,E,z,F,z,G,z,H,z,I,z,J,z,K,z,L);
xlabel(<span class="string">'Time (months)'</span>);ylabel(<span class="string">'AOD
440nm (unitless)'</span>);
</pre><img vspace="5" hspace="5" src="niamey_01.png" alt=""> <p class="footer"><br>
    Published with MATLAB&reg; 7.9<br></p></div><!--
##### SOURCE BEGIN #####
filename='Niamey.xlsx';
sheet=1;
a='A1:A12';
b='B1:B12';
c='C1:C12';
d='D1:D12';
e='E1:E12';
f='F1:F12';
g='G1:G12';
h='H1:H12';
i='I1:I12';
j='JL1:J12';
k='K1:K12';
l='L1:L12';
A=xlsread(filename,1,a);
B=xlsread(filename,1,b);
C=xlsread(filename,1,c);
D=xlsread(filename,1,d);
E=xlsread(filename,1,e);
F=xlsread(filename,1,f);
G=xlsread(filename,1,g);
H=xlsread(filename,1,h);
I=xlsread(filename,1,i);
J=xlsread(filename,1,j);
```

```
K=xlsread(filename,1,k);
L=xlsread(filename,1,l);
z=[1,2,3,4,5,6,7,8,9,10,11,12];
plot(z,A,z,B,z,C,z,D,z,E,z,F,z,G,z,H,z,I,z,J,z,K,z,L);
xlabel('Time (months)'); ylabel('AOD 440nm (unitless)');


##### SOURCE END #####
--></body></html>
```